



Al-afeef, Ala' (2016) *Transmission electron tomography: quality assessment and enhancement for three-dimensional imaging of nanostructures*. PhD thesis.

<http://theses.gla.ac.uk/7683/>

Copyright and moral rights for this thesis are retained by the author

A copy can be downloaded for personal non-commercial research or study, without prior permission or charge

This thesis cannot be reproduced or quoted extensively from without first obtaining permission in writing from the Author

The content must not be changed in any way or sold commercially in any format or medium without the formal permission of the Author

When referring to this work, full bibliographic details including the author, title, awarding institution and date of the thesis must be given

Glasgow Theses Service
<http://theses.gla.ac.uk/>
theses@gla.ac.uk

Transmission Electron Tomography

Quality Assessment and Enhancement for
Three-Dimensional Imaging of Nanostructures



Ala' Sa'd Shhadeh Al-Afeef

Submitted in fulfilment of the requirements for the Degree of
Doctor of Philosophy

School of Computing Science
College of Science and Engineering
University of Glasgow

©Ala' Al-Afeef, July 2016

Abstract

Transmission Electron Tomography: Quality Assessment and Enhancement for Three-Dimensional Imaging of Nanostructures.

Ala' Al-Afeef

Nanotechnology has revolutionised humanity's capability in building microscopic systems by manipulating materials on a molecular and atomic scale. Nanosystems are becoming increasingly smaller and more complex from the chemical perspective which increases the demand for microscopic characterisation techniques. Among others, transmission electron microscopy (TEM) is an indispensable tool that is increasingly used to study the structures of nanosystems down to the molecular and atomic scale. However, despite the effectivity of this tool, it can only provide 2-dimensional projection (shadow) images of the 3D structure, leaving the 3-dimensional information hidden which can lead to incomplete or erroneous characterization. One very promising inspection method is Electron Tomography (ET), which is rapidly becoming an important tool to explore the 3D nano-world. ET provides (sub-)nanometer resolution in all three dimensions of the sample under investigation. However, the fidelity of the ET tomogram that is achieved by current ET reconstruction procedures remains a major challenge. This thesis addresses the assessment and advancement of electron tomographic methods to enable high-fidelity three-dimensional investigations.

A quality assessment investigation was conducted to provide a quality quantitative analysis of the main established ET reconstruction algorithms and to study the influence of the experimental conditions on the quality of the reconstructed ET tomogram. Regular shaped nanoparticles were used as a ground-truth for this study. It is concluded that the fidelity of the post-reconstruction quantitative analysis and segmentation is limited, mainly by the fidelity of the reconstructed ET tomogram. This motivates the development of an improved tomographic reconstruction process.

In this thesis, a novel ET method was proposed, named dictionary learning electron tomography (DLET). DLET is based on the recent mathematical theorem of compressed sensing (CS) which employs the sparsity of ET tomograms to enable accurate reconstruction from undersampled (S)TEM tilt series. DLET learns the sparsifying transform (dictionary) in an adaptive way and reconstructs the tomogram simultaneously from highly undersampled tilt series. In this method, the sparsity is applied on overlapping image patches favouring local structures. Furthermore, the dictionary is adapted to the specific tomogram instance, thereby favouring better sparsity and consequently higher quality reconstructions. The reconstruction algorithm is based on an alternating procedure that learns the sparsifying dictionary and employs it to remove artifacts and noise in one step, and then restores the tomogram data in the other step.

Simulation and real ET experiments of several morphologies are performed with a variety of setups. Reconstruction results validate its efficiency in both noiseless and noisy cases and show that it yields an improved reconstruction quality with fast convergence. The proposed method enables the recovery of high-fidelity information without the need to worry about what sparsifying transform to select or whether the images used strictly follow the pre-conditions of a certain transform (e.g. strictly piecewise constant for Total Variation minimisation). This can also avoid artifacts that can be introduced by specific sparsifying transforms (e.g. the staircase artifacts that may result when using Total Variation minimisation).

Moreover, this thesis shows how reliable elementally sensitive tomography using EELS is possible with the aid of both appropriate use of Dual electron energy loss spectroscopy (DualEELS) and the DLET compressed sensing algorithm to make the best use of the limited data volume and signal to noise inherent in core-loss electron energy loss spectroscopy (EELS) from nanoparticles of an industrially important material.

Taken together, the results presented in this thesis demonstrates how high-fidelity ET reconstructions can be achieved using a compressed sensing approach.



To my parents Jina and Sa'd,
thank you for giving me my roots and teaching me to fly.
To Hiba, Hadeel, Shefa, Mona, Hind, Wael, Mahmoud, Deya and Moh,
for their endless love, support and encouragement on every adventure,
especially this one.

Always in my heart wherever I am.

Acknowledgements

The work presented in this thesis would not have been possible without the encouragement and support of numerous people, who I would like to thank from the bottom of my heart.

First and foremost I would like to express my deepest gratitude to my supervisor Dr. Paul Cockshott. It has been an honour to be his Ph.D student and pleasure to conduct this research under his supervision. I am thankful for his advice, support and giving the freedom and the flexibility to explore different avenues.

Always encouraging, I owe immense gratitude to my supervisor Dr. Ian MacLaren who found somehow the right balance between honesty and kindness. He has taught me, both consciously and un-consciously, how good work is done. I appreciate all his contributions of ideas, time and support to make my Ph.D experience stimulating and productive. The enthusiasm and joy he has for his research were motivational and contagious for me. I am also thankful for the excellent role model he has provided; I could not imagine a better mentor.

I also extend my gratitude to Dr. Stephen McVitie for providing guidance. I am grateful for his suggestions which had indeed helped me to improvise on my work. Innumerable times he has been more helpful than I could have imagined. One simply could not wish for a better, more supportive supervisors.

I would also like to extend my thanks to the technicians in the Kelvin Nanocharacterisation Centre for their role in managing the practicalities, in particular, Dr. Sam McFadzean our senior technician who keeps everything running and for maintaining the JEOL ARM200cF microscope which had been used in the tomography experiments in chapter 3 and 5. Mr. Colin How for his technical support to use the FEI Tecnai T20 electron microscope, and for rescuing me from many microscope disasters while examining samples for tomography, as well as Mr. William Smith for his help in obtaining the lamella sample using the FIB System.

I am also grateful to all of our collaborators, especially: Prof. Grant J. Jensen and Elitza I. Tocheva from Jensen Lab at Caltech. Prof. Younan Xia and Aleksey

Ruditskiy at Georgia Tech. Prof. Ifor Samuel, Dr. Alexander Alekseev, Dr. Gordon J Hedley, and Dr. Oleg A Ageev from School of Physics, University of St Andrews. Dr. Peter Eschbach from Oregon State University. I also thank Prof. Rik Brydson and colleagues for their several discussions during the Royal Microscopical Society Electron Microscopy summer school 2013. I also thank Prof. Anders Christian Hansen, the University of Cambridge for his fruitful discussion on compressed sensing. I am very much thankful to Paul Midgley, David B. Williams and C. Barry Carter for their advice and comments during the IFSM School for young scientists 2014.

I would like to extend my appreciation to Ian Zuazo and Patrick Bargés for providing the VC extraction replica and Joanna Bobynko for her help in processing the EELS data from it. I also like to thank and acknowledge the very generous contributions of Prof. Alan Craven's to the discussions that sorted chapter 5 out.

I would also like to thank all my colleague in the Computer Vision and Graphics group (CVG) group in the school of computing sciences and members of the Materials and Condensed Matter Physics (MCMP) group in school of physics and astronomy, who have contributed immensely to my personal and professional time at Glasgow University. The two groups have been a source of friendships as well as good advice and collaboration.

I am grateful to Scottish Informatics and Computer Science Alliance (SICSA) for funding training and other activities in computing sciences that were a great source of knowledge and collaborations for me. I extend my gratitude to Ms. Heather Lambie (Adviser of Studies) for promptly helping out with all the administrative issues including the internship at Argonne National Laboratory in Chicago, USA.

I gratefully acknowledge the funding by Lord Kelvin/Adam Smith Scholarship that made my Ph.D. work possible.

Finally, I would like to thanks, everyone who was supporting me through all the entire process.

"Nothing in life is to be feared, it is only to be understood. Now is the time to understand more, so that we may fear less."

- Marie Curie, 1867 – 1934

Declaration

I declare that, except where explicit reference is made to the contribution of others, this dissertation is the result of my own work and has not been submitted for any other degree at the University of Glasgow or any other institution.

This work was supported by Lord Kelvin/Adam Smith Scholarship at the University of Glasgow.

Ala' Al-Afeef
Glasgow, July 2016

Abbreviations

ADF	-	Annular Dark Field
ART	-	Algebraic Reconstruction Technique
BF	-	Bright-Field
CTF	-	Contrast Transfer Function
CCD	-	Charged Coupled Device
CT	-	Computed Tomography
CS	-	Compressed Sensing
DQE	-	Detective Quantum Efficiency
DCT	-	Discrete Cosine Transform
DF-TEM	-	Dark Field Transmission Electron Microscopy
DFoc	-	Depth of FOCus
DART	-	Discrete Algebraic Reconstruction Technique
DLET	-	dictionary Learning Electron Tomography
EELS	-	Electron Energy-Loss Spectroscopy
ET	-	Electron Tomography
EM	-	Electron Microscopy
EF-TEM	-	Energy Filtered Transmission Electron Microscopy
FFT	-	Fast Fourier Transform
GIF	-	Gatan Imaging Filter
HAADF	-	High-Angle Annular Dark-Field
MRI	-	Magnetic Resonance Imaging
MTF	-	Modulation Transfer Function
MI	-	Mutual Information
nm	-	Nano Meter
NUFFT	-	Non-Uniform Fast Fourier Transform

Abbreviations

PSF	-	Point Spread Function
ROI	-	Region Of Interest
SEM	-	Scanning Electron Microscopy
STEM	-	Scanning Transmission Electron Microscopy
SIRT	-	Simultaneous Iterative Reconstruction Technique
SNR	-	Signal-to-Noise Ratio
TEM	-	Transmission Electron Microscope
TV	-	Total Variation
WBP	-	Weighted Back-Projection
X-ray CAT	-	Computer-Aided Tomography or Computed Axial Tomography

Contents

1	Introduction	1
1.1	Thesis statement	2
1.2	Scope of thesis	3
1.3	Contributions	3
1.4	Publications	5
1.5	Thesis outline	6
2	Introduction to electron tomography	8
2.1	Introduction to transmission electron microscopy (TEM)	9
2.1.1	The development of electron microscopy	9
2.1.2	The structure of the TEM	12
2.1.3	Electron beam–specimen interactions	17
2.1.4	Imaging techniques in a TEM	20
2.1.5	Spectroscopy in the TEM/STEM	25
2.1.6	Radiation damage & contamination	31
2.1.7	Aberration-corrected S/TEM	32
2.2	Electron tomography: foundations and methods	34
2.2.1	From 2D to 3D electron microscopy	34
2.2.2	Brief history of tomography	35
2.2.3	Principles of tomographic image reconstruction	38
2.3	Practical aspects of electron tomography	43
2.3.1	Specimen preparation	43
2.3.2	Acquisition of tilt series - geometry	45
2.3.3	Tilt series alignment	54
2.3.4	Reconstruction of tomographic tilt series	56
2.3.5	Tomogram segmentation and quantification	68
2.3.6	Visualization	69
2.4	Conclusions	70

3	Quality assessment of electron tomography for TEM/STEM imaging	72
3.1	Introduction	73
3.2	Experimental methods	74
3.2.1	Materials and sample preparation	74
3.2.2	Instrumentation and experiment	74
3.2.3	Quality evaluation methods	76
3.3	Influence of reconstruction methods	79
3.4	Effect of the radial under-sampling	81
3.5	Effect of the missing wedge	84
3.6	Effects of mis-alignment	89
3.7	Conclusion	90
4	Compressed sensing electron tomography and the DLET algorithm	91
4.1	Introduction	92
4.2	Compressive sensing theory	95
4.2.1	Dictionary Learning	98
4.3	Methodology	101
4.3.1	Proposed Algorithm	102
4.3.2	Parameters	106
4.3.3	Objective function convergence	106
4.3.4	Termination criterion and computational complexity	107
4.4	Numerical simulation	107
4.4.1	Image quality metrics	108
4.4.2	Simulation study 1: the modified SheppLogan phantom	109
4.4.3	Simulation study 2: CS-phantom	113
4.4.4	Parameter Comparison	119
4.5	Organic photovoltaic solar cells 3D-morphology	121
4.5.1	Simulation study	123
4.5.2	Experimental results	126
4.6	Ebola virus-like particles 3D reconstruction using DLET	130
4.6.1	Motivation	130
4.6.2	Experimental	134
4.6.3	Results and discussion	134
4.7	Conclusion	135

5	Chemically sensitive electron tomography using DLET	137
5.1	Introduction	138
5.2	Methods	140
5.2.1	Advanced high strength steels and vanadium allows	140
5.2.2	Materials and sample preparation	140
5.2.3	Instrumentation and experiment	141
5.2.4	Post-acquisition procedure	143
5.2.5	Three dimensional image reconstruction	146
5.2.6	Visualisation	147
5.3	Simulations and experimental results	148
5.3.1	Simulation study: Reconstructions on simulated tilt series from an idealised octahedron	148
5.3.2	Experimental study: Reconstructions on experimental maps from DualEELS	152
5.4	Conclusion	158
6	Further applications of electron tomography using DLET	159
6.1	Acetonema longum bacteria	159
6.1.1	Background and motivation	160
6.1.2	Experimental procedure and results	161
6.2	Carbon nanofiber for fuel cell catalysts	165
6.2.1	Experimental procedure and results	166
6.3	Conclusion	171
7	Conclusions and Outlook	172
A	Supplementary movies	177
	References	179
	Index	207

List of Tables

3.1	Quality measures for under-sampling of MgO nanocube experiments	84
3.2	Quality measures for under-sampling of the nanospheres case. . .	85
3.3	Quality measures for the missing wedge study on MgO nanocube dataset	86
3.4	Quality measure for the missing wedge on the nanospheres.	89
3.5	Quality measures for misalignment of the MgO nanocube dataset.	90
3.6	Quality measures for misalignment of the nanospheres dataset. . .	90
4.1	Noise and Undersampling Evaluation	117
4.2	Quality metric values of CS-phantom reconstruction in Fig.4.13. .	119
4.3	Patch Size Parameter Evaluation Of DLET (n)	119
4.4	Parameter Evaluation Dictionary Size	120
4.5	Parameter Evaluation Discrepancy level (ϵ)	120
4.6	Quality metric values for the polymer solar cell reconstructions . .	126
5.1	Quality metric values of simulation reconstruction in Fig.5.4. . . .	150

List of Figures

2.1	Conventional TEM setup	13
2.2	Schematic diagram of a CCD detector	15
2.3	Image resolution in CCD Camera	16
2.4	Elastic scattering	18
2.5	Bragg diffraction	18
2.6	Inelastic scattering	19
2.7	Microscope setup for STEM imaging	21
2.8	Magnesium Oxide STEM imaging	22
2.9	Essential aspects of TEM	24
2.10	An EELS spectrum	27
2.11	Gatan imaging filter (GIF)	28
2.12	Energy Filtered TEM (EFTEM)	29
2.13	Radiation damage of Silver nanoparticle	32
2.14	Aberrations in electron lens	33
2.15	Schematic illustrating the data collection and reconstruction principles for electron tomography	35
2.16	Radon transform	39
2.17	Radon transform of a point object	40
2.18	Central slice theorem	41
2.19	the relations between real, Fourier and Radon space	42
2.20	Radial and Cartesian sampling geometry	43
2.21	The main stages of electron tomography	44
2.22	TEM Grid	45
2.23	Polepiece space limitation	46
2.24	Specimen holders	47
2.25	Reconstruction artifacts	48
2.26	Shadowing effect	49
2.27	Thickness and focus	50
2.28	Double tilt and rotate stage	51
2.29	EELS spectrum	52

2.30 Tilt axis misalignment	54
2.31 Back-projection	58
2.32 The Projection geometry for tomographic problem	59
2.33 Illustration of the Picard condition (PC)	61
2.34 Semi-convergence in tomographic reconstruction	63
2.35 SIRT flowchart	65
2.36 Under-sampling in ET	67
2.37 Feline Calicivirus	70
3.1 MgO HAADF–STEM projections images and their reconstruction	75
3.2 Nanosphere BF-TEM projections images and their reconstruction	77
3.3 Segmented surface of the MgO reconstruction, fitted to an ideal cube	80
3.4 Segmented surface of the nanosphere reconstruction, fitted to an arithmetic sphere	80
3.5 The radial under-sampling effect on the quality of the MgO recon- struction.	82
3.6 The radial under-sampling effect on the quality of the nanosphere reconstruction.	83
3.7 The missing wedge under-sampling effect on the quality of the MgO nanocubes reconstruction.	87
3.8 The missing wedge under-sampling effect on the quality of the nanosphere reconstruction.	88
4.1 Schematic illustration of sparse representation.	94
4.2 A schematic illustration of patch-based processing of images . . .	99
4.3 An example of a learned dictionary	100
4.4 DLET algorithm	104
4.5 DLET algorithm data flow diagram	105
4.6 Simulated Sinograms from the phantom in Fig.4.8(a).	110
4.7 Sampling masks	110
4.8 Simulation study 1: low noise fully sampled sinogram	113
4.9 Simulation study 1: high noise fully sampled sinogram	114
4.10 Simulation study 1: noiseless under-sampled sinogram	115
4.11 Simulation study 1: noiseless highly under-sampled sinogram . . .	116
4.12 Intensity line profile of Simulation study 1.	117
4.13 Visual assessment of the missing wedge artifact.	118

4.14	Quality limit for higher under-sampling factors	121
4.15	EFTEM tomography tilt-series projection	122
4.16	Oblate spheroid illustration.	123
4.17	Simulated mesh model of polymer solar cell sample	124
4.18	Volume rendering of noisy simulated solar cells	127
4.19	OrthoSlice of noisy simulated solar cells	128
4.20	Reconstructions of solar cells PTB7:PC ₇₁ BM polymer blend. . . .	131
4.21	Cross-sectional slices of solar cells reconstructions.	132
4.22	Direct Volume Rendering of PTB7:PC ₇₁ BM polymer blend.	133
5.1	Schematic illustration of tomography using DualEELS that has been performed in this work	142
5.2	HAADF-STEM projection 2D images and EELS elemental maps .	143
5.3	Tilt-axis misalignment effect of vanadium carbide particle	146
5.4	Simulation of octahedron VC _x	151
5.5	A comparison of the simulated octahedron VC _x using SIRT and the DLET algorithm	152
5.6	Reconstructions of the experimental Vanadium tilt-series	153
5.7	A comparison of reconstructions of the VC _x precipitate from the V-L _{2,3} signal using SIRT and the DLET algorithm	155
5.8	Reconstructions of vanadium precipitates from the experimental HAADF signal	156
5.9	Line profile through the red dotted line indicated in (a) Fig.5.6a2	157
5.10	Orthogonal slice and Line profile through the centre of 3D recon- struction from the Raw Data	157
5.11	Volume rendered of Vanadium Maps and Carbon maps reconstruc- tions.	158
6.1	Example of cryoTEM projection of A. longum bacteria cells.	162
6.2	Visual assessment of the A. longum reconstruction using a total of 121 images.	163
6.3	Visual assessment of the A. longum reconstruction using a total of 25 images.	164
6.4	Shows the auto-segmentation results of the microcompartments in A. longum.	165
6.5	Example of bright-field images of the CNF/HPANI-Pt sample. . .	167

6.6	Visual assessment of the CNF/HPANI-Pt reconstruction using a total of 130 images.	169
6.7	Segmentation of CNF/HPANI-Pt reconstruction.	170

“
I think it's much more interesting to live not knowing
”
than to have answers which might be wrong.

Richard Feynman, 1981

1

Introduction

THE key expertise for industrial utilisation of nanoscience is the ability to control matter at the nanoscale which allows us to design and produce nanostructures and devices with advanced functionality and performance. For instance, in health and life science, electronics, the R&D areas of functional and structural composite materials and energy, the first products are being introduced that make use of nanotechnology. For manufacturing these products mainly conventional but outperformed technologies are used that just make things smaller; examples are the current production of integrated circuits or active catalytic nanoparticles (TiO₂ or Ag).

The full potential of the nanoworld for striking and peculiar (physical) functionality for e.g. quantum informatics, optical antennas for light concentrators or artificial photosynthesis or spintronics, however, only can be developed when tools exist to provide (sub-)nanometer precision for the making and subsequent quality verification of nanostructures. Moreover, in order to move nanotechnology from the experimental stage to industrial production, accurate forms of product

inspection are required. Small discrepancies in the organisation of nanostructures may lead to huge degradations in performance (Oregon and Grfitzeli, 1991).

A leading tool to explore the nano-world is transmission electron microscopy (TEM) which provides nanoscale imaging and spectroscopy. TEM is an indispensable tool to characterise and reveal properties of nanostructures in materials and biological sciences. However, standard TEM image is only a 2D projection (shadow) image of the 3D structure, leaving the 3-D information hidden. This can lead to incomplete or erroneous characterisation Williams and Carter (2009, Chapter 1).

One very useful inspection method is Electron Tomography (ET), which is becoming a leading tool to explore the 3D nano-world. ET provides (sub-)nanometer resolution in all three dimensions of the sample volume under investigation (Kübel et al., 2005; Subramaniam et al., 2007). However, it is recognised clearly by the TEM community that there are reasons to doubt the accuracy of the results achieved by current ET reconstruction procedures (Kübel et al., 2005). Successful 3D analysis relies on several processing steps, and presently, each step significantly degrades the achievable precision of the result. Therefore, a quality assessment study of the existing ET measurement protocols is now essential. Also, improved procedures are necessary to achieve higher fidelity, quantitative 3D TEM analysis that is also capable of studying a range of important structures that cannot currently be analysed. This can substantially boost ET to its ultimate performance and allow the design of new nano-molecular architectures and devices.

1.1 Thesis statement

There is currently a pressing demand for establishing a methodology allowing for reliable and quantitative volume analysis of the 3D reconstructions of nanostructures based on electron tomography (ET).

This thesis argues that: by harnessing prior knowledge about the specimen in the ET reconstruction process, it is possible to enhance the fidelity of the 3D algorithmic reconstruction from the tilt series in a way that improves the accuracy of segmentation and quantitative analysis produced in ET investigation.

We demonstrate this by developing and applying an improved reconstruction method that utilises the theory of *compressed sensing* and *dictionary learning*,

to different specimens in material and biological sciences, after having explored the quality limitations of current ET reconstruction process of the various experimental settings.

1.2 Scope of thesis

The main theme of this thesis is concentrated on nanoparticle morphology via STEM, including Bright-Field (BFTEM), Energy Filtered (EFTEM) and Dual Electron Energy-Loss Spectroscopy (DualEELS) tomography. There are three overlapping topics:

- Conducting a quality assignment investigation to quantify the quality of the established ET reconstruction algorithms.
- Advancing 3D TEM by the development of high-fidelity ET techniques.
- Exploring the relevant ET 3D imaging applications of this new ET method.

1.3 Contributions

ET has emerged as the leading method used to extract 3D information of nanostructures in the TEM. ET has given us many insights in both the physical and biological sciences. Basically, it begins with the collection of a tilt series of 2D TEM shadow images by tilting the specimen with respect to the electron beam. The 3D information is then reconstructed by processing this tilt series using computational algorithms. However, despite their rich 3D information capacity, limitations exist in current ET procedures which hinder the ability to extract reliable quantitative data.

In this work, a detailed quantitative quality assignment investigation of ET tomographic reconstructions is described specifically using MgO nanocubes and nanospheres as ground truth objects. Both of these nanoparticles are of well-known morphology and have regular geometrical shapes which allow the quality assessment of the ET reconstruction. The study includes the effect of the main experimental factors: the tilt increment, missing wedge size, tilt axis mis-alignment and algorithm type. This assessment shows that the fidelity of the quantitative analysis is limited mainly by the accuracy of the reconstruction, which in turn, is

sensitive to the limited sampling of the input projections. The study concluded that there is a need to improve the ET reconstruction algorithms in order to achieve high-fidelity reconstructions from limited tilt series.

The reconstruction process in ET is considered a very challenging inverse problem. This is mainly due to limitations in the acquisition process, which makes this inverse problem ill-posed (i.e. a unique solution may not exist). Furthermore, reconstruction usually suffers from missing wedge artefacts (e.g., star, fan, blurring, and elongation artefacts). In this work, a new ET reconstruction method was developed. This new method was named dictionary learning electron tomography (DLET). In DLET, the ET reconstruction was enhanced by introducing prior knowledge about the specimen during the reconstruction process. The prior-knowledge approach was based on the mathematical theory of compressed sensing (CS) which has drawn significant attention in signal processing fields. This rests on the principle that, if redundancy exists in a signal one can reconstruct it from far fewer measurements than required by the Shannon-Nyquist sampling theorem. It is shown that the prior knowledge harnessed in compressed sensing is extremely powerful for the recovery of under-sampled signals.

Also, this work provided a solution to the main problem that limits the application of compressive sensing to ET studies. Specifically, the CS-based ET methods require that the reconstructed object is sparse (compact) in some transform domain (e.g., Total Variation (TV)). However, a fixed sparsifying transform may only be applicable to a very limited type of specimens. For example, a TV transform can be effective for ET reconstruction if the object under study can be described as a piecewise constant. However, this is not true for many samples and, in general, this assumption is often partially achieved. This limitation was eliminated by introducing dictionary learning which provides an adaptive sparsifying transform that is tailored for the sample under study. This approach provides opportunity to study numerous samples and also extend the fidelity of CS-based ET methods.

Elementally sensitive ET in STEM using DualEELS is then investigated. It is demonstrated that this can be used to produce an EELS signal that is linearly dependent on the projected density of the element in each pixel. This linearisation is important to satisfy the projection requirement of tomography to achieve a reliable elementally sensitive EELS tomography and avoid reconstruction artefacts

(such as the cupping artefact). It also demonstrated that a high-fidelity reconstruction can be achieved, even from very few projections, using DLET which enables a reliable segmentation and quantitative analysis without requiring an excessive radiation dose to the sample. A comparison between DLET and SIRT ET tomograms that were reconstructed using VC precipitates extracted from steel in a carbon replica is also provided.

The last chapter of this thesis describes the application of compressed sensing to ET reconstruction in material and biological sciences. The efficacy of DLET is then qualitatively evaluated and it shows appreciable performance enhancements over conventional reconstruction algorithms. It also demonstrates that the enhanced contrast of the DLET tomograms enables automatic (or semi-automatic) segmentation procedures for extracting surfaces for quantitative studies. Such segmentation is often subject to time-consuming and user-dependent manual procedures when reconstructed using conventional ET methods. The high fidelity and robust reconstruction produced by a compressed sensing approach could open the door to new ET investigations.

1.4 Publications

A significant portion of the research presented in this thesis has been peer-reviewed and published in various academic venues. The author of this thesis is the primary author of most the publications, which are also based on the work presented in this thesis. Much of the text in the thesis is taken from following publications:

- [1] **Ala AlAfeef**, W.Paul Cockshott, Ian MacLaren, and Stephen McVitie. Electron tomography image reconstruction using data-driven adaptive compressed sensing. *Journal of Scanning Microscopies*, 38(3), 2016.
- [2] **Ala AlAfeef**, Joanna Bobynko, W Paul Cockshott, Alan J Craven, Ian Zuazo, Patrick Barges, and Ian MacLaren. Linear chemically sensitive electron tomography using dualeels and dictionary-based compressed sensing. *Ultramicroscopy*, 107:96–106, 2016.
- [3] Alexander Alekseev, Gordon J Hedley, **Ala AlAfeef**, Oleg A Ageev, and Ifor DW Samuel. Morphology and local electrical properties of PTB7:PC71 BM blends. *Journal of Materials Chemistry A*, 3(16):8706–8714, 2015.

- [4] **Ala AlAfeef** Ala AlAfeef, W.Paul Cockshott, and Ian MacLaren. Dictionary based reconstruction of the 3D morphology of ebola virus. In *Microscopy and Microanalysis MM2015*, 21(S3): 905–906, 2015.
- [5] **Ala AlAfeef**, W. Paul Cockshott, Patrick Barges, Ian Zuazo, Joanna Bobynko, Alan J. Craven, and Ian Maclaren. Linear chemically sensitive electron tomography using DualEELS and compressed sensing. *Microscopy and Microanalysis*, 21(S3): 2341–2342, 2015.
- [6] **Ala AlAfeef**, Alexander Alekseev, Ian MacLaren, and Paul Cockshott. Electron tomography based on a total generalized variation minimization reconstruction technique. In *Picture Coding Symposium (PCS)*, pages 95–99, May 2015.
- [7] **Ala AlAfeef**, P Cockshott, I MacLaren, and S McVitie. Compressed Sensing Electron tomography using adaptive dictionaries: a simulation study. *J.Phys.: Conf. Ser.*, 522(1):012021, June 2014.
- [8] **Ala AlAfeef**, Alexander Alekseev, Gordon J Hedley, Ifor DW Samuel, Cockshott Paul, MacLaren Ian, and McVitie Stephen. Electron tomography of ptb7:pc70bm. In *IMC2013, Prague, Czech Republic*, 2014.

1.5 Thesis outline

The thesis is organised to progress from quality assessment of current ET technique, through to the development of ET methods with new capabilities and their applications.

Chapter 2 presents an overview of S/TEM principles and the imaging modes used. The relevant foundation, practices, and recent advances of ET are reviewed in detail.

Chapter 3 addresses the influence of the experimental conditions on the quality of the reconstructed ET tomogram. The presented results motivate the development of improved ET reconstruction via dictionary learning and compressed sensing.

Chapter 4 deals specifically with ET reconstruction method development. Firstly, the main aspects of compressed sensing theory are introduced, along with their applications to ET. Then, the DLET method is detailed. In the final

part of this chapter, the DLET approach is evaluated using a simulation study that is provided as a proof-of-principle, then by two investigations of samples from material and biological sciences.

Chapter 5 details an investigation on the use for DualEELS in elementally sensitive ET in the STEM. It shows that reliable EELS tomography of VC precipitates is possible with appropriate use of DualEELS and a compressed sensing based reconstruction algorithm to overcome the low sampling and limited signal to noise inherent in core-loss EELS.

Chapter 6 presents a qualitative study of samples from materials science and the biological sciences. It is shown that the results obtained have a higher contrast and a reduced noise which enables reliable automated segmentation. This advantage helps to produce higher quality and robust segmentation results for quantitative studies with less labour and a reduced subjective bias that can be introduced by the operator.

Final conclusions and areas for fruitful future work are given in chapter 7.

“When we look through the little universe that we know, and think of the transmission of electrical force and of the transmission of magnetic force and of the transmission of light, we have no right to assume that there may not be something else that our philosophy does not dream of”

Lord Kelvin, 1904

2

Introduction to electron tomography

NANOTECHNOLOGY has revolutionised the industry’s ability in building microscopic nanosystems by manipulating materials on a molecular and atomic scale. The prefix ‘nano’ is used because of the dependence on physical size which is observed close to the nanoscale, somewhere around 10^{-9} metre. Nanosystems are becoming increasingly more complex and smaller from the chemical perspective which increases the demand for microscopic characterisation techniques. Among many, transmission electron microscopy (TEM) is an indispensable tool that is increasingly used to study the structures of nanosystems down to the molecular and atomic scale. However, despite the effectiveness of this tool, it can only provide a 2–D projection (shadow) images of 3–D structure which can lead to incomplete or erroneous characterization especially when knowing that our visual system is equipped to handle light reflection images rather than light transmission ones [Williams and Carter \(2009, Chapter 1\)](#). To overcome this limitation, Electron Tomography (ET) is widely used to reconstruct a 3D representation of the structure using 2D series of projection images that are

2.1 Introduction to transmission electron microscopy (TEM)

taken at a different orientations of the specimen. Enhancing and quality assessing the 3D characterisation of nanostructures using electron tomography is the main purpose of this work.

In this chapter the foundations, established practices and state-of-the-art methods in electron tomography (ET) are reviewed, along with, limitations and opportunities. The main limitation of electron tomography is the so-called missing wedge of images for most kinds of specimens, due to unavoidable technical limitations, which reduces the angular range that can be acquired practically. Also, many samples do not stand unlimited radiation doses, and this limits the number of projections that may be recorded and/or the SNR in each projection. These problems severely degrade the quality of reconstruction and introduce artifacts that are not part of the original object. Conventional reconstruction ET algorithms do not provide an adequate solution from such limited measurements and, therefore, are considered an important limiting factor for image reconstruction fidelity in ET (Arslan et al., 2006). This provides a motivation for the work in chapters 4 and 6, where new dictionary based compressed sensing approach for ET reconstruction is introduced and investigated.

This chapter also outlines the primary TEM imaging techniques that were used in this thesis and described the reasons behind their use. These includes bright field TEM, annular dark-field scanning TEM, energy filtered TEM and spectroscopic DualEELS TEM technique.

2.1 Introduction to transmission electron microscopy (TEM)

2.1.1 The development of electron microscopy

The first electron microscope prototype was constructed in 1931 by Max Knoll and Ernst Ruska who, in 1986, was awarded the Nobel Prize for his fundamental work in electron optics, and for the design of the first electron microscope¹. The

¹The invention of the electron microscope sometimes attributed to Reinhold Rudenberg since he was the first to patent the idea. Actually, he did not contribute to the development of the first electron microscope. When Rudenberg submitted his patent request, Knoll and Ruska had already finished the first prototype [Freundlich 1963]

2.1 Introduction to transmission electron microscopy (TEM)

imaging capabilities of electron microscopy was improved since its first development. The first customised electron microscope (the 'Siemens Super Microscope') was introduced in 1939. Further developments were disrupted because of the Second World War, in which a leading laboratory (Siemens laboratory) was bombed, and two leading researchers died (Heinz Mueller and Friedrich Krause). Following the war, electron microscopes were again being built and led to "Elmiskop 1" in 1954 (Ruska, 1987).

The development of the electron microscope was a result of significant scientific breakthroughs that can be summarised as:

- In 1874, the German physicist *Ernst Abbe* established the theory of optical imaging experimentally and declared that the resolution in microscopy is limited by the wavelength of the illumination source. This discovery led to the following theoretical question: *Is it possible to use an illumination source of wavelength shorter than light? moreover, How?*

The answer to the first question came later by two Nobel Prize Laureates:

- in 1896, Sir Joseph Thomson (Cambridge) proved experimentally the existence of highly charged light particles called *electrons* (Thomson, 1966, p. 145-153) and
- in 1924, Louis de Broglie (Paris), introduces the theory of electron matter waves (the wave properties of moving particles) which when applied to electrons, shows that the wavelength (λ_{e^-}) of accelerated electrons is related to their kinetic energy (E) when neglecting the relativistic effects as: $\lambda_{e^-} \approx \frac{1.22}{E^{1/2}}$, where λ_{e^-} is in nanometer unit and E in electrons volts. Resolution can therefore be boosted by increasing the accelerating voltage. For example, an electron wavelength of (3.7-2 pm) can be achieved with a high acceleration voltage of (100–300 kV). Such wavelength is much smaller than a wavelength in the optical microscope (which is typically around 400–600 nm) and than the typical atomic diameter of 200 pm (De Broglie, 1929).

and the second part of the question was answered in

- 1925, by Hans Busch (Germany) who showed mathematically the possibility to deflect electrons in a similar way to optical lenses (Ruska, 1987), and

2.1 Introduction to transmission electron microscopy (TEM)

- 1927, by another two Nobel laureates in physics, Sir George Thomson (Cambridge) and Clinton Davisson (USA), with their experimental discovery of electron diffraction ([Davisson, 1995](#)).

Because the moving electron wavelength is several orders of magnitude smaller than the wavelength of light, these breakthroughs made it possible that nanoscale objects could be imaged by mean of electron beam and lenses ([Freundlich, 1963](#)).

- In 1931, All the pieces in the theoretical puzzle behind the electron microscope was put together by Ernst Ruska and Max Knoll (Technical University of Berlin), leading to the first (two stage) $\times 16$ magnification electron microscope ([Ruska, 1987](#)).
- In 1933, Ruska built an electron microscope that exceeded the resolution attainable with a light microscope ([Wilson, 1993](#)).
- In 1934, The publication of the first EM micrograph of a biological specimen (a $15 \mu\text{m}$ thick specimen of sundew plant tissue) by [Marton \(1934\)](#).
- In 1938, Development of the first scanning electron microscope (SEM) and the scanning transmission electron microscope (STEM) by [Ardenne \(1938\)](#).
- In 1952, Palade and Claude shared the Nobel Prize in 1974 for their discoveries in applying electron microscopy to study the functional structure of the cell that was considered a breakthrough in the development of modern cell biology.
- In 1982, First edition of an influential text on high-resolution electron microscopy ([Spence, 1981](#)).

Despite the fact that the resolution of a TEM microscope is away much better than that which can be achieved with a light microscope, the practical resolution in TEM was worse than 1\AA due to geometric aberrations of the electromagnetic lenses, principally spherical aberration which causes the electron rays on the sides to be focused at closer focal points [Batson et al. \(2002\)](#). This aberration is a consequence of the geometry of focussing with a cylindrically symmetric magnetic field [MacLaren and Ramasse \(2014\)](#). Cylindrical electromagnetic lenses have a

2.1 Introduction to transmission electron microscopy (TEM)

positive focal length (i.e. are converging lenses) and have positive spherical aberration. To get negative spherical aberration, a negative focal length is required, and there are no cylindrical diverging lenses for electrons. Aberration is unavoidable and was recognized early on in the history of TEM (Scherzer, 1936). The limitation of aberration has been overcome during the last decade using aberration correctors enabling the resolution to enter the sub-angstrom limits for both the TEM (Haider et al., 1995; Lentzen et al., 2002; Rose, 1971; Zach and Haider, 1995) and the STEM (Krivanek et al., 1999, 2015). For a more comprehensive review, the interested reader is referred to the review by MacLaren and Ramasse (2014) and the references therein.

Since its early development, electron microscopy has been applied to many fields ranging from biological material (such as cells, viruses, and plants) to material science (such as catalysis, glasses, metals, nanoparticles, electronic devices and more). In recent years, tomographic reconstruction of 3-D structures using electron microscopy has become possible and has been applied in many of these fields (more details will be given in the subsequent chapters). For a more complete list of important events in electron microscopy history, please refer to (Haguenau et al., 2003).

2.1.2 The structure of the TEM

A schematic illustration of the TEM structure is presented in Figure. 2.1. The electron-emitter (gun) is the source of illumination in a TEM and can be either a thermionic gun or field emission gun (FEG) Williams and Carter (2009, Chapter 5). FEG emitters are more commonly used nowadays to produce an electron beam that is more coherent and monochromatic, smaller in diameter and with higher brightness than can be achieved with conventional thermionic emitters such as LaB₆ or tungsten filaments that are of limited emitting life and reliability Williams and Carter (2009, Chapter 5). The TEM column consists of a condenser system, objective lenses, projection system and detectors. The condenser system consists mainly of two or more electromagnetic lenses and an aperture. These lenses are used to control beam spot size and convergence to form an electron beam of the desired intensity, size and convergence angle at the specimen. By inserting a condenser aperture, only the electrons of a path close to the optic axes is allowed to pass through the aperture disc (around 40–160 mm radius). The sample is placed in a dedicated TEM holder that can be inserted in the TEM

2.1 Introduction to transmission electron microscopy (TEM)

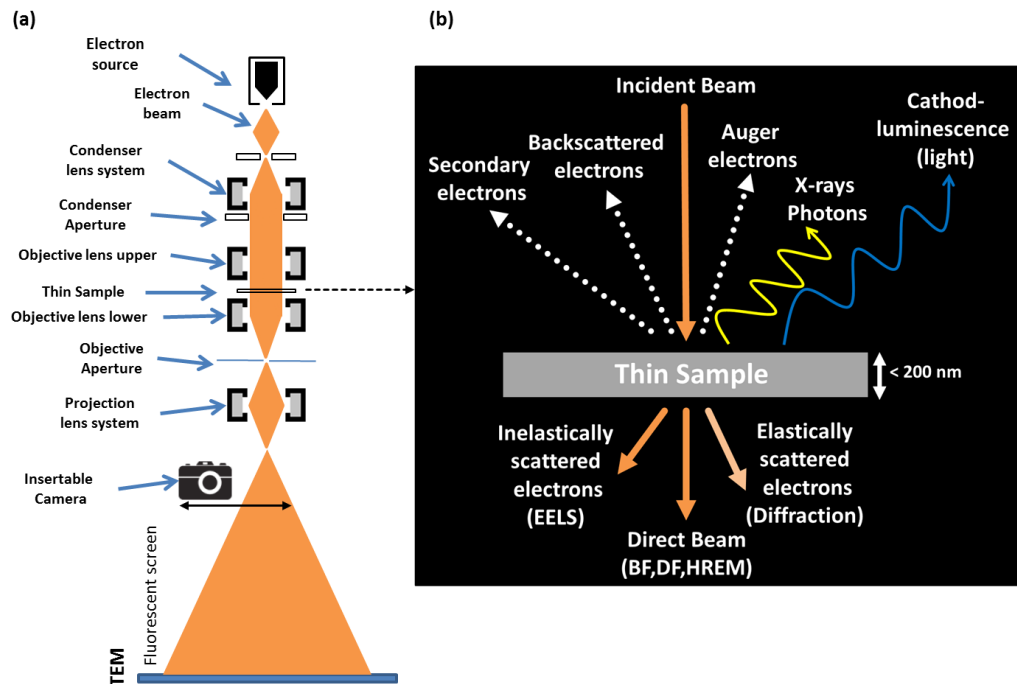


Figure 2.1 | Conventional TEM setup, (a) the structure of the TEM start from the top with the illumination source and condenser system. The objective lens system forms a diffraction pattern in the back focal plane, and an image can be generated in the image plane by inserting the objective aperture in the back focal plane. The projection system enlarges this image and projects it onto the viewing screen. (b) Electron beam–specimen interactions and the generated signals. Diagram re-drawn partially from (Williams and Carter, 2009).

vacuum chamber allowing the beam to interact with the specimen Williams and Carter (2009, Chapter 6). There are different types of TEM holders (see section 2.3.2). The objective lens forms a diffraction pattern in the back focal plane and is used to form a magnified initial image, usually up to 50 times. An objective aperture can be inserted in the back focal plane to improve the contrast of the final image by selecting those electrons which will contribute to the image and reduce the effect of aberration of the objective lens. It can also be used to select a specific spot of the diffraction pattern. A selected area diffraction (SAD) aperture can be inserted in the imaging planes to choose from which part of the specimen to obtain the diffraction pattern. Magnification in the electron microscope can be varied by changing the strength of the projector and intermediate lenses system. The object input plane of this system can be either the image plane or the back focal plane of the objective lens system. The final image is viewed on a fluo-

2.1 Introduction to transmission electron microscopy (TEM)

cent screen or captured using detector device. A typical TEM is usually equipped with one or more detector such as: charged coupled device (CCD), Annular Dark Field (ADF) detector, spectrometer (e.g., Gatan Imaging Filter (GIF)), or a new generation of CCD devices that detect the electrons directly without the need for a scintillator layer to convert electron into photons (direct detectors).

2.1.2.1 The nature of the detector System

TEM electron micrograph are formed when a thin specimen scatters electrons that are transmitted through it; the information contained in this micrograph is a result of a difference in electron flux through each point in the projected image (i.e., the contrast); this is why EM images are monochrome (grayscale). Resulted images are then, magnified and projected onto a fluorescent screen within the microscope column and captured using imaging devices.

Fluorescent screen The ¹is located under the lenses system. The screen is viewed through a lead–glass window which is equipped with radiation shielding to protect the operator against x–rays. The viewing screen in a TEM is coated with a material such as phosphor grains that glows when it is hit by electrons, displaying the image. A typical screen is coated with phosphor grains of 50μ size since, the size of grains should be small enough so that eyes cannot resolve individual grains. The viewing screen is also modified to display magnified projections at different shades of green light (light with a wavelength of 550 nm). The secret behind the green light lies in being in the middle of the visible spectrum, which is best relaxing for the eyes. Many modern TEM still relies on an analogue screen (e.g., JEOL ARM200F).

Moving to digital recording and display, brings with it the opportunity of processing the image to enhance the information before presentation or publication. Historically, electron microscopists have used micrograph electron film since the beginnings, until the new developments in TEM, particularly electron tomography and cryo–electron microscopy, pressed for the needs of digital imaging, and recently has seen the common use of the CCD in all fields of TEM.

¹Also known as CRT, which stands for cathode-ray tube

2.1 Introduction to transmission electron microscopy (TEM)

Charge–Coupled Device (CCD) Detectors Because of developments in computing, there is great interest in recording TEM images via CCD cameras that are advancing rapidly. CCDs have much greater range of intensities (dynamic range of CCD is equivalent of 2–3 films), are rapid, linear in response, uniform in output, have an anti–blooming technology and can record electrons at high detective quantum efficiency (lowering the dosage to radiation sensitive specimen). However, The, relatively, higher spatial resolution of films is the only property that favours it over CCD cameras (Fan and Ellisman, 2000; Faruqi and Andrews, 1997; Jin et al., 2008; Williams and Carter, 2009). CCDs are

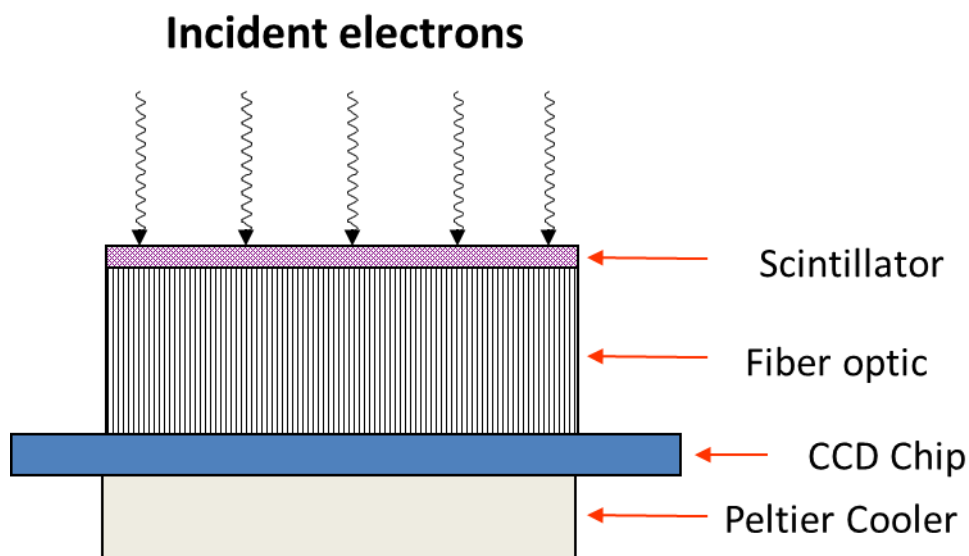


Figure 2.2 | Schematic diagram of a detector, CCD detectors usually operate on an indirect detection method, using a phosphor as the first element in the detector. The scintillator is optically coupled to a CCD by a fiber–optic plate.

metal–insulator–silicon devices that store charges generated by light or electron beams. CCD arrays consist of several million (mega) of pixels which are individual capacitors that are electrically isolated from each other through the creation of potential wells under each CCD cell so that they can accumulate charge in proportion to the incident radiation intensity. Due to radiation damage and signal saturation (Roberts et al., 1982), it is not useful to place the CCDs directly to the electron illumination. Thus, a phosphorescent mineral and a scintillator are required to convert the electron image to a photonic image. The resulting photon image is then transferred to the CCD using a suitable light optical coupling

2.1 Introduction to transmission electron microscopy (TEM)

element (Daberkow et al., 1996). Figure. 2.2 shows a schematic of a typical CCD detector system. The size of the CCD can be expanded by stitching together multiple CCD images which can be controlled via software (Williams and Carter, 2009).

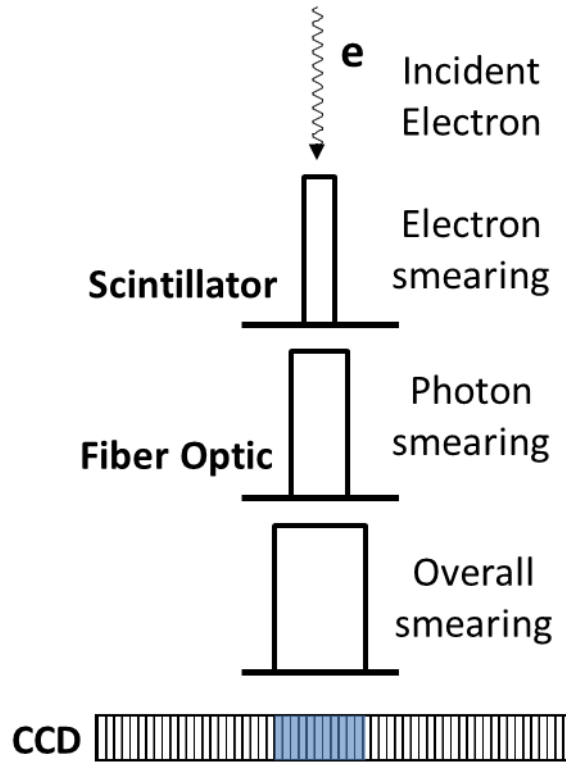


Figure 2.3 | Image resolution in CCD Camera.

To compare the properties of recording devices, the concept of the *detection quantum efficiency* (DQE) is used. If a given detector has a linear response, then the DQE is defined as

$$DQE = \frac{(S/N)_{out}^2}{(S/N)_{in}^2} \quad (2.1)$$

Where S/N is the signal-to-noise ratio of the output or input signal. A perfect detector has a $DQE = 1$ and in practice all detectors have a $DQE < 1$.

In addition to the DQE, the quality of image detector may also be characterized by the number of available pixels and the dynamic range (Daberkow et al., 1996). The CCD chip, when cooled, enables the storage of images with a higher signal-to-noise ratio.

2.1 Introduction to transmission electron microscopy (TEM)

The main drawback of CCD detectors is the limited spatial resolution and sensitivity which are fundamentally limited by the electron–to–photon conversion process in the scintillation. This is caused mainly by multiple light scattering within the phosphor and the fiber optics which causes the signal to be shared between numbers of adjacent pixels (Figure. 2.3) in the CCD, resulting in a loss of resolution.

2.1.3 Electron beam–specimen interactions

Electrons are strongly scattered because they are charged particles. When a high-energy beam of electrons interacts with the matter of a thin specimen, different scattering process occurs by the electron cloud and by the nucleus of an atom in the specimen. This scattering generates different signals (as illustrated in Figure. 2.1b) which can be detected in various types of TEM. The scattering processes generate the contrast in the projection image and can be categorized as elastic or inelastic.

2.1.3.1 Elastic scattering

An incident electron entering into the electron cloud of an atom is attracted by the positive potential of the nucleus. This interaction can be described using Coulomb’s law in Equation. 2.2.

$$F_C = \frac{1}{4\pi\epsilon_0} \frac{Q_1 Q_2}{r_2^2}. \quad (2.2)$$

2.1 Introduction to transmission electron microscopy (TEM)

Where F_C is the Coulombic force between the incident electron Q_1 and the nucleus Q_2 with a distance r between them and ϵ_0 the dielectric constant. The shorter the distance between them (i.e. smaller r), the larger the force F that deflects the electron towards the core, and as a result, the larger is the scattering angle. This scattering is elastic, as the scattered electron conserves, approximately, all of its kinetic energy. Also, this elastic scattering process is called Rutherford scattering and is employed in STEM (Z-contrast imaging).

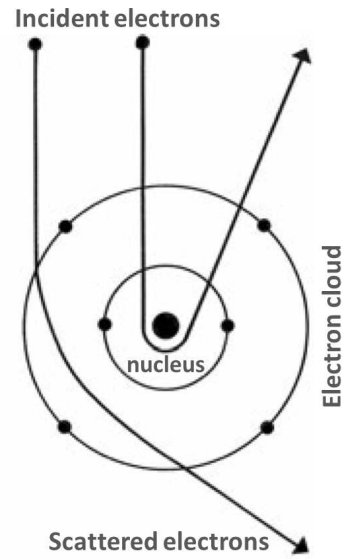


Figure 2.4 | Elastic scattering.

The model in Equation. 2.2 explains the basic contrast mechanisms in (S)TEM. In the mass-thickness contrast, regions in the sample with heavy atoms appear with darker contrast in the projected image than such with light atoms (mass contrast). This happens due to the stronger interaction between electrons and heavy atoms (with high charge Q_2) compared to light atoms. Also, in thick areas, more electron scattering events occur; therefore, these regions appear darker compared to thin regions (thickness contrast). This mass-thickness contrast is central in both bright and dark field imaging.

2.1.3.2 Bragg scattering

Rutherford scattering model is only valid for single nuclei and does not consider regular lattice of crystalline materials.

When a crystalline specimen is transmitted by electrons, each atom in such a regular lattice acts as a scattering point. The scattered electron waves may interact with each other either forming constructive or destructive interference, which gives rise to a diffraction pattern (bragg diffractions). This is formed by phase difference caused by scattering at atomic planes with inter-planar spacing d and can

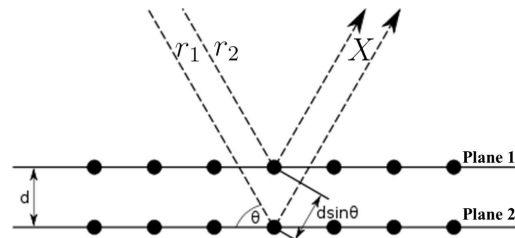


Figure 2.5 | Bragg diffraction.

2.1 Introduction to transmission electron microscopy (TEM)

be explained using Bragg's Law:

$$n\lambda = 2d \sin(\theta) \quad (2.3)$$

Where λ is the wavelength of the incident electron beam, n is an integer, θ angles of incidence. In Figure. 2.5, if the path difference ($2d \sin[\theta]$) is equal to an integer multiple n of the wavelength λ , then rays r_1 and r_2 will be scattered and arrive at point X in the same phase (i.e. constructive interference). This will result in a diffraction patterns in the back focal plane of the objective lens. In real specimens, all contrast mechanisms, namely mass–thickness and Bragg contrast, occur simultaneously, making the interpretation of TEM images sometimes difficult.

2.1.3.3 Inelastic scattering

The electrons of the high–energy incident beam can transfer a significant amount of energy to an inner shell electron of an atom (ionization), causing the ejection of this electron and filling up the empty place by an electron with higher energy from an outer shell (Figure. 2.6). This process also causes the emission of characteristic Auger electrons or X–rays. The incident electron is scattered inelastically and loses a certain amount of energy (ionization energy). This lost energy can be analysed using the electron energy loss spectroscopy (EELS) as explained in section 2.1.5.

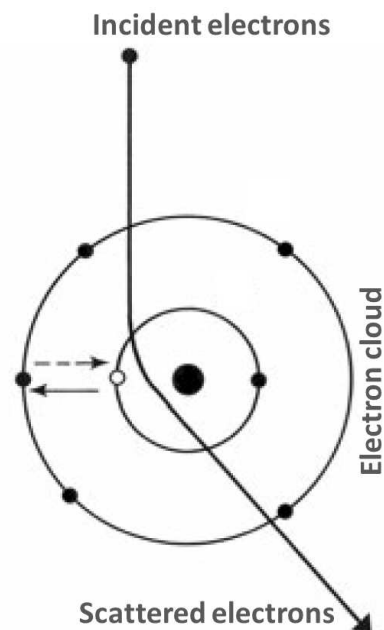


Figure 2.6 | Inelastic scattering.

2.1.4 Imaging techniques in a TEM

2.1.4.1 Conventional TEM and scanning TEM

In this section, we will justify the reasons behind using the BFTEM and STEM imaging modes for different specimens in this thesis. The modern TEM allows a variety of signals to be recorded. There are two primary modes of TEM operation that must be considered: (1) Conventional-TEM (Figure. 2.1a and Figure. 2.9), and (2) Scanning TEM (STEM) as sketched in Figure. 2.7. The Conventional-TEM mode uses parallel illumination, and usually the bright-field (BF) signal is commonly used. In the STEM mode, the electron probe is focused on a single point in the specimen and the image is formed by the raster scanning. The high angle annular dark field (HAADF) signal is usually used in the STEM. An experimental example of MgO cubes STEM imaging is presented in Figure. 2.8.

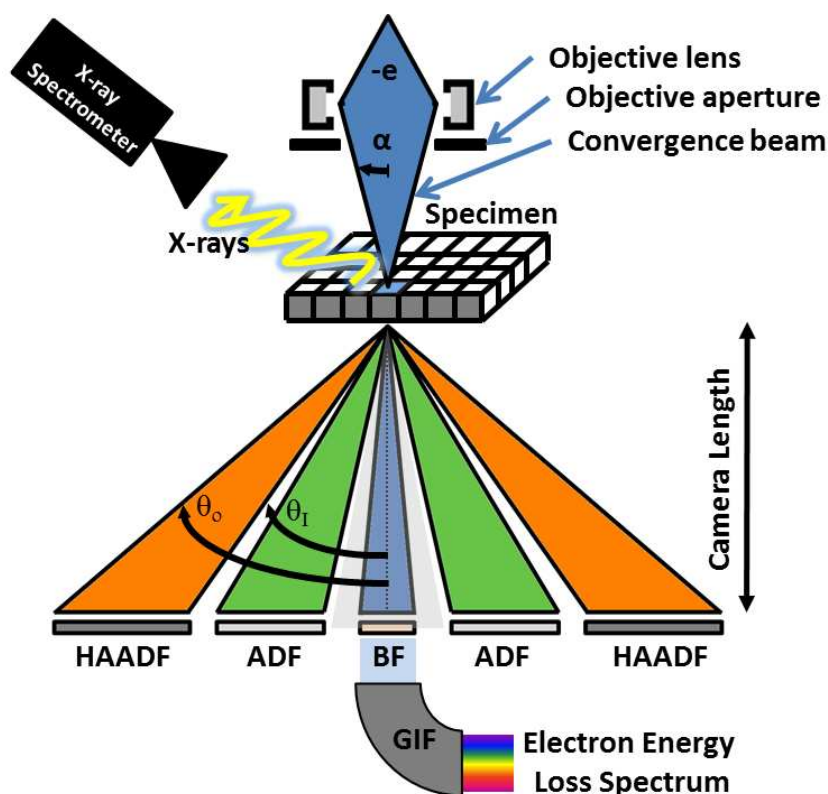


Figure 2.7 | Microscope setup for STEM imaging, specimen is rastered by a focused convergent probe (with semi-convergence angle α), and the transmitted radiation is detected. This radiation passes through the specimen and may be scattered to an angle. Annular detectors pick up the un-scattered or scattered electrons as bright-field or dark-field signals, respectively. In HAADF-STEM mode, the ADF detector is set to detect scattered electrons between inner (θ_{in}) and outer (θ_{out}) collection angles. This setting can be tuned by adjusting the camera length of the ADF detector.

Essentially, the reasons for choosing conventional TEM or STEM for morphological study is well established in the literature. For the biological research (such as, virology and cellular studies), BF-TEM is considered the predominant approach for 3-D imaging (Medalia et al., 2002; Milne and Subramaniam, 2009), While for material science studies (e.g., nanoparticle) STEM is becoming more popular (e.g., (Midgley and Weyland, 2003; Pennycook, 1989; Pennycook and Nellist, 1999, 2011; Thomas and Midgley, 2011)) especially for studying 3D nanoparticle morphology using ET (Banhart, 2008a; Friedrich et al., 2009; Midgley and Dunin-Borkowski, 2009; Midgley and Weyland, 2003; Midgley et al., 2006; Weyland and Midgley, 2004).

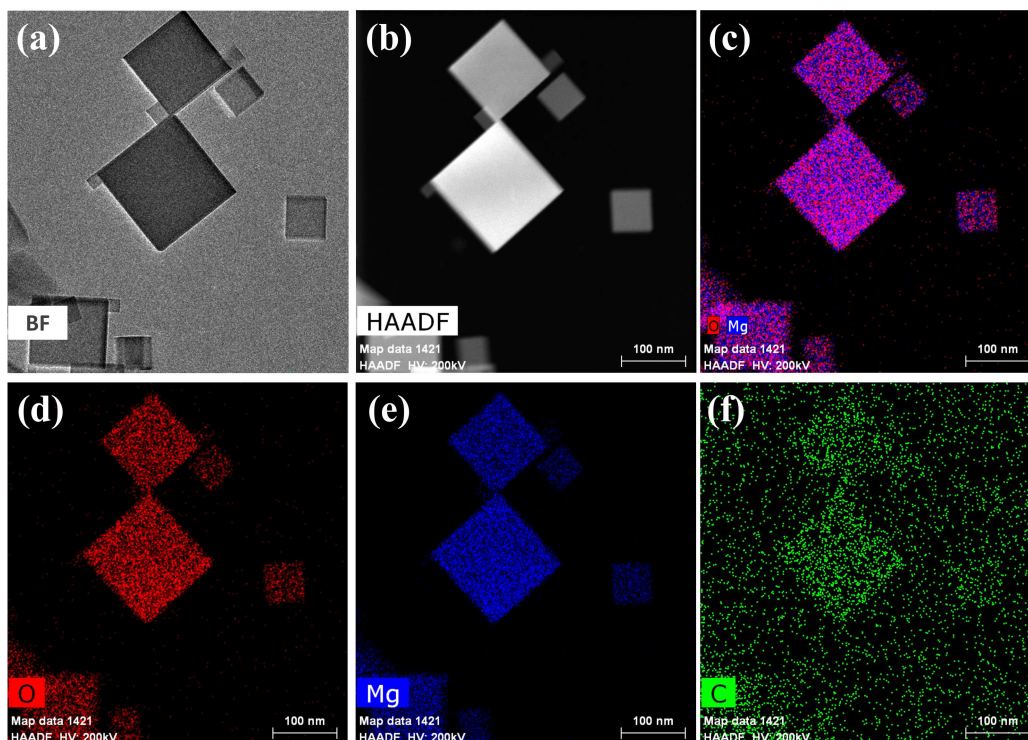


Figure 2.8 | Magnesium Oxide STEM imaging, acquired using different modes in STEM: a) BF-TEM, b) HAADF-STEM, and the energy-dispersive X-ray spectroscopy (EDS) maps of c) oxygen/magnesium, d) oxygen, e) magnesium and f) carbon elements.

Although BF-TEM is very popular for biological sample studies and has been used for a long time in material science. It is not easy to interpret the BF images due to many reasons, mainly the non-linearity of BF signal, in general, on thickness (Midgley and Weyland, 2003). Moreover, this complicates the interpretation of contrast which can be a result of specimen thickness or changes of the electron optical settings (mainly defocus). Another limitation of the BF-TEM, especially for crystalline materials, is that the contrast can be a mix of mass-thickness contrast and diffraction contrast (Bragg scattering) which further complicates the general interpretation (Midgley, 2005). This limitation hinders the application of ET due to the lack of the projection requirement¹ as explained in section 2.3.4. Also, chemical sensitivity is weak in BF-TEM, which is a critical limitation especially when seeking to resolve the small features of the specimen against the support (e.g., amorphous solar cell against carbon support film) (Yang, 2012).

¹Monotonic variation in intensity with specimen thickness

2.1 Introduction to transmission electron microscopy (TEM)

Unlike the parallel field mode in conventional TEM, which relies on the maintenance of phase coherence across neighbouring points to generate meaningful image contrast, STEM contrast depends on discriminating the scattering angles. Detection is usually incoherent and, viz., is less sensitive to the scattering mechanism. Another significant practical advantage of STEM is that it does not require defocusing to generate contrast, which consequently, eliminates the corresponding complications. Furthermore, the scanning nature of the STEM enables the possibility of dynamic focusing which allows the imaging conditions to be uniform across a tilted specimen. HAADF–STEM imaging typically sensitive to atomic (Z) number and shows, to some extent, a monotonic relationship between intensity with the thickness.

The work in this thesis has primarily focused on the use of electron tomography using (S)TEM imaging for material science specimens due to this advantages. The main imaging modes used are HAADF–STEM, EF–TEM, and DualEELS. Also, in chapter 6, ET case studies from biological sciences are demonstrated using BF–TEM. In the next sections, a description and the reason behind adopting these imaging modes is given.

2.1.4.2 Bright Field Transmission Electron Microscopy

The Bright Field (BF–TEM) is one of the simplest and widely used imaging mode in TEM. It is based on a parallel beam illumination source and the resulting contrast can be either mass–thickness or diffraction contrast. The mass–thickness contrast is usually dominant in the biological and amorphous materials while diffraction contrast is dominant in the crystalline specimen as explained in section 2.1.3.2. This contrast mechanism is based on Bragg scattering and is widely used for characterizing the atomic structure since it is sensitive to the orientation and periodicity of the atomic lattice. An optimised contrast for crystalline materials can be obtained using Dark field (DF–TEM) imaging mode by inserting an objective aperture in the back focal plane to block the central diffraction spot and to select a specific diffraction spot. Figure. 2.9 shows the ray diagram of the BF–TEM and DF–TEM mode. Figure. 2.13 shows an experimental

BF–TEM and DF–TEM of Silver nanocubes.

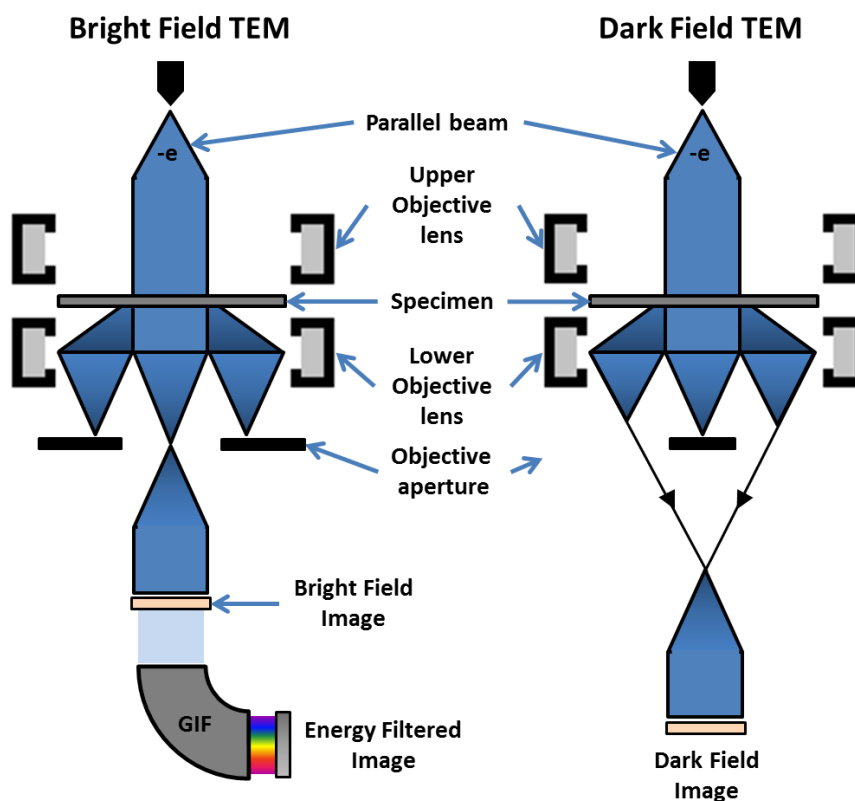


Figure 2.9 | Essential aspects of TEM, Electron ray diagram of Bright Field and dark field TEM. Diagram re-drawn partially from (Williams and Carter, 2009).

2.1.4.3 Annular dark-field scanning transmission electron microscopy

Conventional electron microscopy uses BF-TEM contrast, due to its biological origins, however for materials specimens, BF images can be unacceptable because of the non-monotonic contrast generated by diffraction or Fresnel fringe. Therefore, alternative contrast mechanism should be used. The Z-contrast imaging is a suitable approach to overcome this limitation, using the HAADF-STEM.

Figure. 2.7 illustrate the principal aspects of STEM. In this mode, the electron beam is converged to a small probe and focused at the specimen. This beam is then moved point-by-point across an area of the specimen, and the generated signal is recorded for each point. The annular detector is used to generate an ADF signal. This detector integrates the signal from electrons that are scattered to relatively high angles (50-200 mrad). The angular range of the scattered electrons determines the contrast of the STEM image. BF images are typically

2.1 Introduction to transmission electron microscopy (TEM)

formed using an axial detector and both the unscattered transmitted electron and the low angle scattered electron are detected making Bragg diffraction the main contributor for the image contrast. When increasing the collection angle, electrons that are scattered elastically to higher angles (Rutherford scattering) and thermal diffusive scattered electrons are collected in addition to the Bragg scattering. When further increasing the collection angle to a very high angle (50 mrad), the contrast becomes dominated by Rutherford-like and thermal diffuse scattering, and the diffraction effects are further reduced. This means that the image intensity should vary monotonically with the thickness of the specimen and is approximately proportional to the power of the dominant atomic number (Z^n) in the specimen integrated over the thickness. The value of n lies in the interval [1.1-2] and depends mainly on the inner and outer collection angles (θ_{in} and θ_{out} in Figure. 2.7) of the angular STEM detector (LeBeau and Stemmer, 2008; Treacy, 2011). The collection angle can be adjusted by changing the camera length of the detector. A higher collection angle can be achieved by shorting the camera length and vice versa. This mode that uses very high detection angle is also known as HAADF-STEM and proves ideal for tomographic reconstruction as it generates strong contrast that has a monotonic relationship with thickness. The ADF-STEM signal was successfully used for electron tomography of crystalline specimens (e.g., Midgley et al., 2001; Weyland et al., 2001). Figure.2.8 presents an example of the HAADF-STEM projection image. For more details about the principles of STEM imaging, the reader is advised to consult (Pennycook et al., 2007) and the earlier work by (Pennycook, 1989; Pennycook and Nellist, 1999).

2.1.5 Spectroscopy in the TEM/STEM

The incident electron can be scattered elastically or inelastically when interacting with the specimen as described in section 2.1.3. This processes can be studied in detail by appropriate spectroscopies. In TEM, spectroscopic signals can be recorded to aid the BF and DF imaging modes. Energy dispersive X-ray spectroscopy (EDXS) and electron energy-loss spectroscopy (EELS) are the most established techniques.

In the EDXS mode, the detector is placed on one side on the microscope column to detect the X-rays emitted from the specimen when exposed to the electron beam. This technique can be used for elemental identification by detecting the x-ray that is emitted by the inelastically scattered electrons when passing

2.1 Introduction to transmission electron microscopy (TEM)

through the specimen. EDX tomography was applied for 3D–nanoscale chemically sensitive microscopy (as in, [Haberfehlner et al., 2014a](#); [Saghi et al., 2007](#)). On the other hand, EELS is a powerful spectroscopy technique which provides an energy–loss spectrum to characterise the specimen. This energy–loss spectrum is more useful than an X–ray spectrum that only contains elemental information. In fact, elemental imaging is an effective aspect of the high-energy-loss EELS, because both the superior spatial resolution and the lower detection limits than EDX (i.e., single–atom detection are more easily achievable in EELS) ([Williams and Carter, 2009](#), Chapter 39). Also of the simple elemental distribution, EELS is capable of delivering a wealth of information such as absolute thickness, absolute composition, chemical phase, oxidation state, optical via the detection of surface plasmons, electrical conductivity, band gaps, etc. These cannot be obtained using EDX ([Williams and Carter, 2009](#), Chapter 37).

In this thesis, we are going to use EELS among other imaging modes for tomography. Despite that EDX is not used in this work, the EDXS tomography procedure is related to the scope of ET work in chapters 4. [Williams and Carter \(2009\)](#) and [Egerton \(2011\)](#) provided a broad cover of these techniques. Recent development is covered by [Brydson and Hondow \(2011\)](#); [Hofer et al. \(2016\)](#); [Pennycook and Nellist \(2011\)](#).

2.1.5.1 Principles of electron energy loss spectroscopy

EELS spectroscopy deals with the electron excitation process which results in the fast electron losing a distinctive amount of energy. These transmitted electrons are directed into a high–resolution electron spectrometer that produces an energy–loss spectrum showing the number of electrons scattered as a function of their kinetic energy.

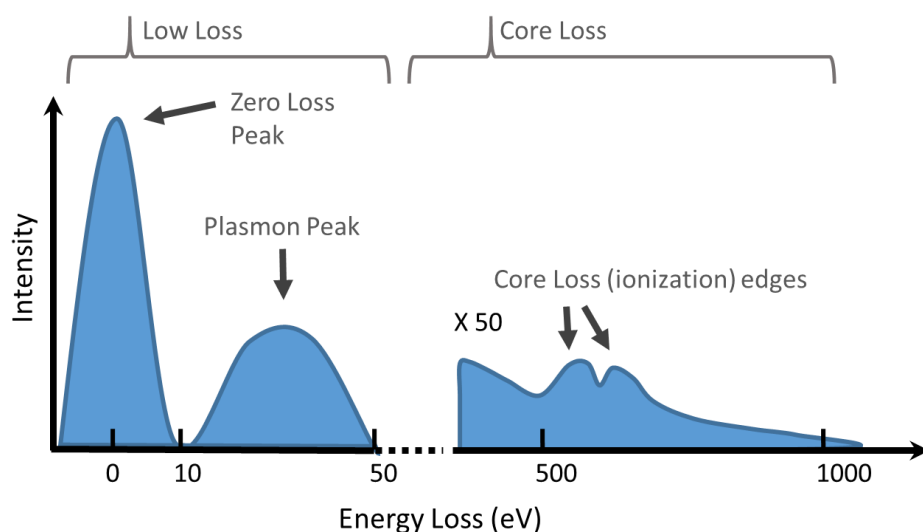


Figure 2.10 | An EELS spectrum, consists of the zero-loss peak and the plasmon peak, which are both an order of magnitude more intense than the small ionization edges in the high energy-loss range. The representation of the high-loss region is often strongly enhanced. After [Williams and Carter \(2009, Chapter 37\)](#).

The EELS spectrum, exemplified in Figure. 2.10, split up into the low-loss and high-loss regions, with ≈ 50 eV being the arbitrary break point. The low-loss region contains information from the more weakly bound conduction and valence band electrons, while the high-loss region contains primarily elemental information from the more tightly bound, core-shell electrons and also details about bonding and atomic distribution. The low-loss regime contains two very intense peaks; the zero-loss peak (ZLP) and the plasmon peak (PP). The ZLP contains mainly electrons that have only interacted elastically or without suffering any measurable energy loss. The PP arises mainly from the inelastic interaction with the conductive electrons of the specimen. With higher energy loss, the intensity decreases, accordingly which makes it more convenient to use a logarithmic scale to represent the spectrum. The high-loss regime of the spectrum is superimposed by the smoothly decreasing intensity from the low-loss region and contains edges (rather than peaks). These edges are used to characterise the chemical elements of the sample since it corresponds to a specific binding energy, (i.e., ionization threshold) that must be transferred from the incident electron to expel an inner-shell electron during the ionisation process. The overall signal intensity drops rapidly with increasing energy loss, reaching negligible levels

2.1 Introduction to transmission electron microscopy (TEM)

above ≈ 2 keV (Williams and Carter, 2009, Chapter 37), which defines the energy limits of this technique. Figure. 2.11 shows a schematic illustration of the main components in a GIF detector and the electron ray diagram in EELS mode.

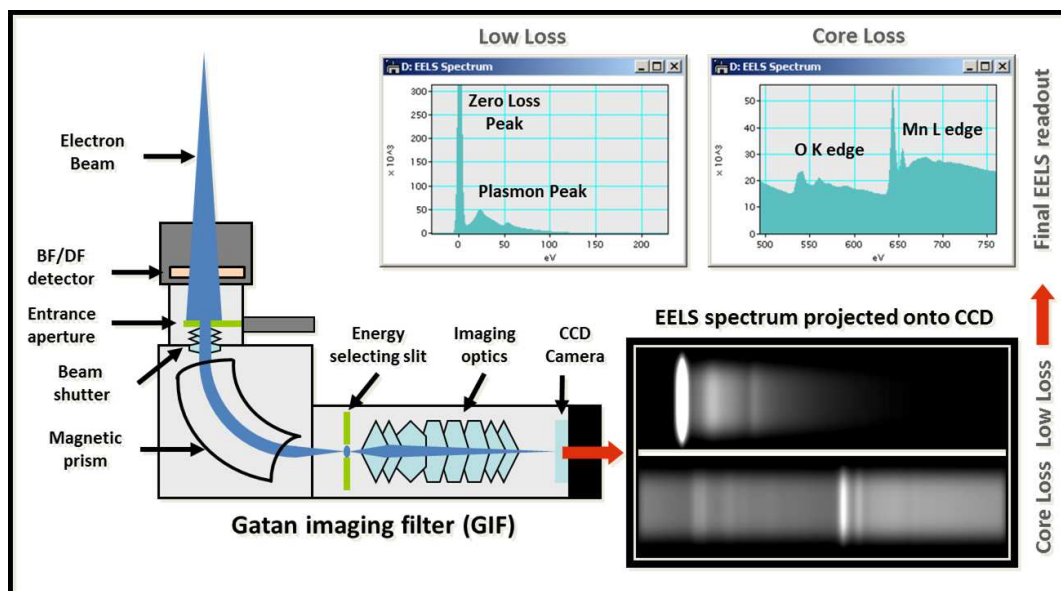


Figure 2.11 | Gatan imaging filter (GIF), Schematic illustration of GIF detector showing the key components. The electrons are chromatically dispersed by a magnetic prism according to their kinetic energy. Energy selecting slits restrict the contribution from the beam to only electrons within a certain energy range. An image can be recorded on the CCD camera.

2.1.5.2 Energy Filtered Transmission Electron Microscopy (EFTEM) Imaging

The energy loss of the scattered electrons can be detected using a CCD in the energy dispersive plane which can be formed by deflecting electrons using a magnetic prism. A specific energy loss can be selected by inserting a piezo-controlled energy-selecting slit following the prism in the GIF system. In this way, only the electrons with a certain range of energies can pass through, and capture an image that represents a specific chemical element. This technique is referred to as *energy filtered TEM (EFTEM)*. It should be mentioned here that, the EF-TEM imaging is not straightforward due to the dominant background signal in the energy loss spectrum. Therefore the spectrum data needs to be processed using model fitting methods to remove the effect of the background signal (Midgley and Weyland,

2.1 Introduction to transmission electron microscopy (TEM)

2003; Weyland and Midgley, 2003). Figure 2.12 shows a schematic illustration of EFTEM mode and two EFTEM elemental maps of solar cells sample showing the carbon and sulphur distribution.

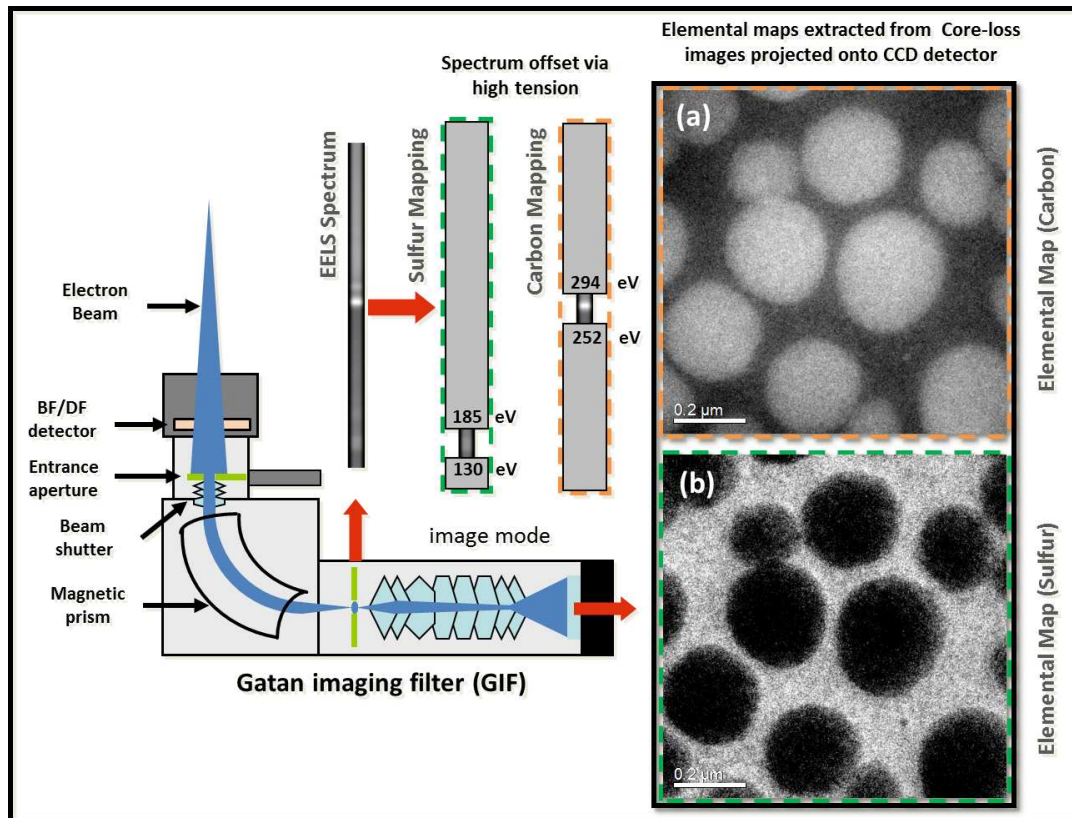


Figure 2.12 | Energy Filtered TEM (EFTEM), The energy selecting slit is adjusted to only allow electrons which have lost a specific amount of energy to obtain elementally sensitive images. a) EFTEM images on PTB7:PC₇₁BM solar cells sample showing the carbon and b) sulphur distribution.

2.1.5.3 DualEELS spectrum imaging

EELS is a powerful technique and can be more effective when combined with modern TEM with higher spatial resolution and aberration correction where a probe size of sub 0.1 nm (Falke et al., 2005). The spectrum imaging technique, with modern computer-controlled microscopes, allows a range of data to be captured at each pixel in the STEM mode.

The dynamic range in an EELS spectrum covering the energy loss range 02 keV can be 10⁶ or higher, and this can be challenging as CCD detectors are

2.1 Introduction to transmission electron microscopy (TEM)

usually of a lower dynamic range and cannot record the whole spectrum in a single acquisition. Also in practice, it is even more challenging if the minimum signal is at the readout noise level which makes the signal-to-noise (SNR) ratio very low. In fact, to get a decent SNR ratio for detailed analysis of the data, a minimum signal of 1% of saturation is required and hence useful data can only be recorded over a specific intensity range (e.g., 10^2 with CCD of 10^4 dynamic range) in a single acquisition (Scott et al., 2008a). Thus, the low loss region containing the zero loss peak (ZLP) must be recorded separately from the core loss region. Both the low loss and core loss regions are required to evoke the maximum information and allow correction of the elastic and multiple inelastic scattering effects.

One of the challenges when using GIF detectors is to record the low loss and one or more core loss spectra, each with adequate SNR ratio, without being subject to the significant time penalties that arise when the integration time is changed. Another challenge with older commercial instruments (such as., GIF200 (Krivanek et al., 1991)), is that the shortest integration time is set by the speed of the beam shutter, which is usually electromagnetic in nature and therefore; has a minimum shutter time of the order of tens of milliseconds which is long.

Using the GIF Quantum detector (Gubbens et al., 2010a), the high-speed DualEELS mode (Scott et al., 2008a) allows the simultaneous acquisition of core-loss spectrum and the corresponding low-loss spectrum, before moving on to the next pixel, and combining both spectra into a single continuous data set with no energy or spatial drift artifacts. With the full range spectral data, advanced analysis techniques such as Fourier logarithmic deconvolution can be applied. DualEELS acquisition is also fully integrated into STEM mode EELS spectrum imaging and uses a $1 \mu s$ electrostatic shutter which shortens the integration time by orders of magnitude and allows both the core loss and low loss regions to be acquired under the same electron optical conditions. The electrostatic deflector (shutter) is placed in front of the CCD camera and alternately reflects the spectrum perpendicular to the dispersive direction to opposite halves of the CCD camera. The voltage on the prism drift tube is changed between the different exposures so that one spectrum contains the core-loss region of interest and the low-loss spectrum in the other. The low-loss intensity is typically several orders of magnitude higher than that of the core-loss therefor; the low loss region is acquired with a short dwell time of the drift tube and the core loss

2.1 Introduction to transmission electron microscopy (TEM)

part with a much longer dwell time. There is a well-defined ratio between the two times so that, in principle, the intensities of the two regions can be scaled to the same incident charge.

The capability to accurately align and calibrate spectra using DualEELS has great potential to allow information to be extracted from small chemical shifts. In this thesis, the DualEELS acquisition is used for the chemically sensitive ET reconstruction of vanadium carbide precipitates on an extraction replica prepared from a vanadium micro alloyed high manganese steel as detailed in chapter 5 and (AlAfeef et al., 2016, 2015b).

2.1.6 Radiation damage & contamination

Besides providing valuable information, the electron beam used in an electron microscope (TEM or STEM) can adversely affect the sample during examination in various ways. The most significant effects, as identified by Egerton et al. (2004), are: ionization damage (radiolysis), displacement damage, sputtering, heating, electrostatic charging, and hydrocarbon contamination.

Minimising the beam-induced changes is one of the factors that a microscopist usually take into consideration, to obtain a *original-state* analysis of the specimen. Reducing the beam energy can potentially reduce both sputtering and atom displacement damage, however, it can increase the ionisation damage and heating effects. Also, decreasing the electron dose leads to lower SNR of the signal and may cause artifacts which reduce the fidelity of analysis.

Hydrocarbon contamination occurs when mobile hydrocarbon molecules are polymerized on the surface the specimen by the incoming or outgoing electrons as shown in Figure. 2.13. This builds up, increases in thickness as the radiation proceeds. The problem of specimen contamination has been greatly reduced, compared to the early days of electron microscopy, with the steady improvement of the vacuum in the S/TEM. Nevertheless, it is not yet eliminated as the specimen itself can act as a local source of hydrocarbons. There are techniques which can be used to reduce this beam-induced contamination (such as, sample cleaning using plasma, sample baking to desorb hydrocarbons from its surface or inserting a 'cold finger to distract contaminants). For ET, the problem of beam-induced damage and contamination is critical as multiple images (tilts) need to be acquired for the tomographic reconstruction. If the specimen changes during the

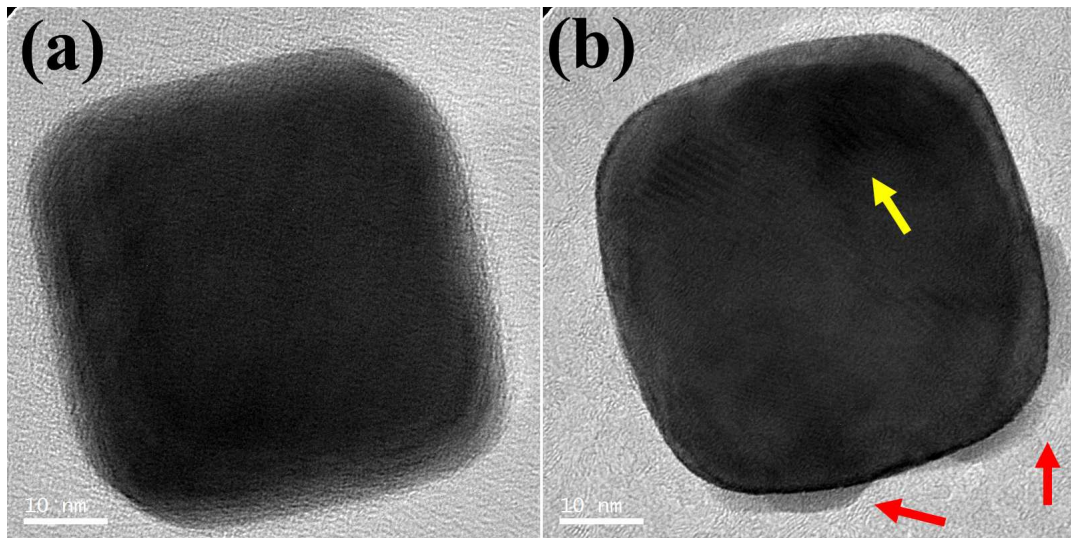


Figure 2.13 | Radiation damage of Silver nanoparticle, after being left under the electron beam for a) 1, b) 30 minutes. The top row shows the BF–TEM images. Note the carbon deposition on the edges of the cube (indicated by the red arrows). Also, the sharp edges of the Ag nanocube is changing into a round shape over time.

acquisition or the projection images are of a low SNR, then the fidelity of tomographic reconstruction will be limited. It is obvious that lower exposure time of the electron beam will reduce beam–induced damage and contamination for ET. Therefore, there is a compelling reason to develop methods of reconstruction and sensing that reduce the required electron exposure, as addressed in chapters 3 and 5.

2.1.7 Aberration-corrected S/TEM

Electron microscopes achieve prominent spatial resolution. Theoretically, an electron beams of 2.5 pm (2.5×10^{-12} m) should be obtained when accelerating the electrons to 200 keV, 3.7 pm for 100 keV and 4.9 pm for 60 keV which is much shorter than the typical atomic diameter of 200 pm. Unfortunately, such resolution has never been obtained in electron microscopes, for many reasons. The most important one is the large *aberrations* of electron lenses.

For round lenses, the main aberration coefficients are typically similar to the focal length of the lenses. The aberrations are unavoidable, as was identified early on in the history of electron microscopy, as highlighted by [Scherzer \(1936\)](#), and

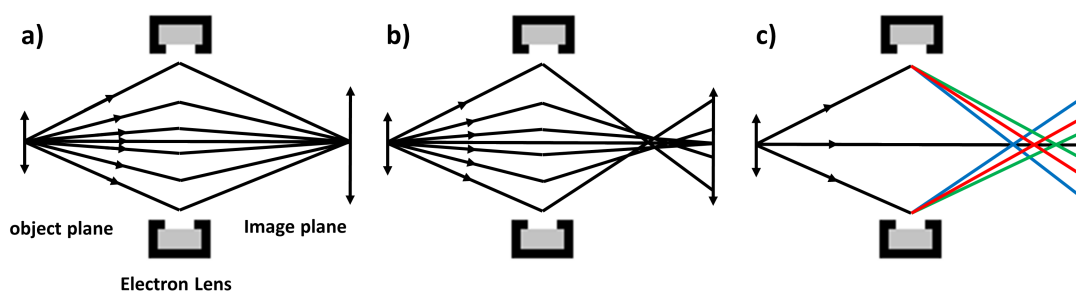


Figure 2.14 | Aberrations in electron lens, (a) An ideal lens focuses a point source to a single point in the image. (b) Spherical aberration: occurs due to the increased focusing of electron rays when they strike a lens near its edge, in comparison with those that strike nearer the centre. (c) Chromatic aberration: the lens is unable to bring all electron rays with different energy to the same focal point.

of two main types: spherical aberration and chromatic aberration. Both of which limit the resolution of the S/TEM to around 250 pm at 60 keV [Krivanek et al. \(2015\)](#). This is typically not sufficient to resolve individual atoms tightly packed in a solid.

Figure. [2.14\(b\)](#) shows how spherical aberration reduce lens performance by focusing rays passing through different locations of the lens to different points. Chromatic aberration, as in Figure. [2.14\(c\)](#), is also a common problem that occurs when the lens is unable to bring all wavelengths of electron rays to be focused at the same position in the focal plane.

Many attempts at aberration correction had been made since early days, however it was not until the 1990s with the availability of the required computational power, computer memory, efficient algorithms, and stability of electrical components that enables the reduction of the aberration problem to a practical levels using aberration correctors. In this work, an aberration corrected microscope is used to image Magnesium Oxide (MgO) nanocubes and nanospheres as in chapter [3](#) and vanadium carbonitride particles as in chapter [5](#). A summary of recent developments of aberration–corrected STEM is provided by [Krivanek et al. \(2015\)](#); [MacLaren and Ramasse \(2014\)](#).

2.2 Electron tomography: foundations and methods

Tomography is a method of producing (reconstructing) a section of the internal structures of an object. Technically, tomography¹ means to reconstruct the 3D structure of objects from a series of 2–D projections (Frank, 2010; Mobus and Inkson, 2007). Electron tomography refers to any technique that applies the transmission electron microscope (TEM) to record a series of 2D projections of an object (specimen) from various directions by incrementally tilting that object in a multiple directions with respect to the electron beam and uses these projections to generate a 3–D reconstruction (tomograms) of the reconstructed object (Frank, 2010; McIntosh et al., 2005).

In this section, a review of the foundations, practices and established reconstruction methods in electron tomography (ET) is given. Along with the main limiting factors that hinder ET. This includes the under–sampling of the measurements in ET due to the practical limitation in the acquisition process that limits the number of images in a tilt series that can be acquired. Conventional reconstruction methods does not usually provide accurate results from such limited measurements. This limitations motivates the work in chapters 3 and 5, where new ET reconstruction methods are provided.

2.2.1 From 2D to 3D electron microscopy

As stated in section 2.1, S/TEM is an indispensable tool for materials characterisation; however, any TEM or STEM image is a 2–D projection of a 3D specimen and this is a fundamental limitation as the depth dimension is lost. Although, it might be sufficient when studying periodic or isotropic structures; however, when imaging asymmetric structures, relying on 2D projections only may lead to an incomplete characterisation (see Williams and Carter, 2009, chapter 1).

Therefore, the goal of ET methods is to retrieve the 3D information from 2D projection images. This can be performed by tilting the specimen and recording a *tilt series* (2D projection images) at different tilting angles. These tilt series

¹The compound word 'Tomography' is derived from the Greek word *tomo* that means a cut, section.

need then to be aligned and reconstructed using a mathematical algorithm as schematically illustrated in Figure. 2.15.

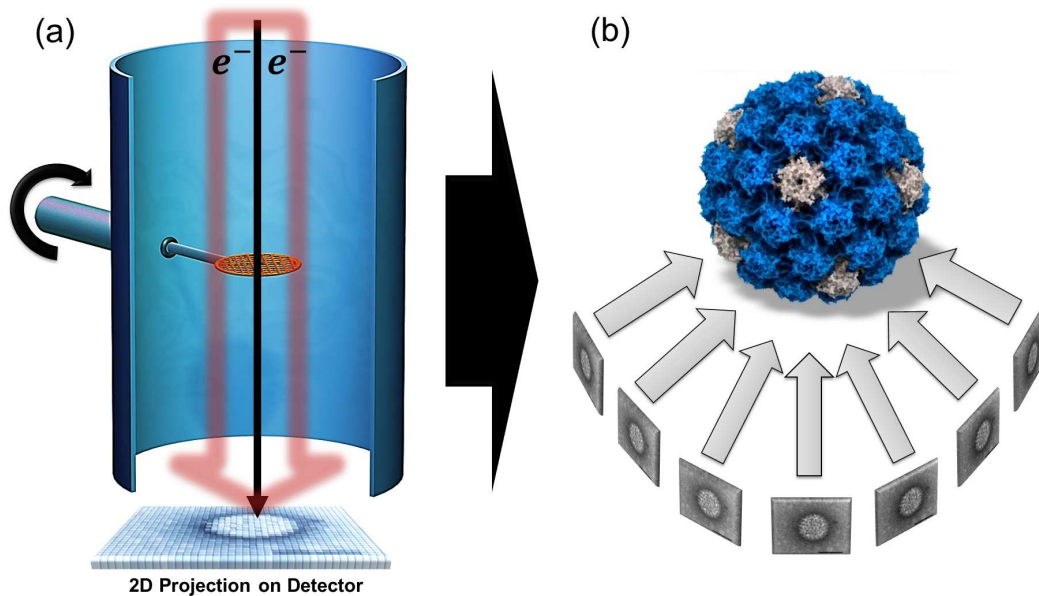


Figure 2.15 | Schematic illustrating the data collection and reconstruction principles for electron tomography: (a) The specimen is tilted relative to the electron beam and a tilt series of projection images is acquired. (b) The tilt series are then aligned and reconstructed to generate a 3–D tomogram of the specimen. This tomogram can be segmented to generate a 3D model for quantitative study. The segmented model of the virus was provided by [Bhella and Goodfellow \(2011\)](#).

2.2.2 Brief history of tomography

The mathematical foundations behind tomography were first introduced by the Australian mathematician [Radon \(1917\)](#). In his pioneering work, he introduced the Radon transform which explains the relationship between a 2D object to its infinite 1D projections. When inverting the Radon transform, the 2D object can be fully restored from its projections. Radon's work did not get much interest at that time due to computational requirement and complexity. [Bracewell \(1956\)](#) was the first to put Radon's theory into practice by reconstructing 2D slices of solar microwave emission from 1D profiles recorded by a radio telescope.

Tomographic methods were further studied by [Cormack \(1963\)](#) and employed by [Hounsfield \(1973\)](#) in the design of the first CT scanner and later the computed

axial tomography (CAT) which gave both of them the Nobel Prize for medicine in 1979 (Hounsfield, 1981). The work on computerised tomography led to other applications that were awarded the Nobel Prize: in chemistry for (Klug, 1983) for his work on crystallographic electron microscopy and medicine for (Lauterbur, 2004) and (Mansfield, 2004) for their work on magnetic resonance imaging (MRI).

The first example of 3D reconstruction using TEM was by DeRosier and Klug (1968) in which they obtained a 3D reconstruction of the T4 bacteriophage's tail from a single 2D image, benefiting from the prior knowledge of the helical symmetry of the tail. Also, the work by Hart (1968) defined the principles of ET for reconstructing asymmetric 3D objects from a tilt series of 2D TEM projections. These two papers are generally considered the starting point of ET.

ET is currently widely used both in material and biological sciences with significant research impact. It is also among (if not the most) successful method of 3D analysis in TEM till now. Alternative 3D TEM imaging modes are reviewed in the next section.

2.2.2.1 Alternative methods

In this section, a briefly description is provided of the techniques that may be complementary to ET. These methods includes: traditional stereo microscopy, single particle microscopy (SPM) and the relatively recent and promising type of 3D STEM imaging that is based on depth sectioning. Also, atom-probe tomography and mechanical sectioning of materials using focused ion beam is described.

Stereology is an old established discipline that is similar in principle to tomography. The stereo microscopy techniques are based on acquiring two pictures of the same area with tilting for few degrees, then showing the two images simultaneously to the operator's eyes using a stereo viewer. This relative shift (parallax shift) between the two images is perceived by our visual cortex as a relative depth difference and can be used to calculate the relative depth of a feature (Williams and Carter, 2009, chapter 29). Although stereo microscopy is well established, however, it can yield only partial 3D information in TEM. The theory of electron stereomicroscopy is reviewed by Nankivell (1963) and applications of stereo techniques in electron microscopy are summarised by Hudson (1973).

Single-particle electron cryo-microscopy (SPEM), abbreviated to cryo-EM or SPEM (Frank, 2006b; Henderson, 2004) is closely related to ET as it is capable

of providing 3D analysis for nano-structures. In SPEM, images of the random distribution of orientations of identical specimens, such as viruses and ribosome, are classified according to their viewing angles and reconstructed. SPEM can provide an isotropic 3D reconstruction if a large number of particle images are used. The reconstruction procedures of SPEM is very similar to ET, and many of the methods proposed in this thesis apply to SPEM. SPEM is usually possible when multiple identical copies of the specimen are possible; this is why SPEM is very popular in biological fields while ET is widely used in the physical sciences. It should also be mentioned here that, SPEM can be susceptible to pitfalls and reconstructing erroneous features especially when electron exposure are limited. The most recent *Einstein from noise* pitfall (Henderson, 2013) is a case in point, in which the investigator thinks that they have acquired true images of their particles, however; in reality, nearly all of their data are pure noise.

Depth sectioning based 3D-imaging (Nellist et al., 2006; Nellist and Wang, 2012) is among the recent developments in the physical sciences. The reduced depth of focus in a state-of-the-art STEM systems, which is now just a few nanometres, enables the possibility to explore the 3D information of the sample at a nanoscale resolution by focusing the beam to examine features at a specific layer in the sample, a technique known as *optical sectioning*. This improvement arises from the possibility to increase the numerical aperture of the objective lens that aberration correction enables, which reduces the depth of focus (DFoc) of the imaging process. For example, the DFoc of a typical uncorrected TEM of 200 kV is around 32 nm. With aberration correctors, the numerical aperture can be increased to around 35 mrad, which yields a DoF of 3 nm, which is below the thickness of most samples. Also, this enables an entire 3D image to be formed by recording a focal series of 2D images similar to the confocal configuration in light-optical microscopes. Each of these 2D-images can be considered as a slice of the full 3D image. This technique is also referred as scanning confocal electron microscopy (SCEM). The SCEM and STEM depth-sectioning have recently reviewed by Nellist and Wang (2012). Although the foundations of these promising techniques have been established, these techniques are still very much in its infancy and may be slightly ahead of its time regarding the technology required beside it also requires expensive aberration-corrected instruments.

Other techniques for nanoscale 3D-imaging and analysis of materials cannot go without brief mention, includes atom-probe tomography and mechanical sec-

tioning using a focused ion beam (FIB). Atom–probe tomography (Miller and Forbes, 2009) allows single–atom counting of a 3D structure. It takes advantage of the field evaporation of individual atoms from a sharp tip, which are then identified via time–of–flight spectroscopy. The trajectory of each atom after evaporation is used to determine its location within the sample. However, this technique requires pre–conditioning of the specimen, such as to be conductors and fabricated into sharp needles. Also, because it counts individual atoms, the analysed volume is limited to around 100 nm in diameter by 100 nm in depth with a data–collection time of several hours (Kelly and Miller, 2007).

In mechanical sectioning (Uchic et al., 2011), the sample is milled and then imaged or analysed. The experiments usually involve material volumes that are typical $\geq 1000 \text{ mm}^3$ with voxel size down to tens of nanometres. This method can be effective when a combination of spatial coverage and resolution is required for the analysis. However, experiments with FIB tomography can require significant time to complete (days), depending on the type of data that is collected and the volume size that is examined. Also, it may not be suitable for materials that are sensitive to ion beam or when a specific analytical method requires low–damage surfaces. The applications of FIB microscopes for 3D materials characterisation is usually performed at the micro–scale.

Electron tomography is a powerful tool to investigate a variety of nanomaterials with nanometer-scale resolution. Electron microscopes equipped with aberration-corrected electron lenses have pushed the resolution to the atomic level enabling electron tomography with atomic-scale resolution. Three-dimensional information in atomic-scale is critical to understand the specific relationship between the physical–chemical properties and the atomic structure of nanomaterials (Bals et al., 2016; Chen et al., 2013; Saghi et al., 2009; Scott et al., 2012; Xu et al., 2015). A review of the latest progress in the field of atomic-resolution electron tomography is provided by Bals et al. (2016). Other novel techniques for atomic–resolution electron tomography had been proposed such as the Big Bang tomography by Van-Dyck et al. (2012).

2.2.3 Principles of tomographic image reconstruction

The foundational principles of tomography relies mathematically on the *Radon transform* (Radon, 1917) and *Fourier transform* (Bracewell, 1956). In this section, the theoretical background of tomography are explained.

2.2.3.1 The Radon Transform

The reconstruction process of ET involves generating a 3D volume data from several 2D projections of a real space object, described by the function $f(x, y, z)$, viewed from different angles. Since the 2D projections in ET are acquired in single axis parallel beam geometry (i.e., tilting around the y -axis while the electron beam is parallel to the microscope optical axis), the volume reconstruction problem can be simplified by reconstructing each 2D slice $f(x, y = SectionNumber, z)$ from the corresponding 1D projections (i.e., slice-by-slice 2D reconstruction of a 3D volume). The process of projecting $f(x, const, z)$ with increment ds along lines L determined by a tilt angle θ , is referred to as Radon transformation R (Radon, 1917):

$$R_{y_i}(l, \theta) = \int_L f(x, y_i, z) ds, \tag{2.4}$$

The discrete outcome of this projecting process is called *Sinogram*. Figure. 2.16 shows a graphical presentation of the Radon transform. This relationship

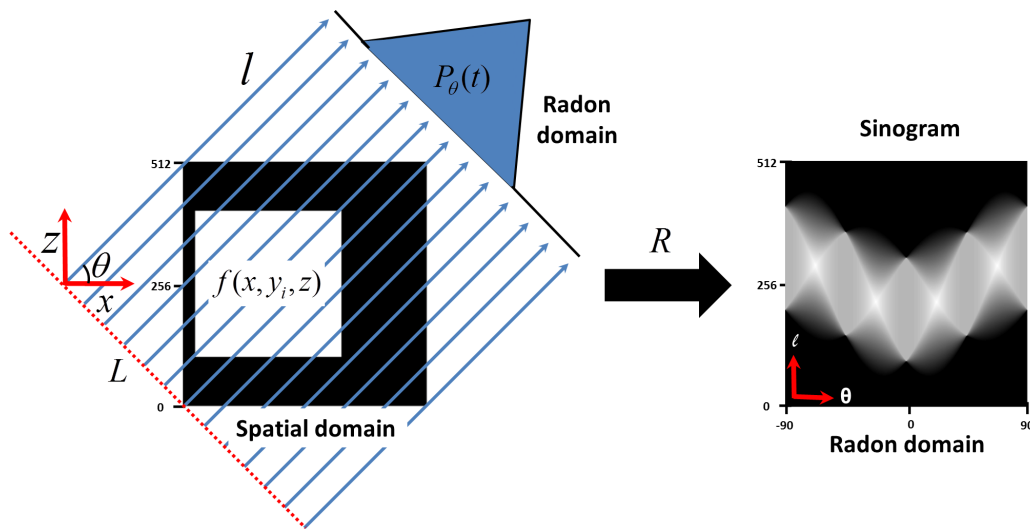


Figure 2.16 | Radon transform, The square object here is defined by function f on the 2D real space co-ordinates (x, z) and the Radon transform (R) converts the coordinates of the data into Radon space (l, θ) , where l is the line perpendicular to the projection direction and θ is the projection angle.

can be also described using the polar coordinates (Deans, 1983; Midgley and Weyland, 2003). A point in polar space (r, θ) is a line in Radon space (l, θ) with $l = r \cos(\theta - \phi)$. The Radon geometry is illustrated in Figure. 2.17. In principle,

given a sufficient number of projections, the object $f(x, y_i, z)$, can be recovered from the Radon domain by an inversion of the Radon transform (R^{-1}).

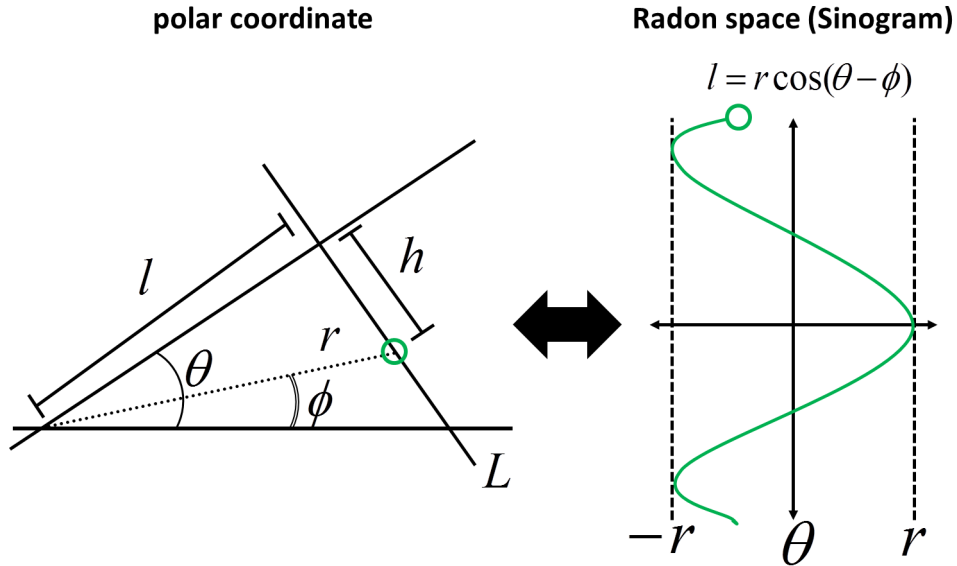


Figure 2.17 | Radon transform of a point object, Relationship between polar space (r, θ) and Radon space (l, θ) and shows how a point object is projected through the tilt series. After (Weyland and Midgley, 2004)

2.2.3.2 The Central Slice Theorem

The *central slice theorem* states that the Fourier transform of a projection of an object at a given angle is equivalent to a central plane through the Fourier transform of the object at an angle that is perpendicular to the projection direction (Cramer and Wold, 1936; Deans, 1983; Kak and Slaney, 2001). Hence by taking 1D Fourier transform of projections at many different angles, many Fourier slices will be sampled. Figure. 2.18 illustrates the theorem for 2D object from its 1D projections, which can be extended to 3D object in the 3D Fourier space.

The proof of this theorem is simple and direct. Suppose $f(x, z)$ is a 2D object that is transformed to the Fourier domain as:

$$F(u, v) = \int_{-\infty}^{+\infty} \int_{-\infty}^{+\infty} f(x, z) e^{-2\pi i(xu+vz)} dx dz. \quad (2.5)$$

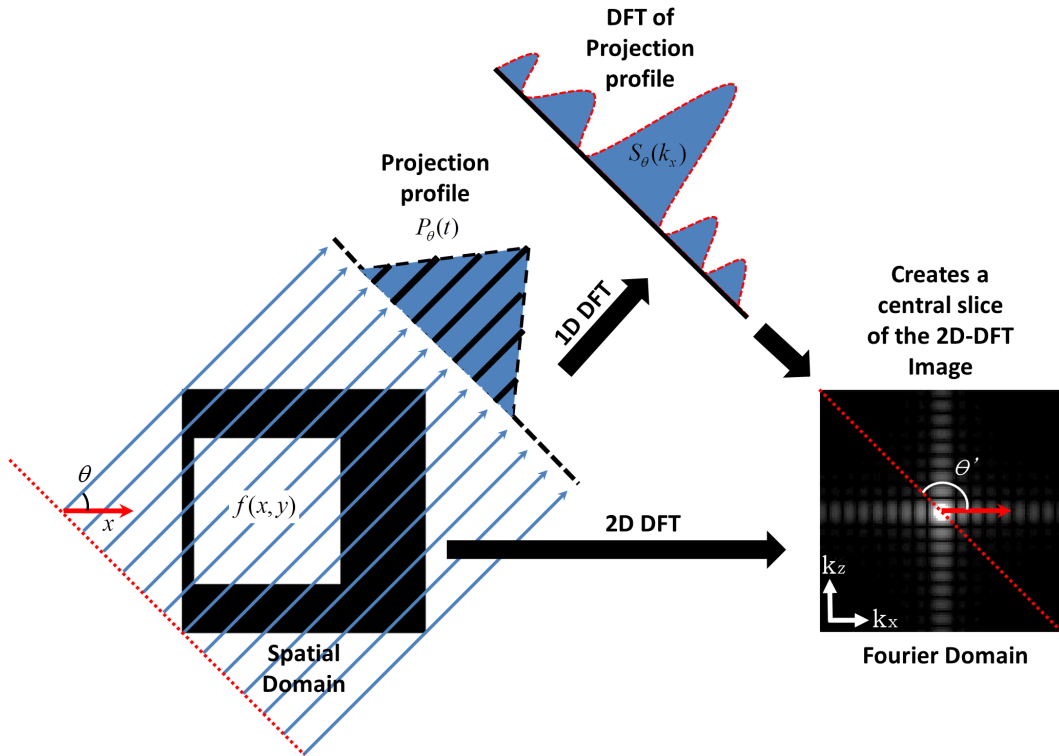


Figure 2.18 | Central slice theorem, schematic illustration of the mathematical concept of the Central slice theorem in 2D. The projection of a 2D object $f(x, z)$ in real domain is a 1D measurement $P_\theta(t)$ in the radon domain. The 1D Fourier transform of $P_\theta(t)$ is equivalent to a central slice $S_\theta(k_x)$ through the 2D Fourier transform of the 2D object $f(x, z)$.

moreover, projected along z direction as:

$$p_{\theta=90}(x) = \int_{-\infty}^{+\infty} f(x, z) dz. \quad (2.6)$$

The central slice through the Fourier transform that is perpendicular to the projection direction can then be driven as:

$$F(u, 0) = \int_{-\infty}^{+\infty} \left(\int_{-\infty}^{+\infty} f(x, z) dz \right) e^{-2\pi i(xu)} dx = \int_{-\infty}^{+\infty} p_\theta(x) e^{-2\pi i(xu)} dx. \quad (2.7)$$

Which is equivalent to the 1D Fourier transform of the projection $p_\theta(x)$. In principle, the reconstruction can be obtained by applying the inverse Fourier transform to the sum of all lines through the Fourier domain. However, this will

result in a blurry reconstruction due to the over sampling of the low-frequency components as illustrated in Figure. 2.20. This oversampling can be reduced by filtering (such as Ram-lack and Hamming filters). It should also be pointed here that, due to the radial symmetry, an interpolation step is required before the inverted Fourier transform can be applied. This interpolation is not exact and can be a source of large error especially, with a limited number of projection. The relationships between spatial, Radon and Fourier domain are illustrated in Figure. 2.19.

In addition to the Fourier inversion approach, the tomographic reconstruction process can be also approached using a real space *back-projection* method. In general, it is not straightforward to apply either of these approaches due to practical issues in ET which is reviewed in the following sections.

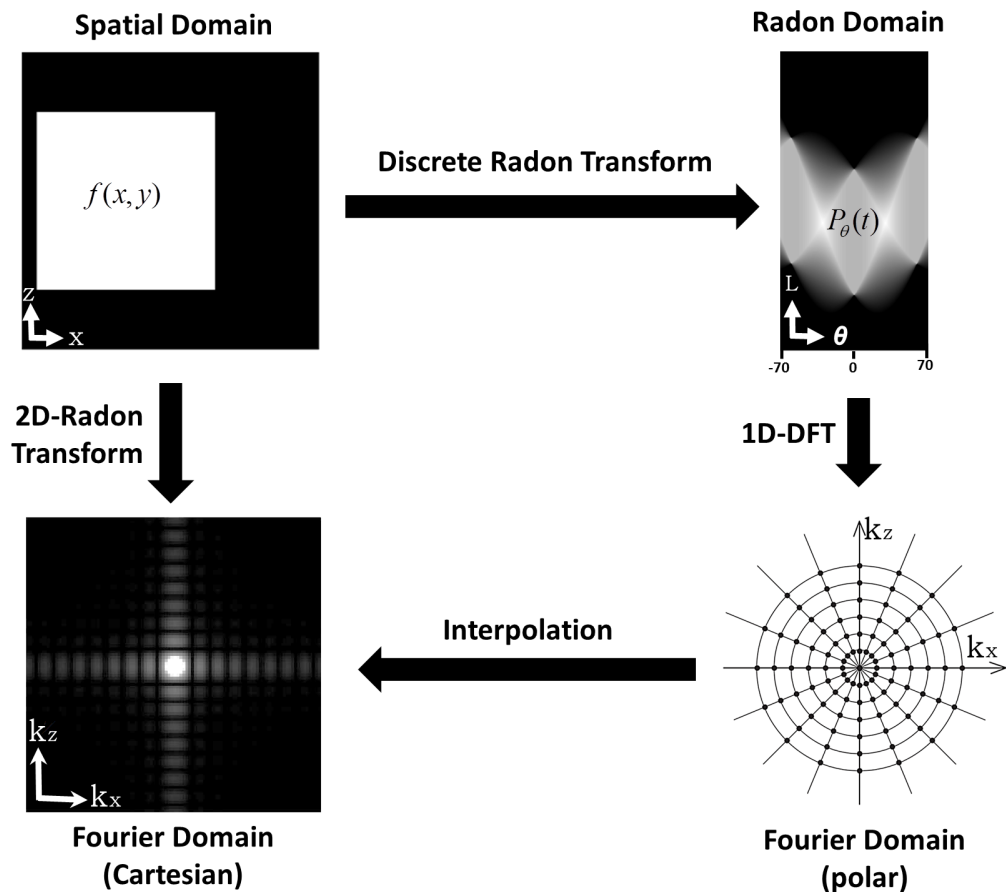


Figure 2.19 | Illustration, the relations between real, Fourier and Radon space.

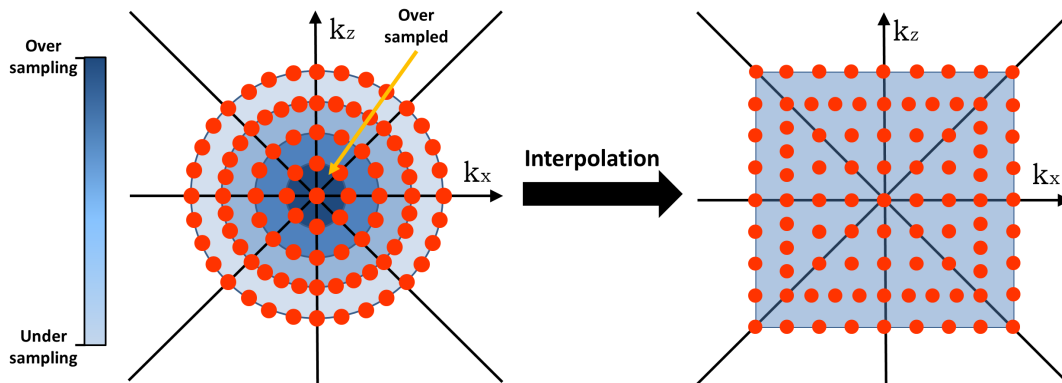


Figure 2.20 | Radial and Cartesian sampling geometry, In the radial sampling, the low-frequency components of the Fourier space are over sampled compared to the high-frequency components. An interpolation is required to convert the radial geometry into Cartesian before applying the inverse Fourier transform.

2.3 Practical aspects of electron tomography

Electron tomography consists of a number of stages which is summarised in Figure. 2.21. These stages are reviewed hereinafter. Detailed reviews of ET practices in the physical sciences are provided in (Pennycook and Nellist, 2011, chapter 8), (Banhart, 2008a, chapter 11 and 12), (Midgley and Weyland, 2003; Mobus and Inkson, 2007).

2.3.1 Specimen preparation

Specimen preparation is a very broad subject, there are books devoted to this topic only. Different approaches exist for many materials, and these approaches vary depending on many factors such as: material type, time constraints, availability of equipment, operator skill, and safety (to the microscope and investigator). For TEM specimens, the sample must be electron transparent (as possible) and representative of the material under-study. It should also be uniformly thin, conducting, non-magnetic and stable under the electron beam and in the laboratory environment.

In general, the specimens can be categorised into two main groups: conventional specimens resting on a support grid and self-supporting specimens (Williams and Carter, 2009, Chapter 10). The simplest form of specimens for the first type can be made from several droplets that contain the specimen, dis-

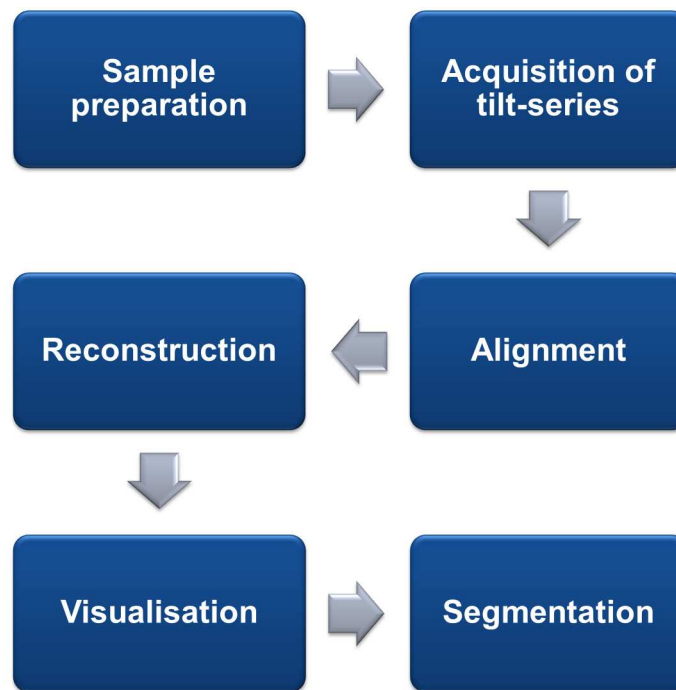


Figure 2.21 | The main stages of electron tomography.

persed on a support grid with a thin carbon layer. The grid is usually made of Cu but could be Au, Ni, Be, C or Pt. An example of conventional TEM grid is showed in Figure. 2.22(ai). Although these support grids are convenient and easy to handle, they might not have the capability to be tilted to high angles without shadowing effects (as illustrated in Figure. 2.26). This shadowing effect occurs when the electron beam is blocked by the grid bars at high tilting angles which prevent the acquisition of projection images. Therefore, special grids with larger grid size and thinner bars are more suitable for tomography. These grids enable higher tilting angles and provide a high percentage of open area and may be enforced with perforated support foil (e.g., QUANTIFOIL) with a pre-defined hole size, shape and arrangement. Figure. 2.22(b) show an illustration of tomography grids. A self-supporting specimen is one where the whole specimen consists of one material (which can be a composite). This specimen are usually prepared using focused ion beam (FIB) and can be shaped as a rod, needle or slab (Hernndez-Saz et al., 2013, Chapter 9). A detailed review of Specimen preparation in electron microscopy is given by (Williams and Carter, 2009, Chapter 10).

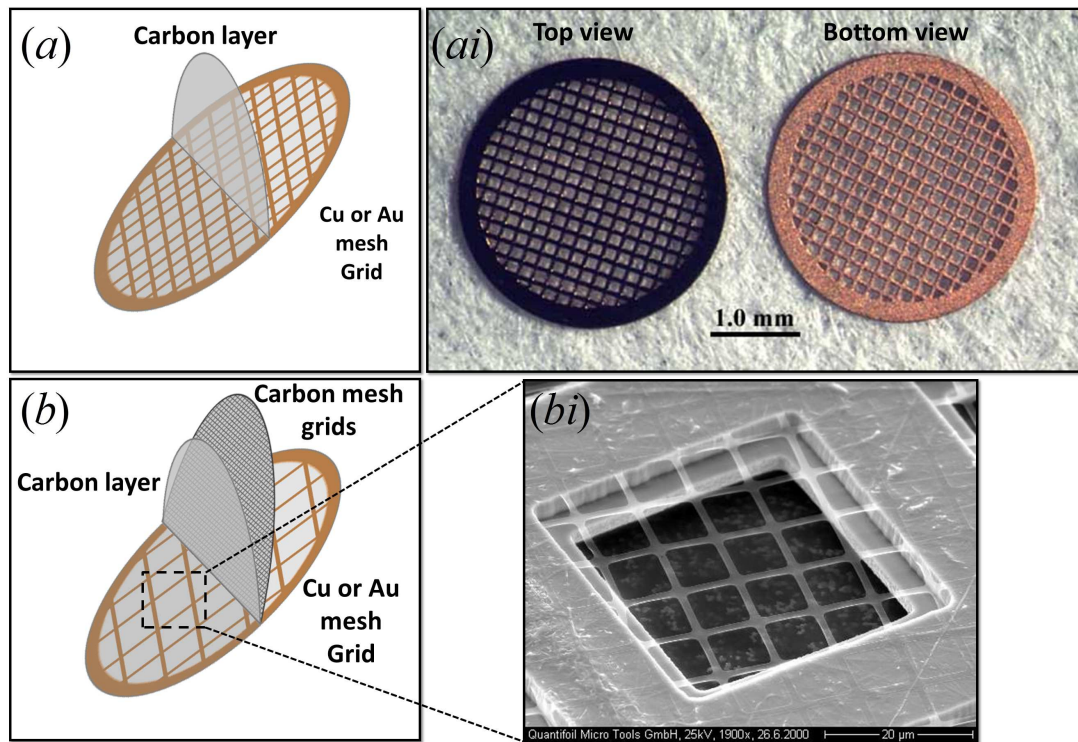


Figure 2.22 | TEM Grid, a) illustration of ai) conventional TEM sample support Cu mesh grid with carbon film. b) illustration of QUANTIFOIL holey carbon grid with the thin carbon layer, bi) shows an SEM image of the surface of the QUANTIFOIL (bi was adapted from Quantifoil Micro Tools GmbH).

2.3.2 Acquisition of tilt series - geometry

In ET, the specimen is tilted in a goniometer inside the vacuum of the TEM—column during acquisition, and an image is acquired at each tilt step. The resulting set of images is often referred to as a tilt—series. The single—axis tilt acquisition scheme is the most commonly used geometry in ET, because of its simplicity for data acquisition and reconstruction.

Single-axis acquisition geometry In an ET experiment, higher resolution of tomographic reconstruction is achieved, in principle, with higher radial sampling of projections and wider tilting range. However, this radial sampling is limited due to several technical restrictions. Firstly, the limited space between the polepieces of the objective lens of the S/TEM (Figure. 2.23) which limits the angular range over which the specimen can be tilted. Therefore, the tilting range of a typical specimen holder is limited to $\pm 35^\circ$, which leaves a *missing*

2.3 Practical aspects of electron tomography

wedge of un-sampled information that degrades in the quality of reconstruction and causes artifacts such as elongation in the direction of the optic axis. Figure.

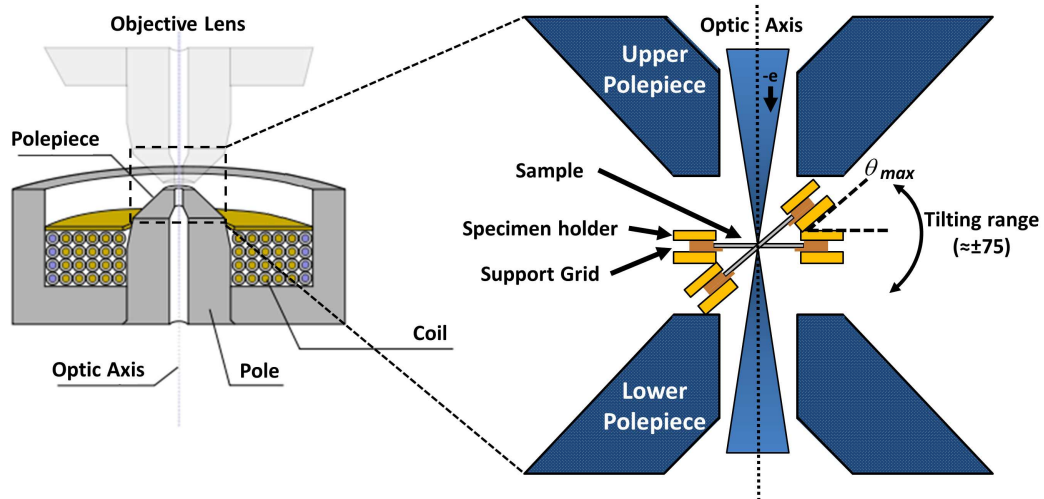


Figure 2.23 | Polepiece space limitation, the maximum tilting angle of θ_{max} is limited by the space between the polepieces of the objective lens of the S/TEM. Partially re-drawn from (Williams and Carter, 2009).

2.25 illustrates the effect of finite tilt increment and limited angular tilt range on the reconstruction of a ring phantom. This pole–piece gap must be kept short in order to minimise the effects of spherical and chromatic aberration (Arslan et al., 2006; Brydson, 2011). As dedicated short profile tomography holders were developed (e.g. Figure. 2.24b) and enabled tilting the sample to high angles ($\approx \pm 80^\circ$) and reduced the missing wedge. These tomography holders are now common, however another limitation may occur at high tilt angles and limit the useful projection image that can be acquired. These limitation can be:

- The shadowing effect from the specimen holder or grid (as explained in section 2.3.1 and Figure. 2.26).
- The increase in projected thickness of the sample at the high tilt angles, which significantly, reduces the resolution and SNR in images and may cause the sample to be no longer *electron transparent* (Figure. 2.27).
- The limited focusing (or more specifically, the *depth-of-field*) of the beam may add regions of the specimen that are out of focus (Figure. 2.27).

2.3 Practical aspects of electron tomography

To reduce the missing wedge problem, other sampling geometries has been proposed, namely *dual-axis* (Mastronarde, 1997; Pawel Penczek and Frank, 1995) and *On-axis* tomography (Kawase et al., 2007).

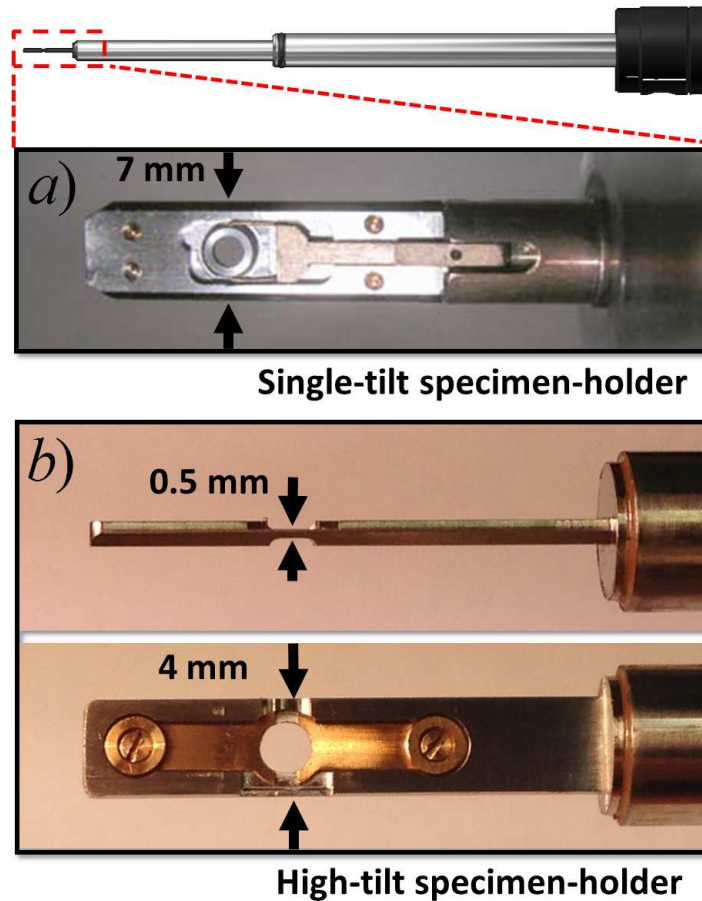


Figure 2.24 | Specimen holders, Shows the Tip of A) Single Tilt Holder Limited to $\pm 30^\circ$, b) Gatan high tilt tomography holder (Model:916) with a maximum tilt range $\pm 75 - 80^\circ$ which can be reached due to the low profile tip.

Dual-axis acquisition geometry In this geometry, another tilt series of the specimen is acquired to reduce the missing wedge artifacts in the reconstruction. As illustrated in Figure. 2.28, two orthogonal tilt series can be acquired around both the α and β planes¹, which when reconstructed, the missing wedge can be

¹Other types of double tilt tomography holders are not equipped with a β tilt mechanism, in this case, it is still possible to acquire another orthogonal tilt series by rotate the sample by 90° in the tomography holder plane (i.e. γ plane) and acquiring another tilt series using the α tilt.

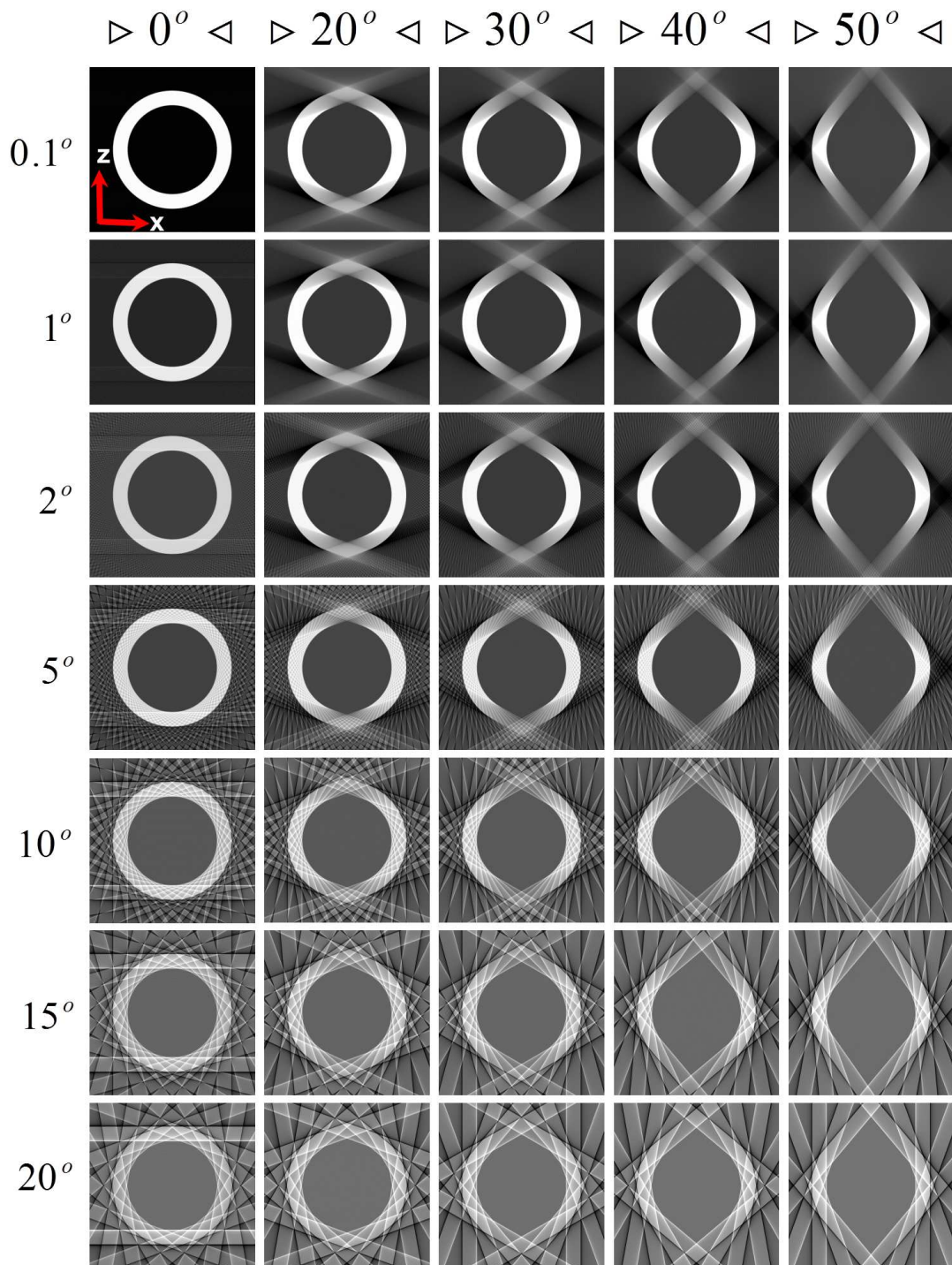


Figure 2.25 | Reconstruction artifacts, the effect of missing wedge and finite tilt increment on tomographic reconstruction of a ring phantom, reconstructed using weighted back-projection. The columns headings represent variations in missing wedges of the tilting axis (y -axis) while the rows headings denote the projections tilt increment for each reconstruction. The evident elongation and streaks tangent to the edges of phantom and along the projection directions can be seen in the reconstruction.

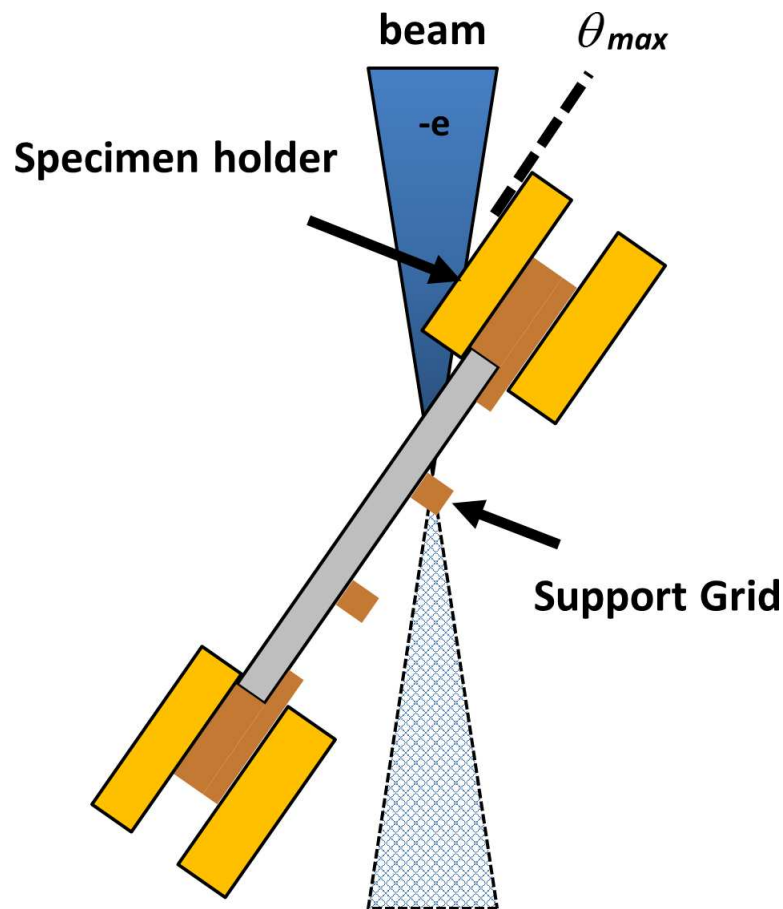


Figure 2.26 | Shadowing effect, the support grid or holder may shadow the region of interest which limits angular sampling in ET.

reduced into a missing pyramid in the Fourier domain (Figure. 2.29). Dual-axis tomography leads to a higher quality reconstruction and resolution, however, there are disadvantages associated with this approach especially for beam sensitive materials and contamination as it increases the exposure time. Also, it is not straightforward to align and reconstruct the dual tilt series. Although, this method is successful in biological sciences (e.g., virology as in: [Tran et al., 2014](#)) where alignment using fiducial marker ([Frank, 2010](#), chapter 5) method is used to align the tilt series and combine the reconstructed volumes, however, this method is not popular in material sciences and was applied in a limited number of cases (e.g. [Arslan et al., 2006](#); [Goris et al., 2013a](#); [Mastronarde, 1997](#); [Pawel Penczek and Frank, 1995](#); [Tong et al., 2006](#); [Tong and Midgley, 2006](#)).

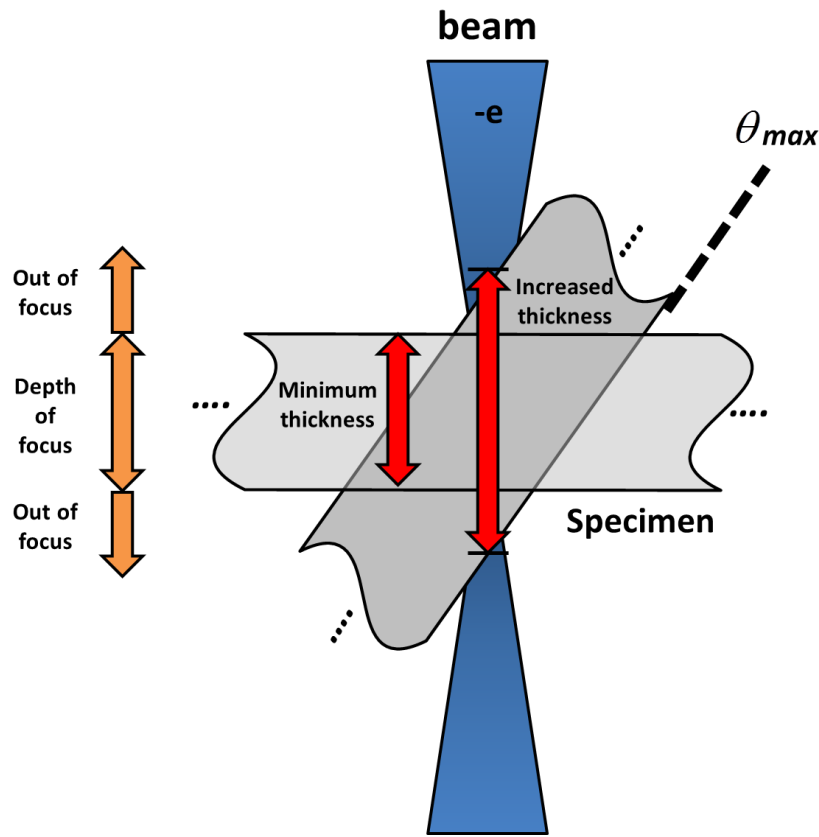


Figure 2.27 | Thickness and focus, the projected thickness of slab-type samples increases by $(1/\cos\theta)$, where θ is the tilt angle, reaching 3.8 times the initial thickness at a tilt of $\pm 75^\circ$. Also blurry images can result when parts of the specimen that contributes to the projection images are out of focus, which is a direct result of the limited depth-of-field of the electron beam.

Other acquisition geometry As discussed previously in section 2.3.1, it is possible to shape certain types of specimens as a needle-like using FIB Nanoprocessing. Such sample geometry allows $\pm 90^\circ$ image acquisition, when using a dedicated on-axis holder, which eliminates two main problems that the slab-type TEM samples suffer from (i.e. shadowing and thickness increases) (Haberfehlner et al., 2014a; Jarausich et al., 2009; Kato et al., 2008; Yaguchi et al., 2008). Therefore, the missing wedge of information can be eliminated and stable quality of projection can be obtained even from relatively thick specimens. This greatly reduces the artifacts and improves the resolution in the final 3D reconstruction.

There is a growing interest in the preparation of needle-like, especially for spectroscopic tomography where the quality of a sampled signal greatly depends

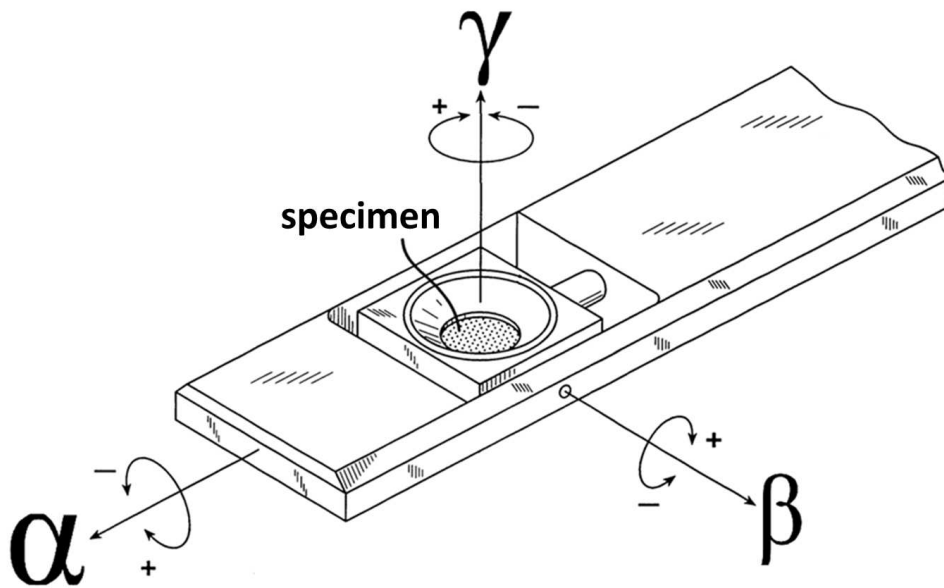


Figure 2.28 | Double tilt and rotate stage, schematic diagram showing the principle of Double-tilt stage. The specimen holder can tilt a specimen in two axes, α tilt in the direction of the X-axis and β tilt in the Y-axis. Also the specimen can be rotated around $\pm 360^\circ$ of the γ plane. After [Alani et al. \(2002\)](#) and [Frank \(2010, chapter 1\)](#).

on the thickness of the specimen ([Yaguchi et al., 2008](#)). However, for ET, the quality of reconstruction can be still limited due to the finite angular increment of the radial sampling between each projection. Also, there are other difficulties associated with this method; that is: it can only be applied to samples that can be self-supporting and are stable under the FIB. Also, it requires a dedicated tomography holders (the On-Axis rotation tomography holders) that can hold a cylindrical specimen cartridge. Therefore, this technique is used on a limited number of studies ([Haberfehlner et al., 2014a](#); [Jarausch et al., 2009](#); [Kato et al., 2008](#)). Two types of incrementing schemes between tilt angles are usually used:

1. Linear data collection scheme: fixed for the entire tilting range.
2. Saxton data collection scheme: continuously decreases with increasing tilt angle (by a scaling factor of $\cos \theta$, where θ is the tilt angle). This scheme is usually preferred with thin-film samples (e.g., solar cells as in: [van Bavel](#)

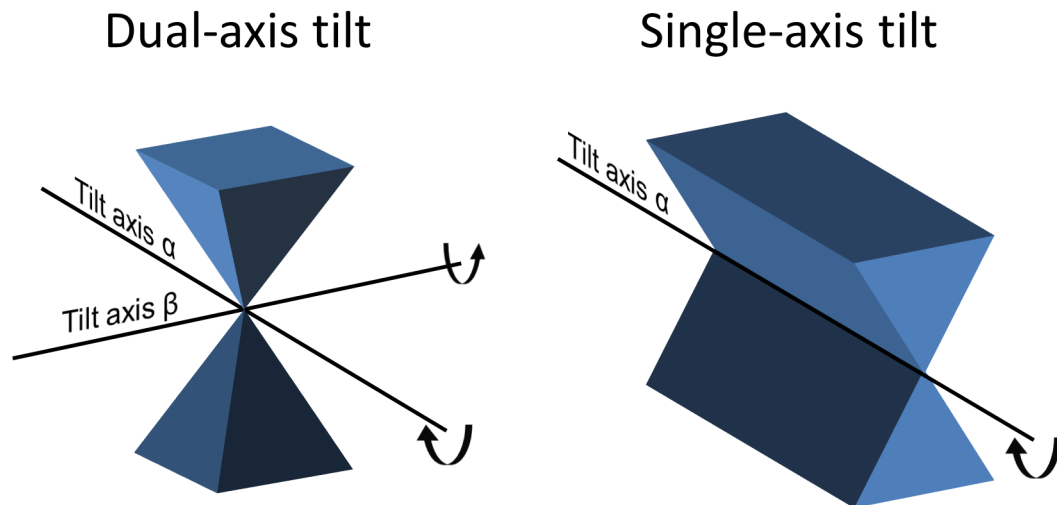


Figure 2.29 | Missing wedge, missing wedge in single-axis tomography reduced into a missing pyramid when using dual-axis acquisition geometry. After [Arslan et al. \(2006\)](#).

and [Loos, 2010](#)) since the thickness of such samples increases steeply with higher tilting angle. This will result in sampling larger number of images at higher tilt-angles which help to maintain a stable resolution throughout the tilt series and thus improve the quality of the final reconstruction ([Saxton et al., 1984](#)).

Other less common tilting geometries had been proposed such as: *multiple-axis* ([Messaudi et al., 2006](#)) and *conical* ([Lanzavecchia et al., 2005](#); [Zampighi et al., 2005](#)). ([Frank, 2006a](#)) provided a review of acquisition geometry in ET.

Automated data acquisition Acquisition of TEM tilt series is a very much of computer-automated (or semi-automated) process, nowadays. This automation has extended ET to beam-sensitive specimens, especially in biological sciences, where damage by inelastic processes is a critical problem ([Koster et al., 1992, 1997](#)). In the physical sciences, ET can be severely limited by both the knock-on damage and contamination. Such problems can be significantly reduced with automated low-dose protocols ([Leschner et al., 2010](#)). The ET acquisition process involves several steps: tilting, image tracking, to minimize shifts between images, and focusing. The first step involves tilting the specimen to a specific angle and tracking the features of interest to keep it in a central position (x and y planes)

2.3 Practical aspects of electron tomography

of the field of view. Such image shifts occur usually due to the unavoidable drift in the sample stage caused by different mechanical vibrations (e.g. motors, thermal expansion) (Zheng et al., 2010). Such image shifts can be handled using of various algorithms using a reference image (Koster et al., 1992) or predicted positions (Zheng et al., 2004) or both (Koster et al., 1997). It is also critical to keep the sample at the correct eucentric height in order to minimise drift during tilting and avoid large shifts which result in losing the feature of interest. Small remaining shifts are handled in the image alignment step (section 2.3.3). Following the tracking step, the need to be focused before acquiring. The sample is then filtered, and the previous steps are applied till reaching the highest possible tilt angle.

EM data acquisition for single (Koster et al., 1997) and dual-tilt (Zheng et al., 2009), have been automated and is provided by many software packages, such as: commercially by DigitalMicrograph from Gatan and Xplore3D from FEI, or non-commercially (such as SerialEM Mastronarde, 2005) from Boulder Laboratory. Although, automated acquisition is promising in reducing the exposure time, it is sensitive to parameter tuning (such as, focus interval, image filter and acquisition time) and can be limited in some cases especially when it is not possible to focus the images automatically.

Focusing during acquisition When a sample is tilted to high angles, the problem of the lack of uniform focus may arise when different regions of the specimen are out of focus (Figure. 2.27). This will result with an image of different focusing values (blurred) for different regions. Such problem can reduce the quality of tomographic reconstruction. This problem can be reduced using a dynamic focus option in STEM imaging mode. This allows the STEM to optimise the focusing values for each raster line. This option becomes more important with highly convergent beams where the depth-of-focus¹ is limited.

Since TEM imaging uses a fixed focus, only a very narrow area can be optimally focused on for obtaining images of highly tilted specimens. Therefore, the introduction of a sufficiently large defocus is required in TEM tomography. However, the scanning beam can be focused flexibly in STEM. Therefore, the entire image area can be optimally focused on, even in highly tilted specimens, and

¹The range of the thickness in the sample plane which can remain focused in the projection.

defocusing becomes unnecessary (Aoyama et al., 2008). The STEM tomography system used in this study is capable of providing the dynamic focus function.

2.3.3 Tilt series alignment

One of the major problems during the acquisition process is the shift of specimen caused by the mechanical (or thermal) instability of specimen holder. Therefore, it is crucial, for obtaining a high-quality tomographic reconstruction, to carefully align the tilt series after been acquired. It is also important to align the tilt series to a common tilt axis with a sub-pixel accuracy. The inaccurate estimation of the tilting axis causes the distinctive *arcing* artifacts (as in Figure. 2.30).

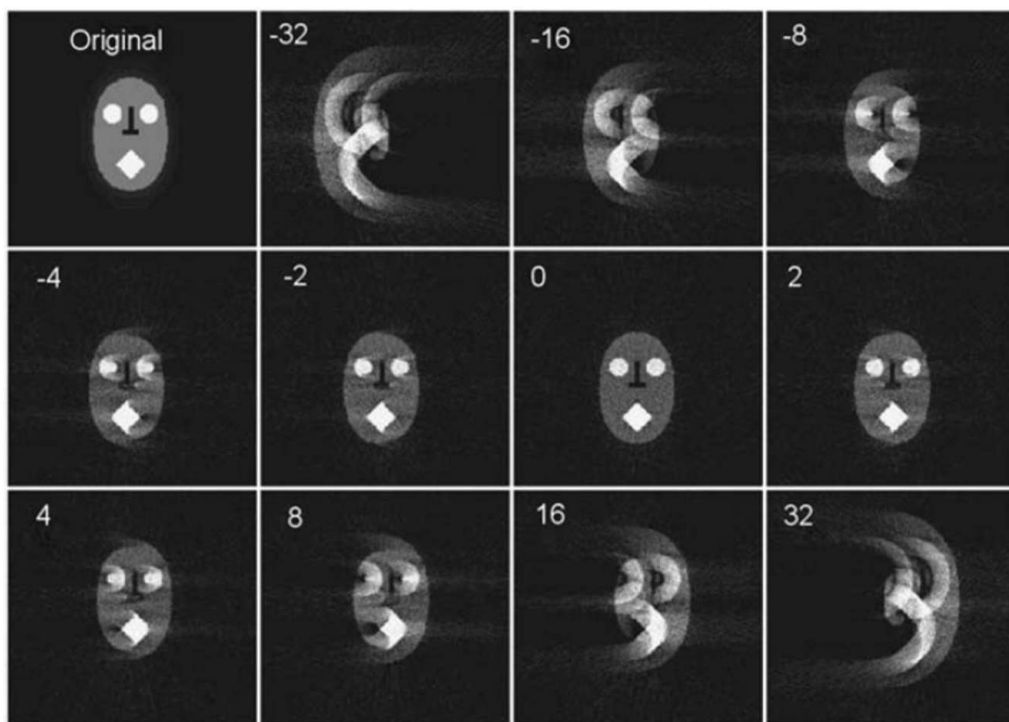


Figure 2.30 | Tilt axis misalignment, the arcing artifacts are shown in the reconstruction of the head phantom. The numbers indicate the magnitude and the direction of misalignment that was introduced perpendicular to the tilting axis. Adapted from Kirkland and Hutchison (2007, figure 6.19).

There are two types of alignment methods, fiducial marker-based alignment, and marker-free alignment. Fiducial marker-based alignment (Kremer et al., 1996) is performed by placing reference points (heavy-metal markers, often, 510 nm-diameter gold particles) in the specimen. The coordinates of these markers are

2.3 Practical aspects of electron tomography

tracked on each projection manually or automatically, followed by calculating an alignment model using least-squares procedures (e.g., Frank, 2006a, p. 197) that minimise the error of the alignment as a function of the angle of the tilt axis and lateral translations. Gold beads can be localized very accurately, even at a high tilt angle, because of their typically high contrast compared to the background and their round shape. This is why, this approach is accurate and very common in biological applications, where projection images usually sufferer from limited contrast. Also, it can be efficient in correcting the projection series for image rotation, and magnification change that might occur during the acquisition¹. However, fiducial markers are usually hard to apply in material science as the gold beads may interfere with the sample and introduce undesirable artifacts, in addition to difficulties such as finding enough gold beads at the region of interest and the very time-consuming labour involved.

Alternatively, the marker-free alignment methods, which do not require any sample manipulation before data acquisition, can be applied. These methods can be sub-categorised into correlation methods and feature-based methods (Frank, 2010, chapter 6). Alignment by Correlation methods, such as cross-correlation (Guckenberger, 1982; Winkler and Taylor, 2006) have been widely used in the physical sciences, and few studies in biological sciences (e.g., Dai et al., 2013). Cross-correlation is implemented by computing the cross-correlation² coefficients between two adjacent images. Then the relative shift between the two images can be obtained by the position of the maximum value of the cross-correlation image. However, this method depends critically on the availability of distinctive high-contrast objects in the image. This limitation might hinder the accuracy of alignment compared to marker-based approach, especially with low-contrast imaging. Also, the effect of noise and tilting results in a blurry cross-correlation maxima which affect the accuracy of alignment. A band-pass or edge detection filters are usually applied to reduce this problem. Iterative cross-correlation approach (as in Winkler and Taylor, 2006) are commonly available in commercial ET packages. It works by generating a tomogram and correlating with re-projections from it to minimise the re-projection error. This method is considered a standard routine in ET applications in material sciences and considered the first step of

¹By incorporating these parameters into the alignment model. However, some of such additional parameters may have a large degree of freedom. Therefore, several gold markers may be needed to reduce the uncertainty of these parameters.

²The inverted Fourier transforms F^{-1} of the product of the Fourier transform F of the first image and the complex conjugate of the F of the second one.

alignment before applying other methods. Feature-based methods utilize image features as virtual markers and align images iteratively by minimizing the re-projection error of virtual markers. The principle of feature-based alignment is same as that of marker alignment. For more details of alignment methods in ET, the reader is referred to (Frank, 2010, chapter 6). In this thesis, different alignment methods were used and are described in the relevant sections.

2.3.4 Reconstruction of tomographic tilt series

As shown in section 2.3.2 and 2.3.3, ET is performed in a very limited practical conditions, compared to many other tomographic techniques (e.g., CT). Consequently, reconstructing a faithful representation of the sample is a challenge and has been studied by many groups since the first application was published by DeRosier and Klug (1968).

Established ET reconstruction algorithms that are discussed in this thesis are, weighted back-projection (WBP) and simultaneous iterative reconstruction technique (SIRT) (Gilbert, 1972). Other methods such as the discrete algebraic reconstruction technique (DART) and weighted SIRT (W-SIRT) are mentioned briefly. It should be noted that, before the reconstruction algorithm can be applied, there is an important condition that needs to be fulfilled, known as the *Projection Requirement*.

Projection Requirement As defined by the Radon transform (Equation. 2.4 in section 2.2.3.1), the ideal projection is a summation of line integrals through the object. This integral summation can be of some physical property (e.g. density, magnetic or electronic properties of materials). In ET, this ideal projection' is hard to achieve and therefore, a more relaxed condition is usually accepted instead, known as *projection requirement* (Hawkes, 2006). Therefore, it is generally regarded as sufficient that TEM intensity response, at the minimum, be a monotonic function of a projected physical quantity (Hawkes, 2006).

For non-crystalline materials (e.g., biological samples), mass-thickness contrast is the primary imaging mechanism in TEM. This contrast satisfies, approximately, the projection requirement for ET. However, for crystalline materials, mass-thickness does not meet the projection requirement due to the coherent nature of TEM illumination which results in a strong, nonlinear interaction between electrons and the specimen (as in Figure. 2.13). This will lead to a non-monotonic

image intensity variations for crystalline materials at different tilts. Instead, an incoherent scanning (STEM) imaging modes (e.g., high angle annular dark field-HAADF) are employed for crystalline materials tomography (Midgley and Weyland, 2003). Consequently, both imaging techniques have been widely used in ET. If the imaging process is non-linear (e.g. intensity is a decaying exponential function of thickness), then some pre-processing of the images may be required before reconstruction is sensible or possible (Van-den Broek et al., 2012).

Weighted back-projection (WBP) The WBP is one of the most widely used reconstruction technique in ET due to its speed and simplicity. In the simplest form of back-projection (Deans, 1983; Pennycook and Nellist, 1999), each projection is smeared back into the tomogram at the projection angle. In practice, given a sufficient number of projections, the tomographic reconstruction of an object can be obtained by back-projecting all projections as illustrated in Figure. 2.2. However, back projection reconstructions typically produce tomograms with blurred features, as in Figure. 2.31. This degradation of fine spatial details happens because of the oversampling of the low-frequency information (corresponding to larger detail in the spatial domain) near the center of the Fourier domain, as illustrated in Figure. 2.36 and 2.20, compared to the high frequencies (corresponding to small spatial details). This can be corrected by convolving the reconstructed tomogram with a simple ramp-like weighting filter¹ to balance the uneven sampling distribution in Fourier domain (Deans, 1983). WBP is highly parallelisable, and the implementation on GPU graphics cards or multi-cores CPUs produce a significantly faster reconstructions (Frank, 2010, chapter 8). However, due to a discrete number of projections acquired and the missing wedge of information, reconstructions using WBP usually contains serious artifact which complicates the interpretation of the resulted tomograms. In addition to the presence of noise in the projections which further reduce the accuracy of the reconstruction process.

It should be remarked that there is a fundamental connection between the Radon transform and the Fourier transform for the tomographic reconstruction, as previously discussed in section 2.2.3.2 and Figure. 2.19, such that both theoretically provide equivalent methods. However, the implementation of the forward

¹i.e., with an amplitude that increases linearly to a maximum at a high cut-off value.

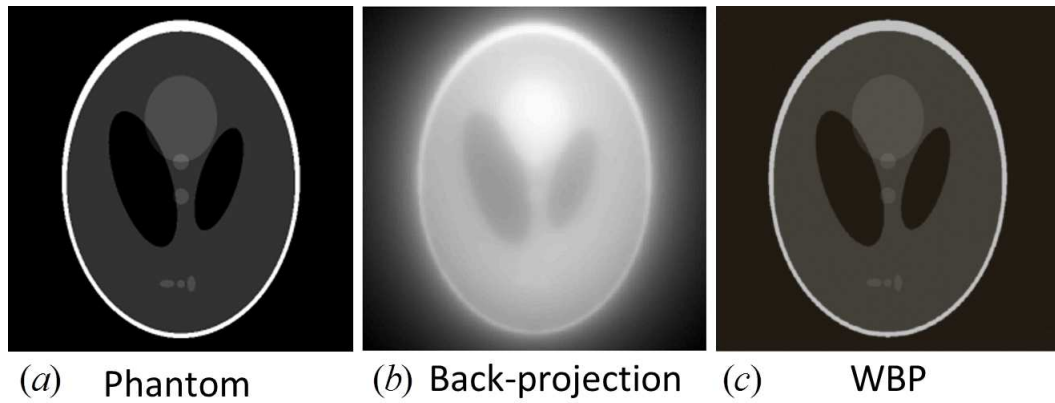


Figure 2.31 | Back-projection, shows the difference between the simple back-projection with blurred features in (b) and the weighted back-projection in (c).

and inverse Radon transforms in real space is often preferred over the implementation in the Fourier domain as it avoids the interpolation¹ errors associated with of the Fourier-based implementations (Radermacher, 1988). Nevertheless, new interpolation methods (e.g., Min-Max NUFFT approach (Fessler et al., 2003)) that provide higher interpolation accuracy, have made it feasible to apply the reconstruction in the Fourier domain. Fourier-based methods are computationally faster than real space methods due to the utilisation of the fast Fourier algorithm (FFT) (Rockmore, 2000). Such advantage in speed is important for implementing ET iterative reconstruction methods.

Regularisation reconstruction methods Mathematically, the projection process can be discretised as a large linear system of equations (Figure. 2.32) of the form:

$$A_{m \times n} \times x_{n \times 1} = B_{m \times 1}, \quad B = \hat{B} + e \quad (2.8)$$

Where $x \in \mathbb{R}^n$ is a real-valued vector of size n in the real space \mathbb{R} and represents the unknown tomogram (a vector representation of a 2D image representing a slice through 3D object). $A \in \mathbb{R}^{m \times n}$ is the projection matrix (i.e., discrete Radon transform operator) that transforms x into projection measurements $B \in \mathbb{R}^m$ in the sinogram domain, with $m = \text{number of projections} \times \text{number of pixel in each projection}$ and e is an error term modelling measurement errors. \hat{B} denotes the

¹To convert the data between the polar co-ordinates and Cartesian co-ordinate systems. also known as *gridding* process.

2.3 Practical aspects of electron tomography

exact measurements and is under-sampled, when m smaller than n (i.e. $R_{\theta < 180^\circ}$) by one or several orders of magnitude indicating severe under-sampling. The ET problem is underdetermined due to the under-sampling of the tilt series. The projection matrix A can be constructed using the ray diagram in Figure. 2.32. To make a reconstruction of the object x , one has to solve the inverse problem

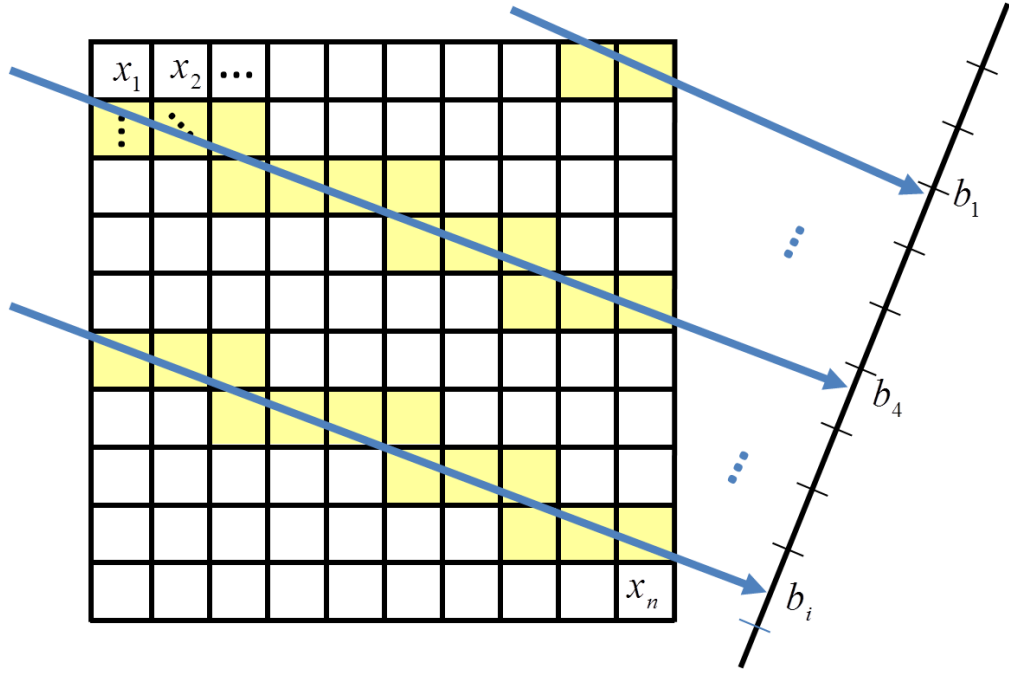


Figure 2.32 | The Projection geometry for tomographic problem., An element a_{ij} in the projection matrix A can be constructed by computing the contribution percentage of each pixel x_i in the projected object x to the ray that result in pixel b_j in the projection matrix B .

in (Equation. 2.8) for recovering the unknown vector x from the measurements b . However, the inverse of A does not exist and therefore, other methods must be used, such as singular value decomposition (SVD). SVD provides a means to obtain the solution of previous equation directly. A can be decomposed as

$$A = U\Sigma V^T = \sum_{i=1}^n u_i \sigma_i v_i^T. \quad (2.9)$$

where, $\Sigma \in \mathbb{R}^{m \times n}$ is a diagonal matrix with the singular values, satisfying

$$\Sigma = \text{diag}(\sigma_1, \dots, \sigma_n), \quad \sigma_1 \geq \sigma_2 \geq \dots \geq \sigma_n \geq 0.$$

2.3 Practical aspects of electron tomography

Matrices $U \in \mathbb{R}^{m \times m}$ and $V \in \mathbb{R}^{n \times n}$ contains the left and right singular vectors:

$$U = (u_1, \dots, u_m), \quad V = (v_1, \dots, v_n).$$

and contains orthonormal columns (i.e., $U^T U = V^T V = I$). If the inverse of A exist, then it is given by

$$A^{-1} = V \Sigma^{-1} U^T, \quad \Sigma^{-1} = \left[\frac{1}{\sigma_1}, \dots, \frac{1}{\sigma_n} \right]. \quad (2.10)$$

Therefore, when substituting Equation. 2.10 in Equation. 2.8, the reconstruction problem can now be formulated as in (Equation. 2.11) when expressed in terms of the generalized SVD associated with the regularization problem. x^* is usually called the *Naive solution*.

$$x^* = V \Sigma^{-1} U^T B = \sum_{i=1}^n \frac{u_i^T B}{\sigma_i} v_i. \quad (2.11)$$

However, the inverse problem described by A is a discrete ill-posed problem (as characterised by the large condition number of matrix A ¹), this also implies that x^* is very sensitive to the noise in measured data B . This might result in x^* to be very far from the exact solution. An approximate solution, that is less sensitive to the perturbations in the measurements B , can be obtained by regularisation methods. These methods enforces regularity on the computed solution (i.e., by introducing additional prior-knowledge constraints or applying smoothness in some sense) which lead to suppressing the noisy component and prevent over-fitting during the reconstruction process (Hansen, 2010, chapter 2).

The approximation properties of regularized solutions need to satisfy the discrete *Picard condition (PC)* for obtaining good regularized solutions. That is if the coefficients $u_i^T B$ of Equation. 2.11 on average, decay to zero faster than the singular values σ_i , then the regularized solution x^* is guaranteed to have approximately the same properties as the exact solution x (Hansen, 1990; Varah, 1979). The Picard condition plays an important role in the analysis of discrete ill-posed problems.

The behaviour of the regularisation method can be revealed when investigating the SVD coefficients $u_i^T B$ and $\frac{u_i^T B}{\sigma_i}$ of (Equation. 2.11). The plot of there

¹ $cond(A) = \|A\|_2 \|A^{-1}\|_2 = \sigma_1 / \sigma_n$

2.3 Practical aspects of electron tomography

coefficients along with the singular values σ_i is usually referred as the Picard plot. Figure. 2.33, shows the Picard plot of the tomography problem (Equation. 2.11) for both the noisy and noise-free measurements B . The horizontal-axes represent the index i while the vertical shows the values of the coefficients. Higher index values correspond to the higher frequency information. Singular vectors σ_i corresponding to large singular values (low i) carry mainly low-frequency information, while singular vectors corresponding to the smaller singular values (large i) tend to represent high-frequency information. In Figure. 2.33(a), it is clear that the coefficients $u_i^T B$ decay faster than σ_i , which satisfy the PC. However, in Figure. 2.33(b), despite the initial decay of the SVD coefficients $u_i^T B$, they start to increase for larger index values i until they level off at a plateau determined by the noise. Most regularisation methods can be expressed using a Filtered SVD

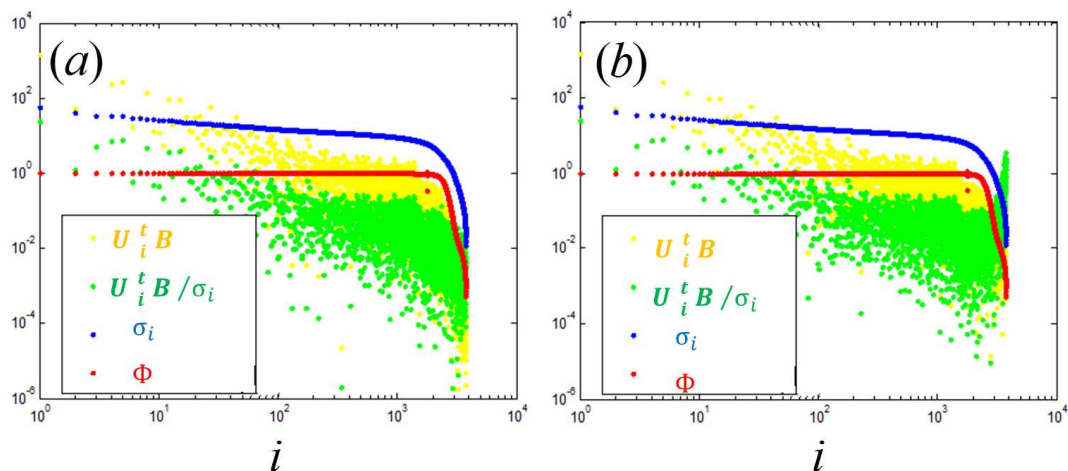


Figure 2.33 | Illustration of the Picard condition (PC), (a) shows the Picard plot for the noise free case of Equation 2.11, (b) shows how the SVD components changes after adding Gaussian noise to the measurements B . The PC is satisfied in (a) but not in (b) for $\sigma_i > 10^{3.4}$.

expansion:

$$x^* = \sum_{i=1}^n \phi_{[i]}^{[k]} \frac{u_i^T B}{\sigma_i} v_i \quad (2.12)$$

where $\phi_{[i]}^{[k]}$ are the spectral filters associated with the regularisation method. Several regularisation methods have been proposed to solve ill-posed problems. These methods include Truncated SVD, Tikhonov or iterative regularisation methods (e.g., SIRT) for large scale problems. These methods depends critically on the

regularisation parameters and require tuning to yield a proper solution (Hansen, 2010).

Simultaneous iterative reconstruction techniques (SIRT) The rapid advancement in computing power and the availability of sufficient memory has made it possible to implement more-complex reconstruction algorithms, such as the simultaneous iterative reconstruction technique (SIRT) (Gilbert, 1972; Herman, 2009; Kak and Slaney, 2001). SIRT constrain the reconstruction process to produce a tomogram that is consistent with the measured projections. SIRT starts from an initial reconstruction obtained using WBP. This reconstruction is then linearly re-projected along the original tilt direction of the experimental projections and the difference is computed simultaneously, either by subtraction in additive techniques or division in multiplicative techniques. Then the current reconstruction is improved by adding (or multiplying) the obtained difference. This procedure iterates till the maximum number of iterations is reached. Figure. 2.35 illustrates the principles of SIRT.

SIRT is nowadays a common reconstruction method that is favoured due to its robustness to noise. However, similar to WBP, it still requires a large number of projections with a reduced missing wedge to produce optimum results. Furthermore, SIRT suffers from what is called semi-convergence (Elfving et al., 2012), whereby initial iterations converges towards better estimations of the solution before the reconstruction quality degrades with more refinement steps (Figure. 2.34). The semi-convergence of projected iterative methods has been realised in several papers (e.g., Benvenuto et al., 2010; Elfving et al., 2012; Herman, 2009). However, it should be mentioned that the number of iteration is a critical parameter and is highly affected by the noise level in the projection and therefore, need to be estimated independently for each experiment. In practice, this parameter is estimated visually which can lead to subjective results. Mathematically, the iterative process of the SIRT algorithm for updating vector \hat{x}_{t+1} can be represented as in Equation. 2.13, with positive relaxation parameters sequence $\{\lambda_t\}$.

$$\hat{x}_{t+1} = \hat{x}_t + \lambda_t A' M (B - A \hat{x}_t), t = 0, 1, \dots, t^{Max} \quad (2.13)$$

Several well-known SIRT variations can be written in the form of (Equation. 2.13) for appropriate choices of the matrix M . Hansen (2010) and Banhart

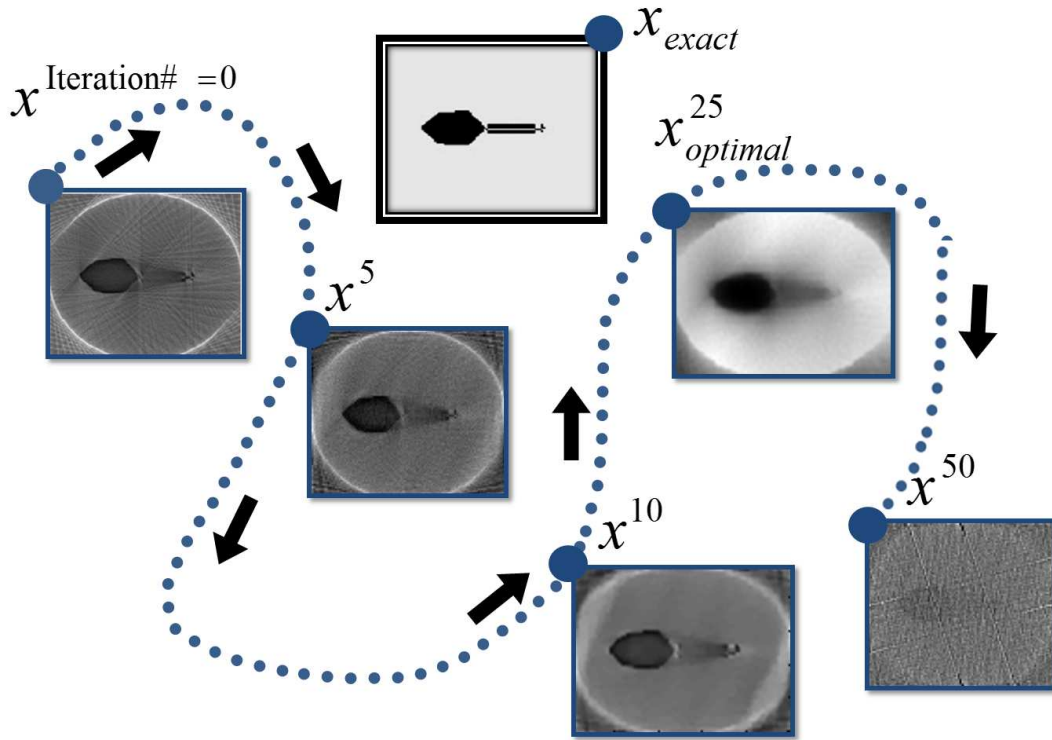


Figure 2.34 | Semi-convergence in tomographic reconstruction, the initial iterates tend to a better approximation of the exact solution but above a certain number of iterations they begin to deteriorate.

(2008a) provided a comparison between different SIRT forms. Setting M to the identity, the classical common variant, *Landweber method* (Landweber, 1951) can be used as a least squares optimisation (Gregor and Benson, 2008) of the form:

$$\hat{x} = \arg \min_x \|A\hat{x} - B\|_2^2 \quad (2.14)$$

The spectral filters ϕ_i^{sp} of the Landweber SIRT method can be expressed as:

$$\phi_i^{[k]} = 1 - (1 - \omega\sigma_i^2)^k \quad (2.15)$$

where k is the iteration number (which is the regularisation parameter). Equation. 2.15 provide an explanation of the semi-convergence behaviour (Figure. 2.34) of the SIRT algorithm. When the number of iteration k increases, more SVD components are effectively included in the solution. This means with large

k more high frequency spectral component which might contains noise are being included in the solution while a low k means that the solution will lack the high spectral information and can be blurry. A detailed mathematical elaboration of the established methods in ET can be found in (Deans, 1983; Frank, 2010; Herman, 2009; Kak and Slaney, 2001; Natterer, 1986) and (Penczek, 2010).

Recent reconstruction methods The quality of reconstruction can be further enhanced by incorporating further knowledge about the specimen during the reconstruction process. Several methods had been proposed recently for ET reconstruction and employs prior knowledge constraints about the specimen, such as grey level as in the discrete tomography methods (such as the discrete algebraic reconstruction technique DART (Batenburg et al., 2009) which can provide a good approximation of the reconstructions if there are information about the gray-level/density of the specimen's features and it is possible to describe the features in discrete terms. This technique had gained interest in atomic resolution electron tomography where it is possible to harness the fact that crystals are discrete assemblies of atoms (atomicity) (Jinschek et al., 2008). Other recently proposed ET algorithms include:

- **Weighted-SIRT (WSIRT):** This method showed an improved resolution and reduced reconstruction error compared to SIRT. It is based on a hybrid reconstruction approach than combines WBP and SIRT (Wolf et al., 2014).
- **Direct iterative reconstruction of computed tomography trajectories (DIRECT):** This method showed an improved resolution and contrast from noisy and incomplete dataset compared to SIRT algorithm (Lange et al., 2011).
- **Object-based reconstruction methods:** They employ prior knowledge about the shape and geometry to refine the reconstruction. These methods are considered a different class of the ET reconstruction methods and is usually based on modeling the imaging process (Alpers et al., 2013).

A new class of ET 3D reconstruction methods that employ the recent new paradigm shift in signal processing (known as *compressed sensing*) are gaining popularity. These methods use prior knowledge about signal sparsity to overcome the problems arising from under-sampling and the missing wedge (e.g., DLET Al-Afeef et al., 2016). Chapter 4, address these methods.

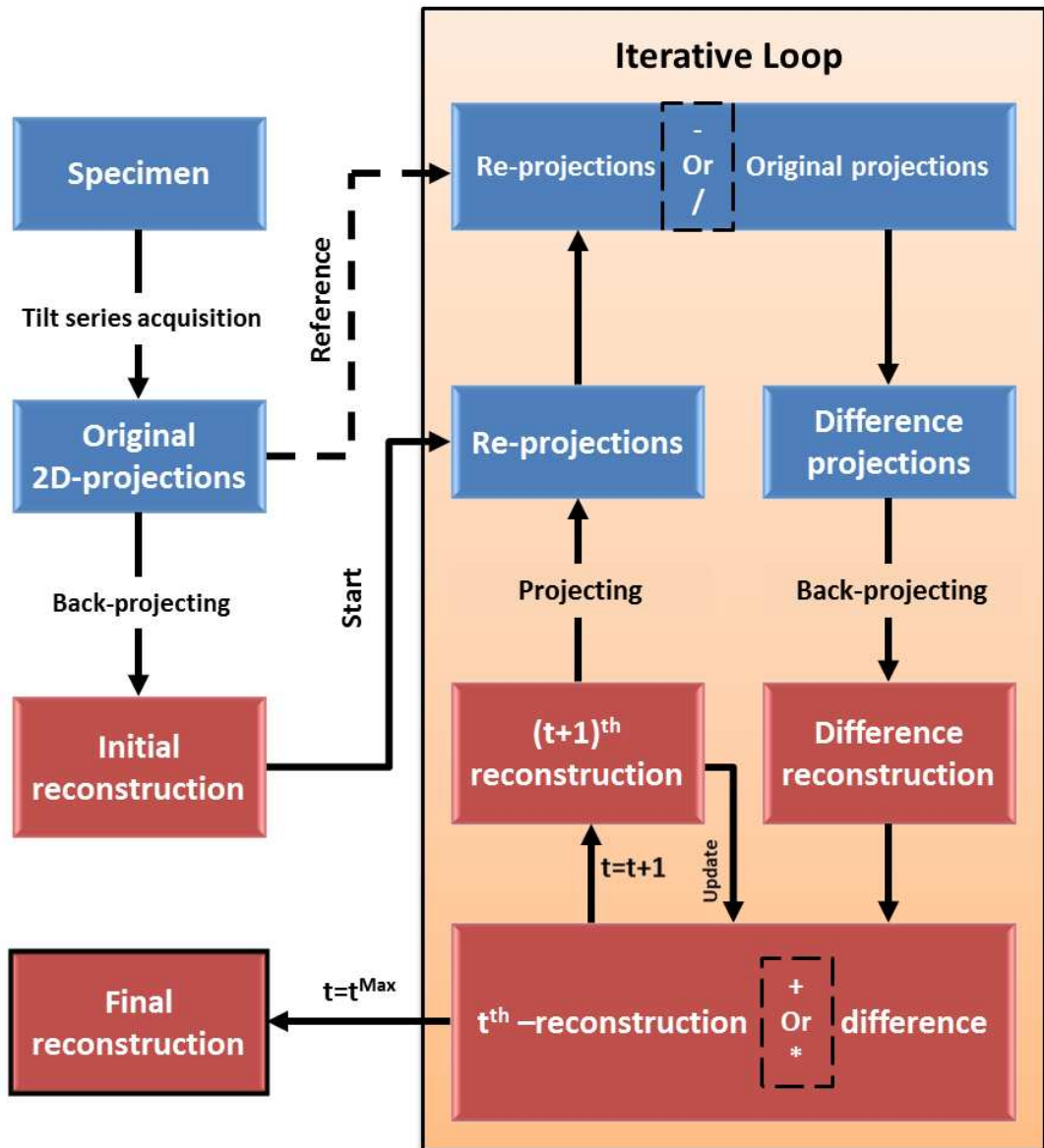


Figure 2.35 | SIRT flowchart, illustrating how iterative reconstruction is implemented for a $t = t^{Max}$ iterations. After [Kirkland and Hutchison \(2007, chapter 6\)](#).

Reconstruction resolution and artefacts Due to the limited sampling of tomographic-acquisition in ET, the reconstruction from a single-axis tilt series result in anisotropic resolution. This also lead to serious artefacts in the reconstructions (Friedrich et al., 2009, 2005; Midgley and Weyland, 2003; Wang et al., 2012).

The missing wedge causes two main problems. The first problem is that certain structures may be misshapen or even completely absent from the tomogram depending on their orientation to the tilting axis (Sugimori et al., 2005; van Bavel and Loos, 2010). The second problem, is the elongation e_{zx} of the reconstructed volume in the direction parallel to the electron beam (i.e. this result in distorted features and the distance measurements along the z-axis have to be taken with care as shown in Figure. 2.25) (Radermacher and Hoppe, 1980). The work of Radermacher (1988) showed that this elongation e_{zx} depends on the size of the missing wedge (viz., the maximum tilt angle θ_α) and is related using Equation. 2.16.

$$e_{zx} = \sqrt{\frac{\theta_\alpha + \sin \theta_\alpha \cos \theta_\alpha}{\theta_\alpha - \sin \theta_\alpha \cos \theta_\alpha}} \quad (2.16)$$

Using Equation. 2.16, elongation of 1.3 times is expected in the z-direction for a θ_α of $\pm 70^\circ$, 1.55 times for $\pm 60^\circ$, and 1.9 times elongation for $\pm 50^\circ$ which are a significant distortion. Experimental studies, however, showed that Equation. 2.16 provided an over-estimation of the elongation. A detailed study by Kawase et al. (2007) on the observed missing wedge impact on a rod-shaped specimen (that are tilted around $\pm 90^\circ$), showed the following experimentally measured elongation factors: 1.10 for $\pm 70^\circ$ and 1.23 for $\pm 60^\circ$. Other studies (e.g. van Bavel and Loos, 2010, on gold particles) support this observation.

The limited angular sampling causes shading or streaking (Figure. 2.25) in the reconstructed image, seriously degrades the reconstruction resolution and make it vary with direction (CAO et al., 2009). The resolution along the tilt axis direction is determined by the resolution of the original TEM projection image and the alignment accuracy. The resolution along the axis that is perpendicular to both the beam direction and the tilt axis (y), depends on the number of projections (N) and the diameter (D) of the reconstructed volume as derived by Crowther et al. (1970) as in equation. 2.17. When the specimen's thickness T is

known, D can be computed as $D = \frac{T}{\cos \theta_\alpha}$.

$$d_y = \frac{\pi D}{N} = \frac{\pi T}{N \cos \theta_\alpha} \quad (2.17)$$

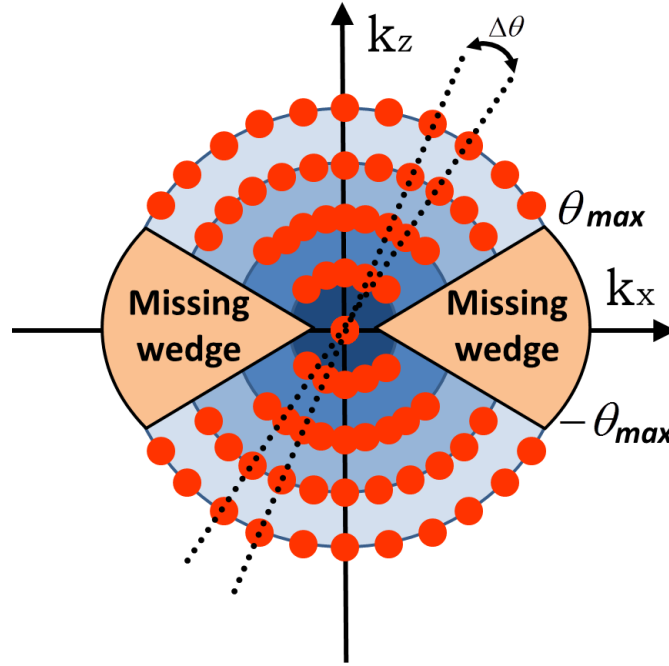


Figure 2.36 | Under-sampling in ET, Shows the tilt series sampling in the reciprocal space. Each dotted line represent a tilt projection (Fourier slice) at θ . The angular increment on each Fourier slice varies with $\delta\theta$. The data is oversampled at low spatial frequencies near the centre, which yields a blurred version of the object if not compensated for in the reconstruction method. The missing wedge of information is illustrated between θ_{max} and $-\theta_{max}$.

Figure. 2.36 illustrates the geometry of Equation. 2.17. The maximum resolution through the specimen thickness (i.e. along the electron beam direction) can be approximated using resolution d_y , however, due to the missing wedge, it is subject to additional deterioration by a value of e_{zx} as shown by Radermacher (1988) in Equation. 2.18.

$$d_z = d_y \cdot e_{zx} = \frac{\pi T}{N \cos \theta_\alpha} \sqrt{\frac{\theta_\alpha + \sin \theta_\alpha \cos \theta_\alpha}{\theta_\alpha - \sin \theta_\alpha \cos \theta_\alpha}} \quad (2.18)$$

It should be noted that, although the resolution approximation in Equation. 2.17 and 2.18 are frequently cited in EM literature, the general validity of these expressions has been questioned (Friedrich et al., 2007; van Bavel and Loos, 2010; Weyland et al., 2001; Ziese et al., 2002) and by Frank (2006a, chapter 10). Other methods for measuring resolution had been proposed (Chen et al., 2014; Mezerji et al., 2011; Vulović et al., 2013).

Such methods are based on empirical measuring. However, this method can be difficult to apply and usually not consistent with their predicted resolution. In general, no straightforward widely accepted approach exists (Frank, 2006a, chapter 4). The general consensus is that, the tomographic study of any particular object should be unique and the resolution should be derived from other factors such as the noise level of data (SNR), number/angular distribution of projections (Frank, 2006a, chapter 10), shape of the object and type of the reconstruction method (Midgley and Weyland, 2003).

2.3.5 Tomogram segmentation and quantification

In order to obtain a quantitative analysis, the 3D reconstructed volume requires to be segmented. During this segmentation step, each voxel (or gray level) in the reconstructed tomogram needs to be assigned to a specific features or compositions that represent the original object (e.g., nanoparticle and background). Following this, quantitative information (e.g., volume percentage and surface area) can be obtained.

The quality of segmentation is highly affected by the quality of the 3D reconstruction. Therefore, segmentation is usually achieved by manual procedures, where the features in a 3-D reconstruction are interpreted by highlighting voxels (or boundaries) belonging to the features of interest in each slice of the reconstructed 3D tomogram. This is very time-consuming, labour intensive and usually led to subjective interpretation. Alternatively, automatic or semi-automatic segmentation methods can be used. The importance of such methods has increased over recent years especially for biological sciences.

Several advanced segmentation methods had been proposed mainly from the biological ET community. The most common and straightforward automatic segmentation method is by thresholding (e.g., Otsu method (Otsu, 1975b) or multi-level Otsu method). In this method, the boundary between materials is determined by choosing the optimal separation grey level which is specified by

minimising the interclass variance of the tomogram histogram. This method can be effective with high-quality images with sharp intensity difference between different materials. However, in practice, such sharp boundaries are rarely achieved due to reconstruction and imaging artifacts, and, therefore, these methods may result in over/underestimation of the boundaries between different features and the background. More sophisticated automatic segmentation methods proposed, i.e. Watershed (Beucher and Meyer, 1992; Vincent and Soille, 1991), gradient vector diffusion (Bajaj et al., 2003). Recent reviews summarising other advanced segmentation methods are provided by Frank (2006a, chapter 11) (Banhart, 2008a; Fernandez, 2013; Volkman, 2010).

It is critical to point out that, it is often preconceived that segmentation procedure needs to be developed as a case-by-case basis. The segmentation algorithms outcomes are highly influenced by the quality of tomographic reconstructions and often fails when applied to poor quality and noisy reconstruction. Therefore, a high fidelity reconstruction (as clearly demonstrated in chapter 3) will simplify the segmentation procedures and enables higher quality quantification results.

2.3.6 Visualization

Optimal visualization of the 3D reconstruction is critical for successful characterization and quantification of 3D structures. Several visualization techniques can be used to interpret the 3D volume. In this thesis, three main techniques of visualisation, are used: orthoslices, volume rendering and surface rendering. Figure. 2.37 shows an illustration of these techniques for the 3D volume of Feline Calicivirus (FCV). Orthoslices, are the most trivial way of visualisation, where 2D slices through the 3D volume are shown. The intensity in orthoslice images represent the intensity distribution (or often the density) of a feature in the 3D structure, which differ from the 2-D projections intensity that represent a summation of the whole structure in a single tilting angle direction. Orthoslices are usually carried out perpendicular (orthogonal) to the primary axes (x,y,z) and accurately reveals the true distribution of intensity in the 3D reconstruction, compared to other visualisation methods (Kirkland and Hutchison, 2007, chapter 6). An orthoslice through the 3D reconstruction of FCV is shown in Figure. 2.37 (a).

Volume rendering, on the other hand, is a very intuitive method in which properties of interest are emphasised by setting voxels with different intensity ranges, to a specific optical characteristic, such as Luminance, colour, texture

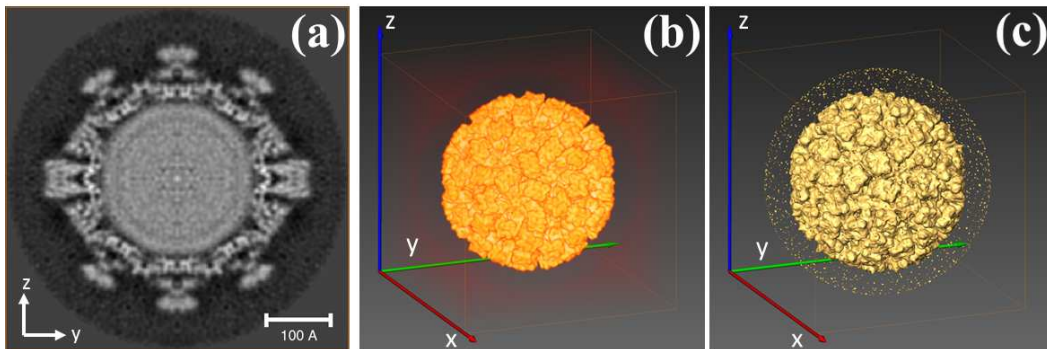


Figure 2.37 | Feline Calicivirus, (a) An orthoslice through the 3D reconstructed volume of FCV. (b) shows a volume rendering and (c) isosurface renderings of the FCV volume which provides a direct 3-D qualitative information. The segmented model of the virus is provided by [Bhella and Goodfellow \(2011\)](#).

or transparency. This type of rendering can give immediate information about the localization of features in the 3D volume. Therefore, they are preferred to visualising internal structures and subtle variations. An illustration of a volume rendering rendering is given in Figure. 2.37(b).

The surface rendering (*isosurface*) reduces the volume data into a set of surfaces. A set of polygons is generated by selecting a single threshold intensity within the volume data. They are favoured for revealing certain morphologies and topography in a fast manner (e.g., Figure. 2.37(c)).

2.4 Conclusions

In this chapter, the background material of this thesis has been introduced and discussed. An overview is given of the general principle of the transmission electron microscopy (section 2.2) and the primary S/TEM imaging modes that is used in this thesis (chapter 4, 5 and 6).

The foundations of electron tomography (section 2.1) is reviewed. It is shown that ET a 3D characterisation technique that is now widely used for materials in both the physical and biological sciences. The practical aspects of ET was discussed (Section 2.3). It has also underlined several limitations that need to be conquered to improve the fidelity of ET studies. The limited angular sampling of ET acquisition lead to the degradation of the ET reconstruction and limit its fidelity. This motivates the development of advanced reconstruction methods in

chapter 4 by incorporating additional *prior knowledge* in the ET reconstruction process, to produce high-fidelity reconstructions. This is preceded by a quality assessment study in chapter 3. In chapter 5, advanced signal modes in ET is used to reveal the chemical information of VC nanoparticles. Finally, additional cases from both material and biological science are examined using ET via both traditional and the proposed advanced ET method in chapter 6.

”
If you can not measure it, you can not improve it”

Lord Kelvin, 1883

3

Quality assessment of electron tomography for TEM/STEM imaging

This chapter studies the influence of the experimental conditions on the quality of the reconstructed ET tomogram. Regular shaped nanoparticles are used for testing tomograms obtained using the conventional weighted backprojection (WBP) and simultaneous iterative reconstruction technique (SIRT) methods against different experimental setups. The volumetric reconstruction is then followed by quantitative quality analysis. It is concluded that the fidelity of the post-reconstruction quantitative analysis and segmentation is limited, mainly by the fidelity of the tomogram. This motivates the development of an improved tomographic reconstruction process, as addressed in the subsequent chapters.

3.1 Introduction

As introduced in chapter 2, the ET process begins with the acquisition of a tilt series which is then reconstructed using an algorithm to produce a 3D tomogram to be segmented for quantitative analysis. There are many experimental parameters that need to be determined before acquisition, which include: tilt increment, electron dose, acquisition time, and acquisition scheme. Following the acquisition, image alignment parameters (such as the type of alignment procedure) and image reconstruction parameters (such as, type of algorithm used, and the number of iterations) needs to be chosen and can affect the quality of the tomogram.

It might be correct to assume that a lower tilt increment and a higher acquisition time will lead to a higher quality tomograms, However, this will increase the electron dose and might damage the sample and hinder the ability to image the sample in its original state as mentioned in section 2.1.6 in chapter 2. Therefore, the proper trade-off needs to be found between minimisation of damage and reconstruction quality.

WBP and SIRT methods are commonly used in ET. WBP has been one of the most widely used algorithms due to the high computational efficiency and the linearity of its steps. However, the main disadvantage that hinders WBP is the sensitivity to the tilt under-sampling which produces streaking artefacts that interfere with the reconstructed object. On the other hand, the SIRT method, although it is computationally more expensive, generates reconstructions of a better visual quality and is more robust to noisy data. Consequently, SIRT has become an increasingly popular ET reconstruction method.

The performance of the above algorithms has been mainly examined using experimental data (Goris et al., 2013b; Leary et al., 2013a; Saghi et al., 2011), which in general lack any ground-truth information about the exact 3D structure of the specimens. In this chapter, a detailed quantitative study is provided for both WBP and SIRT using nanocubes and nanospheres. Both of these materials are of well-known morphology and have regular geometrical shapes which makes the quality assessment of the ET reconstruction quantifiable with higher accuracy. The study includes the effect of three main experimental factors: the tilt increment, missing wedge size, tilt axis mis-alignment.

3.2 Experimental methods

3.2.1 Materials and sample preparation

In this work, magnesium oxide (MgO) nanocubes and nanospheres are used to assess the quality of 3-D reconstruction. The MgO nanoparticles (or so-called MgO smoke particles) are electron transparent and stable under the electron beam therefore, they can be directly examined by TEM (Williams and Carter, 2009). They are constituted by individual, nearly perfect, separated regular cubic microcrystals dominated by the high crystallographic quality, characterized by well-defined low index [001], [010] and [100] faces (McKenna et al., 2007; Scarano et al., 2004; Spoto et al., 2004), with a low concentration of defects, which makes them perfect samples to test the accuracy of 3D reconstruction. The morphology and associated properties are discussed in more details by Klabunde (2004).

The polystyrene nanospheres are also optimal for testing tomographic reconstruction methods. These polystyrene particles are usually used as a size standard for calibration in particle size analysis. The nanospheres that were purchased from Thermo Scientific Inc. with an average diameter of $46 \text{ nm} \pm 2 \text{ nm}$.

3.2.2 Instrumentation and experiment

MgO smoke nanocubes were prepared by burning magnesium ribbons in the ambient air. The use of this method for producing samples for TEM characterisation was first described by Heidenreich (1942). The smoke was directly collected on TEM Quantifoil grids and stored in a vacuum desiccator to reduce the contact to humidity which might reduce the sharpness of these cubes, as reported by Geysermans et al. (2009). The tomography experiment was performed on a JEOL ARM200F STEM equipped with a cold field emission gun and operated at 200kV. The sample was held in a JEOL tomography holder which allows a nominal tilt range of $\pm 80^\circ$, although, in practice, we were limited to a range of $\pm 75^\circ$ because of shadowing from grid bars on the sample support; images were recorded at 2° intervals in this range. Figure 3.1(a and b) shows HAADF-STEM images acquired at different tilt angles. The edge length of the nanocubes is on the order of a few tens of nanometers. Figure 3.1(c and d) shows the reconstruction of these tilt series using both WBP and SIRT.

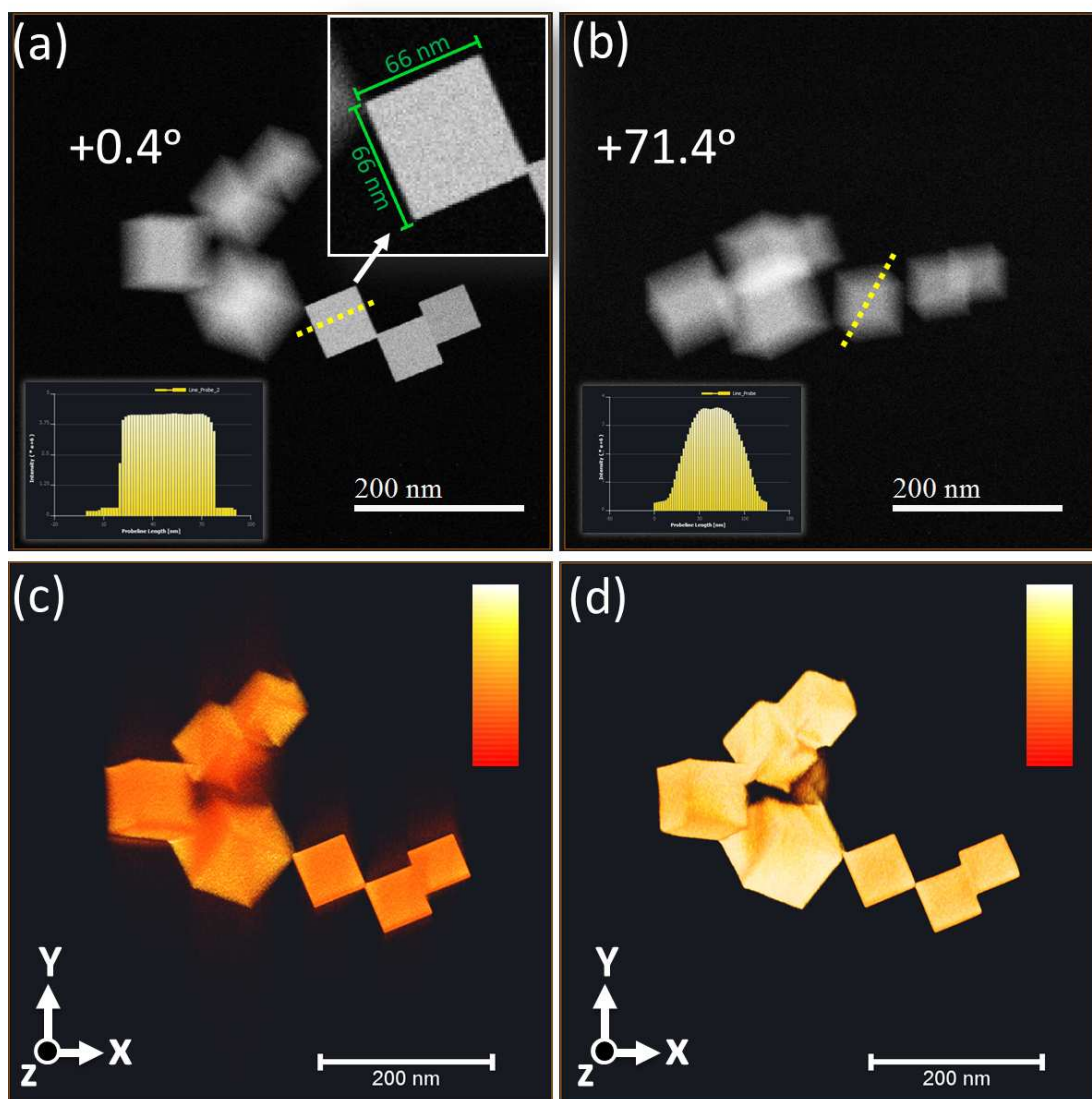


Figure 3.1 | Example MgO HAADF-STEM projection images acquired at (a) $+0.4^\circ$ and (b) $+71.4^\circ$. The detector was set to make sure that it will not saturate as the thickness increases when tilting the cubes and avoid truncation error in the projection images. The cube that is highlighted in (a) was selected for quantitative study and shows no saturation when it is tilted to its maximum thickness in (b) as can be seen in the intensity profile. The second row shows a voxel projection visualisations of the reconstruction of this tilt series using (c) WBP and (d) SIRT. These visualisations were created using the volume-rendering module in AMIRA with a restricted display windows and the alpha value (overall transparency) decreased until the density from the object(s) prevailed over the background.

The nanosphere sample was prepared by depositing the nanoparticles from suspension onto a holey carbon TEM grid. The particles were first, thoroughly dispersed by immersing the suspension of the nanospheres in an ultrasonic bath for 10 minutes then diluting using distilled water. Finally, a drop of the suspension with nanoparticles was deposited onto the TEM grid. The sample was then left to dry in under the heat of a table lamp before it was examined in the TEM. These nanospheres were also used as fiducial markers in the organic photovoltaic solar cells sample (section 4.5 in chapter 4). The electron tomography tilt series was acquired over a tilt range of $\pm 62^\circ$, with an increment of 1° between consecutive projections using an FEI Tecnai T20 TEM operated at 200 kV and equipped with a Gatan GIF2000 Imaging Filter. The bright field transmission electron microscopy (BF-TEM) imaging mode was used. Figure 3.2 shows BF-TEM images of a nanosphere with diameter 64nm and their reconstruction.

Regarding the reconstruction algorithms, all reconstructions were performed using IMOD (Mastronarde, 2006). WBP tomograms were based on ramp filter. As mentioned in section 2.3.4 in chapter 2, determining the optimal iteration number in SIRT is critical, and this is usually selected empirically. Large numbers of iterations will produce a solution that is similar to the weighted back projection algorithm (which can be problematic (Hansen, 2010)), while very small iterations will produce less accurate reconstruction and lose important features of the tomogram. In this work, a strategy was adopted for deciding the optimal SIRT iteration number (detailed in section 4.4.2 in chapter 4). The iteration number was selected after investigating which a number of iterations gave the maximum quality regarding the Structural SIMilarity (SSIM) metric¹ (Wang et al., 2004) by running SIRT for 100 iterations on a simulated projections and recording the quality metric values for each iteration. It was found that an iteration number of 15 gives the optimal SSIM values which are also in agreement with the IMOD guidelines².

3.2.3 Quality evaluation methods

A quantitative comparison is made with respect to quantitative metrics: the reconstructed cube's diagonal length, surface area, volume, in addition to resolution

¹For further details about the SSIM metric, please refer to section 4.4.1 in chapter 4 of this thesis.

²To select an iteration number in the range 8 to 25.

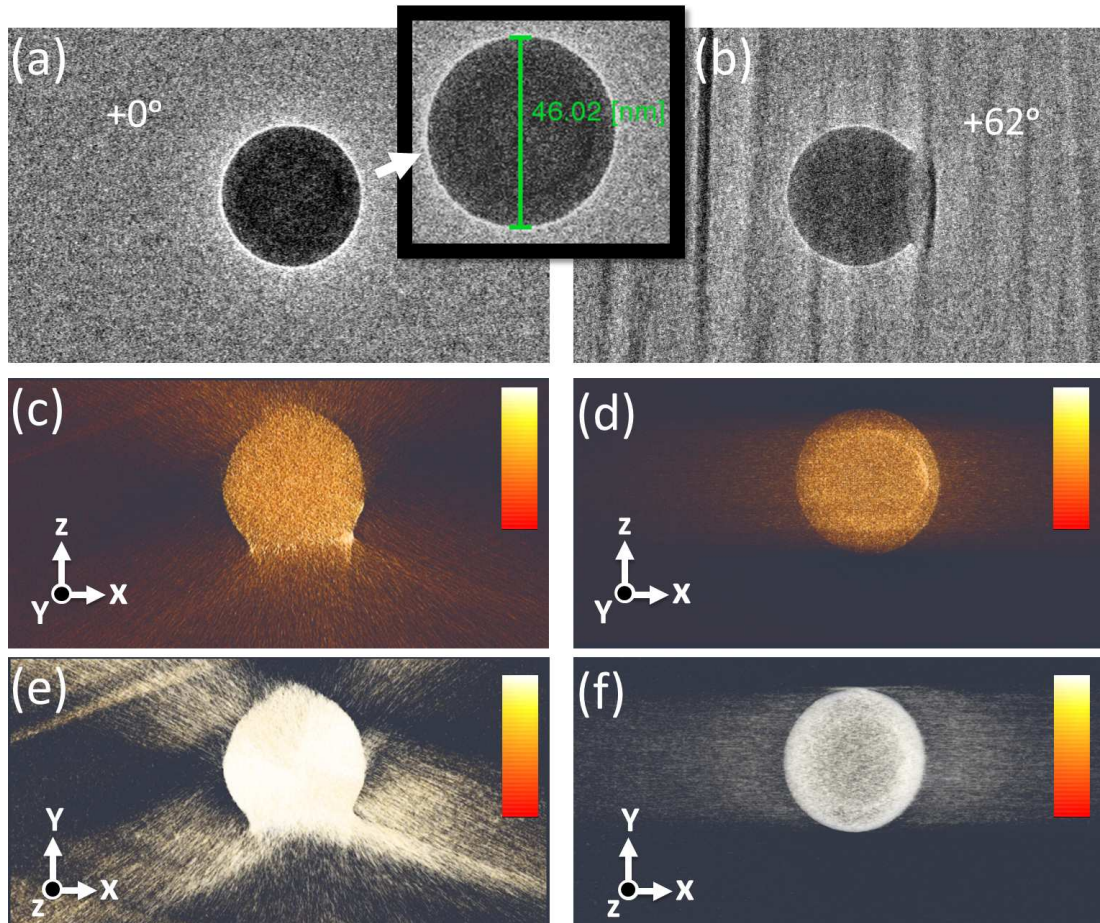


Figure 3.2 | Example nanosphere BF-TEM projection images acquired at (a) $+0^\circ$ and (b) $+62^\circ$. The nanosphere is attached to the carbon layer with what is believed to be ice as in (b). The second row shows the reconstruction of this tilt series using (c,d) WBP and (e,f) SIRT.

measuring. The resolution measure in ET, as described earlier in section 2.3.4 in chapter 2, several techniques have been aimed to approximate the resolution in ET but no straightforward widely accepted method exists yet. Classical studies of resolution in ET by Crowther et al. (1970) and Radermacher (1988) are only based on sampling considerations. Other approaches have been introduced, but no straightforward method exists (Harauz and van Heel, 1986; Koster and Bárcena, 2007). It should be also noted that, since the achievable resolution is also influenced by blurring and noise in the reconstruction, both need to be considered in the resolution measurement as well.

In this work, edge intensity profiles have been used to determine the resolution measure. It is based on the assumption that: the intensity profiles taken across the reconstructed particle, should be, in theory, constant for both the HAADF and BF-TEM imaging modes as they satisfy the projection requirement for tomography for this particular samples. Since the morphology of the test object is well known, it is possible to evaluate the resolution in an accurate way by comparing the simulated ground-truth model with the reconstruction. The method begins by taking edge intensity profiles across three orthogonal directions of the ground-truth object and the reconstruction. This is to take accounts for anisotropy caused by the missing wedge which makes the resolution vary across X, Y and Z dimensions.

In the ground-truth model, the edge intensity profile should be a step function. In practice, this step function is convolved (i.e. degraded) with a one-dimensional point spread function (1D PSF) which is called the edge spread function (ESF) (Carazo, 1992) leading to a sigmoidal profile. Information about the intensity range, the background intensity, the edge position, and the edge steepness can be extracted, by curve fitting the measured profiles to an appropriate ESF containing these four unknown parameters. The resolution is defined by the inverse of the edge steepness which can be obtained by the full-width-at-half-maximum of the first derivative of the fitted ESF. Each measured profile is characterised separately to obtain a resolution measure for the X, Y, and Z directions. Similar approaches have been used previously to measure the accuracy of optical imaging devices (Yin et al., 1990) and for ET (Mezerji et al., 2011).

3.3 Influence of reconstruction methods

In this section, the effect of the reconstruction algorithm (mainly, WBP and SIRT) is investigated both visually and quantitatively. Following the reconstruction of the tilt series for both samples, the tomograms were segmented using automated procedure based on the Otsu threshold method (Otsu, 1975b) to avoid the subjective nature of the manual segmentation. An arithmetic cube (for the MgO sample) and sphere (for the nanosphere sample) was fitted to each surface to provide a visual assessment as in Figure 3.3 and Figure 3.4. The fitting strategy was to find a transform A that applies rotations and a uniform scale factor that minimises the root mean square distance (Euclidean measure) between the points on the segmented model surface to the corresponding points on the reference octahedron surface. This was performed using the iterative closest point algorithm (ICP) (Besl and McKay, 1992). Movie Ch4-M01 and Ch4-M02 in appendix A, shows a 360° volume rendering views and the segmented surface of the MgO nanocubes and the nanosphers respectively.

The resolution procedure was applied to all reconstructions in this work in addition to measuring the object's diagonal. Table 3.1 shows the quantitative measures for the MgO reconstruction.

It was not possible for the analytical fitting procedure to fit the model to the data points to extract the resolution from the nanosphere reconstructions. This was due to the noisy reconstruction. Therefore the reconstructions were filtered before resolution extraction as in table 3.2. The filtering was using the anisotropic diffusion (AD) technique (Perona and Malik, 1990). The AD filtering is typically used in image processing to remove noise from digital images with minimal edge blurring (Weickert, 1998). It should be noted that this denoising step further degrades the resolution of the reconstruction.

Both qualitative and quantitative measures show that WBP does not provide a reliable reconstruction and good resolution in the missing wedge direction compared to SIRT. In the next section, the robustness of each algorithm is tested against the radial under-sampling.

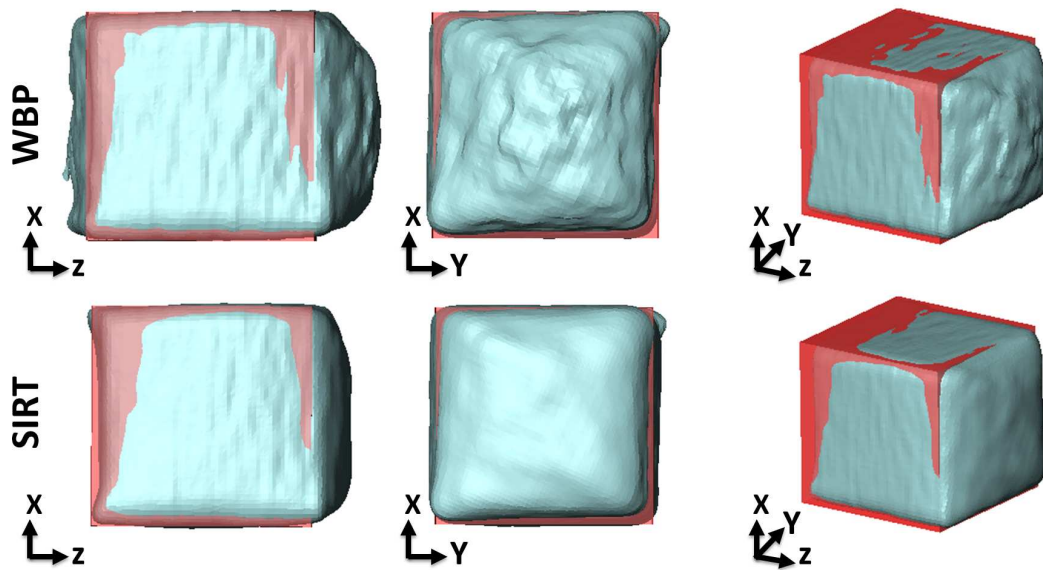


Figure 3.3 | Segmented surface of the MgO reconstruction, using the full tilt series, fitted to an arithmetic cube. The SIRT reconstruction shows a reduced elongation compared to WBP.

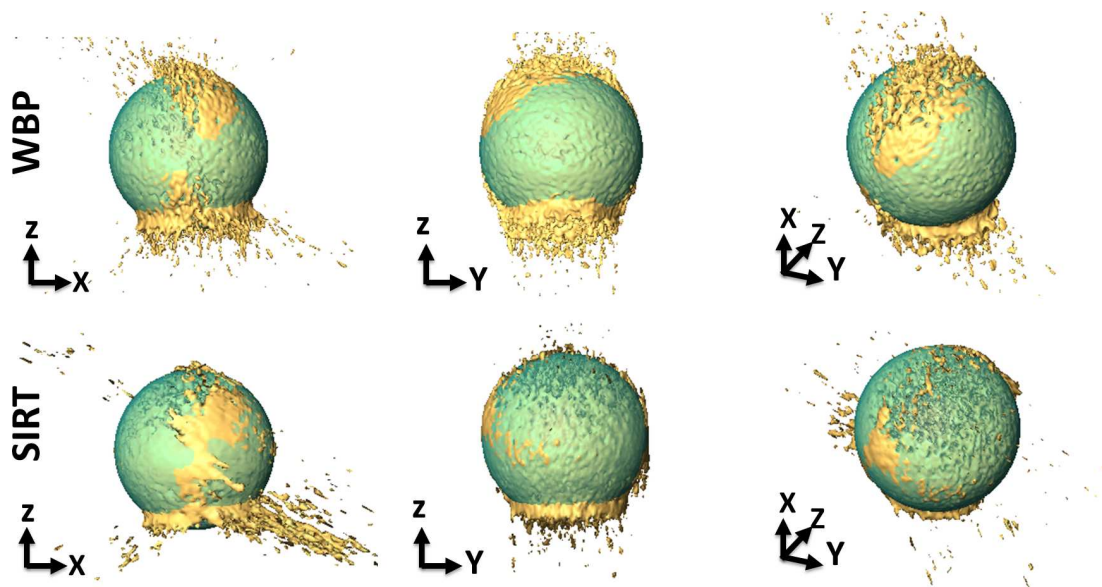


Figure 3.4 | Isosurface of the nanosphere reconstruction, using the full tilt series, fitted to an arithmetic sphere. The SIRT reconstruction shows a reduced elongation compared to WBP.

3.4 Effect of the radial under-sampling

In this section, the robustness of tomography reconstruction using WBP and SIRT is quantified. The tilt series of both the MgO and nanospheres are reduced to different radial under-sampling angles and different quality measures are computed.

Figure 3.5 and figure 3.6 show XZ-orthoslices through reconstructions. These slices are presented with a linear mapping between the maximum and minimum values of pixel in each image. The missing wedge direction is parallel to the z -axis on the orthoslices which is also parallel to the optic axis and perpendicular to the x -axis.

The results show that the quality of reconstruction deteriorates severely with reducing the number of tilts in the reconstruction. This is also confirmed by the resolution degradation in all axes (e.g. the z -axis, approximately by a factor of -1.25 for $\theta=2^\circ$ to 8°). Also, WBP shows the worst visual quality and resolution. The SIRT results in Figure 3.5, shows more robust tomograms compared to WBP, which drops significantly with increasing the tilt increments (especially after 6° which shows that the auto-segmentation procedure failed to produce cubic shaped reconstruction). SIRT continues to produce similar results even with high degree of under-sampling (8°), however, beyond this, the segmented surface failed to preserve the cubic shape of the nanocube (as indicated by the arrows). In figure 3.6, despite the noisy tilt series, the SIRT tomograms have higher contrast than the WBP. It should be mentioned here, that the auto-segmentation procedure failed to generate any meaningful surface from the tomograms in figure 3.6 without applying filtering.

Table 3.1 lists the quality limits for the MgO nanocube case. Both of the volume and surface area values of the segmented cube are more robust for the SIRT tomograms while increasing rapidly in WBP case, indicating sensitivity to under-sampling. Also, the diagonal elongation, which was extracted from the segmented surface, is more consistent in the SIRT case. Table 3.2 list the quality limits for the nanosphere case, which also confirms these observations. The resolution degradation was larger, and it was not possible to measure the resolution of WBP tomograms with tilt increments of 16° and 20° due to noisy reconstruction. It can be seen that the SIRT provide a higher quality than WBP tomograms. WBP yield a worse resolution in the low under-sampling cases.

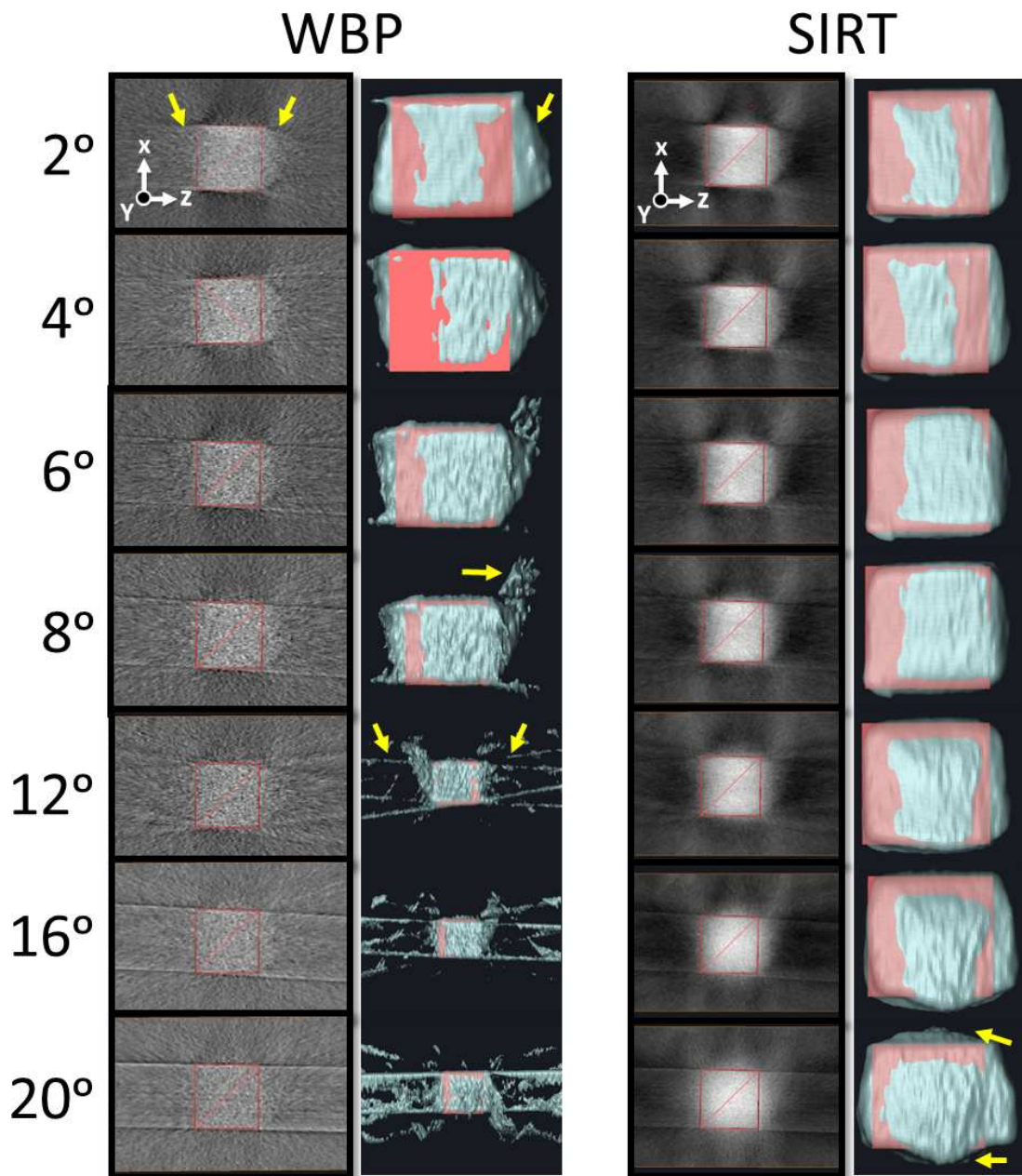


Figure 3.5 | Shows the radial under-sampling effect on the quality of the MgO reconstruction, with the tilt increment marked for each row. Each row shows an orthoslice extracted from the centre of the reconstructed MgO nanocube with an edge length of 66nm and a segmented surface fitted the ideal cube (red line). The tilt series was reduced in each case to represent a tilting between $\pm 75^\circ$ with various increments as indicated by the number. The SIRT results show a more robust quality compared to WBP.

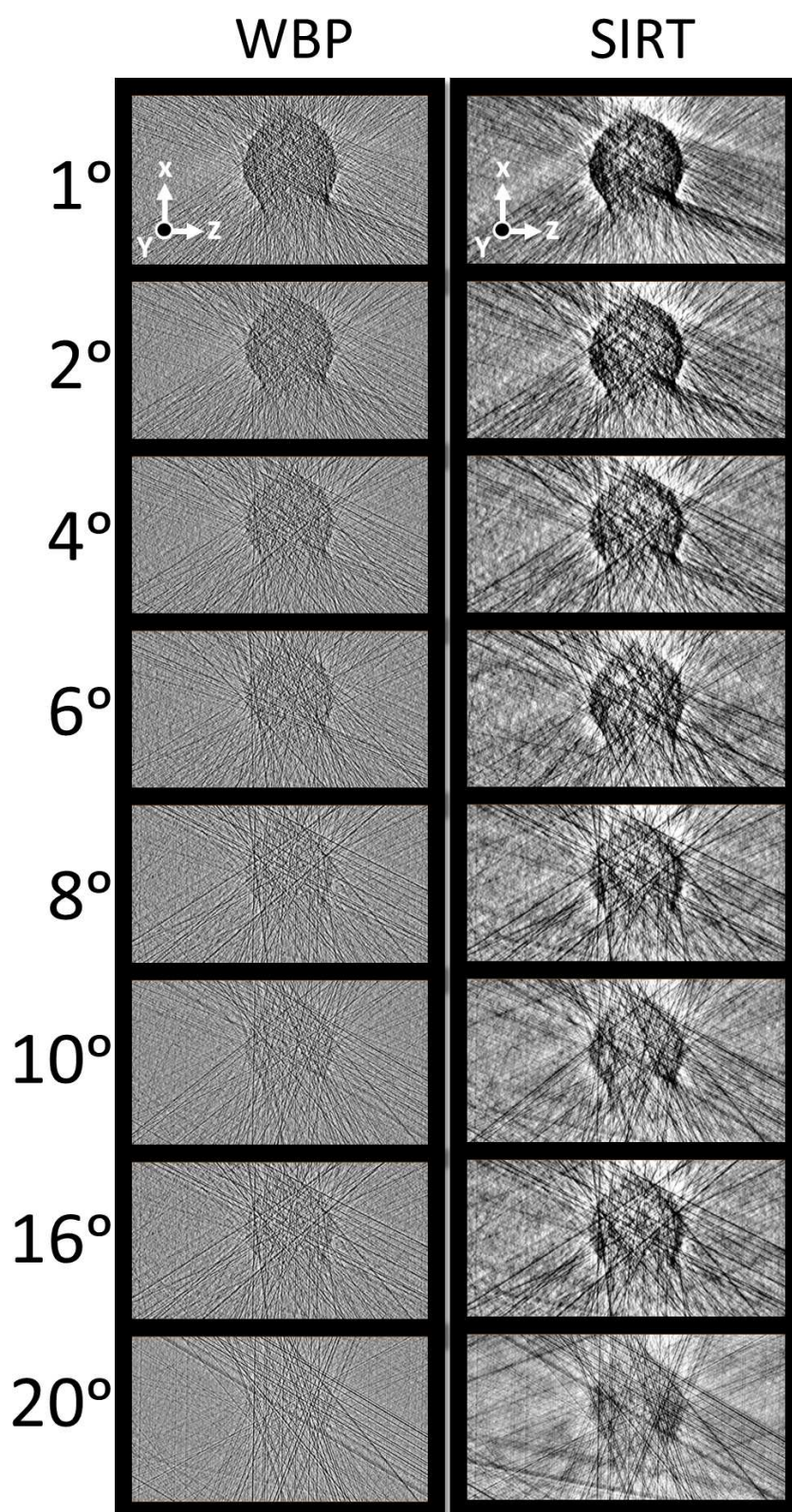


Figure 3.6 | Shows The radial under-sampling effect on the quality of the nanosphere reconstruction. Each row shows an orthoslice extracted from the centre of the nanospheres with a diameter of 46nm. The tilt series was reduced in each case to represent a tilting between $\pm 62^\circ$, with various increments as indicated by the numbers for each row.

Table 3.1 | Quality measure for under-sampling of the MgO nanocube case.

Method	Tilt	Volume (%)	Area (%)	3D Resolution (nm)		
	θ			x-axis	y-axis	z-axis
WBP	2°	1.18	1.03	1.5 ± 0.3	1.3 ± 0.3	4.7 ± 0.3
	4°	1.23	1.07	2.1 ± 0.3	1.5 ± 0.3	5.1 ± 0.3
	6°	1.23	1.07	2.9 ± 0.3	1.8 ± 0.3	5.9 ± 0.3
	8°	1.43	1.39	3.6 ± 0.3	2.1 ± 0.3	8.3 ± 0.3
	12°	2.21	5.10	4.9 ± 0.3	3.9 ± 0.3	21.1 ± 0.3
	16°	2.59	6.66	–	–	–
	20°	3.35	7.70	–	–	–
SIRT	2°	1.09	0.97	1.4 ± 0.3	0.3 ± 0.3	3.4 ± 0.3
	4°	1.09	0.97	2.0 ± 0.3	0.8 ± 0.3	4.3 ± 0.3
	6°	1.10	0.97	2.3 ± 0.3	0.9 ± 0.3	6.1 ± 0.3
	8°	1.11	0.97	2.5 ± 0.3	1.1 ± 0.3	7.2 ± 0.3
	12°	1.13	0.98	2.8 ± 0.3	1.9 ± 0.3	8.7 ± 0.3
	16°	1.22	1.01	3.1 ± 0.3	2.1 ± 0.3	9.2 ± 0.3
	20°	1.46	1.15	5.2 ± 0.3	3.8 ± 0.3	12.6 ± 0.3

3.5 Effect of the missing wedge

As detailed in section 2.3.4 in chapter 2, the limitation of the missing wedge cause image artifacts that prominently appear in the XZ orthoslise. The missing wedge causes the elongation e_{zx} of the reconstructed objects in the direction parallel to the electron beam (i.e. along the z-axis) (Radermacher and Hoppe, 1980). The work of Radermacher (1988) showed that this elongation e_{zx} depends on the size of the missing wedge (viz., the maximum tilt angle α_{max}) and is related using Equation. 3.1.

$$e_{zx} = \sqrt{\frac{\alpha_{max} + \sin \alpha_{max} \cos \alpha_{max}}{\alpha_{max} - \sin \alpha_{max} \cos \alpha_{max}}} \quad (3.1)$$

Using Equation. 3.1, an elongation of 1.3 times is expected in the z-direction for a θ_α of $\pm 70^\circ$, 1.55 times for $\pm 60^\circ$, and 1.9 times elongation for $\pm 50^\circ$ which are considered a significant distortion. Experimental studies, however, showed that Equation. 3.1 provided an over-estimation of the elongation. A detailed study by Kawase et al. (2007) on the observed missing wedge impact on a rod-shaped

Table 3.2 | Quality measure for under-sampling of the nanosphere dataset. The nanosphere had a recorded diameter of 46nm acquired over tilt range $\pm 62^\circ$ and a pixel size of 0.29nm per pixel. The resolution fitting procedure was applied after filtering the tomogram using the anisotropic diffusion technique.

Method	Tilt	3D Resolution (nm)		
	θ	x-axis	y-axis	z-axis
WBP	1°	4.7 ± 0.3	4.5 ± 0.3	6.6 ± 0.3
	2°	5.1 ± 0.3	4.9 ± 0.3	7.2 ± 0.3
	4°	6.4 ± 0.3	5.8 ± 0.3	11.5 ± 0.3
	6°	7.9 ± 0.3	7.3 ± 0.3	24.2 ± 0.3
	8°	9.7 ± 0.3	8.5 ± 0.3	29.7 ± 0.3
	16°	13.7 ± 0.3	12.3 ± 0.3	–
	20°	–	–	–
SIRT	1°	2.0 ± 0.3	2.4 ± 0.3	6.1 ± 0.3
	2°	3.8 ± 0.3	3.4 ± 0.3	7.1 ± 0.3
	4°	4.9 ± 0.3	4.5 ± 0.3	9.1 ± 0.3
	6°	6.1 ± 0.3	5.7 ± 0.3	11.1 ± 0.3
	8°	7.5 ± 0.3	5.3 ± 0.3	15.1 ± 0.3
	16°	9.0 ± 0.3	7.7 ± 0.3	23.1 ± 0.3
	20°	11.3 ± 0.3	8.8 ± 0.3	–

specimen of spherical zirconia grains (tilted around $\pm 90^\circ$), showed the following experimentally measured elongation factors: 1.10 for $\pm 70^\circ$ and 1.23 for $\pm 60^\circ$. Other studies (e.g. [van Bavel and Loos, 2010](#), on spherical gold particles) support this observation.

In this work, 3D tomograms were reconstructed from exactly the same tilt series of the MgO and nanosphere samples, and were repeated with various maximum tilt angles, $\pm \alpha_{max}^o$. Figure 3.7 shows the XZ cross-sections of the MgO specimen from $\alpha_{max}^o = \pm 70^\circ$ to $\pm 55^\circ$ in 2 increments. Figure 3.8 shows the XZ cross-sections of the nanosphere specimen from $\alpha_{max}^o = \pm 62^\circ$ to $\pm 32^\circ$ in 1 increments.

As can be observed, the missing wedge degrades the reconstruction with lower sampling (as can be seen with the volume and surface area percentage increase in table 3.3). The elongation factor e_{zx} was calculated based on the segmented surfaces and the fitted mathematical model. Values of the elongation factors

that was obtained experimentally from the MgO cube in table 3.3, indicates that Equation. 3.1 provides an under-estimation of the elongation of the MgO cube based on WBP reconstruction and a fair-estimation of the elongation of the MgO cube based on SIRT reconstruction. However, for the nanosphere case, the values of e_{zx} in table 3.4 shows that Equation. 3.1 provides an over-estimation of the elongation for this particular morphology. The nanosphere case is consistent with the observation in the empirical studies by Kawase et al. (2007); van Bavel and Loos (2010). This indicates that, an accurate estimation of elongation in ET needs to include consideration of the shape of the object under study.

The resolution measurements of the XZ slices are provided in table 3.3 for the MgO case and, table 3.4 for the nanosphere case. It shows that the resolution in the Z-direction degrades when the missing wedge increases. For instance, the resolution of WBP reconstruction in table 3.3 decreases by a factor of (≈ -2.6) for $\alpha_{max}=70^\circ$ to 55° , and a factor of (≈ -2.3) for the SIRT results. The degradation was higher for the nanosphere sample. These quantitative results shows how severe missing wedge artifacts can affect the fidelity of the reconstruction.

Table 3.3 | Quality measures for the missing wedge study on the MgO nanocube dataset.

Method	Tilt α_{max}	Volume (%)	Area (%)	$e_{zx}^{experimental}$ (%)	$e_{zx}^{theoretical}$ (%)	3D Resolution (nm) z-axis
WBP	$\pm 70^\circ$	1.29	1.12	1.56 ± 0.3	1.31	4.9 ± 0.3
	$\pm 65^\circ$	1.38	1.21	1.73 ± 0.5	1.42	6.3 ± 0.3
	$\pm 60^\circ$	1.72	1.63	2.35 ± 0.5	1.55	8.4 ± 0.3
	$\pm 55^\circ$	2.89	3.99	2.24 ± 0.7	1.71	12.9 ± 0.3
SIRT	$\pm 70^\circ$	1.13	1.01	1.27 ± 0.2	1.31	3.6 ± 0.3
	$\pm 65^\circ$	1.18	1.11	1.42 ± 0.3	1.42	3.9 ± 0.3
	$\pm 60^\circ$	1.25	1.24	1.54 ± 0.5	1.55	5.7 ± 0.3
	$\pm 55^\circ$	1.61	2.11	1.68 ± 0.6	1.71	8.4 ± 0.3

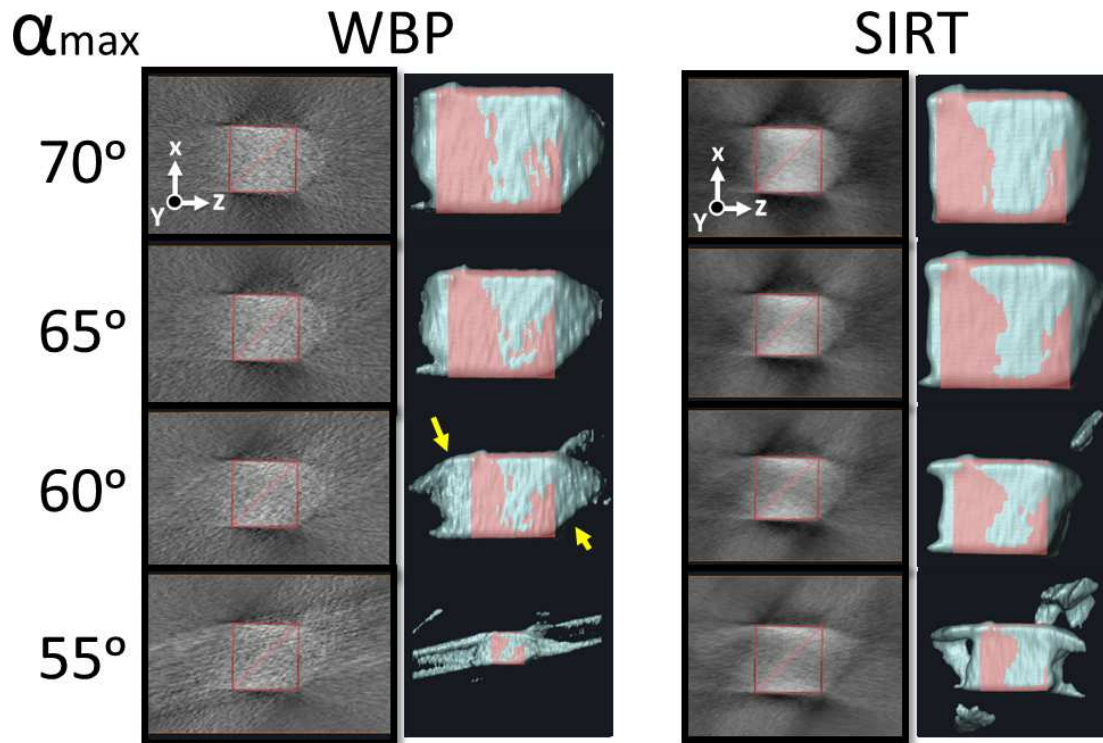


Figure 3.7 | Shows the effects of missing wedge under-sampling on the quality of the MgO nanocubes reconstruction. Each row shows an orthoslice extracted from the centre of the reconstructed tomogram and the corresponding segmented volume fitted to ideal cube (red line). The tilt series was reduced in each case to represent a missing wedge various sizes as indicated by the numbers. Note the increased elongation of the object and the reduction of density inside the cube area (i.e. Cupping artefact) in the reconstructions of SIRT.

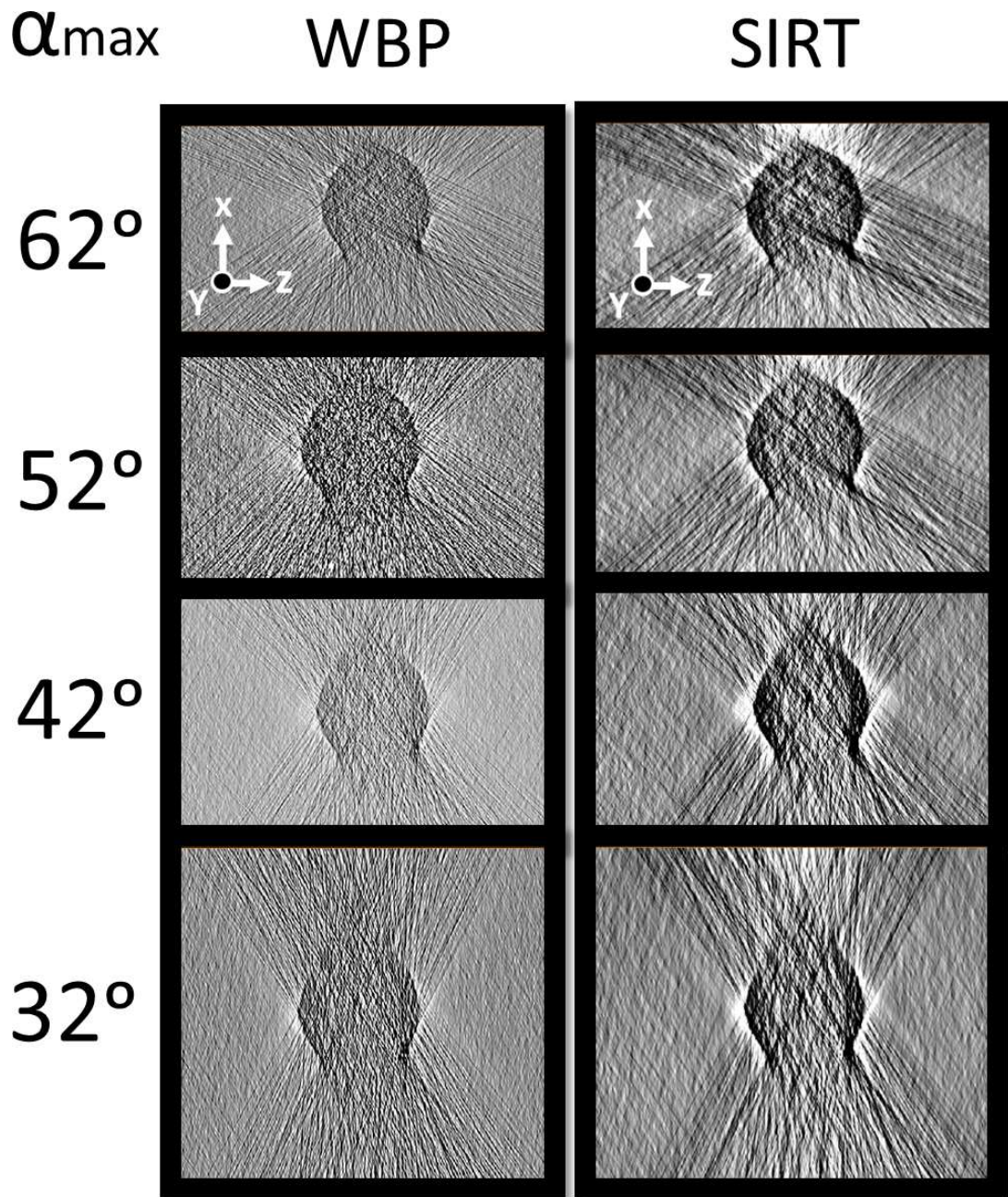


Figure 3.8 | Shows the effects of missing wedge under-sampling on the quality of the nanosphere reconstruction. Each row shows an orthoslice extracted from the centre of the reconstructed tomogram and the corresponding segmented volume fitted to ideal sphere. The tilt series was reduced in each case to represent a missing wedge various sizes as indicated the numbers.

Table 3.4 | Quality measure for the missing wedge study on nanospheres. The resolution fitting procedure was applied after filtering the tomogram using the anisotropic diffusion technique.

Method	Tilt α_{max}	$e_{zx}^{experimental}$ (%)	$e_{zx}^{theoretical}$ (%)	3D Resolution (nm) z-axis
WBP	$\pm 62^\circ$	1.25 ± 0.5	1.50	6.6 ± 0.3
	$\pm 52^\circ$	1.35 ± 0.6	1.82	9.2 ± 0.3
	$\pm 42^\circ$	1.52 ± 0.6	2.28	19.3 ± 0.3
	$\pm 32^\circ$	1.69 ± 0.8	3.04	–
SIRT	$\pm 62^\circ$	1.22 ± 0.4	1.50	6.1 ± 0.3
	$\pm 52^\circ$	1.33 ± 0.4	1.82	7.4 ± 0.3
	$\pm 42^\circ$	1.52 ± 0.6	2.28	12.1 ± 0.3
	$\pm 32^\circ$	1.67 ± 0.6	3.04	–

3.6 Effects of mis-alignment

As discussed in section 2.3.3 in chapter 2, it is important to align the tilt series to a common tilt axis with a sub-pixel accuracy. The inaccurate estimation of the tilting axis causes the distinctive *arc*ing artifacts (as in Figure. 2.30 in chapter 2). This also will spread the density of the reconstructed object and distort the shape.

To investigate the effect of the mis-alignment of the tilting axis on the quality of reconstruction, the tilt series of the MgO and nanosphere samples were used. After applying the cross-correlation alignment technique to correct for the image shifts and finishing the alignment step in IMOD, the tilting axis was mis-aligned by 7 pixels lateral shift. Such mis-alignment error is realistic for practical tomography experiments (Leary et al., 2013b; Saghi et al., 2011). The mis-aligned tilt series were then reconstructed using WBP and SIRT with 20 iterations in IMOD.

The resolution measurements of the X,Y and Z slices are provided in table 3.5 for the MgO case and, Table 3.6 for the nanosphere case. The results show degradation of the resolution for the mis-aligned dataset.

Table 3.5 | Quality measures for misalignment of the MgO nanocube dataset.

Method	Alignment	3D Resolution (nm)		
		x-axis	y-axis	z-axis
WBP	aligned	1.5±0.3	1.3±0.3	4.7±0.3
	mis-aligned	1.8±0.3	1.5±0.3	4.8±0.3
SIRT	aligned	1.4±0.3	0.3 ±0.3	3.4±0.3
	mis-aligned	1.8±0.3	0.5 ±0.3	3.6±0.3

Table 3.6 | Quality measures for misalignment of the nanospheres dataset.

Method	Alignment	3D Resolution (nm)		
		x-axis	y-axis	z-axis
WBP	aligned	4.7±0.3	4.5±0.3	6.6±0.3
	mis-aligned	5.2±0.3	4.9±0.3	6.9±0.3
SIRT	aligned	2.0±0.3	2.4±0.3	6.1±0.3
	mis-aligned	2.4±0.3	2.7±0.3	6.4±0.3

3.7 Conclusion

In this chapter, the influence of the experimental conditions on the quality of the ET reconstruction was studied qualitatively and quantitatively. The originality of this work lays in using a regular shaped nanoparticles for testing a reconstruction obtained using well established ET methods against different experimental setups.

It is shown that the performance of the reconstruction methods, under investigation, declines with the tilt under-sampling and larger missing wedges. In summary, SIRT algorithm is the least sensitive to changes in angular sampling. There is no advantage of SIRT on WBP in suppressing the elongation artefacts and degradation of resolution along the beam direction, especially in low sampling cases. This elongation and resolution degradation is a significant challenge for quantification. Finally, the elongation factor varies with the shape of the object, under study and the misaligned tilt axis causes a slight degradation of resolution.

It is concluded that the reconstruction algorithm employed is one of the main limiting factors of the fidelity of quantitative analysis. This motivates the development of an improved tomographic reconstruction process as attempted in the subsequent chapters.

“*Measure what can be measured*”

Galileo Galilei, 1883

“*In light of the data deluge we are facing today, it is perhaps time to modify this principle to: Measure what should be measured*”

Thomas Strohmer, Professor of Mathematics,
University of California, 2012

4

Compressed sensing electron tomography and the DLET algorithm

ELECTRON tomography (ET) is an increasingly important technique for the study of the 3-D morphologies of nanostructures. However, due to limitations in the acquisition process, the reconstruction problem is an inverse problem which is considered to be ill-posed (i.e. a unique solution may not exist). Furthermore, reconstruction usually suffers from missing wedge artifacts (e.g., star, fan, blurring, and elongation artifacts). Recently, the mathematical theory of compressed sensing¹ (CS) has drawn quite an amount of attention and has been applied to ET and showed promising results for reducing missing wedge artifacts (e.g. [Goris et al., 2012](#); [Leary et al., 2013b](#); [Saghi et al., 2011](#)). This is based on the principle that, the redundancy existing in a signal can be exploited to reconstruct it from far fewer measurements than required by the

¹also known as compressive sensing, compressive sampling, or sparse sampling.

Shannon-Nyquist sampling theorem. CS theory demonstrates that, a signal can be reconstructed with high probability when it exhibits sparsity in some domain.

This chapter is primarily based on the technical and application papers: (AlAfeef et al., 2015, 2016; Alaa et al., 2014; AlAfeef et al., 2014a; Alekseev et al., 2015).

4.1 Introduction

As detailed in chapter 2, the quality of 3D reconstructed tomograms depends on many different factors, principally the maximum angular range and the number of acquired projections. Consequently, two critical problems arise, as highlighted by Kawase et al. (2007); Midgley and Dunin-Borkowski (2009); Midgley and Weyland (2003): First, the *Missing wedge artifacts* which cause elongation and blurring of the reconstructed object in the direction of the optical axis due to a *missing wedge* of information caused by limited angular range. Secondly, the *Resolution degradation* that results from a limited number of projections (Radermacher, 1988).

The quality of a tomographic reconstruction can be enhanced by including additional prior knowledge about the specimen throughout the reconstruction process. A relatively recent prior knowledge technique, compressive sensing (CS) (Candès et al., 2006; Candès and Wakin, 2008; Donoho, 2006) has been applied with great success in Magnetic Resonance Imaging (MRI) (Candès et al., 2006; Lustig et al., 2007). CS has more recently been applied to ET (Binev et al., 2012; Goris et al., 2012; Leary et al., 2013b; Monsegue et al., 2012; Saghi et al., 2011) and image acquisition for high-resolution scanning TEM (Stevens et al., 2014). It has been demonstrated that, even with reduced datasets, it is possible to reconstruct tomograms with high fidelity and reduced missing wedge artifacts (Saghi et al., 2011). Such advantages make CS an effective method for decreasing beam damage, obtaining reliable, high-resolution morphology, and enabling quantitative measurements from 3D tomograms. The key prior knowledge employed in CS is that the signal is likely to be sparse (compact) in a transform domain as illustrated in figure 4.1(a). If such a sparsifying transform can be determined, the original signal can then be accurately reconstructed from a set of measurements significantly lower than that which would be required by the classical Nyquist

sampling theorem (Candès et al., 2006; Candès and Wakin, 2008; Donoho, 2006; Fornasier and Rauhut, 2011).

As sparsity is the key requirement, to derive any benefit from compressive sensing; researchers have experimented with a variety of sparsifying transforms (Gan, 2007; Lustig et al., 2007; Tsaig and Donoho, 2006). Such transforms hold for signals that are sparse in the standard coordinate basis or other orthonormal basis. One common sparsifying transform is the Total Variation (TV), which is a summation of the Discrete Gradient Transform (DGT) coefficients. In the case of ET, CS algorithms have been suggested for tomographic reconstruction by maximising sparsity in the TV domain. For example, Goris et al. (2012) have investigated the use of a total variation minimisation (TVM) in ET. Saghi et al. (2011) proposed a CS-ET algorithm, which maximises sparsity in both the TV and spatial domains. Also, they showed that CS-ET was able to reconstruct 3D maps from a very limited number of tilt images. Furthermore, Monsegue et al. (2012) showed that elongation artifacts caused by limited angle sampling can be effectively reduced using anisotropic total variation (i.e. decreasing contributions from the missing wedge direction) (Monsegue et al., 2012).

Despite the success of these algorithms, they apply to signals that are sparse in certain predefined (fixed) sparsifying transforms. In many practical examples, the signal under study is not compressible (sparse) in such transforms. For example, TV minimisation can be effective for reconstruction if the object under study can be described as a piecewise constant (i.e. having sharp boundaries as in figure 4.1(a); however, this is not true for many samples as illustrated in figure 4.1(b). Other drawbacks of using the TV operator include over-smoothing of fine structures, difficulties in separating true structures from noise, and a degradation of spatial resolution (which becomes especially apparent in noisy examples). Consequently, there are compelling reasons to investigate alternative sparsifying methods for CS-based ET reconstruction to avoid such difficulties.

The choice of a sparsifying transform is typically decided using some simplifying assumptions, usually utilising a pre-chosen basis set such as steerable wavelets or curvelets. An alternative effective approach is by learning the sparsifying transform directly from examples (i.e. images) adaptively.

This chapter introduces the important aspects of CS theory and applies it to electron tomography (ET) image reconstruction. It also addresses the main performance limitations of CS when being applied to ET. That is, the performance

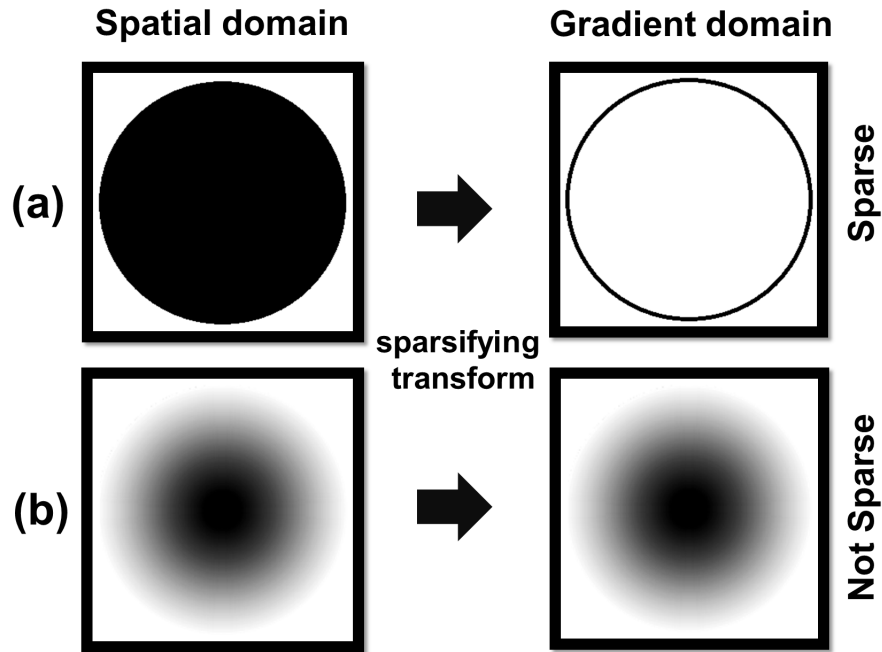


Figure 4.1 | Schematic illustration of sparse representation. (a) a piecewise constant image becomes sparse when transformed to the gradient domain using spatial finite differences transform, while in (b) the number of nonzero pixels in the gradient domain is similar to the original image.

of CS relies heavily on the degree of sparsity in the selected transform domain. The main contribution of this work is the development of a fast and robust numerical algorithm, called DLET, for ET reconstruction and the application to experimental data sets. The algorithm employs a sparse reconstruction technique that incorporates prior information using adaptive sparsifying transform (dictionaries). The dictionary is adapted to the data and is learned during the reconstruction process in a way that leads to a sparser representation of the underlying image. This help to overcome the limitation of CS when using the fixed sparsifying transforms. Finally, the technique is tested using simulated phantoms in both noisy and noiseless cases (section 4.4), a range of experimental data sets (section 4.5, section 4.6 and Chapter 6) and compared to other techniques utilising fixed sparsifying transforms in ET.

4.2 Compressive sensing theory

Compressive sensing (CS), proposed by [Donoho and Tanner \(2005\)](#) and [Candès et al. \(2006\)](#), is one of the major advances in signal processing in the last decade ([Candès and Wakin, 2008](#); [Duarte and Eldar, 2011](#); [Foucart and Rauhut, 2013](#)). Subject to appropriate conditions, it allows one to recover useful information from far fewer measurements than is classically considered possible (namely, Nyquist sampling theorem). CS had been applied successfully in a variety of fundamental applications such as Medical Imaging ([Lustig et al., 2007, 2008](#)), Compressed Imaging ([Duarte et al., 2008](#)), Radar ([Baraniuk and Steeghs, 2007](#)), Communications ([Cotter and Rao, 2002](#)), Robotics ([Mostofi, 2011](#)), Astronomy ([Bobin et al., 2008](#)) and Quantum Information Processing ([Gross et al., 2010](#)). CS employs principles of sparse approximation that is well established in images and audio compression standards such as JPEG and MP3. In the context of ET, the reconstruction problem can be modelled, in the presence of noise, as:

$$B = R_{\theta}x + e \quad (4.1)$$

Where $x \in \mathbb{R}^N$ is a real-valued vector of size N in the real space \mathbb{R} and represents the unknown tomogram (2D image representing a slice through a 3D object). $R_{\theta} \in \mathbb{R}^{M \times N}$ is the discrete Radon transform operator that transforms x into projection measurements $B \in \mathbb{R}^M$ in the sinogram domain and e is an error term modelling measurement errors. B is under-sampled when M smaller than N (i.e. $R_{\theta < 180^{\circ}}$) by one or several orders of magnitude indicating severe undersampling. Sampling is nonadaptive as R does not depend on x .

Assume the unknown tomogram x is sparse (or approximately s -sparse¹) in a domain denoted by Ψ which is a linear operator that transforms from pixel representation into a sparse representation. The representation of x is said to be s -sparse in the Ψ domain if x can be represented by at most s non-zero coefficients and $s \ll N$. If Ψ captures only the most important information about x by $s \ll N$ non-zero coefficients, then x is said to be compressible in Ψ . Let R_u^f be the sampling matrix (i.e. under-sampled Radon transform implemented using the direct Fourier inversion technique discussed in section 2.2.3.2). The standard theory of compressed sensing, asserts that x may be recoverable from under-sampled measurements B given that: x can be compressed by Ψ , and both R_u^f , Ψ

¹Maximum number of non-zero coefficients in X is equal or less than S .

are incoherent (dissimilar) (Candès et al., 2006; Donoho, 2006). The incoherence requirement is to ensure that each measurement in B provides information about many coefficients of x and to ensure that the x coefficients encoding is different for each measurement in B . In the tomography problem, incoherence has been proven empirically (e.g., Lustig et al., 2007). They show that, in incoherent sampling, the undersampling (aliasing) artefacts should spread throughout the sparse domain such that they appear as noise interference. This will enable the recovery of the significant coefficients that stick above the interferences, by a non-linear optimisation process via convex programming.

It should be noted that, despite the lack of mathematical justification for the principle of incoherence in many real-world inverse problems including tomography, CS has been, and continues to be used with great success in many areas (e.g., the pioneering work of Larson et al. (2011); Lustig et al. (2007, 2008)). Furthermore, recent studies suggest that the inverse problem need not be incoherent and sparse, but asymptotically incoherent and asymptotically sparse (Adcock et al., 2013). This significantly more relaxed condition can be satisfied in many inverse problem applications including ET and can narrow the gap between the theoretical and applied sides of the field.

The typical CS model formulation for ET can be expressed as a constrained optimisation problem:

$$\min \|\Psi x\|_1 \quad s.t. \quad \|R_u^f x - B\|_2 \leq \epsilon \quad (4.2)$$

where B is the under-sampled measurement. ϵ is the discrepancy level that controls the fidelity of the reconstruction to the measured data and is usually set above the expected noise level. Ψ is the sparsifying transform which is usually chosen as an orthonormal transform for images. For instance, Ψ can be a wavelet transform, which transforms x into wavelet coefficients Ψx , that are mostly zero (sparse). This objective function promotes sparsity (Chen et al., 1998; Fornasier and Rauhut, 2011) as it minimises the l_1 norm (sum of absolute values) of Ψx , and enforces data consistency using the constraint $\|R_u^f x - B\|_2 \leq \epsilon$. In other words: among all solutions that are consistent with the measured data, equation (4.2) tries to find a simple, sparse solution that is compressible by the transform Ψ .

Different methods can be used to solve this minimisation problem. These include linear programming methods such as basis pursuit (BP) (Chen et al., 1998; Donoho et al., 2006) (which is effective if measurements are noisy), the least absolute shrinkage and selection operator (LASSO) method (Tibshirani, 1996), the focal under-determined system solver (FOCUSS) (Gorodnitsky and Rao, 1997), sparse Bayesian learning (Wipf and Rao, 2004), and other sparse approximation algorithms (Rice, 2015). In many real-world applications, these algorithms usually provide better performance than predicted by the existing theory based on analytical mathematics (Adcock et al., 2013). Alternatively, an approximate solution can be obtained using greedy algorithms, such as orthogonal matching pursuit (OMP) (Tropp and Gilbert, 2007), which are based on replacing the l_1 norm with l_0 quasi-norm (the count of non-zero elements). These algorithms are usually simpler and faster to implement. However, empirical studies had shown that BP is more powerful than OMP (Chen et al., 1998; Tropp, 2004). A recent review of the sparse coding algorithms is provided by Tropp and Wright (2010). For more details on CS theory, we direct the reader to a more extensive coverage in (Davenport et al., 2012) and the CS resources: <http://dsp.rice.edu/cs>.

The success of compressed sensing depends critically on sparsity (Candès and Wakin, 2008). In equation (4.2), the compression degree of the sparsifying transform Ψ , is crucial to achieving high-quality reconstructions. Ψ can be either a fixed or adaptive transform. Fixed transforms have been used successfully in many applications (Binev et al., 2012; Goris et al., 2012; Leary et al., 2013b; Monsegue et al., 2012; Saghi et al., 2011); however, their compression degree may be limited, and in many cases, cannot be applied to any image without satisfying certain pre-conditions. For example, finite-differences (commonly known as Total Variation) performs well for piecewise-constant images since the uniform regions, and discrete boundaries can be well recovered (Leary et al., 2013b; Lustig et al., 2007; Radin et al., 1992). However, for non-piecewise-constant images, the cartoon effect can be damaging for the reconstruction quality (Liu et al., 2015; Sidky and Pan, 2008; Zhang et al., 2013). Therefore, other sparsifying techniques need to be considered for such images.

Furthermore, fixed transforms can produce undesirable artefacts such as blocking, blur, ringing or edge artefacts. For example, the use of Total Variation (TV) in image restoration, can damage fine details, and cause staircase artefacts (Chan et al., 2005). The use of the Discrete Cosines Transform (DCT) or wavelet-based

coding can produce ringing artefacts in an image which appears like ripples or oscillations around sharp contours or edges in the spatial domain (Marziliano et al., 2004). This is caused by truncation of the high-frequency transform coefficients from (DCT) or wavelet-based coding.

Adaptive sparsifying techniques, on the other hand, benefit from the intrinsic sparsity that images usually have, which improves recovery by tailoring the best sparsifying basis (i.e. by dictionary learning). The learning process can be controlled in a way that produces dictionaries with improved sparsifying ability. Recent studies in image processing showed the feasibility of adaptive transform techniques for a variety of problems (Elad and Aharon, 2006; Mairal et al., 2008; Protter and Elad, 2009), with the state of the art results and possible extensions to inverse problems.

4.2.1 Dictionary Learning

Dictionary learning (DL) is the process by which a dictionary adapted to the data is produced. Given a vector $Y \in \mathbb{R}^N$ to represent a training image of size $N_x \times N_y = N$ pixels as in (Fig.4.2-a). $M_i \in \mathbb{R}^{n,S}$ is an operator that extracts Y into S blocks (patches) of size $n = \sqrt{n} \times \sqrt{n}$ pixels represented as $M_i Y = \{y_{i,j}\}_{i=1,j=1}^{S,n}$. These patches are extracted with overlaps and 1 pixel sliding, meaning that the value of each pixel in Y will be included in a maximum of n patches. The maximum number of patches in a training set $S = (N_x - \sqrt{n} + 1)(N_y - \sqrt{n} + 1)$. A dictionary is a matrix $D \in \mathbb{R}^{n,K}$ (Fig.4.2-b) with columns $d_{i=1,2,\dots,K} \in \mathbb{R}^{n \times 1}$, (also called Atoms) which form the basis that is used to approximately represent a given image. D can be initiated by selecting K patches from $M_i Y$. The choice of Y can either be the current tomogram under reconstruction or a high-quality tomogram of a similar specimen.

Let $D \in \mathbb{R}^{n,K}$ be an overcomplete dictionary, by which we mean there are more entries in the dictionary than the required number of linearly independent vectors, the sum of which could be used to exactly represent any given vector as demonstrated in (Fig.4.2-b). Since this always can be done with exactly n linearly independent vectors, this means that the number of entries in the dictionary $K > n$. Suppose an image patch y_i can be represented exactly or approximately as a sparse linear combination of the atoms (as in Fig.4.2-c) drawn from D (i.e., $y_i \approx D\alpha_i$) where $\alpha_i \in \mathbb{R}^K$ is a vector with very few nonzero entries ($\ll n$), typically around 5 atoms are used. Then, the DL process aims to find a possible

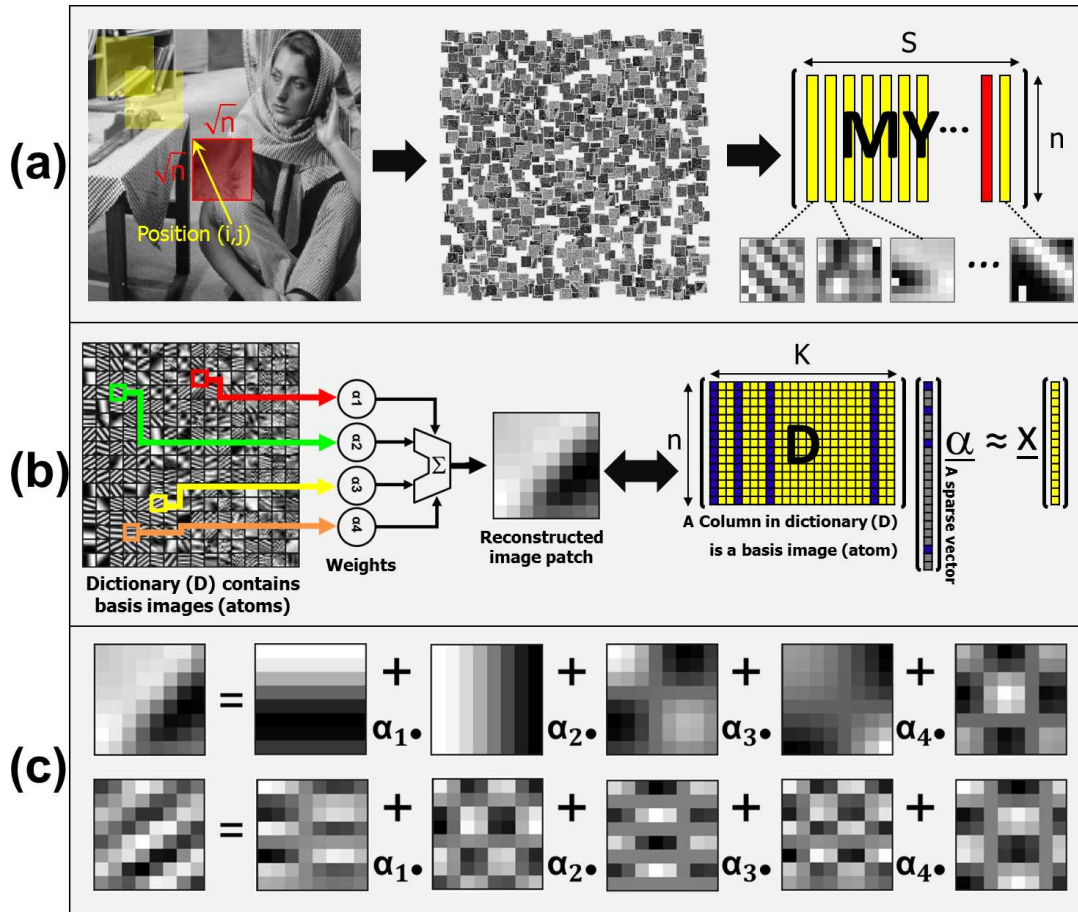


Figure 4.2 | A schematic illustration of (a) patch-based processing of images by breaking the given image Y into overlapping (small) patches to be used in dictionary learning and sparse coding. (b) the sparse coding process, which is the problem of taking a large input image, and finding an approximate decomposition of that image using a linear blend of small images (patches) of commonly occurring subpatterns from a dictionary. The vector α_i is sparse with $K = 5$ nonzero coefficients; the image patch (vector x) is a linear combination of these columns (images patches). (c) the Sparse coding using basis to approximate two patterns. The coefficients α_i are all of the same order of magnitude and are not shown due to space limitations.

optimal dictionary for sparse representation of training samples $M_i Y$. It can be expressed as:

$$\min_{D, \alpha} \sum_i \|M_i Y - D \alpha_i\|_2^2 \quad s.t. \quad \forall i \|\alpha_i\|_0 \leq n_{nz} \quad (4.3)$$

where n_{nz} is the maximum number of atoms that can be used in sparse representation (i.e. the number of non-zero coefficients). The objective function in Eq(4.3) is 'called Orthogonal Matching Pursuit (OMP)' for approximating the fit of a linear model with constraints imposed on the number of non-zero coefficients (i.e. the L_0 quasi-norm). (Fig. 4.2-b) and (4.3) is an example of learned dictionary.

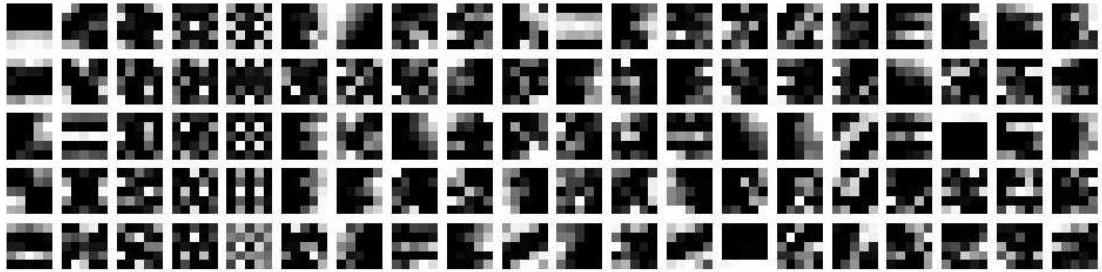


Figure 4.3 | An adaptively learned dictionary consisting of ($K=100$) atoms of 5×5 patches, normalized to the range of $[-1,1]$.

In terms of computational complexity, a problem using the L_0 quasi-norm (as in equation 4.3) is shown to be NP-hard¹ (Davis et al., 1997; Natarajan, 1995). Different techniques have been developed to solve the DL problem in (4.3). These can be classified into three main categories (Tosic and Frossard, 2011): 1) probabilistic learning methods such as Maximum Likelihood methods (Olshausen and Field, 1997) and the Optimal Directions (MOD) method (Engan et al., 1999); 2) clustering or vector quantisation methods, such as Stuart Lloyd’s algorithm (Lloyd, 1982) and its generalisation, the K-SVD method (Aharon et al., 2006); and 3) learning dictionaries with a particular construction. A review of dictionary learning methods is provided by Tosic and Frossard (2011).

Among these methods, the vector quantisation (VQ) approach has been applied successfully in many fields such as in image compression and 3D-microscopic image coding (Cockshott et al., 2003; Tao and Cockshott, 2004). In particular, the K-SVD algorithms have attracted increasing interest recently because of their

¹Non-deterministic polynomial acceptable problem. NP-hard problems cannot be solved in polynomial time.

numerical efficiency and fast convergence (Elad, 2010; Peyré, 2011). The K-SVD algorithm typically iterates between two steps:

1. The Sparse Coding step: the minimisation problem in (4.3) is solved with respect to α_i with at most n_{nz} non-zero coefficient and fixed D . This step can be performed using any pursuit algorithm, however, the OMP method (Tropp and Gilbert, 2007) is typically used.
2. The Dictionary Codebook Update Stage: the columns (atoms) of D are updated sequentially, as well as the corresponding relevant coefficients α_i .

This algorithm continues to iterate between the two steps until it converges, providing a normalised dictionary D (i.e., each atom has a unit norm). Further details about the K-SVD algorithm is provided by Aharon et al. (2006). An in-depth review of the applications of dictionary learning to image processing and computer vision can be found in (Elad, 2010; Wright et al., 2010)

4.3 Methodology

In this work, a dictionary learning based compressive sensing technique for the ET image reconstruction problem is proposed. This technique is named Dictionary Learning for Electron Tomography (DLET). It relies on the prior innovations for CS-MRI (Lustig et al., 2007) and (Elad and Aharon, 2006) for dictionary learning. This section shows that 3D reconstruction quality in ET can be further enhanced when enforcing sparsity using an adaptive dictionary. To solve the ET tomographic reconstruction problem, an over-complete dictionary is used as a regularisation term:

$$x^t \triangleq \min_{x, D, \alpha} \frac{1}{S} \sum_i^S \frac{1}{2} \|M_i x - D \alpha_i\|_2^2 + \lambda \|\alpha_i\|_1 \quad s.t. \quad \|R x - B\|_2^2 \leq \epsilon \quad (4.4)$$

Where $\lambda > 0$ is the sparsity Lagrange multiplier, ϵ controls the discrepancy level to the measured data, t is the iteration number. This cost function enforces sparsity in the image domain x using an adaptive dictionary D and obtains a reconstruction that is consistent with the measured sinogram data B . The first two terms in equation (4.4) optimise the ability of the dictionary to sparsely approximate image patches and enforces sparsity in the D domain. This equation

is subject to a data fidelity constraint in the Radon domain. In the absence of noise, ϵ should equal zero, otherwise, it should be estimated according to standard deviation σ of noise in the measurements. The estimation of ϵ is critical to making this cost function robust to noise.

In ET, a rough estimate of the noise can be performed by calculating a power spectrum of a TEM image acquired without a sample. The resulting curve is approximately a Gaussian function that can be characterized by a mean μ and standard deviation σ (Frank, 2010, Chapter 11). ϵ should be slightly above estimated noise level. Section 4.3.2 provides more details about tuning this parameter.

This adaptive sparsity-based formula in Eq(4.4), is potentially capable of reconstructing tomograms using only the under-sampled sinogram measurements and prior knowledge about the noise level. By regularisation using a patch-based dictionary, missing wedge artifacts and noise can be further suppressed, without introducing new artifacts, compared to other transforms that are based on the relationship of neighbouring pixels. Since patches are extracted with overlap for training the dictionary, the DLET algorithm benefits from an additional averaging operator that can be effective for de-noising and reducing reconstruction artifacts. This is a well-known advantage¹ of the non-local mean denoising methods (Buades et al., 2011). Also, the patch size can be altered depending on the size of the features in the reconstructed image, and this can be very effective in allowing this technique to perform well in separating strong noise from weak structures.

4.3.1 Proposed Algorithm

The proposed DATE algorithm is explained in the data flow diagram in figure 4.5. The image reconstruction optimisation problem in equation (4.4) is solved using an alternating minimisation to optimise x , D and α . This is performed using three stages.

¹Since the DLET is a patch-based approach, (i.e., each pixel in the reconstructed image is an average from different image patches), the variance law in probability theory ensures that if N pixels are averaged, the noise standard deviation of the average is divided by square root of (N).

4.3.1.1 On-line Dictionary Learning

In the first stage, the reconstructed image x is initialised using the Weighted Back Projection (WBP) method in order to reduce data discrepancies. Then, x is fixed and the dictionary D and the sparse representation α are updated by solving the following subproblem:

$$D_t \triangleq \min_D \frac{1}{S} \sum_i^S \frac{1}{2} \|M_i x - D\alpha_i\|_2^2 \quad s.t. \quad \|\alpha_i\|_1 \leq n_{nz} \quad (4.5)$$

Typically, this optimisation problem can be solved efficiently using the K-SVD algorithm (Aharon et al., 2006) to learn the dictionary D dynamically from x during the reconstruction process. A fast implementation of dictionary-learning algorithm of (Mairal et al., 2010) is used to train D . To avoid any scaling problem that might arise, atoms are produced with unit norm. After learning the dictionary, a sparse coding step is executed.

4.3.1.2 Sparse Coding

In the second stage, keeping D and x fixed, α is updated according to the cost function:

$$\alpha_t \triangleq \min_{\alpha} \|\alpha_i\|_1 \quad s.t. \quad \|M_i x - D\alpha_i\|_2^2 \leq \epsilon \quad (4.6)$$

This formulation is called the *basis pursuit denoising* (BPDN) problem. Solving this is very efficient if there is inherent noise in the measured signal (Tropp and Wright, 2010; Van-Den-Berg and Friedlander, 2008). For the ET reconstruction the Poisson model of shot noise is assumed (as in Scott et al., 2012; Williams and Carter, 2009). Sparse coding is applied to all image patches $M_i x$ in order to determine the sparse coefficients α .

4.3.1.3 Image update

Finally, the solution x is updated by reassembling overlapping patches using the transpose of M as $\sum_i^N M_i^T D\alpha_i$ and constructing an intermediate image x^* . In this step, the intensity value of a pixel in x^* is computed by averaging all the corresponding patches that cover it.

The image x^* is then back projected to the fully sampled Radon domain using $R_{\theta} x^*$ to get B^* . Both the new B^* and the measured under-sampled B

are combined to get B^φ , and another iteration of dictionary learning and sparse coding is applied to B^φ to computer B^t . Finally, the new x^{t+1} is formed by $R^{-1}B^t$ as detailed in the DLET Algorithm (4.4). The above procedures are iterated until a stopping criterion is reached (i.e., maximum number of iterations is reached).

```

Algorithm III.1: DLET( $B, n, K, c, \sigma$ )

Data: B - Projections (sinogram)
Initialize:  $t \leftarrow 1, x^t \leftarrow R^{-1}B, \lambda \leftarrow \frac{c}{\sigma}$ 

while Stopping Criteria is not satisfied
    (1) Construct Training set from  $x^t$ 
    (2) Learn Dictionary D using KSVD
    (3) Find sparse coefficients  $\alpha$  using BPDN
    (4) Compute intermediate  $x^*$  from  $D\alpha$ 
    (5) Compute sinogram  $B^*$  of  $x^*$  using  $R_{\theta=(0:180)}$ 
do {
    (6)  $B^\varphi \leftarrow \begin{cases} \lambda B + \frac{B^*}{\lambda+1} & \forall \theta \text{ sampled in B.} \\ B^* & \text{Otherwise.} \end{cases}$ 
    (7) Construct a new Training set from  $B^\varphi$ 
    (8) Apply steps (2-4) using new Training set
    (9) Compute intermediate  $B^t$ 
    (10)  $x^{t+1} \leftarrow R^{-1}B^t$ 
return ( $x$ )—Reconstructed Image
  
```

Figure 4.4 | DLET algorithm to reconstruct ET images from undersampled tilt series.

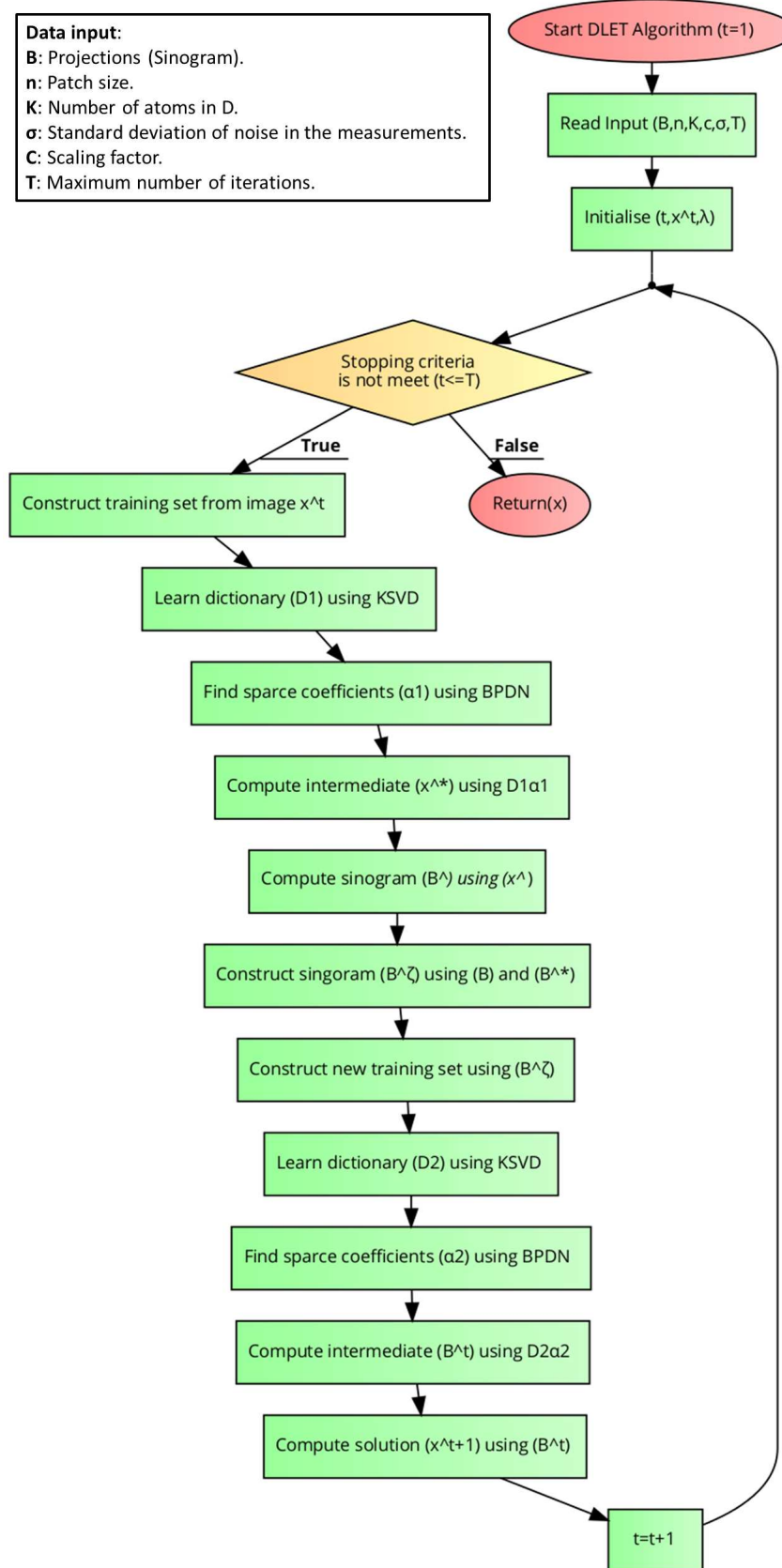


Figure 4.5 | DLET algorithm data flow diagram.

4.3.2 Parameters

The proposed algorithm requires user input for a few parameters:

- **Discrepancy level (ϵ):** controls the allowed tolerance between reconstructed and measured data. Typically, this is mainly affected by the noise standard deviation σ in the measured data and can be computed as: $\epsilon = (C\sigma)^2$, where C is a scaling factor.
- **Patch size (n):** controls the dictionary efficiency in learning features of an image. A large patch size produces more dictionary atoms, which increases the computing cost of the algorithm.
- **Number of atoms (k):** controls degree of over-completeness (redundancy) of the dictionary which improves the sparsity of representation. The number of dictionary atoms should be larger than patch size to ensure good redundancy. [Elad and Aharon \(2006\)](#) shown that a redundancy of ($K = 4n$) would be sufficient for image de-noising problems.

The sensitivity of the DLET algorithm to these parameters was tested (see section [4.4.4](#)).

4.3.3 Objective function convergence

The cost function in [\(4.4\)](#) is non-negative and is solved by alternating between dictionary learning (sub-cost function [4.5](#)), sparse coding (sub-cost function [4.6](#)), and updating the solution x . Each of these terms in the cost function decreases monotonically on iteration, meaning that the objective function in [\(4.4\)](#) also decreases monotonically using the proposed algorithm. However, this monotonic decrement does not guarantee the convergence of the reconstruction process. The convergence of DLET is difficult to prove, and beyond the scope of this work. However, our empirical studies suggest that the proposed algorithm converges in a well-behaved manner.

4.3.4 Termination criterion and computational complexity

The algorithm iterates until a plateau is reached such that successive iterations no longer produce better results. For the simulation study, the algorithm was terminated when a fixed number of iterations is reached. This number is chosen to fall after the convergence plateau. For practical implementation, other common terminating conditions may be included, such as allocated budget (computation time/memory) reached, manual inspection or combinations of the above.

In this work, both dictionary learning and sparse coding are achieved using the SPAM toolbox (Mairal et al., 2010) which is the state-of-the-art approach at the current time and significantly faster than other methods of sparse optimisation (Szlam et al., 2012). The DLET algorithm was prototyped using Matlab and implemented using CUDA C++.

4.4 Numerical simulation

An enhanced ET reconstruction algorithm should be able to avoid artifacts typically seen in conventional ET reconstructions. Artifacts arise mainly for three reasons: missing wedge, radial undersampling, and noise in the measurements. The first two problems cause aliasing in the image domain in the form of streak, blurring and elongation artifacts. The noise in TEM microscope images depends on the experimental conditions, however two types of noise are permanently present: the quantum noise of the electron beam (shot noise) and the noise originated from the image recording system which is usually characterised by a modulation transfer function (MTF) and a detective quantum efficiency (DQE) (Frank, 2010, Chapter 11). The propagation of noise from the sinogram domain into the reconstructed volume domain is a complicated process.

To evaluate the performance of the proposed reconstruction algorithm, two simulation studies were performed. In the first case, a modified version of the well-known Shepp-Logan phantom (Fig. 4.8a) is used. For the second case, a more challenging phantom is used with features that are hard to reconstruct and which are not sparse in the gradient domain as shown in (Fig.4.13). For comparison, we performed the reconstruction using the following methods: WBP,

SIRT, a CSTV-based method, and the proposed DLET approach, using a range of different under-sampling factors and noise levels.

4.4.1 Image quality metrics

With the phantom images as the ground truth, all the reconstructed cases were assessed in terms of two commonly used metrics: Peak Signal-to-Noise Ratio (PSNR) and Structural SIMilarity (SSIM) index. The PSNR was obtained as the ratio between the signal's maximum power (peak reference intensity MAX_I to the power of the signal's noise (root mean square of reconstruction error) $MSE(I_o - I_R)$ as in equation (4.7).

$$PSNR(I_o, I_R) = 10 \cdot \log_{10} \left(\frac{MAX_I}{\sqrt{MSE(I_o, I_R)}} \right) \quad (4.7)$$

The PSNR is measured in decibels (dB) and the higher the PSNR value, the better the quality of the reconstruction.

Although the PSNR is a simple mathematical metric that is commonly used as a distortion metric, it often fails to correlate closely with perceived image quality (Chandler and Hemami, 2007). Consequently, we have chosen to use an additional, more advanced metric, the SSIM index.

The SSIM index is shown to be consistent with visual perception (Wang et al., 2004). The calculation of the SSIM index for the two images ζ and ϱ to be compared begins with computing three similarities: luminance $l(\zeta, \varrho)$, contrast $c(\zeta, \varrho)$ and structures $s(\zeta, \varrho)$ similarity. Local SSIM is defined as:

$$\begin{aligned} LCS(\zeta, \varrho) &= l(\zeta, \varrho) \cdot c(\zeta, \varrho) \cdot s(\zeta, \varrho) \\ &= \left(\frac{2\mu_\zeta\mu_\varrho + C_1}{\mu_\zeta^2 + \mu_\varrho^2 + C_1} \right)^{\alpha_1} \left(\frac{2\sigma_\zeta\sigma_\varrho + C_2}{\sigma_\zeta^2 + \sigma_\varrho^2 + C_2} \right)^{\beta_1} \left(\frac{2\sigma_{\zeta\varrho} + C_3}{\sigma_\zeta^1\sigma_\varrho^1 + C_3} \right)^{\gamma_1} \end{aligned} \quad (4.8)$$

where μ_ζ and μ_ϱ are local means, σ_ζ and σ_ϱ are local standard deviations, and $\sigma_{\zeta\varrho}$ is cross-correlation after subtracting corresponding means. C_1, C_2, C_3 are stabilisers and $\alpha_1 > 0, \beta_1 > 0, \gamma_1 > 0$ are parameters used to adjust the relative importance of the three components. The maximum value of the SSIM index is 1, which indicates perfect structural similarity. In this work, we used

the default values for the parameters in Eq.(9) (as in Wang et al., 2004) with $c_1 = (0.01L)^2$, $c_2 = (0.03L)^2$, $c_3 = c_2/2$, $L = 255$ and $\alpha_1 = \beta_1 = \gamma_1 = 1$.

For further information on image quality metrics, the interested reader is referred to the review by Sayood et al. (2002).

4.4.2 Simulation study 1: the modified SheppLogan phantom

In this section, the proposed DLET technique is compared with conventional ET methods, namely, WBP, SIRT and the CS-based total variation (CSTV) method. The simulated phantom shown in (Fig. 4.8a) is used. This phantom was edited to include a bright circle region in the top part with gradual intensity variation in the background. Such intensity variations can simulate realistic materials in a typical STEM experiment such as solar cells (van Bavel and Loos, 2010). Also, horizontal lines with different thicknesses were added to verify the degree of detail that each algorithm can preserve. Two simulation setups were performed. The first one aimed to test the case of a noisy fully sampled sinogram as in (Fig. 4.6b) and (c) while the second is to test with a noiseless under-sampled sinogram with a missing wedge as in (Fig. 4.6d and e). In order to avoid committing an inverse crime ¹, which happens when the data is inappropriately simulated (Kaipio and Somersalo, 2006, chapter 1), the tilt series were generated using the parallel projection discrete Radon transform, while the reconstruction was coded using Fourier-based methods so that a different system matrix is used for creating projections than in the reconstruction methods. Furthermore, the tilt series was misaligned by randomly shifting each projection by a maximum of $\pm 0.5^\circ$ to account for the alignment imperfections in the experimental ET data. By doing so, critical errors can be avoided when these methods are applied to real ET data.

¹occurs when nearly the same theoretical ingredients are used to invert data in an inverse problem.

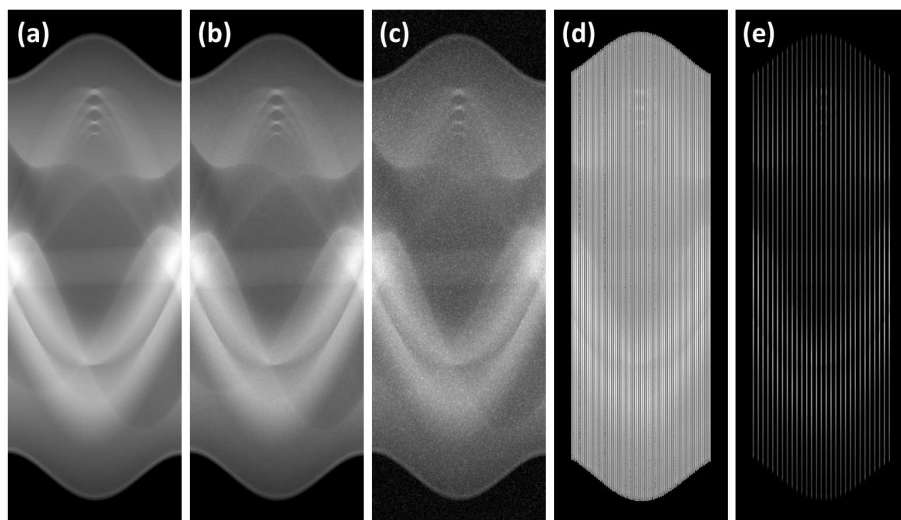


Figure 4.6 | Simulated Sinogram data from the phantom shown in Fig.4.8(a). (a) noiseless fully sampled true sinogram ($512 \text{ pixel} \times 180^\circ$). (b) and (c) noisy fully sampled sinogram with SNR of 52dB and 15dB, respectively. (d) and (e) are noiseless undersampled sinogram obtained using sampling masks in Fig.4.7 with 70 and 28 radial lines, respectively (leaving a 20° missing wedge of un-sampled information).

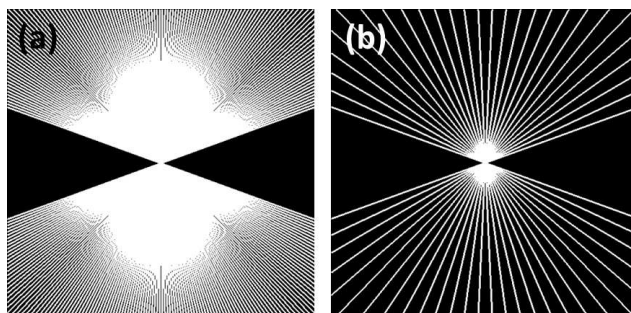


Figure 4.7 | Sampling masks - applied in Fourier domain with a) 70 and b) 28 radial lines, respectively and a missing wedge of 20° similar to a typical STEM tomography setup.

The input data in each case was then prepared by taking the 1D Fourier transform of each projection in a tilt series and sampling it to the corresponding radial line in the 2D Fourier domain using a sampling in Fig.4.7. The WBP reconstruction was performed with a ramp filter in the frequency domain to produce an image in the spatial domain. This image was then used to initialise the SIRT, CSTV and DLET algorithms. SIRT was performed using 32 iterations. This number was selected after investigating which number of iterations gives

the maximum quality in terms of PSNR and SSIM metrics by running SIRT for 100 iterations and recording the quality metric values for each iteration. CSTV reconstruction was performed using the method provided by Lustig et al. (2007) seeking sparsity in gradient and image domain with default regularisation weighting of $\lambda_{TV} = 7$ and $\lambda_{l_1} = 0.1$ respectively. This provides a balance between the loss of fine details and the elimination of ghosting artifacts. With CSTV, 150 conjugate gradient iterations were performed with a re-initialisation every 50 iterations in order to decrease the likelihood of falling into local minima. DLET was run for 20 iterations with the parameters chosen as $n = 64$, $K = 4n$ and $T_0 = 0.5n$. The dictionary learning stage using K-SVD was performed for 20 iterations, with 10^3 overlapping patches extracted from the intermediate image as a training set and a target sparsity of T_0 . The boundary condition is assumed to be reflective in the DLET training set. All implementations were executed on Matlab v7.12 (R2011a) installed on a 64-bit Windows 7 operating system with an Intel Core i5 processor running at 3.10 GHz with 24 GB RAM and a NVIDIA GeForce GTX 460 with 336 cores.

4.4.2.1 Noisy full-sampled setup

To compare ET reconstruction methods with noisy data, the Phantom in (Fig. 4.8a) of 512×512 pixels, was projected into the sinogram domain (Fig. 4.6a) between $\pm 90^\circ$ with 1° tilt increment. This was then corrupted by applying 1) Poisson noise to simulate the shot noise and 2) Gaussian noise with low standard deviation $\sigma = 5$ (Fig. 4.6b) and high $\sigma = 20$ (Fig. 4.6c). In (Fig. 4.8 and 4.9), (b) shows WBP reconstructed images with obvious artifacts and noise. Based on visual assessment, WBP with a Ramp filter cannot successfully remove artifacts in reconstructions. Fig. 4.8 and 4.9, (c) shows the SIRT image with improved reconstruction and contrast ($SSIM = 0.3478$ in Fig. 4.8, $SSIM = 0.1555$ in Fig. 4.9) compared to (0.1748, 0.0886) for WBP. (Fig. 4.8d), CSTV reconstruction shows an effective contrast and noise suppression in homogeneous regions. However, this improvement comes at the cost of losing the fine details of structures and of introducing staircase artifacts in the region with gradual changes of intensity (blue and orange arrows in zoomed images in (Fig. 4.8)); these staircase artefacts can not be suppressed by increasing the λ_{TV} parameter values. In (Fig. 4.9d), CSTV was tuned to de-noise by increasing λ_{TV} , however, it was found that increasing λ_{TV} above 12 will cause the loss of fine details.

Figure 4.8 and 4.9,(e) show results obtained after applying the DLET algorithm, and these are promising showing both noise suppression and the preservation of fine structures. The degradation of visual quality with respect to the phantom image was noticeably lower than for other algorithms when applied to the sinogram with the higher noise level, with a much lower percentage decrease the of SSIM index ($\Delta SSIM = -5.01\%$) compared to CSTV (-63.39%), SIRT (-55.29%) and WBP (-49.31%).

Figures 4.12(a) and (b), shows the intensity line profile comparison along the vertical dashed line in (Fig. 4.8a) and Fig.4.9(a). It can be seen that reconstruction using DLET and CSTV leads to images with a better match to the phantom than the WBP and SIRT results. It is also noticeable that both the CSTV and DLET reconstruction methods can provide a relatively accurate recovery of the homogenous area (see the red arrows in zoomed area of (Fig. 4.8)). In addition, DLET is more robust in cases with high noise (Fig. 4.9e) with better preservation of fine details (see blue arrows in (Fig. 4.8)) and regions with gradual intensity variation (see orange arrows in (Fig. 4.8)). Table.4.1, lists the PSNR and SSIM values computed with respect to the reference phantom images in (Fig. 4.8a).

4.4.2.2 Noiseless under-sampled setup

To verify how each method behaves in the case of undersampling, projections (columns) were removed from the sinogram in (Fig.4.6a) to simulate undersampling between $\pm 70^\circ$ with tilt increment of 2° (Fig.4.6d), and 5° (Fig.4.6e).

As a consequence of such under-sampling, aliasing effects can be seen in both cases as streak artefacts. Also, the missing 20° wedge, located on both sides of sinograms, causes another form of aliasing (i.e. elongation artefacts) which increases the object length in the horizontal direction. Such artefacts can be clearly seen in Fig. 4.10 and 4.11b and c) which show results obtained by WBP and SIRT methods.

Figure 4.10 and 4.11, (d) and (e) show that both DLET and CSTV result in reduced undersampling artifacts. In (Fig. 4.10), the DLET reconstruction shows sharper edges with $SSIM = 0.8256$ compared to 0.4113 of CSTV. In (Fig. 4.11), it was harder to reduce artifacts with the increasing undersampling. However, DLET showed a slightly better visual quality with $SSIM = 0.7857$ compared to 0.3656, 0.2304, 0.1324 for CSTV, SIRT and WBP, respectively. Figure 4.12(c)

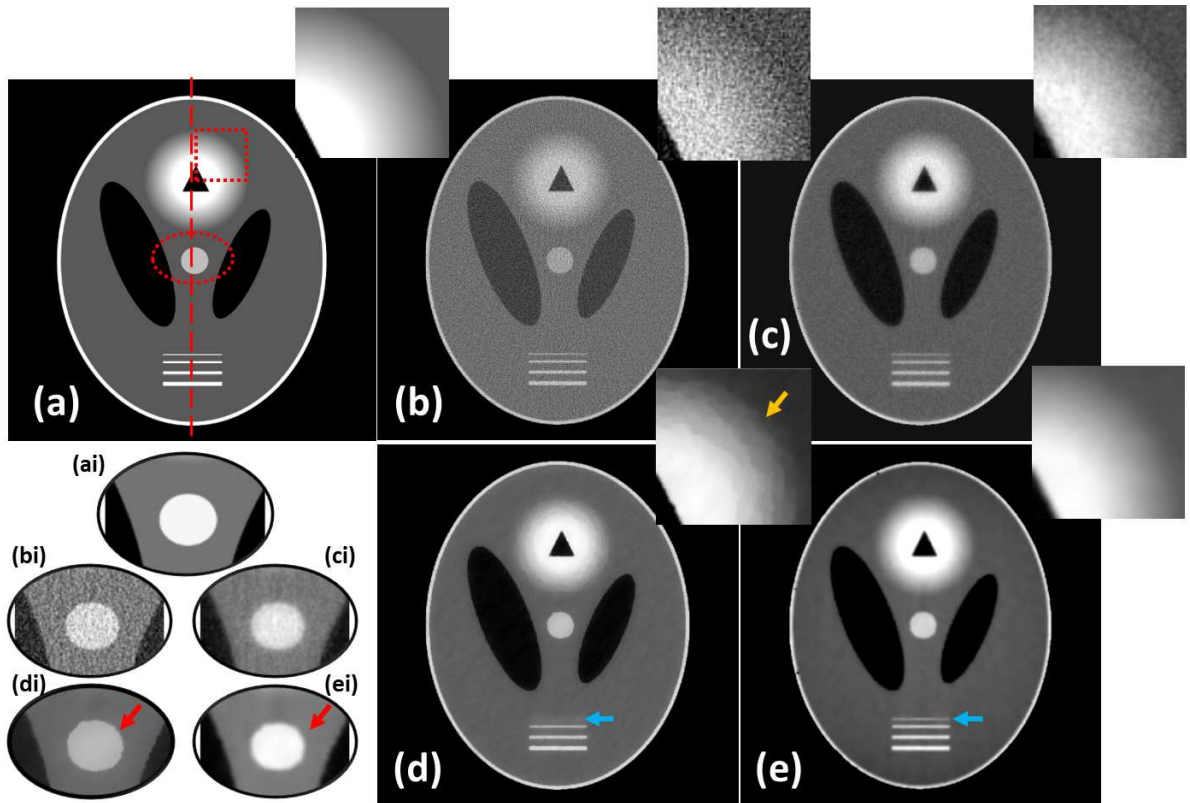


Figure 4.8 | Comparison of different reconstruction algorithms using the noisy fully sampled sinogram in Fig.4.6(b). a) Ground truth, compared to reconstruction using b) WBP, c) SIRT, d) CSTV with $\lambda_{TV} = 7$ and $\lambda_{l_1} = 0.1$, e) DLET with $\epsilon = 1 \times 10^{-7}$. (ai) are zoomed regions extracted from the phantom at the area indicated by oval-dotted region in (a). (bi-ei) are zoomed regions extracted from the corresponding reconstructions in (b-e). For visualisation purposes, the image contrast of zoomed areas is enhanced.

and (d) shows the intensity line profile comparison along the vertical dashed line in (Fig. 4.10a) and (Fig. 4.11a).

4.4.3 Simulation study 2: CS-phantom

In this section, the performance of the DLET reconstruction algorithm is evaluated using the test phantom (the CS-phantom) proposed by [Smith and Welch \(2011\)](#), which is not a piecewise constant image. The CS-phantom (Fig. 4.13-a) is designed for testing the accuracy of CS solvers and the properties of CS reconstruction artifacts. For comparison, we performed the reconstruction based on WBP, SIRT and DLET method using simulated data set. The

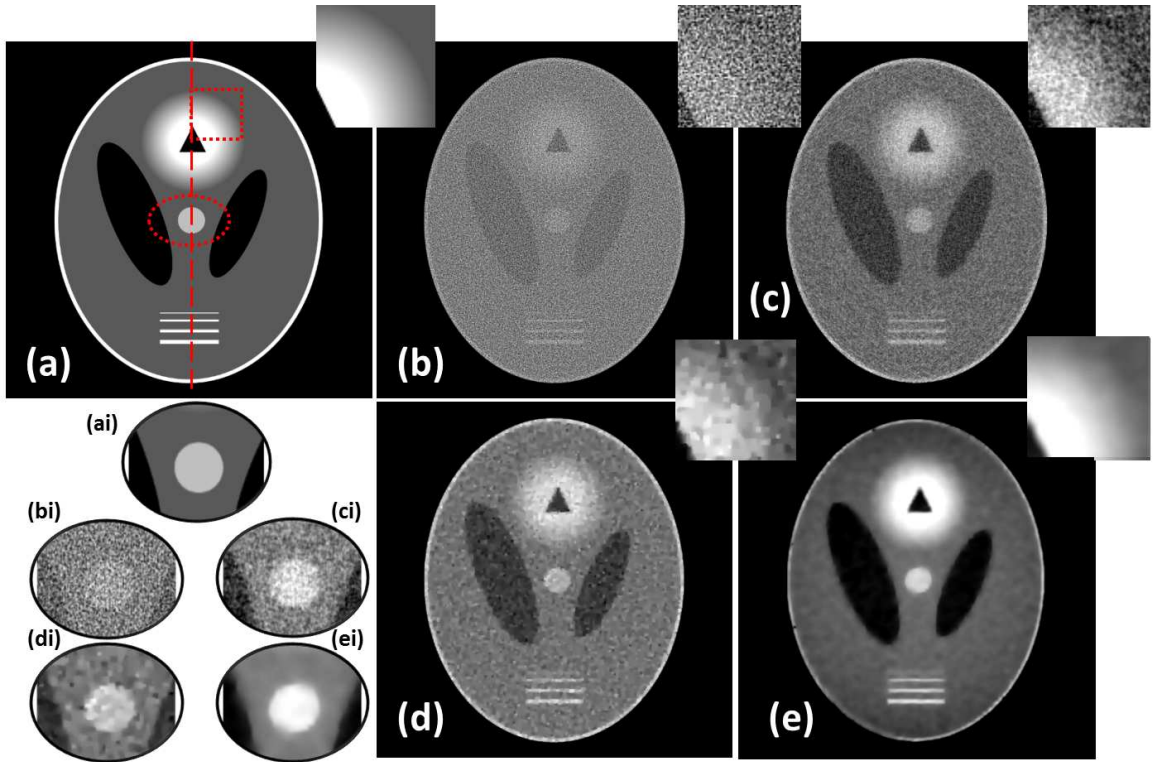


Figure 4.9 | Comparison of different reconstruction algorithms using the noisy fully sampled sinogram in Fig.4.6(c). a) Ground truth, compared to reconstruction using b) WBP, c) SIRT, d) CSTV with $\lambda_{TV} = 12$ and $\lambda_{l_1} = 0.1$, and e) DLET with $\epsilon = 2 \times 10^{-6}$. (ai) are zoomed regions extracted from the phantom at the area indicated by oval-dotted region in (a). (bi-ei) are zoomed regions extracted from the corresponding reconstructions in (b-e). For visualisation purposes, the image contrast of zoomed areas is enhanced.

CSTV-based method was excluded because the CS-phantom is not sparse under a gradient transform, since this violates the requirement for a TV-L1 minimisation. The DLET method was applied using two setups that are based on adaptive dictionary approach. In the first setup, the dictionary was trained using local (i.e. the tomogram under reconstruction) during the reconstruction process. This local dictionary was re-learned on each iteration of the reconstruction process using the tomogram that resulted from the previous iteration. The second setup, a Global dictionary was trained using prior training set that contain features similar to those in the original phantom (e.g. images that contain circles/spheroids with various diameters and centers). The global dictionary was learned only in the first step of the reconstruction process.

An under-sampled tilt series was modelled with 70 noiseless projections with

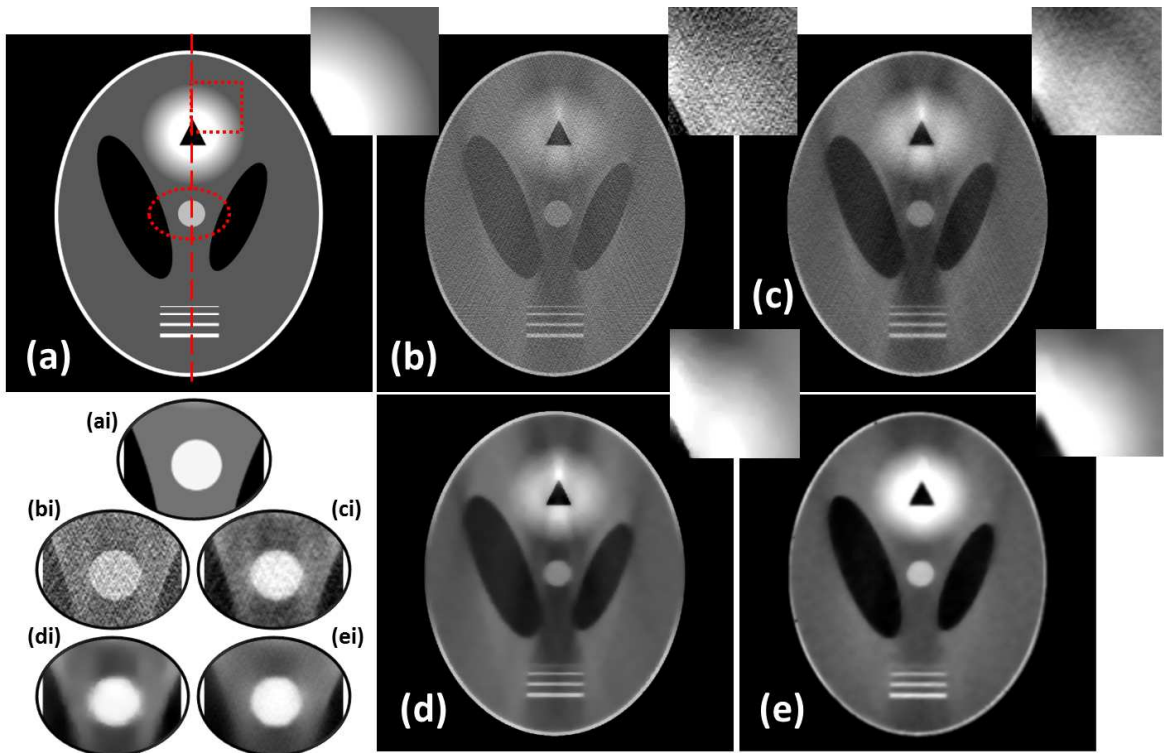


Figure 4.10 | Comparison using noiseless undersampled sinogram in Fig.4.6(d) with 70 radial lines. a) Ground truth, compared to reconstruction using b) WBP, c) SIRT, d) CSTV and e) DLET with $\epsilon = 45 \times 10^{-7}$. (ai) are zoomed regions extracted from the phantom at the area indicated by oval-dotted region in (a). (bi-ei) are zoomed regions extracted from the corresponding reconstructions in (b-e). For visualisation purposes, the image contrast of zoomed areas is enhanced.

2° increments between each projection. The simulation setup described in section (4.4.2) was adopted in preparing sinograms for reconstruction.

To further assess the visual quality of the reconstructions, the tomograms were thresholded based on the image intensity followed by binarization (i.e. setting pixels above a threshold limit to a value of 1/white and the rest to zero/black). The threshold values were obtained via automated thresholding using Otsu’s method (Otsu, 1975b).

Figure (4.13) shows the reconstruction using WBP, CSTV, and DLET. In Fig.4.13(b2), two type of artifacts can be seen; 1) streaking artefacts, which is a prominent kind of aliasing caused by the finite and limited angular sampling in ET, 2) elongation and blurring of the object boundaries (see horizontal red arrow), which occurs primarily due to the missing wedge of unsampled data. The missing wedge direction runs horizontally between the left and right of the image.

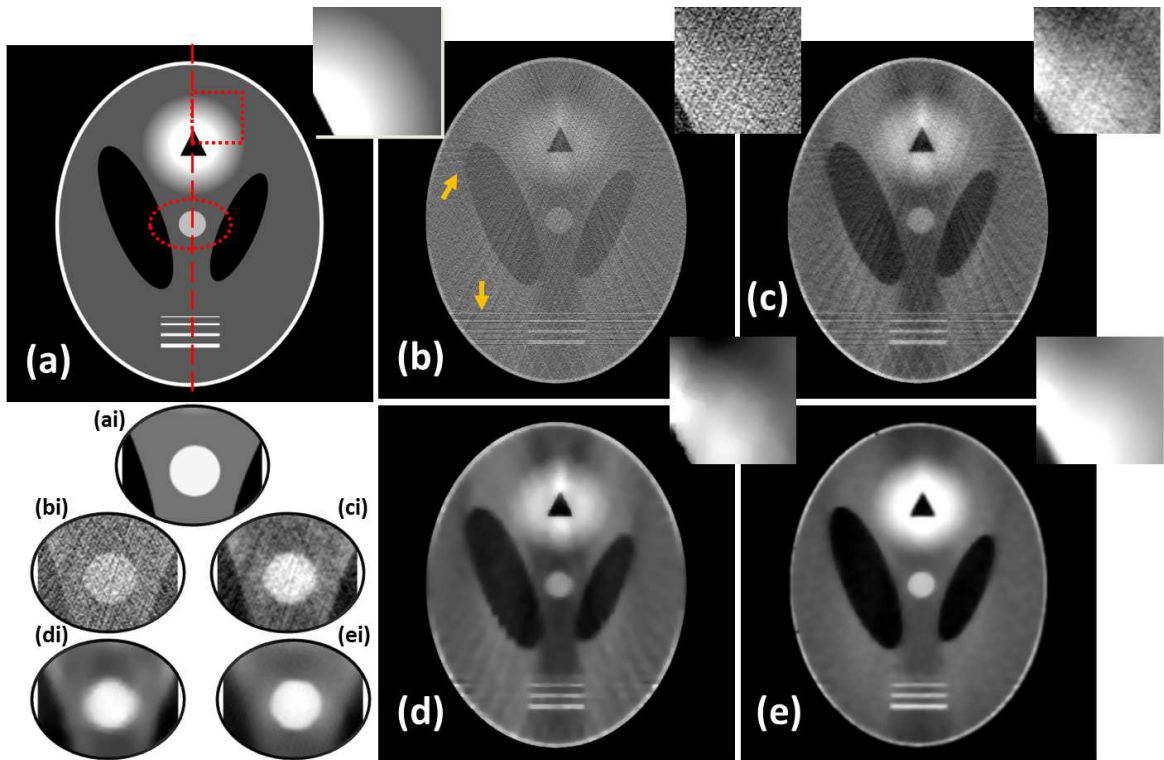


Figure 4.11 | Comparison of different reconstruction algorithms using the noiseless undersampled sinogram in Fig.4.6(e) with 28 radial lines. a) Ground truth, compared to reconstruction using b) WBP, c) SIRT, d) CSTV and e) DLET with $\epsilon = 45 \times 10^{-7}$. (ai) are zoomed regions extracted from the phantom at the area indicated by oval-dotted region in (a). (bi-ei) are zoomed regions extracted from the corresponding reconstructions in (b-e). For visualisation purposes, the image contrast of zoomed areas is enhanced.

The high artefact levels are clear in Fig. 4.13(b1-c1, b2-c2), for both the SIRT and WBP reconstructions, including the well-known artefact of elongation of the reconstructed object in the missing wedge (horizontal) direction. For the DLET reconstruction, Fig.4.13(d1, d2) and Fig.4.13(e1, e2), show further reduction of streaking background artifacts and missing wedge elongation.

The missing wedge direction and object morphology is an important factor that affects the accuracy of the reconstruction. The boundaries of the parallel horizontal lines (indicated by a vertical red arrow) are well reconstructed. This is due to the presence of the significant projection for this shape which is the projection at 0° (horizontal direction) that provides the information about width and distances between each line. However, the horizontal lines (indicated by horizontal red arrow) are difficult to distinguish as the most important projection is in

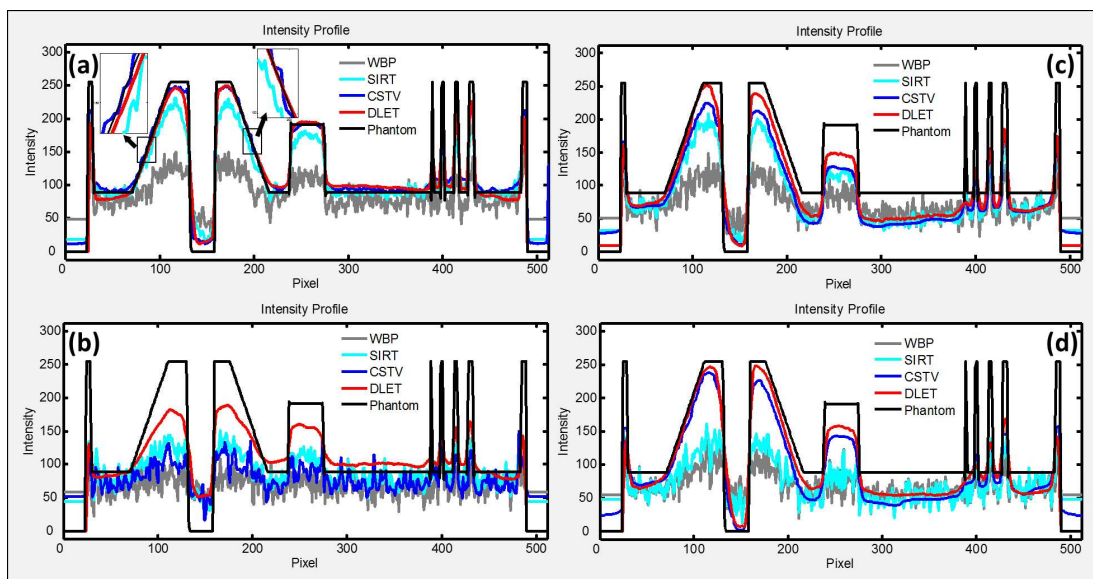


Figure 4.12 | Intensity line profile comparison along the vertical dashed line in a) Fig.4.8(a), b) Fig.4.9(a), c) Fig.4.10(a) and d) Fig.4.11(a). Each figure is a comparison between reference phantom image with reconstruction from WBP, SIRT, CSTV and DLET for different test cases.

Table 4.1 | Noise and Undersampling Evaluation - Quality values of modified Shepp-Logan phantom.

Figure	4.8		4.9		4.10		4.11	
Method/Metric	PSNR	SSIM	PSNR	SSIM	PSNR	SSIM	PSNR	SSIM
WBP	14.40	0.1748	12.19	0.0886	14.61	0.2414	12.64	0.1324
SIRT	20.88	0.3478	14.71	0.1555	16.61	0.2926	15.74	0.2304
CSTV	21.35	0.8552	15.45	0.3131	17.68	0.4113	17.31	0.3656
DLET	21.52	0.8710	17.39	0.8274	18.5941	0.8256	18.24	0.7857

the middle of the missing wedge region (90°). The DLET with global dictionary was able to compensate for most of the missing wedge artefacts when trained using similar examples. However, such examples are not usually available in the case of ET. Although the DLET with local dictionary was not able to compensate for the missing wedge of vertical lines, there was a significant reduction of streaking and elongation artefacts compared to both WBP and SIRT.

The quality metric values are listed in Table (4.2). Quantitatively, the WBP algorithm had the worst results. The SIRT result is slightly better than the WBP result (SSIM of 0.6164 and 0.5651 respectively). However, DLET outperformed both with SSIM 0.8188 with respect to the reference image. Also, the PSNR met-

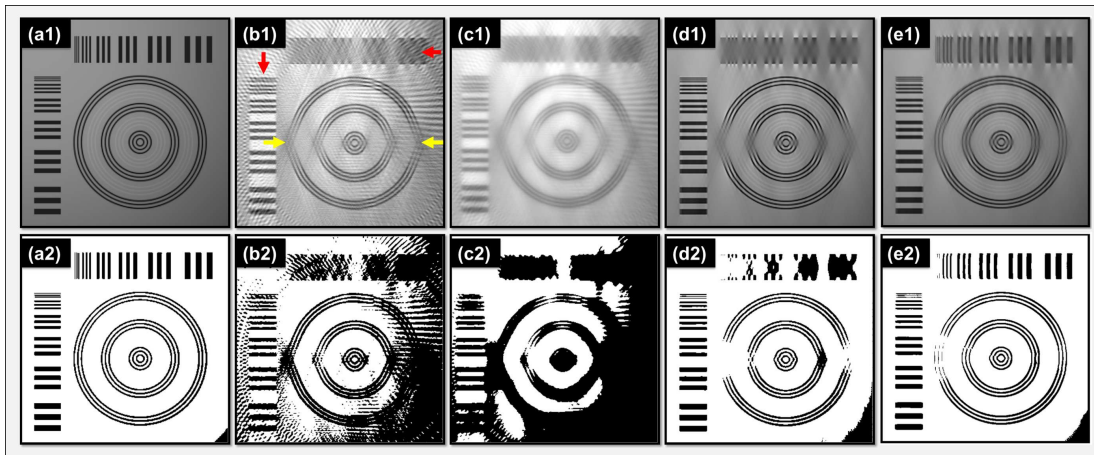


Figure 4.13 | Visual assessment of the missing wedge artifact. The top row is a1) Reference phantom extracted from (Smith and Welch, 2011) which is reconstructed using b1) WBP , c1) SIRT , d1) DLET using local dictionary and e1) DLET using global dictionary. Bottom row, is the corresponding thresholded images obtained after applying automated thresholding using Otsu’s method (Otsu, 1975a).

ric confirms this with values of 24.97 dB compared to 18.73 dB for the SIRT and 14.20 dB for WBP. Also, background artefacts and false elongation are markedly reduced.

Based on this simulation study, it is clear that the use of an adaptive dictionary-based reconstruction method suppresses artefacts due to under-sampling, streaking and elongation far more effectively than conventional compressed sensing electron tomography (Binev et al., 2012; Goris et al., 2012; Saghi et al., 2011) or the well-known weighted back-projection algorithm. Additionally, DLET demonstrated a stable and fast convergence for this particular challenging phantom as shown in various figures suggesting that it will be robust for use in real cases. A particularly promising feature of DLET is the relatively competitive reconstructions than existing methods for significantly under-sampled datasets with large tilt steps, at least up to a certain point at which artefacts start to creep in. Nevertheless, it seems likely that even this limitation could be avoided by using a global dictionary, in order to preserve high spatial frequency structures effectively and to avoid undesirable artefacts due to the high under-sampling. This would make it especially attractive for low-dose electron tomography of beam-sensitive structures, such as biological ultrastructure or polymer solar cells.

Table 4.2 | Quality metric values of CS-phantom reconstruction in Fig.4.13.

Method/Metric	PSNR	SSIM
WBP	14.20	0.5651
SIRT	18.73	0.6164
DLET (Local D)	24.97	0.8188
DLET (Global D)	26.57	0.8964

4.4.4 Parameter Comparison

To evaluate the sensitivity of the DLET algorithm to parameter settings, the algorithm performance in reconstructing the reference CS-phantom in (Smith and Welch, 2011) from 70 projections was investigated by altering a single parameter each time whilst fixing the others at their default values. The parameters assessed were: the dictionary patch size (n), the number of atoms (K) and the discrepancy level (ϵ).

In Table 4.3, the quality of reconstruction continues to improve as the patch size increases from 2×2 to 10×10 pixels. This is to be expected, as each pixel will be a result of the averaging of patches with a larger area.

Table 4.3 | Patch Size Parameter Evaluation OF DLET - Quality values of different runs of DLET from noiseless 70 projections.

Patch Size (n)	PSNR	SSIM	Time (mins)
2	24.34	0.6724	5
4	24.54	0.7647	7
6	24.89	0.8058	15
8	24.97	0.8188	44
10	25.00	0.8224	121

In Table 4.4, the performance metrics reached a plateau when the number of dictionary atoms increased to twice the patch size, meaning that the dictionary contains most of the important atoms that can be found in the training data to produce a good sparsity. The training algorithm used here was initiated using the blocks from the discrete cosine transform (DCT) (as in Elad and Aharon, 2006) and trained on patches extracted from intermediate reconstruction results.

Table 4.4 | Number of Atoms (Dictionary Size) Parameter Evaluation of DLET - Quality values of different runs of DLET from noiseless 70 projections.

Dictionary Size	PSNR	SSIM	Time
64	24.6	0.80	7
128	24.9	0.81	8
192	24.9	0.81	9
256	24.9	0.81	10

In Table 4.5, the quality of reconstruction was maximised when the discrepancy level (ϵ) was increased to 1×10^{-3} and declined slightly for higher values. This behaviour can be explained as follows: when ϵ is set at a precision level that

Table 4.5 | Discrepancy level (ϵ) Parameter Evaluation OF DLET - Quality values for different runs of DLET from noiseless 70 projections as a function of ϵ .

ϵ	PSNR	SSIM	Time
1×10^{-4}	24.60	0.7246	28
1×10^{-3}	24.97	0.8188	16
5×10^{-3}	24.71	0.8002	8
1×10^{-2}	23.87	0.7847	7
1	23.38	0.7257	7
10	23.38	0.6792	6
100	23.38	0.6624	6

is too small, the algorithm includes under-sampling artefacts and noise in the reconstruction during the sparse coding step, which may introduce fake structures. On the other hand, when ϵ is too large, the quality degrades as the sparse solver does not include enough important patches to properly approximate the solution which causes a loss of resolution. Figure. 14 shows the quality limit for higher under-sampling factors using default DLET settings. Both the PSNR and SSIM values of DLET are high even at very large tilt increments such as 25, indicating good removal of artefacts and noise. From these results, it can be seen that satisfactory results can be obtained with a little tuning of (n and K), as the proposed algorithm is not very sensitive to deviation in these parameters. However, the discrepancy level, ϵ , needs to be accurately estimated. It should be mentioned

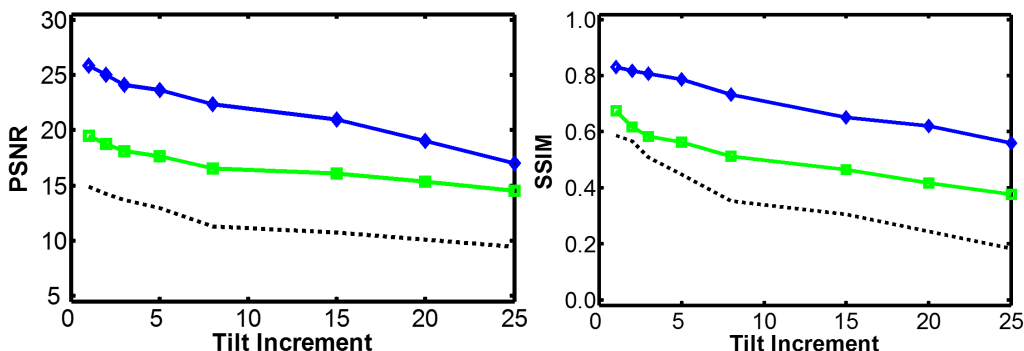


Figure 4.14 | Quality limit for higher under-sampling factors using (dotted) WBP, (squares) SIRT and (diamonds) DLET with higher increment steps between projections.

that the improvement introduced by DLET comes at the cost of a higher computational expense, The execution time of this simulated dataset using the WBP was 0.3 minutes and 0.9 minutes using the SIRT method. This is lower than DLET execution time ($\approx 5 - 16$ minutes). Therefore, a realistic compromise will have to be struck in real application between quality and computational expense.

4.5 Organic photovoltaic solar cells 3D-morphology

In this section, the DLET algorithm is used to study the morphology of a solar cell sample (PTB7:PC₇₁BM blends). In (Alekseev et al., 2015) SIRT reconstruction was used to investigate the shape of PC₇₁BM-rich domains using Energy Filtered TEM (EFTEM). SIRT was able to show a nearly ellipsoidal shape of these domains, however, the reconstruction was noisy which made the segmentation a difficult task. This affects the accuracy of quantitative studies. The sample is a blend of polymer (PTB7) and fullerene derivative (PC₇₁BM) spin-coated from chlorobenzene with average particle size of 200 nm in diameter. The tilt series in (Alekseev et al., 2015) has a low signal-to-noise ratio (SNR) making it an ideal sample to test the denoising capability of DLET. An EFTEM projection from the tilt series is shown in (Fig. 4.15).

Before CS can be applied for tomographic reconstruction of organic solar cells using the EFTEM tilt series, two key criteria need to be satisfied: 1) The contrast mechanisms of the microscope using EFTEM need to obey the projection requirement for tomographic reconstruction (Frank, 2006a; Weyland and Midgley,

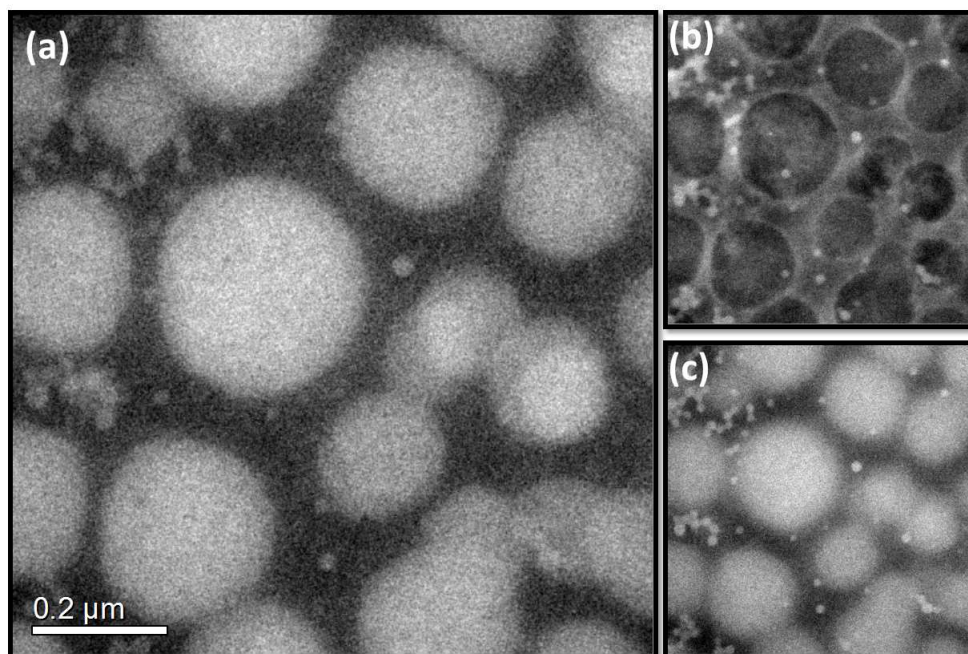


Figure 4.15 | Example EFTEM tomography tilt-series projection of PTB7:PC₇₁BM film- (a) Elemental map of carbon was obtained using the three-window mapping method (Egerton, 2011) by subtracting (b from c), (b) background estimation image produced from two pre-edge EFTEM images, (c) Post-edge image for the C-K edge. The elemental map in (a) shows PC₇₁BM-rich domains (large bright regions) embedded in a PTB7-rich matrix.

2003), 2) A sparsifying transformation must exist for which the tomogram image is sparse when represented by that transformation.

In order to satisfy the first criterion, the intensity of EFTEM images should be a monotonic function of the projected physical quantity. The PTB7:PC₇₁BM blends sample consists mostly of amorphous material; therefore, the EFTEM contrast is principally determined by the total amount of the specific element mapped in the image (Hofer et al., 1997, 1995; Weyland and Midgley, 2003) and should not show diffraction contrast. Therefore, the intensity shown in the elemental map of (Fig. 4.15a) is a projection of a number of atomic species through the structure of the specimen. As such, EFTEM maps for this particular specimen fulfil the projection requirement for tomographic reconstruction. This also means that the reconstructed volume should contain multiple grey levels, corresponding to a range of different reconstructed intensities of the PTB7:PC₇₁BM sample. It should also be noted that the intensity of the reconstructed grey levels, might not be significantly different due to the noise level in the tilt series arising from the

imaging system. For the second criterion, it is possible to reconstruct this sample by seeking sparsity in the gradient domain (i.e., optimisation using total variation) since it is expected for the PC71BM-rich domains to have a uniform composition. However, the boundary between PC₇₁BM domains (carbon-rich) and the PTB7 matrix (sulphur-rich) may not be sharp leading to a range of (non-discrete) grey levels. This makes the reconstruction using TV (i.e. the piecewise constant approximation) inaccurate and may lead to artefacts in reconstruction and lose important details. On the other hand, by using an adaptive data-driven transform via a dictionary learning approach, a sparsifying transform can be tailored to produce a more efficient transform which is crucial for the success of reconstruction using CS. We have performed a simulation study to support the investigation of the experimental data.

4.5.1 Simulation study

To simulate the experimental data, a 3D mesh model of a sphere and two oblate spheroids (see Fig.4.16) was designed using CAD software. The sphere was made with a radius of units (top part of Fig. 4.16) while the spheroids were made with a fixed value for the equatorial axis ($a = 10$ units in Fig. 4.16) and a different length for the polar axis ($c = 4$ and 1 units in Fig. 4.16). Such a model is suitable to simulate the PC₇₁BM-rich domains which are believed to have a spherical shape as can be seen in Fig.4.15 and the cross-section view in Fig.2 in (Alekseev et al., 2015). The simulated mesh model is shown in Fig.4.17. This mesh model is then voxelised using the method of (Nooruddin and Turk, 2003) generate a binary 3D bitmap with voxel values of logical 1 or 0. The voxels represent the boundary and inside region of the 3D object, while the voxels represent the background region.

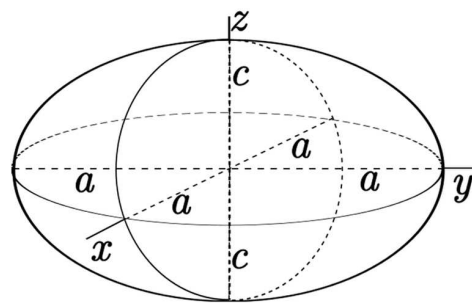


Figure 4.16 | Oblate spheroid : a rotationally symmetric ellipsoid having a polar axis (c) shorter than the diameter of the equatorial axis (a).

The projection tilt series for simulation was generated by applying the discrete Radon transform to the 3D bitmap over a tilt range of $\pm 62^\circ$, with an increment of 2° between consecutive projections around the y-axis. Then the tilt series was

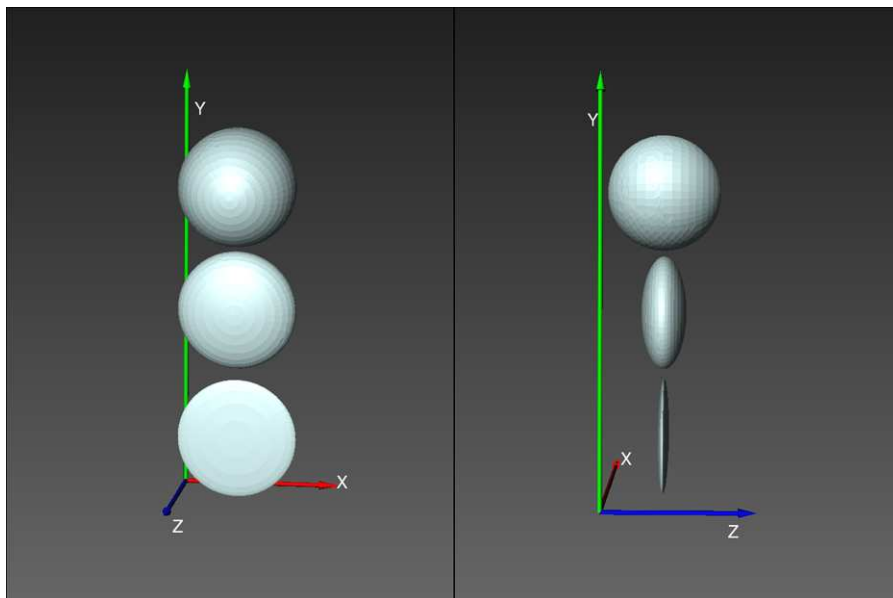


Figure 4.17 | Simulated mesh model for simulating the polymer solar cell top object is a true sphere of radius, $c = 10$, the lower two objects are oblate spheroids with different polar axis lengths, $c = 4, 1$ units, respectively.

scaled to match the approximate mean intensities of the PC_{71}BM -rich domains evaluated from the experimental EFTEM projections. These were then degraded by the addition of shot and Gaussian noise to get a low SNR dataset that roughly simulates the experimental EFTEM projections. The Gaussian noise was estimated in a way that yields an SNR of 7.1, which provides a good visual match to the noise in the experimental images. Finally, quantisation noise is added. The mapping to quantised intensity was assumed to be linear and is added using Equation 4.9:

$$I_q = \text{floor}\left[2^{Bd}\left[\frac{I_{in}}{I_{max}}\right]\right] \quad (4.9)$$

Where I_q is the quantised intensity, Bd is the bit depth, I_{in} is the input intensity from the previous stage and I_{max} is the maximum number of electrons that can be detected by a single pixel of the detector. For this simulation, a quantisation with a bit depth of $Bd = 16$ gives $2^{16} = 65536$ discrete values of intensity that can be assigned. The parameters for WBP and SIRT were as described in section 4.4.2. For the CSTV, finding the appropriate values for λ_{TV} , λ_{l1} parameters for a given data set is generally a trial-and-error process which is made more difficult by the subjective nature of deciding what constitutes a correct recon-

struction. For this reason, the CSTV algorithm was run for a range of different values for the parameters between $[20 - 0]$ for both λ_{TV} and λ_{l1} and choosing the values that maximise the SSIM metric between a 2D XY-slice through the centre in the simulated 3D map as in Fig.4.19(a1-c1) with the corresponding slice in the reconstructed map. The SSIM was shown to be consistent with perceived visual quality (as can be seen in Wang et al., 2004, Fig. 2). For the DLET method, the dictionary size is set to ($K = 256$ atoms) for 8×8 patches ($n = 64$); the dictionary for DL processing is pre-trained from the intermediate image, as a training set, using K-SVD with parameters as follows: 20 iterations are used in dictionary training ($Iter = 20$); the target sparsity limits T_0 is set to $0.5n$ atoms.

To assess the fidelity of reconstruction quantitatively, the normalised Euclidean Distance (NED) metric was used in both the image and sinogram domains. In the image domain, it is defined as: $NED_{img} = \|x - x'\gamma\|_2 / \|x\|_2$ where x is the ground truth map, x' is the reconstructed image and γ is the scaling constant. In the sinogram domain, the quality metric is: $NED_{proj} = \|b - \varphi b'\|_2 / \|b\|_2$ where b is the projection data, b' is the decrease Radon transform of x' and φ is a scaling constant. The scaling factors γ and φ are important for a fair comparison between different algorithms as this will reverse any scaling or negative intensity that might be applied to the simulated data by different numerical implementations used in this paper. The values for γ and φ are obtained in a way that minimises the Euclidean distance metric, which is an unconstrained nonlinear optimisation that can be solved using MATLAB.

Figure 4.18 (a1-c1) shows a volume rendering from the WBP reconstruction. This clearly suffers from blurring, streaking, and missing wedge artefacts, which can also be viewed in the noisy orthoslices in Fig.4.19(a1-c1). The SIRT results in Fig.4.18 (a2-c2) show higher SNR and contrast than of the WBP. SIRT was also able, to some degree, to retrieve the challenging third spheroid that is lost in WBP as indicated by the arrow in Fig.4.19(a2). In the CSTV case, the parameters that maximise the SSIM between the reconstructed and ground truth maps were $\lambda_{TV} = 10$, $\lambda_{l1} = 13$ as shown in Fig 4.18(a3-c3). It can be seen that the CSTV was able to reduce the elongation artefact and noise. However, this came at the cost of losing both of the spheroids. This problem can be ameliorated by decreasing the λ_{l1} contribution to 10 as can be seen in Fig.4.18 (a4-c4). CSTV was able in this case to retrieve the middle sphere. However, this comes at the cost of increasing noise in the reconstruction, as can be seen in the orthoslices in

Table 4.6 | Quality metric values for the polymer solar cell reconstructions

Figure		4.19		4.20
Method/Metric	SSIM	NED_{img}	NED_{proj}	NED_{proj}
WBP	0.0470	0.74	0.56	(a) 0.42
SIRT	0.0840	0.57	0.31	(b) 0.29
CSTV	(a3) 0.7454	0.11	0.08	(d) 0.24
	(a4) 0.5755	0.20	0.15	-
DLET	0.8039	0.08	0.07	(f) 0.23

Fig.4.19(a4-c4). It should also be noted that the CSTV reconstruction was not able to retrieve the second spheroid, even with a lower value of λ_{l1} as the noise remains dominant.

Figure 4.18 (a5-c5) shows the DLET results, and these clearly show reduced noise and minimal missing wedge artefacts. The error tolerance parameter ϵ is set to 2.5×10^5 . It can be clearly seen that all of the spheroids were recovered with good contrast. As for the challenging second spheroid, despite the weak signal, it can be seen that this was much better reconstructed by DLET than by any other algorithm. Such an object is challenging to recover as its intensity is very near to the noise level in the sinogram domain, making it hard to distinguish from the noise. The DLET performed better due to the patch averaging step, where each pixel is an average of the image patches that cover the surrounding area. Also, since the other objects contain similar features, this enhances the sparsifying capability of the learned dictionary. This also enables the use of features from other objects with better contrast to recover objects with noisy pixels in a way that is consistent with the measurements. Table 4.6 shows the quantitative quality measurements for each of the reconstructions in this section.

4.5.2 Experimental results

As stated above, in a previous publication (Alekseev et al., 2015), ET was used to study the 3D morphology of PTB7:PC₇₁BM blends, but only using SIRT. Here the CSTV and DLET are applied to an EFTEM tilt-series of PTB7:PC₇₁BM blends (Fig. 4.15-a), looking for a reconstruction of a higher quality than can be

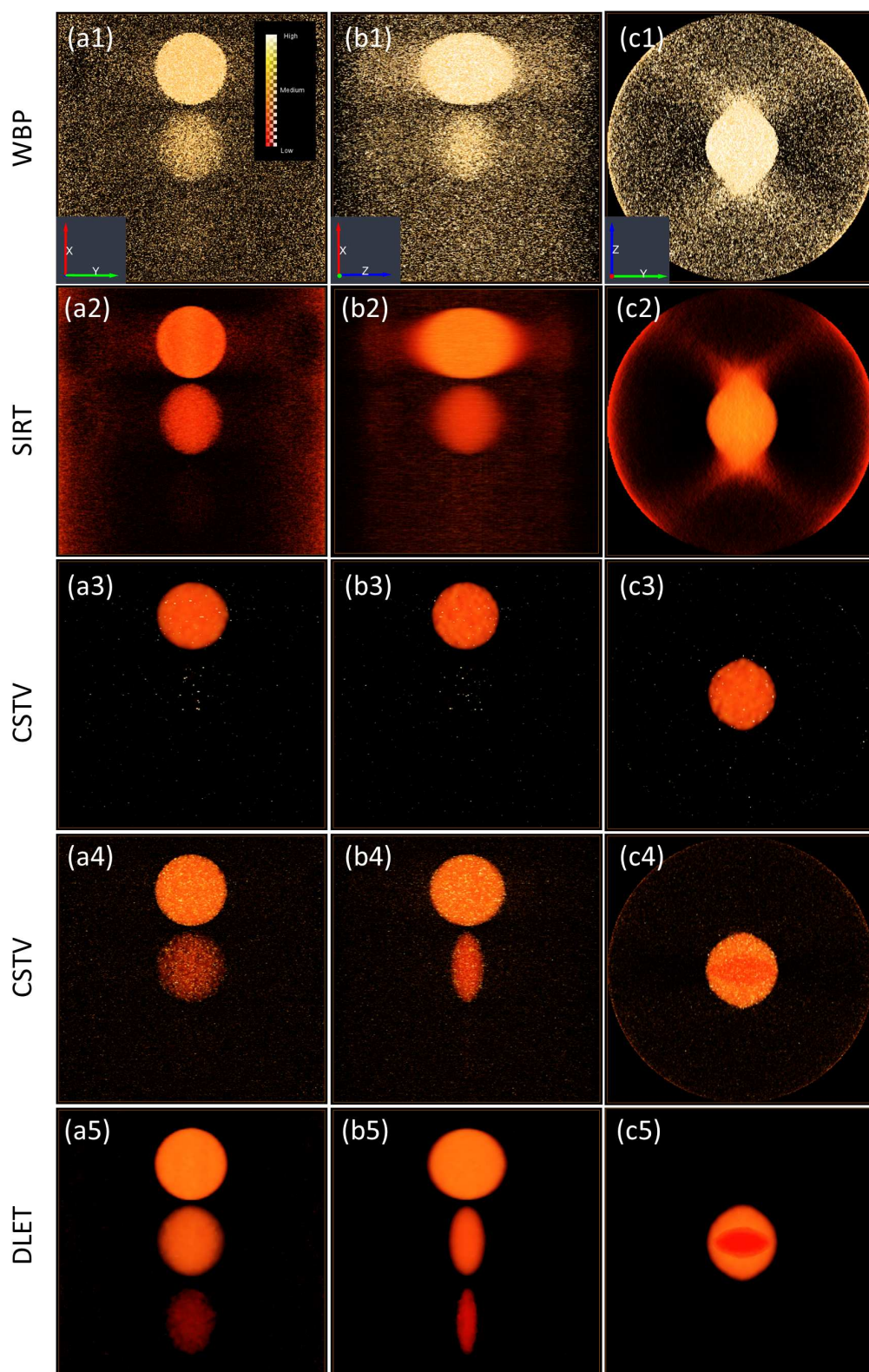


Figure 4.18 | Volume rendering of reconstruction from noisy projections of simulated solar cells- (a1-c1) shows a visualisation WBP (a2-c2) SIRT, (a3-c3) CSTV with $\lambda_{TV} = 10, \lambda_{I1} = 13$, (a4-c4) CSTV $\lambda_{TV} = 10, \lambda_{I1} = 10$, (a5-c5) DLET reconstruction. As before, the a) images are Z-projections, the b) images are Y-projections, and the c) images are X-projections.

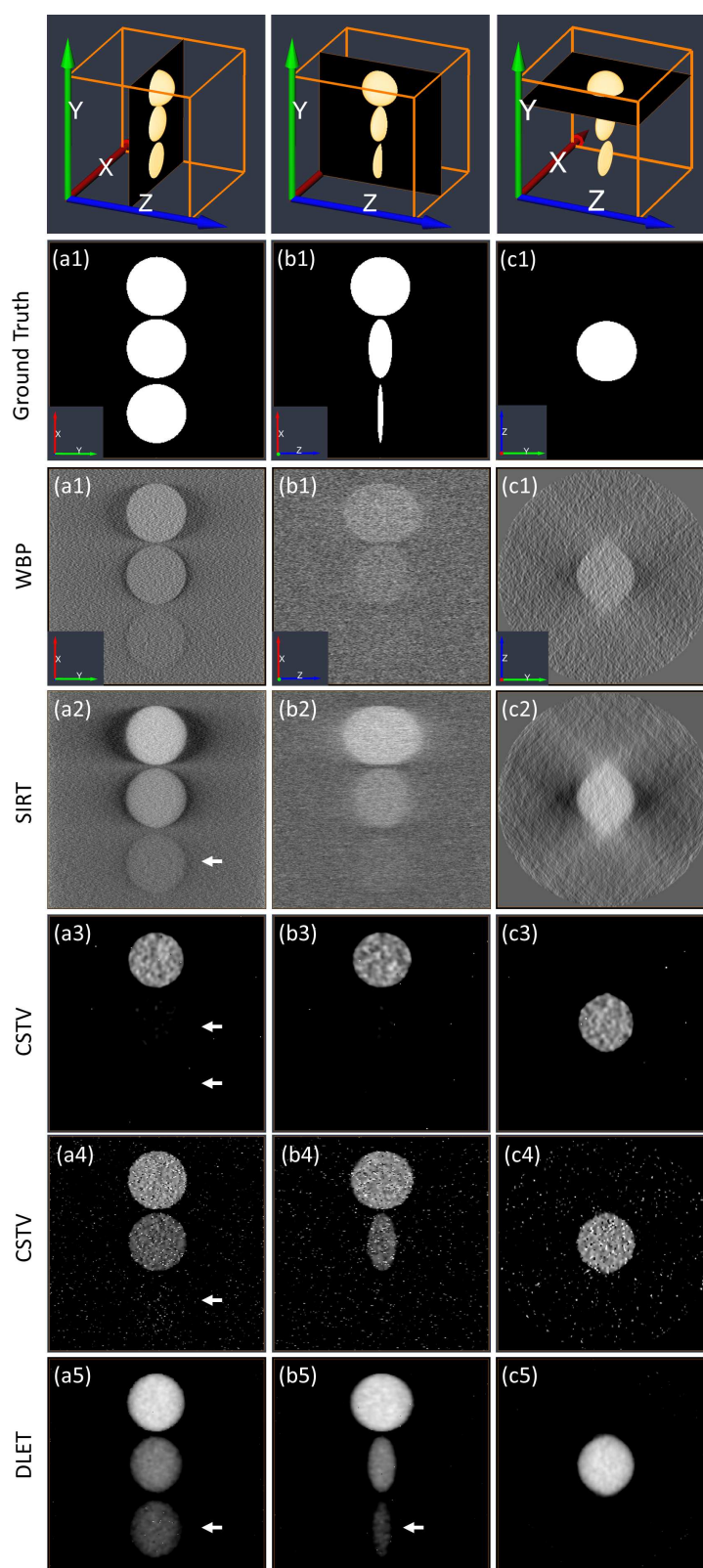


Figure 4.19 | Orthogonal Slices through the reconstructed volume in Fig.4.18.- (a1-c1) shows an orthoslice of WBP reconstruction (a2-c2) SIRT, (a3-c3) CSTV with $\lambda_{TV} = 10, \lambda_{I1} = 13$, (a4-c4) CSTV $\lambda_{TV} = 10, \lambda_{I1} = 10$, (a5-c5) DLET reconstruction. As before, the a) images are slices perpendicular to Z, the b) images are slices perpendicular to Y, and the c) images are slices perpendicular to X.

provided by SIRT and WBP. For this purpose, a tilt series was acquired for a cross-section lamella of the polymer blend with thickness ($\approx 130\text{nm}$), making it electron transparent. The lamella was prepared using a focused ion beam (FIB) lift-out technique. Such thinning is also important to avoid shadowing at higher tilts. The electron tomography dataset was acquired on an FEI Tecnai T20 TEM operated at 200 kV and equipped with a Gatan GIF2000 Imaging Filter. The EFTEM imaging mode was used for energy-selected images for the C-K edge to highlight the PC₇₁BM domains. A tilt series was acquired over a tilt range of $\pm 62^\circ$, with an increment of 2° between consecutive projections. After obtaining the elemental map tilt series, an automated spatial drift correction (alignment) for the EFTEM series was performed with the Statistically Determined Spatial Drift algorithm (Schaffer et al., 2004) using the SDS plugin for DigitalMicrograph (DM). The visualization of all the reconstructions was done using the Amira 6.0 software package from FEI Visualization Sciences Group. More details about imaging conditions can be found in (Alekseev et al., 2015).

Figure 4.20, shows an XY-orthoslice taken at the centre of reconstructed volume using different methods. The WBP and SIRT slices show noisy results in Fig.4.20(a and b) and missing wedge artefacts in the XZ-orthoslices in Fig.4.21(a and b) which are very difficult to segment. Fig.4.20(c and d) shows a reconstruction from CSTV with different values for $\lambda_{TV} = 10, 20$ respectively. The values for λ_{I1} in both slices was 10 and not increased in order not to lose features from the reconstruction. It can be seen that CSTV in slice (c), using parameter values similar to those used in the simulation in Fig.4.18(a4), has a limited ability to reduce the noise. When increasing the λ_{TV} from 10 to 20 in slice (d), the reconstruction noise was further suppressed. However, this came at the expense of introducing staircase artefacts (as indicated by the arrows in the zoomed area). The DLET slices in Fig.4.20(e and f) show reconstruction with higher fidelity for this noisy and reduced dataset. The results are improved when increasing the error tolerance parameter ϵ from 2.5×10^5 to 1.3×10^4 in slice (f), which makes it very easy to segment using (semi-)automated methods. In Fig.4.21(c and d), the elongation of the PC₇₁BM-rich domains is reduced using both CSTV and DLET. However, we noted that different tuning for CSTV parameters will affect the size of PC₇₁BM domains while in the case of DLET, the only effect that was noted is the blurring of the boundaries of the domains when increasing the ϵ above the error levels. Fig.4.22 shows the corresponding volume renderings of reconstructed

volumes. The volume rendering display windows were limited with alpha value (transparency) reduced until the true signal from the object(s) prevailed over the background intensity.

The experimental data results (Fig.4.20, Fig.4.22 , Fig.4.21 and Table 4.6) are consistent with many of the features in the simulation studies. DLET was able to produce clear reconstructions with decreased streaking and missing wedge artefacts. The denoising capability was also demonstrated without sacrificing sharp details or introducing new artefacts. Also, DLET results maintained a higher SNR and contrast compared to other methods in this study, which maintains separation between different independent features (as indicated by the arrows in Fig.4.22-d). When using a value of ϵ that was far too large, the DLET processing will be faster. However, this will result in some loss of genuine signal as the sparse coding step of DLET will tend to approximate each patch in the reconstructed image with large errors, which can introduce some blurring. On the other hand, setting ϵ too small or below the noise level will increase the computing time and will add more noise and artefacts to the reconstructed image.

4.6 Ebola virus-like particles 3D reconstruction using DLET

The filoviruses Ebolavirus (EBOV) and Marburgvirus cause fatal hemorrhagic fevers in humans and other mammals, known as Ebola virus disease (EVD), with mortality rates approaching 90% (Feldmann and Geisbert, 2011) which makes it listed as world health organization risk group 4 pathogen. Ebola virus caused the 2013 – 2015 epidemic in West Africa, which has resulted in at least 11,276 confirmed deaths and 27,678 suspected cases as of 12 July 2015 (WHO, 2015). Consequently, considerable effort is focused on developing therapeutics and vaccines to prevent infections.

4.6.1 Motivation

EBOV infections begins with the attachment the glycoprotein (GP), that is located at the EBOV envelope, to the target cell surfaces (Chandran et al., 2005; Clercq, 2015). Understanding the structural information of GP is of vital interest

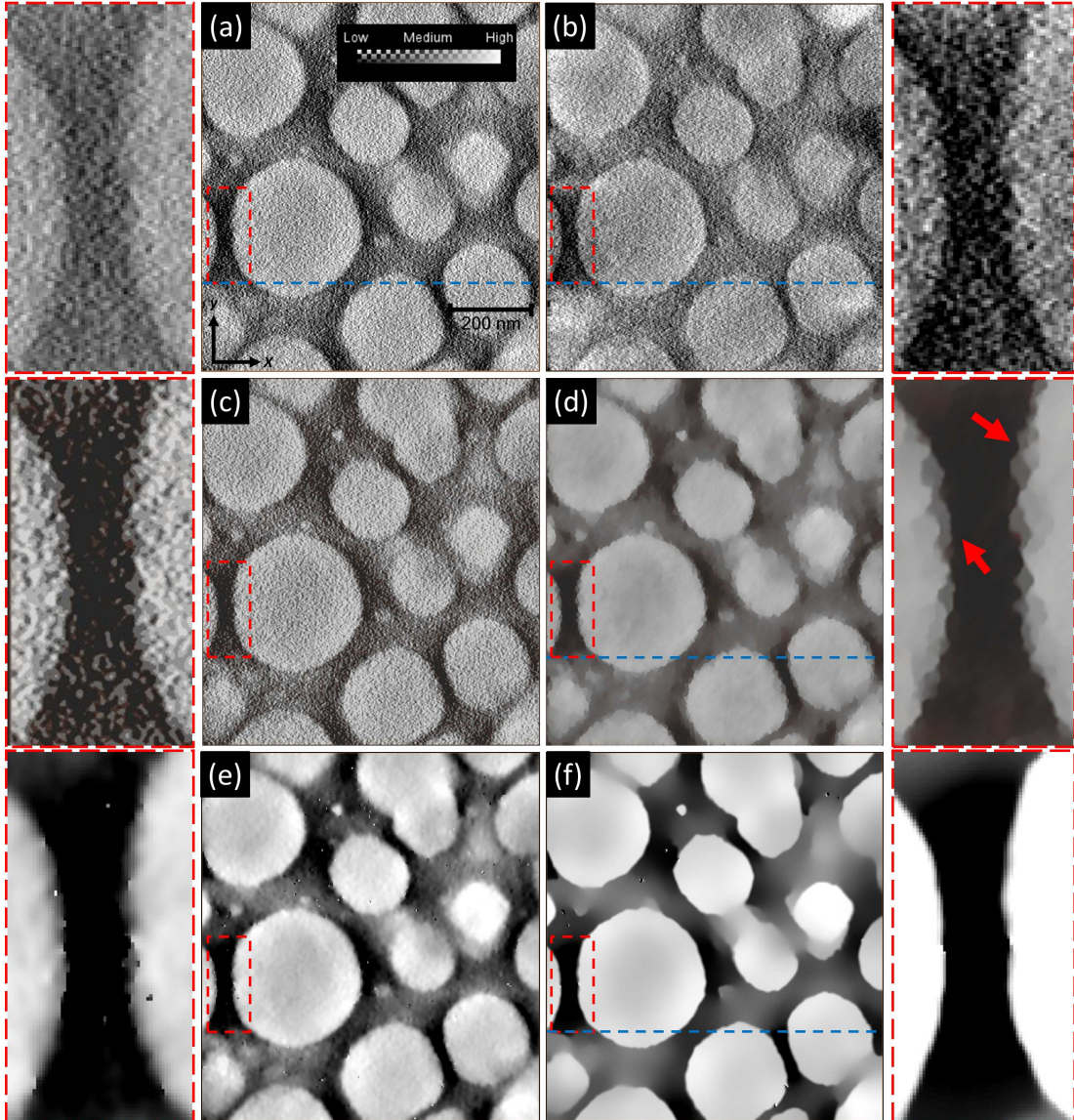


Figure 4.20 | Reconstructions of solar cells PTB7:PC₇₁BM polymer blend from the EFTEM tomography tilt series of Fig.4.15. (a and b) Orthoslices through WBP and SIRT reconstructions, respectively. (c and d) Orthoslices through CSTV reconstructions with $\lambda_{l1} = 10, 20$, respectively and $\lambda_{TV} = 10$ for both. (e and f) Orthoslices through DLET reconstructions with $\epsilon = 2.5 \times 10^5$ and 1.3×10^4 , respectively.

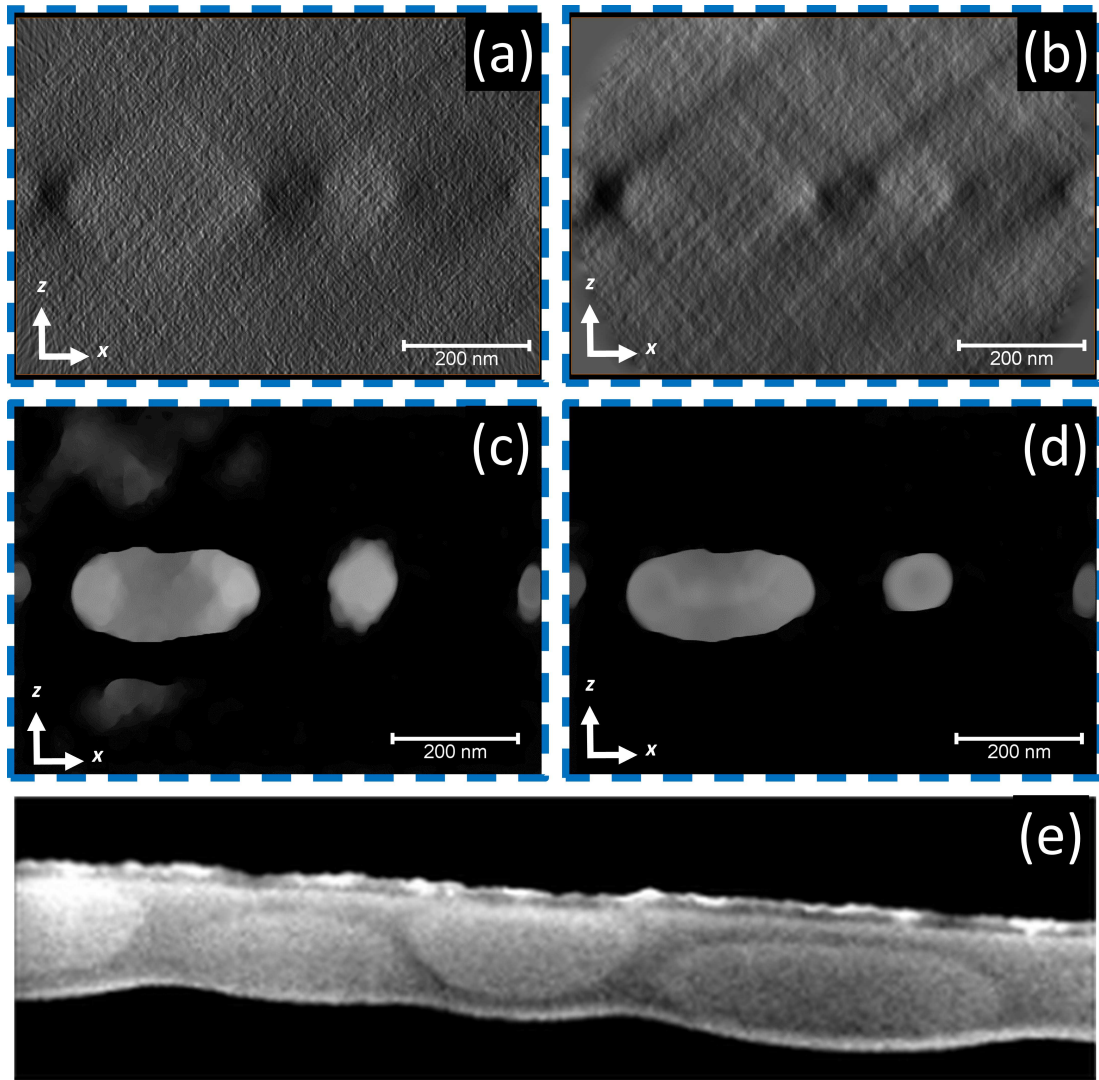


Figure 4.21 | Cross-sectional slices, (a and b) XZ Orthoslices through the dotted blue line indicated on WBP and SIRT reconstructions in Fig.4.20 (a and b), respectively. (c) XZ Orthoslice through the dotted blue line indicated on the CSTV reconstruction in Fig.4.20(c). (d) XZ Orthoslice through the dotted blue line indicated on the DLET reconstruction in Fig.4.20(d). (e) cross-sectional TEM image of the PTB7:PC₇₁BM photoactive layer of the solar cell sample. (See [Alekseev et al., 2015](#), Fig. S1) for other views.

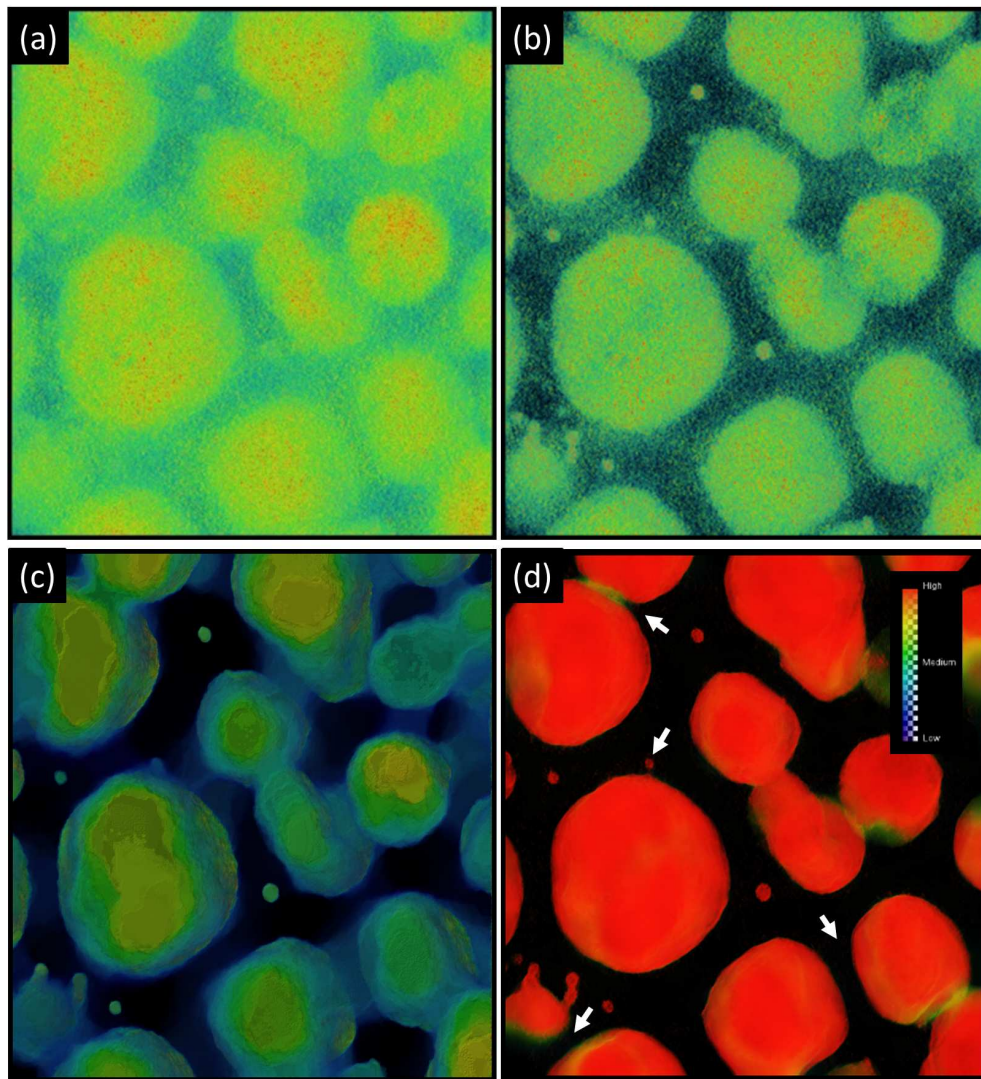


Figure 4.22 | Direct Volume Rendering - 3D perspective view voxel Z-projections of (a) WBP, (b) SIRT, (c) CSTV and (d) DLET.

for improved understanding of the principles of infection strategies to combat the viral infection and is of fundamental interest for EBOV vaccine development (Tran et al., 2014).

Cryo-electron tomography (cryo-ET) (Frank, 2010, chapter 4) is an effective tool for obtaining structural details of complex viral component organization at sub-nanometer resolution. Specifically, concerning EBOV, cryo-ET can be used for studying the arrangement and structural information of the internal viral components of EBOV such as the glycoprotein (GP) spikes on the surface of EBOV which are the target of multiple neutralising antibodies (Qiu et al., 2012).

To determine the three-dimensional structure of glycoprotein in viruses, the

procedure starts with Fiducial-based reconstruction of tomograms using weighted back-projection or SIRT techniques. Following this, single particle data analysis methods can be applied to individual virions to segment the tomograms and pick the GP spikes. Alignment, classification and 3D averaging of the extracted spike volumes can be performed using methods similar to (Bartesaghi et al., 2008) which will result in final density maps from the raw spike images.

However, the final density maps quality is effected by many factors, mainly the reconstruction techniques used. Constructing a tomogram using traditional methods (such as, WBP or SIRT) still suffers from distortion (especially the missing wedge artifacts) due to the limited range of angles sampled. Also, specifically for tomography on sensitive biological materials, low signal-to-noise ratio is a problem due to the need to limit the electron dose over the entire tilt series, resulting in noisy 3D representations as can be seen in Fig.4.23, Fig.4.23(b) and Fig.4.24(b).

This can benefit from compressed sensing reconstruction techniques (such as DLET) and increase the fidelity of tomograms. This work present a visual assignment between tomograms that was constructed using traditional SIRT and the DLET method.

4.6.2 Experimental

Two cryo-tilt series are reconstructed. Both was acquired at approximately 2° intervals from $\pm 60^\circ$ of an Ebola entry-competent virus-like particles (Ebola-VLPs) and published previously by Tran et al. (2014). Automatic fiducial-based alignment of datasets was performed using IMOD software and then reconstructed using DLET algorithm (AlAfeef et al., 2014a). These results are compared to a 3D reconstruction of the same datasets obtained using SIRT algorithm.

4.6.3 Results and discussion

Figure 4.23 shows a comparison between SIRT and DLET for reconstruction ¹ using tilt series 1. In Fig 4.24, DLET gives a noticeable much clearer visibility of the details of the virus and its morphology, including the clearly visible GP spikes

¹Please note that this and the subsequent figure are produced without any segmentation to show the raw results of the reconstruction and to emphasise the clear difference between the results of the two methods.

surrounding particles. Figure 4.24 shows a volume rendering of reconstruction from a second tilt series. Here the DLET shows a clearer reconstruction with a significant decrease of reconstruction noise.

Consequently, this case study shows that the use of this dictionary-based reconstruction algorithm gives major benefits for the reconstruction the 3D volume of viruses from ET datasets of limited tilt range, relatively low signal to noise, and low contrast levels. It is anticipated that the application of this technique will present major advantages in discerning the nanoscale details of virus structure and infection behaviour when being integrated in the cryo-electron tomography and subtomogram averaging of GP spikes procedures (e.g. [Tran et al., 2012](#)) compared to established tomographic reconstruction algorithms.

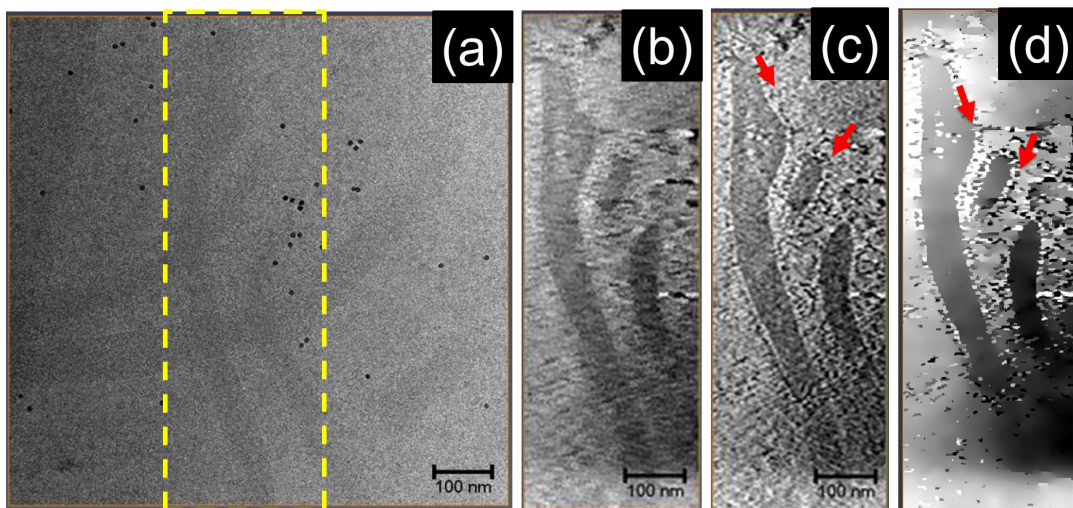


Figure 4.23 | a) Projection at 0° of Ebola-VLP b)XY-Orthoslice obtained through the constructed volume using SIRT, c) DLET with error tolerance $\epsilon = 2 \times 10^{-6}$ and d) DLET with error tolerance $\epsilon = 3 \times 10^{-4}$. The GP spikes are clearly visible surrounding particles as indicated by arrows in (c) and (d).

4.7 Conclusion

This chapter address the ET reconstruction problem, where a tomogram is being reconstructed from an undersampled noisy tilt-series. A novel ET reconstruction method was developed. This new method was named dictionary learning electron tomography (DLET). In DLET, the ET reconstruction was enhanced by

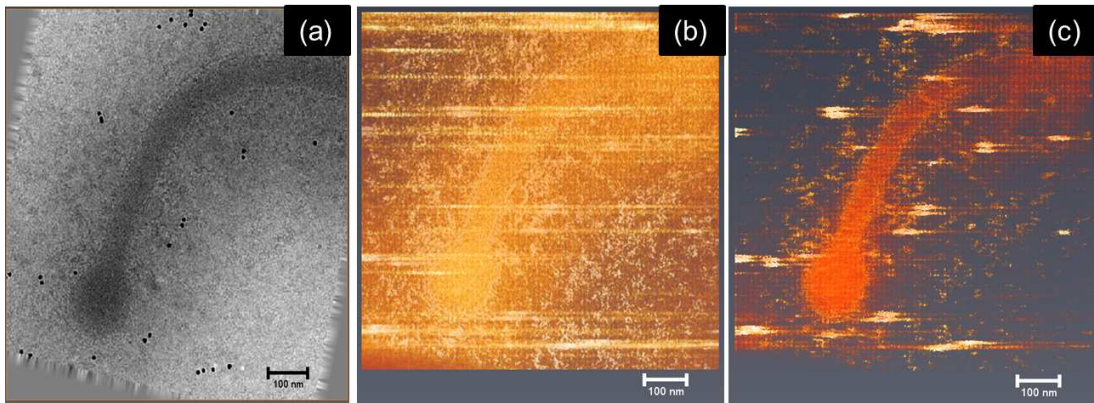


Figure 4.24 | a) Projection image at 0° of Ebola-VLP and gold fiducial markers. The other figures show volume rendering of reconstructed 3D map using (b) SIRT and (c) DLET. Noise and smearing due to markers is reduced in (c).

introducing prior knowledge about the specimen during the reconstruction process. The prior-knowledge approach was based on the mathematical theory of compressed sensing (CS). The approach taken is based on sparse and redundant representations in a way that incorporates prior information through trained dictionaries. The dictionary is learned during the reconstruction process in a way that describes the underlying image content effectively and leads to a sparser representation. The DLET technique was tested using simulated phantoms and experimental data that are known to be difficult to reconstruct using traditional (non-sparse) techniques such as the well-used Total Variation (TV) method in compressed sensing. Reconstruction results validate its efficiency in both noiseless and noisy cases and yield an improved reconstruction quality with fast convergence. The improvement is compared with other techniques that are based on fixed sparsifying transforms in ET and with the conventional algorithms. The proposed method enables the recovery of high-fidelity information without the need to worry about what sparsifying transform to select or whether the images used strictly following the pre-conditions of a certain transform (e.g. strictly piecewise constant for TV). This can also avoid artifacts that can be introduced by specific sparsifying transforms (e.g. staircase artifacts from TV).

”
Nature composes some of her loveliest music for
”
the microscope

Theodore Roszak, *Where the Wasteland Ends*,
1972.

5

Chemically sensitive electron tomography using DLET

IN principle, ET is applicable using any imaging mode that fulfills the projection requirement such that the signal must show, at least, a monotonic relationship with some function of the physical property of the sample (Hawkes, 2006). This condition is approximately fulfilled for mass-thickness contrast in bright field TEM of amorphous biological specimens, and high angle annular dark field (HAADF) STEM imaging of thin specimens. Consequently, both imaging techniques have been widely used in ET. Recently, ET has been performed using electron energy loss spectroscopy (EELS) in the STEM, to achieve a chemically sensitive 3D reconstruction which opens the door for additional possibilities for studying detailed chemistry. Early studies have already shown the feasibility of EELS-STEM tomography (Jarausch et al., 2009; Rebled et al., 2011; Yedra et al., 2012a,b, 2014). Nevertheless, EELS suffers significantly from multiple scattering,

especially for thicker specimens, and this makes the background-subtracted edge signal a non-linear function of thickness, which leads to reconstruction artefacts.

In this chapter, linear chemically sensitive tomography is performed on nanoparticles of an industrially important material, using a probe corrected STEM with an electron spectroscopy system that is equipped with DualEELS capability. Using DualEELS, the low- and high-loss EELS signals can be simultaneously recorded for each pixel in a spectrum image. This allows the subsequent deconvolution of the multiple scattering out of the high-loss signal, resulting in edges with integrated intensities that have a clear linear relationship to thickness. The processed EELS maps are then aligned using a feature-based alignment method and reconstructed using the SIRT and the DLET methods, followed by quantitative analysis of the results.

5.1 Introduction

Recently, ET has been performed using spectroscopic signals, including X-ray spectroscopy, energy-filtered TEM (EFTEM), and electron energy loss spectroscopy (EELS) in the STEM, to achieve a chemically sensitive 3D reconstruction (Jarausch et al., 2009; Yedra et al., 2012b). Additionally, low-loss EELS has recently been used to allow a 3D reconstruction of plasmon modes on silver nanocubes (Nicoletti et al., 2013). While X-rays and EFTEM mainly allow the mapping of elemental contents; core-loss EELS offers additional possibilities for studying detailed chemistry including bonding and valence states using the near-edge structure. Early studies have already shown the feasibility of core-loss EELS-STEM tomography (Jarausch et al., 2009; Yedra et al., 2012a,b). Nevertheless, EELS signals usually contain a significant amount of multiple scattering, except for the thinnest specimens, meaning that the background-subtracted core loss signal is a non-linear function of thickness, which leads to reconstruction artefacts. This also means that the use of single range EELS for 3D reconstruction is only really justifiable for datasets where all projections have a maximum thickness of less than 30% of the mean free path for inelastic scattering (Egerton, 2008, chapter 3).

Extending EELS tomography to thicker specimens requires explicit account be taken of the multiple scattering, which requires that the low loss and core loss signals are simultaneously acquired, i.e. this necessitates the use of DualEELS

(Gubbens et al., 2010b; Scott et al., 2008b) for the data acquisition. The multiple scattering can be dealt with by using either deconvolution (Egerton, 2008, chapter 4) to remove it or modelling (Thomas and Twesten, 2012; Verbeeck and Van-Aert, 2004) to take account of it in the quantification. This latter approach has recently been used by Haberfehlner et al. (2014b) to perform chemically sensitive 3D reconstruction of precipitates in an Al-Si alloy containing Yb.

In principle, the intensity in an EELS edge is given by the equation:

$$I/I_0 = N\sigma \quad (5.1)$$

where I is the intensity for a given energy range above the edge, I_0 is the intensity of the zero loss peak, N is the projected areal density of atoms in the area sampled by the beam and σ is the partial cross-section for the edge of interest for this energy range and for the electron optical parameters used in the experiment (including probe convergence angle, spectrometer collection angle, and primary beam energy). For a constant density material, N will have a linear scaling with thickness and thus, in order to achieve a truly linear relationship between integrated, background-subtracted core-loss signals and thickness, the signal I should be normalised by the intensity present in the zero loss peak I_0 . This normalisation is implicit in the model based approach used by Haberfehlner et al. (2014b) but needs to be performed explicitly if deconvolution, background subtraction and numerical integration of edge intensity are to be used to produce maps for 3-D reconstruction.

This work examines the advantages of using DualEELS for the chemically sensitive reconstruction of vanadium carbide precipitates on an extraction replica prepared from a vanadium microalloyed high manganese steel, as part of an EU RFCS project (Precipitation in High Manganese Steels) using the DLET algorithm for ET. In particular, great emphasis is laid on assessing the reliability of the tomographic reconstruction by comparing results from experimental and simulated tomography dataset calculated from a model particle in the shape of an octahedron.

5.2 Methods

5.2.1 Advanced high strength steels and vanadium allows

High manganese steels are materials with excellent properties in terms of ductility and strength. For automotive applications the formability of these steels is in several cases superior to that of the so called 3^{er} generation steels. To improve crash-behaviour for those applications it is desirable to improve the yield strength and this can be achieved by the precipitation of fine, well-dispersed carbonitrides. In this system, the addition of vanadium is one possible method for precipitating nanoscale carbides. Another issue concerning advanced high strength steels is hydrogen embrittlement. Several publications (e.g., [Depover et al., 2015](#); [Spencer and Duquette, 1998](#); [Szost et al., 2013](#)) suggest the beneficial effect of particles on hydrogen trapping, although the mechanism remains unclear.

5.2.2 Materials and sample preparation

As a suitable test object for experimentation, vanadium carbide particles a carbon extraction replica were used. These particles were extracted from a high manganese steel of composition $22Mn - 0.6C - 0.2V - 0.01N$ (wt.% - Fe - balance) and heat treated at 800° C for 3h to promote precipitation of VC_x . For the extraction the direct carbon replica method was used. In this method, it is necessary to start from an etched sample surface and for that a mirror-polished surface was etched with 2% Nital to reveal the microstructure without damaging the precipitates. This etchant reveals the micro-structure without damaging the precipitates. Then, a carbon film is deposited (30 to 50 nm of thickness) using the Edward E306A coating system. In order to remove the film with the precipitates attached, the film is scarified to obtain a grid of dimension of 3mm and the sample is immersed completely in a nitric acid 20% solution (80 ml of nitric acid and 400 ml of water distilled). This allows the detachment of the square-pieces of carbon replicas. They are then placed in ethanol for rinsing and finally placed on copper grid for TEM examination. After 3h heat treatment relatively large (tens of nm) vanadium carbide particles, with well developed facets are observed. Initial studies have shown that these are often faceted on {111} planes, and that particles appearing approximately octahedral in shape are commonly observed on the replica.

5.2.3 Instrumentation and experiment

The tomography experiment was performed on a JEOL ARM200F scanning transmission electron microscope equipped with a cold field emission gun and operated at 200kV. The probe half-angle was 29 mrad, the probe current was ~ 400 pA and the probe diameter was ~ 1 Å. The acquisition of the datasets and the subsequent processing of tomography data using DualEELS is summarised in Figure 5.1. The EELS spectrum image datasets were recorded using a Gatan GIF Quantum ER using a fast DualEELS mode with a drift tube offset of 150 eV between the low loss and high loss datasets. The collection half angle was 36mrad. The low loss was integrated for 0.000952 s and the high loss for 0.019055 s (i.e. an exposure ratio of 20). The spectrum images were 86 pixels horizontally, but varied in the vertical direction (from 81 – 132 pixels) in order to have sufficient pixels to cover all precipitates of interest (in practice, only a smaller sub-region was used for the reconstruction). Each pixel was 0.99 x 0.99 nm and the total acquisition time for each DualEELS dataset was about 7.5 minutes. The sample was held in a JEOL tomography holder which allows a nominal tilt range of $\pm 80^\circ$, although, in practice, we were limited to a range of approximately -50° to $+50^\circ$ because of shadowing from grid bars on the sample support. Spectrum images were recorded at 10° intervals in this range. Fig. 5.2 shows HAADF-STEM images and EELS elemental maps acquired at different tilt angles, EELS low/core loss spectra from pixels indicated in the projection.

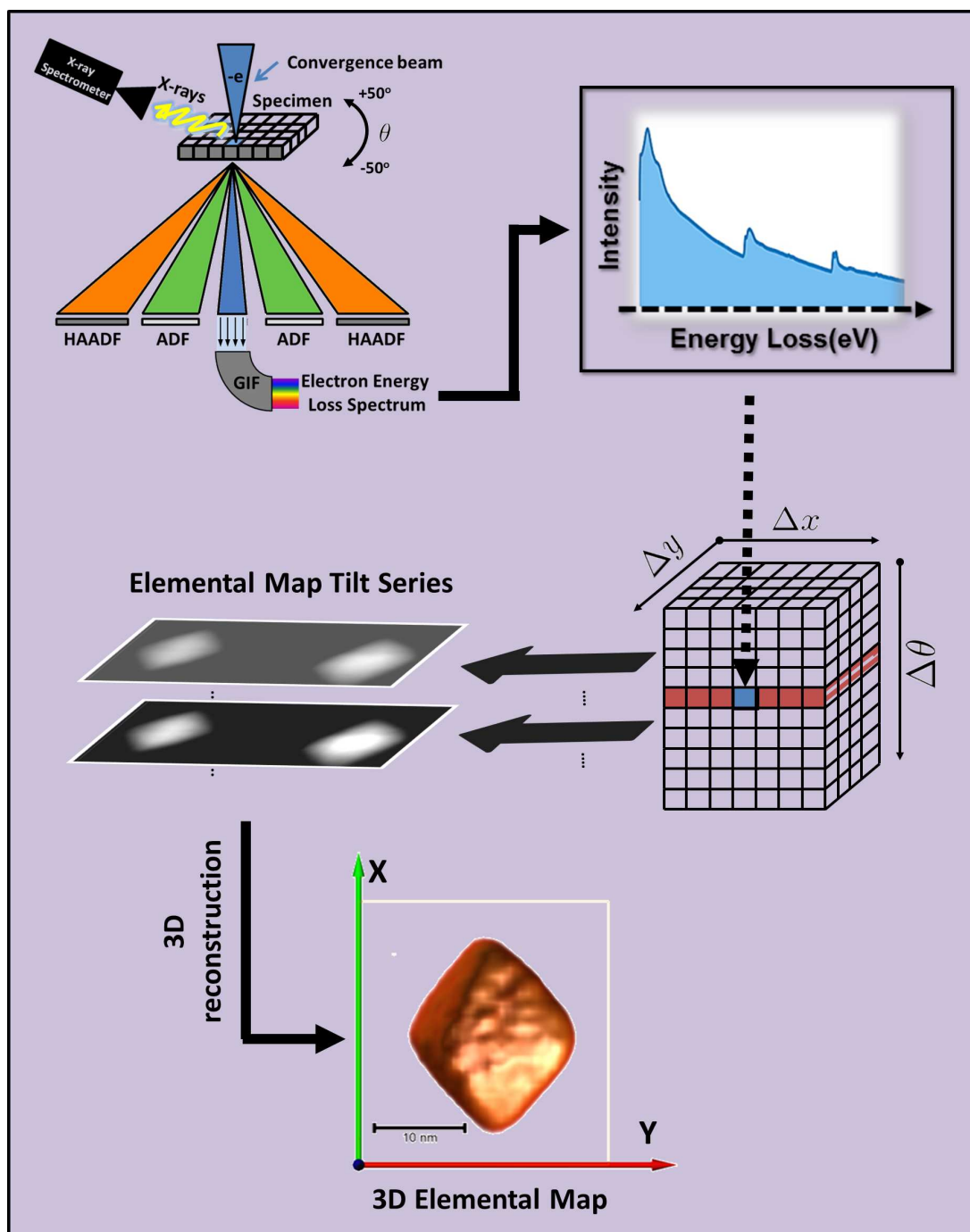


Figure 5.1 | Schematic illustration of tomography using DuallEELS that has been performed in this work. The acquired spectrum-image data set at each tilt in the series is used to generate 2D chemical maps, one for each element under investigation, and thence to reconstruct 3D chemical maps for each element. After [Maign and Twesten \(2009\)](#).

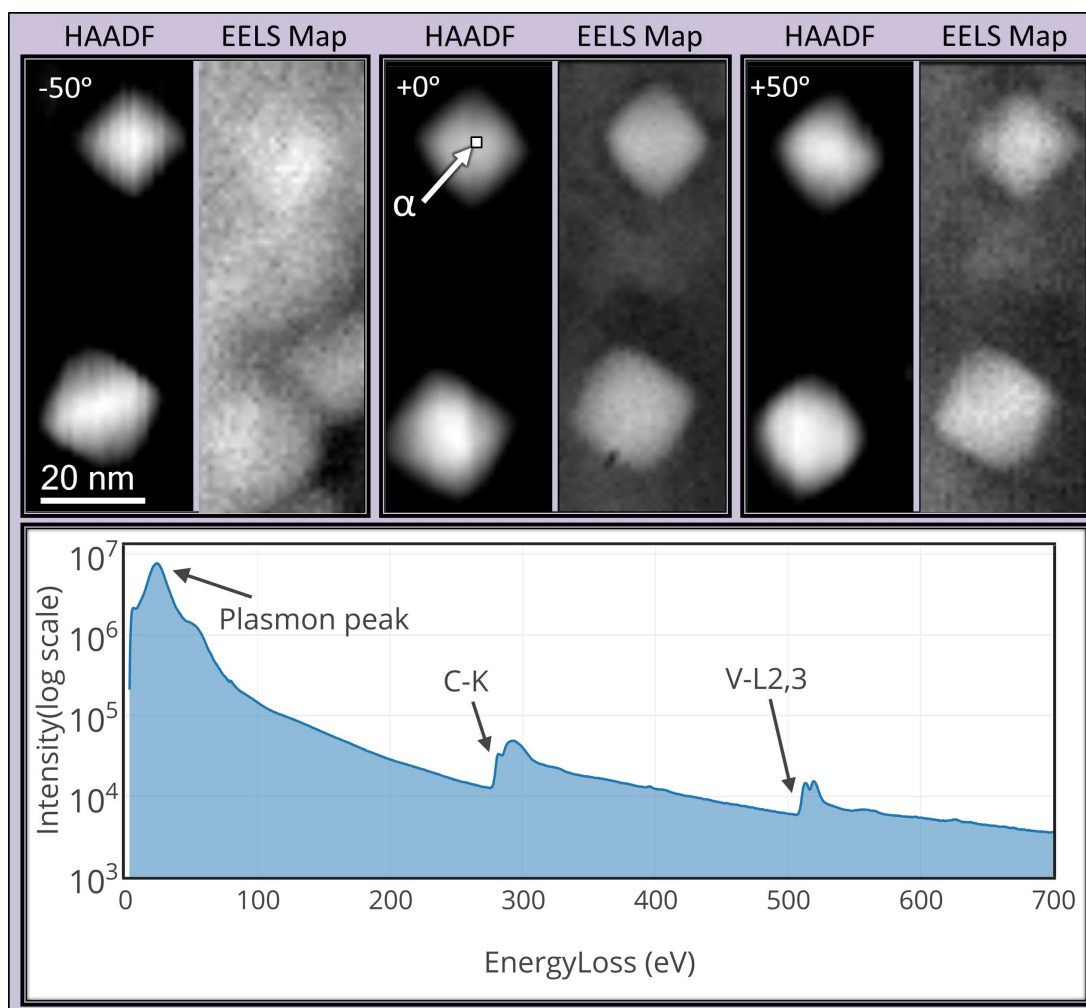


Figure 5.2 | (Top Row) HAADF-STEM projection 2D image and normalised EELS elemental maps of C from the tilt series. (last row) A Fourier-ratio deconvolved EELS spectrum extracted from pixel (α) in the first precipitate, displayed using a log-linear plot.

5.2.4 Post-acquisition procedure

The low loss and high loss spectra were acquired as spectrum images. In a recent publication by [Bobyanko et al. \(2015\)](#), the procedure for the extraction of precipitate signals from a matrix using DualEELS was described. The early stages of this procedure were also applied in the present case: energy alignment, spectrum cropping, subtraction of any stray signal from the low loss spectrum, noise reduction using principal component analysis ([Bosman et al., 2006](#); [Lucas et al., 2013](#); [Lucic et al., 2005](#)), splicing of the low loss and high loss spectra, and Fourier-

log deconvolution to remove the multiple scattering ¹. Following this, vanadium elemental maps were extracted from each spectrum image using background subtraction with a window from 470-505 eV and signal integrated with a window from 505-555 eV. (This energy range is only usable in the absence of any oxygen in the sample, which was the case for this extraction replica). Similarly, for carbon, all maps were produced using a background window from 245-275 eV and a signal window from 280-340 eV. Finally, all maps were normalised by I_0 , the intensity of the zero loss peak, to produce maps that should have a linear relationship of the intensity to the projected atomic content in each pixel.

Fig. 5.2 shows HAADF-STEM images and EELS elemental maps of C acquired at different tilt angles, together with a spliced and deconvolved EELS spectrum (on a log scale) showing both the low loss and core loss regions in a single spectrum from one pixel on a precipitate in the 0° projection. The tilt axis is vertical in the orientation of this figure. It may be noted that the carbon contribution from the support is asymmetric about the 0° tilt position. It was assumed that the carbon replica was not completely flat and that a higher effective angle to the surface normal was seen at -50° than at +50°.

The resulting tilt sequences of projected normalised 2D elemental maps for C and V were then aligned to a common tilting axis and used as the input for the tomographic reconstruction as outlined in Fig. 5.1 (in this case for V). To allow demonstration of the advantages of using deconvoluted data, a sequence of maps was also created in the same way, but without removing the effects of multiple scattering by deconvolution, but still normalising by the division of the edge intensity by I_0 .

To obtain high-quality reconstructed results, accurate alignment is critical before reconstruction. The conventional alignment approach that is commonly used in electron tomography depends on the cross-correlation between neighbouring projections (Frank, 2006a; Guckenberger, 1982). This approach was not accurate in aligning our current data set. Fig.5.3(a) show an XZ slice from SIRT reconstruction of a tilt series that was aligned using cross-correlation method. The tilt axis still suffers from a degree of misalignment; which causes the reconstruction to smear out into 'arcs'.

¹Data processing was performed using Digital Micrograph software. Image acquisition was performed by Dr. Ian MacLaren.

To overcome this limitation, a feature-based alignment method using contour detection and centre of gravity approach was adopted (AlAfeef et al., 2016, Appendix A). The tilt series alignment was performed using the HAADF-STEM images that were acquired simultaneously with the EELS spectra. The alignment process is initiated with the cross-correlated tilt series to decrease degree of freedom. For each tilt, a high-performance contour detector (globalPb) (Arbelaez et al., 2011) was applied to detect the boundary of features in the tilt series in order to calculate the centre of gravity with sub-pixel accuracy. After detecting the boundaries of particles, the tilt series is masked to remove the background pixels, and the weighted centroid of particles in each image is calculated. The resulting centroids are then tracked and treated as virtual markers to generate a model that is used to align the tilt series in IMOD (Mastronarde, 2006). The images are transformed so that they represent projections of particles tilted around the Y axis, as well as to refine the projection angles. This is performed after calculating the rotation, translation, and scaling (magnification) to be applied to each image. Finally, the alignment process was iterated to minimise the re-projection error of virtual markers. ¹ An alternative approach for complex samples can be achieved by using Scale-Invariant Feature Transform (SIFT) (Lowe, 1999) similar to (Han et al., 2014). The absence of the crescent-shaped artifacts in the experimental results in Fig.5.3(b) indicate that this approach provide accurate alignment compared to cross-correlation methods for the dataset in this study.

¹We found that the convergence rate of this approach for our data set was fast and does not differ significantly from the first iteration.

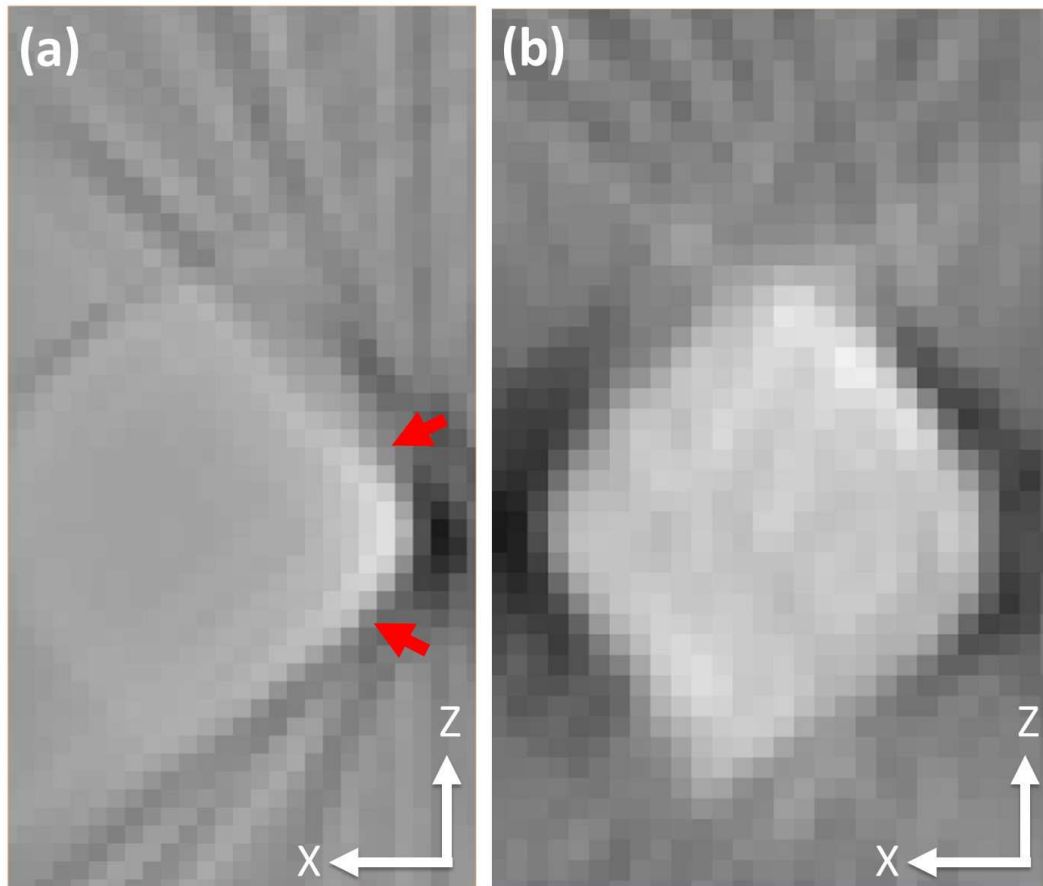


Figure 5.3 | The effect of tilt-axis misalignment, on the reconstruction of a vanadium carbide precipitate. (a) XZ slice from a SIRT Reconstruction of a tilt series that was aligned using a standard cross-correlation method. A distinctive arcing artefact is observed, which is a known signature of misalignment. The curvature of this arcing is dependent on the direction and the magnitude of misalignment. (The interested reader is referred to Fig.11.4 in (Banhart, 2008b) for further clarification). (b) The same slice after using the improved feature-based alignment procedure described in (AlAfeef et al., 2016, Appendix A).

5.2.5 Three dimensional image reconstruction

The reconstruction of 3D elemental maps was performed using SIRT algorithm, as well DLET (Al-Afeef et al., 2016; AlAfeef et al., 2014b, 2015a). SIRT reconstructions were performed using IMOD (Mastronarde, 2006). Determining the optimal iteration number in SIRT is critical and this is usually selected empirically. Large numbers of iterations will produce a solution that is similar to the

weighted back projection algorithm (which can be problematic (Al-Afeef et al., 2016)), while very small iterations will produce less accurate reconstruction and lose important features of the tomogram. In this work, the IMOD guideline (Mastronarde, 2006) was followed which is to select an iteration number in the range 8 – 25. It was found that 15 iterations provided a visually sensible solution.

The DLET parallel implementation was run for 20 iterations with dictionary learning stage performed for 20 iterations. All implementations were executed on Matlab v7.12 (R2013a) installed on a 64-bit Windows 7 operating system with an Intel Core i5 processor running at 3.10 GHz with 24 GB memory and NVIDIA GPU card with 336 cores.

5.2.6 Visualisation

Following the image reconstruction step, the constructed volume was then segmented, to generate triangulated surfaces, and visualised. The segmentation was performed using the Otsu method (Otsu, 1975a) which is an automated thresholding technique to avoid subjective judgment. All visualization performed here were using AMIRA (FEI – Visualization Sciences Group). Orthoslices through reconstructions are shown with linear mapping between the maximum and minimum values of pixel in each image. The labeled y -axis on each orthoslice, is parallel to the tilt axis, the z -axis is parallel to the optic-axis at zero tilt (which is also the missing wedge direction), the x -direction is orthogonal to both. The reconstruction's voxel projection views were generated using the volume-rendering module in AMIRA. Its histogram windows were restricted to only show the true signal from the reconstructed object prevailed over the background intensity. An arithmetic octahedron was fitted to each surface to provide a visual assessment as in Fig.5.5 and Fig.5.7. The fitting strategy was to find a transform A that applies rotations and a uniform scale factor that minimises the root mean square distance (Euclidean measure) between the points on the segmented model surface to the corresponding points on the reference octahedron surface. This was performed using the iterative closest point algorithm (ICP) (Besl and McKay, 1992).

5.3 Simulations and experimental results

A simulation study was performed to support the investigation of the experimental data.

5.3.1 Simulation study: Reconstructions on simulated tilt series from an idealised octahedron

Since the precipitates are expected to approximate to octahedra in shape, a realistic looking octahedral precipitate was computer generated and the imaging process was then simulated upon these particles. The simulated tilt series were obtained taking in to consideration the imaging conditions, such as detector resolution, bit depth and intensity. ET reconstruction was then performed on the simulated tilt series.

5.3.1.1 Generation of simulated octahedral precipitate tilt series:

The simulated test object should have one solid component shaped as a regular octahedron, defined as the shape which is formed by connecting all the face centres of a cube. This will have 8 faces, angles between edges are 90° , and angles between faces meeting at an edge are 70.5° and angles between sides meeting across a point are 109.5° . To simulate the experimental data closely, a 3D model (mesh model) was created using CAD software. This mesh model is then voxelised using (Patil and Ravi, 2005). The voxelisation involves converting geometric objects from their continuous geometric representation into a set of voxels that best approximates the original object. The result is a binary 3D matrix with voxel values of logical 1 to represent the boundary and inside region of 3D object or 0 to represent the background.

This 3D matrix is spatially quantised in a way that simulates what would be an ideal output from the detector of the STEM imaging process (i.e. each octahedron object requires a box of approximately 23^3 pixels to be represented as similar to the real precipitates in the experimental EELS elemental-map tilt series). Fig.5.4(a1-c1) show the simulated octahedra from three orthogonal projections. To simulate the imaging process, the Radon transform for parallel-beam geometry is performed upon the sampled 3D matrix at 10° intervals from $\pm 50^\circ$ rotations. Then, shot and quantisation noise is included in the simulated images.

All simulation was performed using MATLAB (Mathworks Inc.), reconstructed using IMOD (Mastrorade, 2006) and visualised using AMIRA (FEI).

The Radon transform represents the path-length of the rays in the material, which is determined by taking line integrals through the sample between the source and detector to generate the projection image I_{out} . The simulated projections were scaled to a mean value equivalent to the mean of the EELS elemental maps, and subsequently corrupted by shot, Gaussian and quantisation noise to get a low SNR dataset. This should nicely approximate the signal seen by HAADF imaging in the STEM (which should be close to linear for low object thicknesses) or EELS edge intensities, after correction for multiple scattering (which should be linear with thickness).

5.3.1.2 Addition of noise and quantisation

It was assumed that only shot and Gaussian noise are present in the detected intensity. Shot noise originates because the electron quanta reach the detector at irregular intervals. Therefore, the number of electrons detected in a fixed time period will vary, following Poisson statistics. The SNR on each pixel is equal to $\sqrt{I_{out}}$. Gaussian noise with standard deviation ρ was added to the projections, to simulate electronic noise in the amplifier system, resulting in a dataset with lower SNR. The ρ parameter was approximated to mimic the experimental projections.

In any electron detecting system, there is a limited number of possible discrete values of electrons that can be detected. For digital processing, the continuous intensity of detected intensity needs to be converted into a discrete value, (i.e. Quantised). Quantisation is the process of mapping measurements values from a continuous scale to a discrete value. Quantising with a bit depth of L gives 2^L discrete values of intensity that can be assigned. The mapping process between the detected intensity and quantised intensity was assumed to be equal to I_{out} . The formulation for the quantised intensity I_Q detected at each pixel after the addition of noise is:

$$I_Q(\ell, p, \theta) = \lfloor 2^L \frac{P(I_{out}) + \mathcal{N}(I_{out}, \rho)}{I_{in}} \rfloor \quad (5.2)$$

Where $P(x)$ returns a random number taken from a Poisson distribution with a mean (and variance) of x and L is the pixel bit depth and $\mathcal{N}(x, \rho)$ returns a random number taken from a Gaussian distribution with a mean of x and variance

Table 5.1 | Quality metric values of simulation reconstruction in Fig.5.4.

Method/Metric	PSNR	SSIM
SIRT	16.61	29.25%
DLET	19.51	82.26%

of ρ . With the phantom images as the ground truth, the reconstructed simulation was assessed regarding two commonly used metrics: Peak Signal-to-Noise Ratio ¹ (PSNR) (Huynh-Thu and Ghanbari, 2008) and Structural SIMilarity (SSIM) index (Wang et al., 2004). For further details about the PSNR and the SSIM metrics, please refer to section 4.4.1 in chapter 4 of this thesis.

5.3.1.3 Simulation Results

Figure.5.4(a2-c2) shows the SIRT and DLET reconstructions from the simulated 10 projection tilt series of a vanadium carbide octahedron. As can be seen, the SIRT reconstruction obviously suffers from elongation and boundaries blurring in the missing wedge (\mathbf{z}) direction. Also, as expected, it suffers from streaking artifacts due to the limited angular range. These artifacts are obviously reduced in the corresponding DLET reconstruction as can be seen in Fig.5.4 (a3-c3), where it is clear that the DLET reconstruction has accurately recovered the simulated 3D phantom. Also, the denoising capability of the adaptive sparsifying transform in DLET has produced a near uniform intensity across the background. It should further be noted that SIRT orthoslices falsely show a reduced density in the centre of the octahedron, whereas the correct uniform density through the octahedron is reproduced by the DLET algorithm. The quality metrics for the reconstruction (Table 5.1) confirm the effectiveness of the adaptive sparsifying transform.

Figure.5.5 shows the result of fitting the reconstruction results from simulations to an idealised octahedron. The SIRT reconstruction (Fig.5.5a) is clearly elongated in the missing wedge (\mathbf{z} -direction) as indicated by the arrows. This artefact is significantly reduced in the DLET reconstruction as shown in (Fig.5.5b).

¹For further details about the PSNR and SSIM metric, please refer to section 4.4.1 in chapter 4 of this thesis.

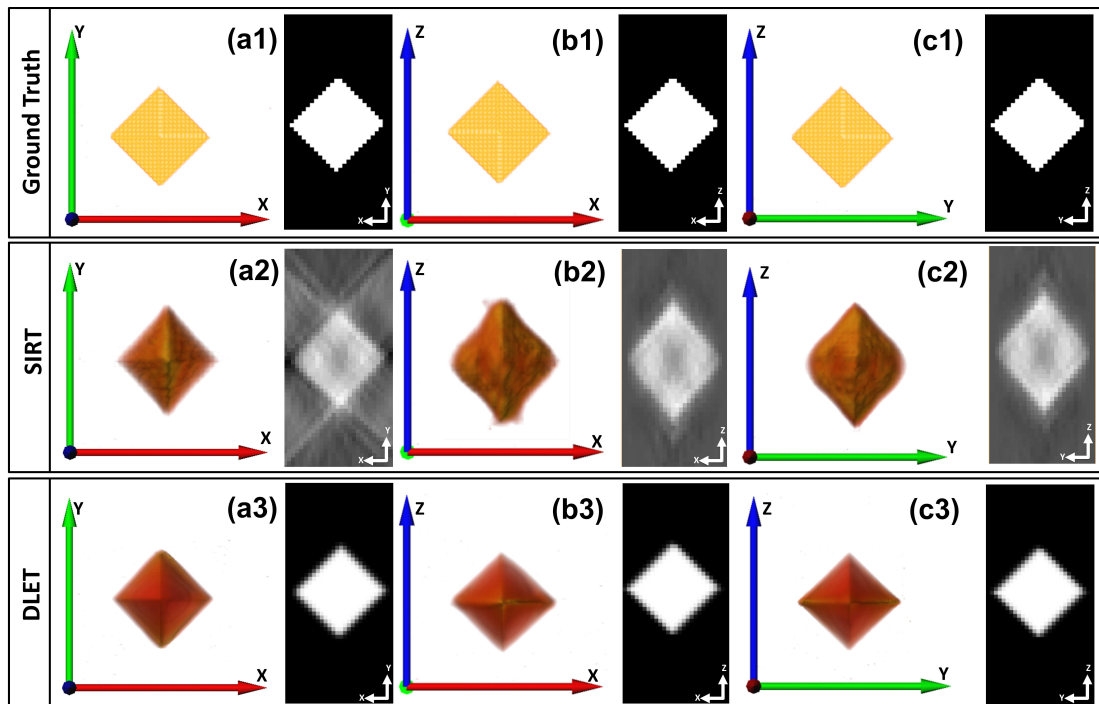


Figure 5.4 | Simulation of 3D reconstruction of an octahedron from a tilt series of 50° to 50° , (a1-c1) volume rendering of the original object along the three principal axes of the octahedron, together with orthoslices taken from the central slice for each the corresponding view (on black backgrounds). (a2-c2) SIRT and (a3-c3) DLET reconstructions from simulated projections, together with their central orthoslices. For visualisation purposes, the image intensities of the orthoslices were enhanced.

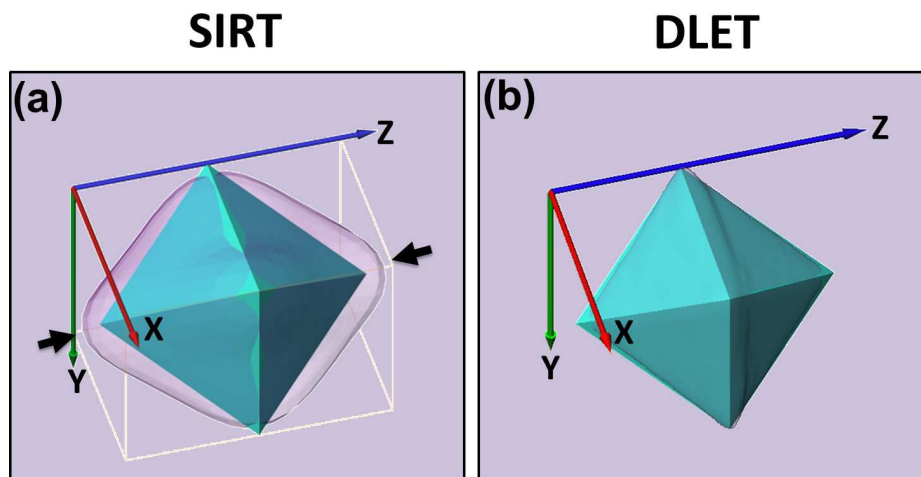


Figure 5.5 | A comparison, of reconstructions of the simulated octahedron VC_x using (a) SIRT and the (b) DLET algorithm showing a comparison to an idealized octahedron. Note that the distortion in the z (missing wedge) direction is much reduced using DLET.

5.3.2 Experimental study: Reconstructions on experimental maps from DualEELS

After extracting 11 different maps from the DualEELS spectrum images of an area containing two precipitates, the 3D vanadium map was reconstructed using both SIRT and DLET. The resulting reconstruction comparison is shown in Fig.5.6.

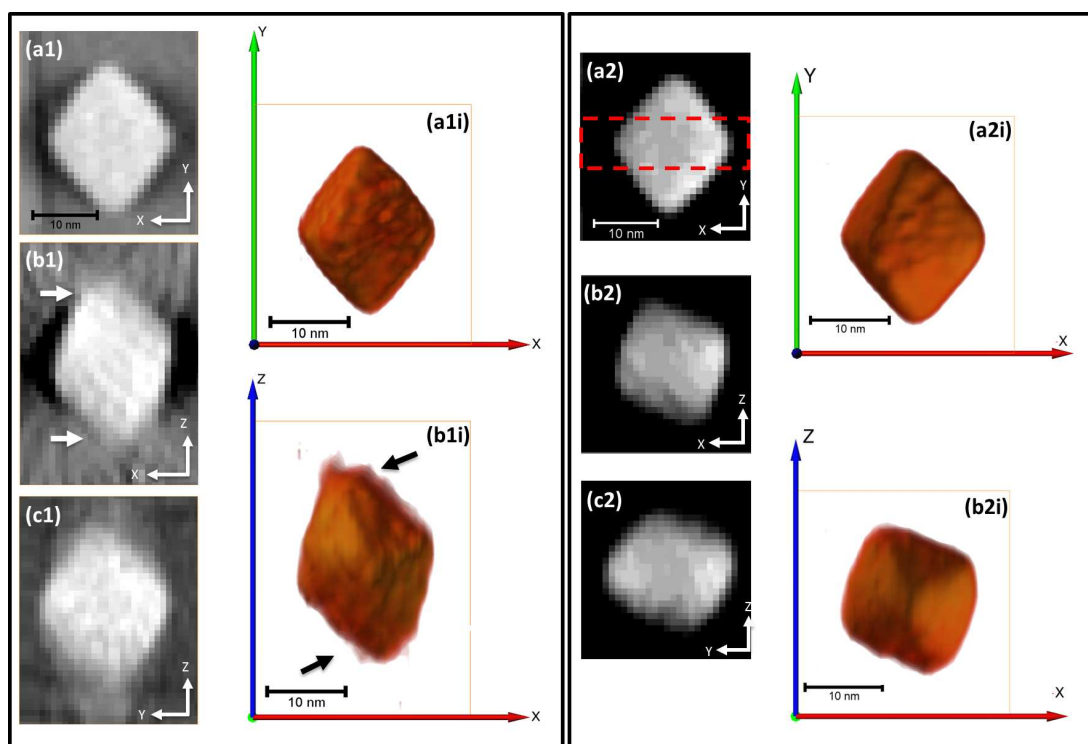


Figure 5.6 | Reconstructions of the Vanadium signal, in VC precipitates from the experimental DualEELS tomography tilt-series. (a1-c1) Orthogonal slices through reconstructions using SIRT. (a1i-b1i) 3D perspective view from which (a1) and (b1) were extracted respectively. (a2-c2) Orthogonal slices through reconstructions using DLET. (a2i-b2i) 3D perspective view from which (a2) and (b2) were extracted, respectively.

OrthoSlices through reconstructed EELS elemental maps of the VC_x precipitate from the $V-L_{2,3}$ signal are shown to the left in 5.6(a1-c1) for SIRT and to the right in 5.6(a2-c2) for DLET. As can be seen, DLET provided a reconstruction with reduced noise and a clear separation between the particles and the background signal. This makes the segmentation step much more straightforward and provides high-fidelity surfaces for quantitative analysis. For comparison, a 3D reconstruction performed on the HAADF signal recorded simultaneously with the collection of the DualEELS spectrum images is shown in Fig.5.8 (a1-c1) are for DLET and (a2-c2) are for SIRT. The HAADF data reconstructs in a very similar manner to the EELS, giving confidence that the reconstruction is reliable.

It is also clear that the use of DLET together with DualEELS to accurately reconstruct a signal that is a linear function of thickness has resulted in well-behaved orthoslices with constant density throughout the thickness (i.e. no cupping arte-

facts (Saghi et al., 2008; Van-den Broek et al., 2012)), as is clearly shown in Fig. 5.9 for both the $V - L_{2,3}$ maps and the HAADF maps. This is of particular importance, and for comparison, a DLET reconstruction is also shown using EELS maps made without deconvolution to remove the effects of plural scattering in the spectra in Fig. 5.10 together with the same profile through the centre of the precipitate. In this case, even in a relatively thin precipitate, there is a subtle, but noticeable cupping artefact. It is anticipated that such artefacts would be far worse in thicker precipitates examined with EELS tomography.

The streaking and blurring present after using SIRT is also absent in the DLET reconstruction. These results accord well with the simulation study, and it is clear that reconstruction using DLET has massively outperformed SIRT for reconstruction fidelity, and the results are particularly impressive considering just 11 projections were used. This really demonstrates the usefulness of this compressed sensing approach to 3D reconstruction of spectroscopic mapping data such data is always likely to be limited in signal to noise by its very nature, since the total possible signal will be limited by either how much radiation dose can be applied to the sample before it is altered significantly or by the available time for data collection.

For a further comparison of SIRT versus DLET, Fig. 5.7 show surface rendered views of segmented 3D EELS elemental map fitted to idealised octahedra, again showing very clearly the massive z -elongation that results from the use of SIRT. just as was predicted in our simulation study above.

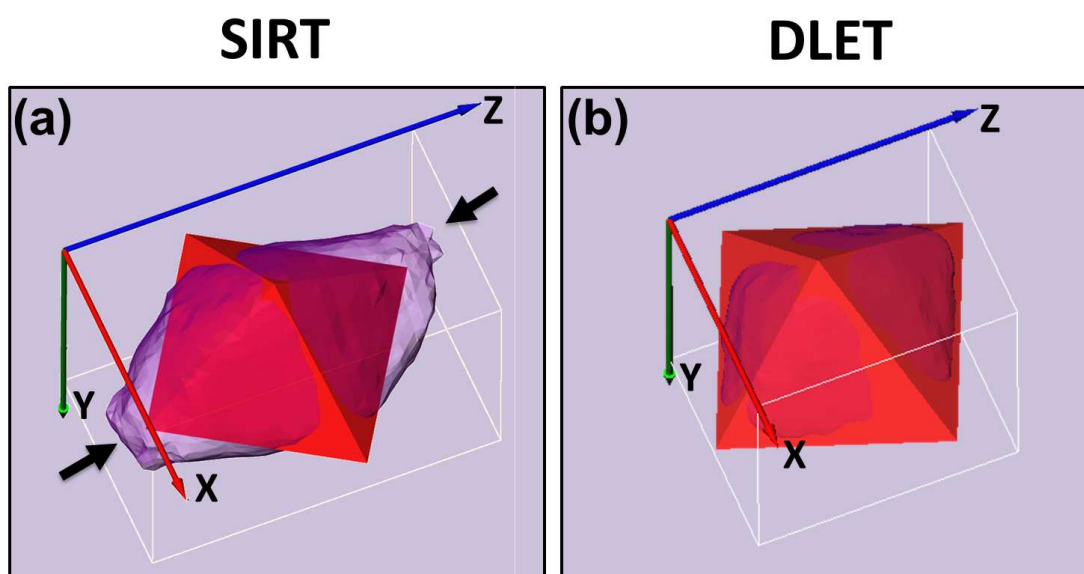


Figure 5.7 | A comparison, of reconstructions of the VC_x precipitate from the V-L_{2,3} signal using (a) SIRT and the (b) DLET algorithm showing a comparison to an idealized octahedron. Note that the distortion in the Z (missing wedge) direction is much reduced using DLET.

Movie Ch5-M01 in Appendix A, shows 360° volume rendering views and the segmented surface of the reconstructed EELS dataset. It should be noted, that whilst the precipitate approximates to an ideal octahedron, corners and edges are not as sharp as in the ideal geometric shape: this is entirely as would be expected since single atoms for corners or lines of single atoms for edges are unlikely to be thermodynamically stable, and it is likely that both corners and edges would be somewhat rounded to minimise surface energy.

With the benefit of the DLET algorithm in combination with EELS maps for C and V from deconvoluted data, it is therefore possible to produce 3D renderings of the actual structure of the carbon extraction replica, as shown in Figure 5.11, showing both the carbon and the partially embedded VC precipitates. A full 3D rendering of this is also shown in Movie Ch5-M02 in Appendix A. Perhaps unsurprisingly, parts of the precipitates are encapsulated within the carbon, whilst other parts protrude beyond it. Moreover, the roughness of the carbon surface is clear, which is a reflection of the surface roughness of the steel that the replica was extracted from after the initial etch. The use of such 3D reconstructions may in future also help to better understand the replica extraction process.

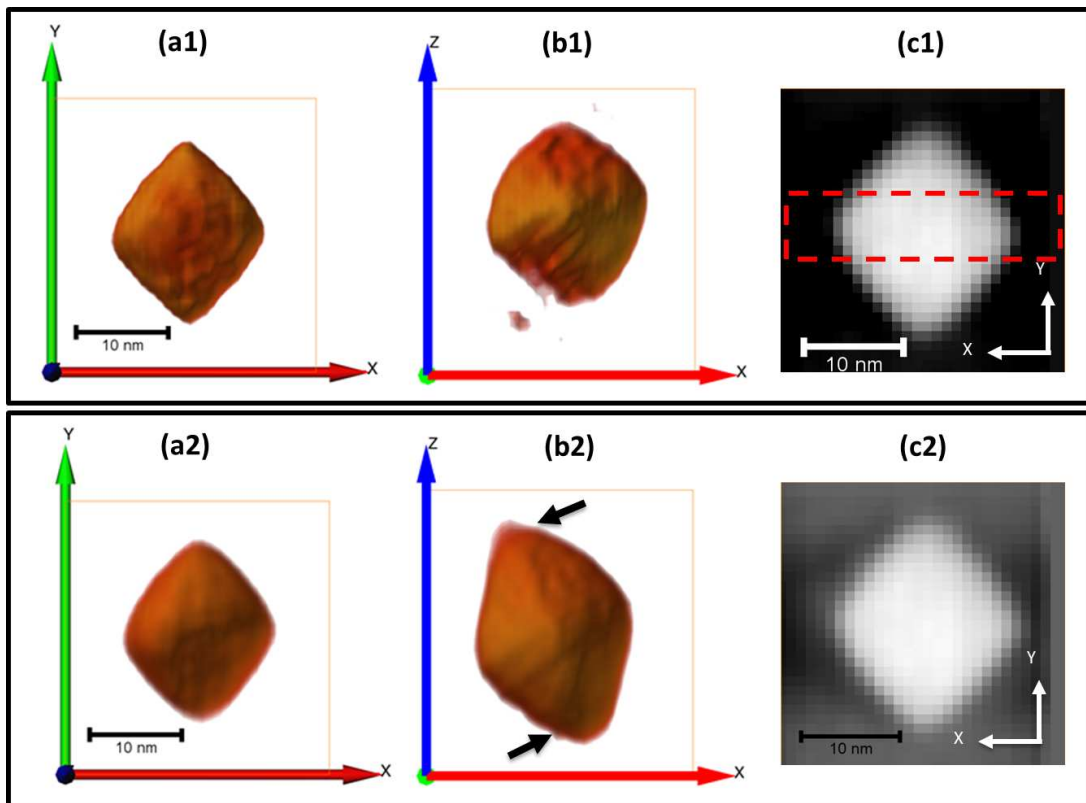


Figure 5.8 | Reconstructions of Vanadium precipitates, from the experimental HAADF signal recorded simultaneously with EELS dataset. (a1-b1) 3D perspective view voxel projections of reconstruction using DLET, (c1) Orthogonal slice through the centre of volume in a1. (a2-b2) 3D perspective view voxel projections of reconstruction using SIRT, (c2) Orthogonal slice through the centre of volume in a2.

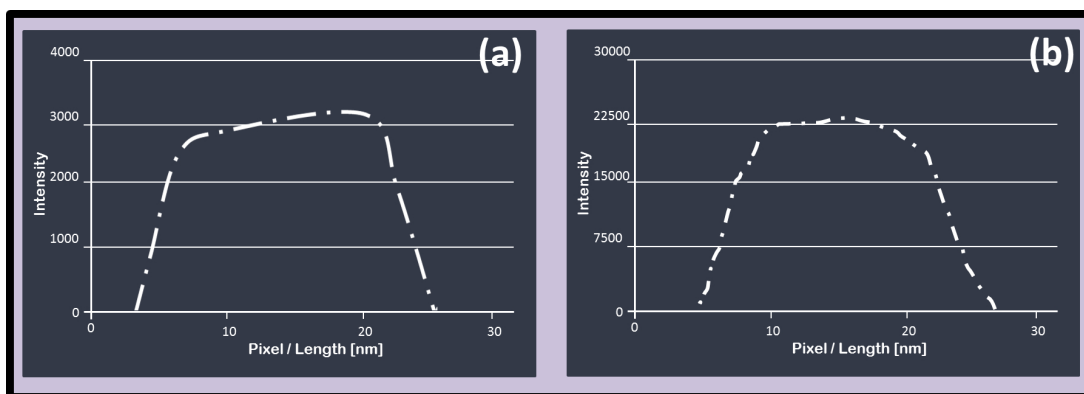


Figure 5.9 | Averaged line profile, through the region of the orthoslices between the red dotted lines indicated in (a) Fig.6a2, which is a DLET reconstruction of EELS elemental maps, and (b) Fig.5.8-c1, which is a DLET reconstruction of HAADF tilt series. Neither show any cupping artifacts.

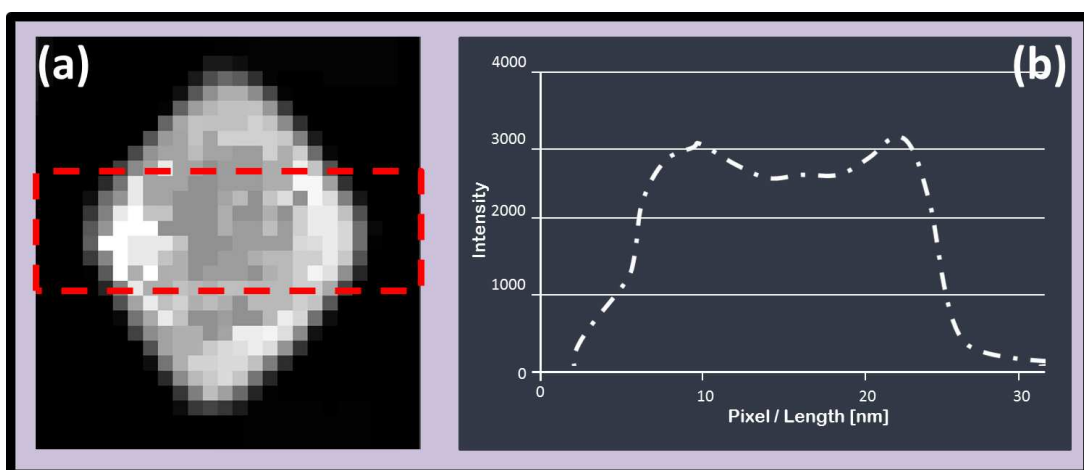


Figure 5.10 | Cupping artefacts resulting from omitting deconvolution to remove multiple scattering from the EELS data (a) Orthogonal slice through the centre of the DLET 3D reconstruction from the raw normalised V-L_{2,3} signal (i.e. without applying deconvolution), (b) Average Line profile integrated vertically through the red dotted area indicated in (a).

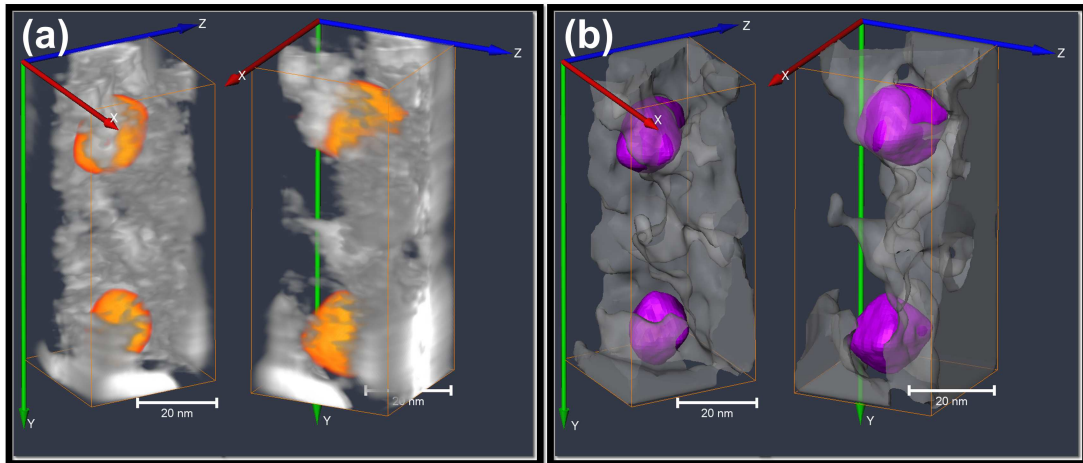


Figure 5.11 | (a) Volume rendered views of the combined volume resulted from reconstructions of Vanadium Maps and Carbon maps. (b) Surface rendered views of the segmented volume of (a).

5.4 Conclusion

The originality of this chapter lays in showing the importance of using DualEELS to generate EELS maps without multiple scattering for generating correct 3D reconstruction of the chemistry of materials using EELS. This, when combined with the DLET algorithm, is shown in both simulation and experiment to do an excellent job of reconstructing the 3D shape of octahedral vanadium carbide precipitates. These are shown to deviate slightly from pure octahedra in reality, but the use of the DLET algorithm was found to be important for quantitative measures since the SIRT algorithm distorts the shape significantly in the missing wedge (z) direction.

This work could easily be extended to encompass changes in near-edge EELS fine structure in order to produce 3D views of chemical form or bonding in nanostructured materials.

”
The life and soul of science is its practical application”

Lord Kelvin, Electrical Units of Measurement, 1883.

”
It is only in the microscope that our life looks so big”

Arthur Schopenhauer, 1788-1860.

6

Further applications of electron tomography using DLET

THIS chapter discuss the general application of DLET algorithm for characterising the 3D morphology of two samples in material and biological sciences.

6.1 Acetonema longum bacteria

Bacteria are very diverse organisms that are able of surviving nearly anywhere on the planet. They show a variety of different cell morphologies, and some are capable of sporulation which can produce dormant spores that can live for a long periods in harsh environmental conditions.

Many types of bacteria have been studied extensively over the past decades in many diverse areas, however, even in well-studied model bacteria, there still

many fundamental questions remain to be answered (Vollmer, 2012): how do bacteria extend their envelope layers during cell division? How do cell growth and envelope growth coordinate? How the cell shape of bacteria is sustained while the stress-bearing peptidoglycan layer is enlarged? How do bacteria achieve major reorganisation of the cell wall during differentiation when forming spore? Also, taking into consideration the theory of evolution where all species evolved from a common ancestral cell, an important question arise: how have these different cell-envelope architectures evolved?

Electron cryo-tomography (ECT) is an indispensable tool for revealing the answers of many of the remaining fundamental questions about bacteria. ECT allows thin samples (such as small bacterial cells) to be imaged in 3D in a nearly native state to macromolecular resolution (Tocheva et al., 2010). In ECT, cells are imaged in a vitreous, "frozen-hydrated" state in a cryo-transmission electron microscope (cryo-TEM) at low temperature (typically $< -180^{\circ}\text{C}$). A tilt series of images is then collected through the sample which is then reconstructed to obtain the 3D-tomogram. ECT is well known for providing higher quality 3D-imaging and for the preserving important details better than conventional approaches such as chemical fixing, dehydration, plastic embedding, sectioning, and staining of the samples which can introduce misleading artifacts (Pilhofer et al., 2010). ECT has been used to image different types of bacterial cells (e.g., Oikonomou and Jensen, 2016; Tocheva et al., 2010).

6.1.1 Background and motivation

Acetonema longum (*A. longum*) is a Gram-negative (double-membraned) bacterium that is interesting from three standpoints: First, it provides important clues to the possible origin of the second membrane typical of Gram-negative bacteria. Secondly, it is a small cell bacterium that is able to sporulate. Sporulation has been well studied in other type of bacterium (such as *B. subtilis*) (Kane and Breznak, 1991), However, such bacterium cells are relatively large, which makes it difficult to make an electron transparent sample to achieve high resolution imaging. *A. longum* circumvented these disadvantages as the cells are somewhat smaller which provides a unique opportunity to study the biology of membrane generation during sporulation. Third, *A. longum* contains microcompartments (Tocheva et al., 2014). It is widely thought that the main function of such structures is to isolate certain biochemical reactions within the cytoplasm.

The morphology, contents, and functions of these microcompartments are active areas of research (Tocheva et al., 2014, 2011).

In this study, a cryoTEM tilt series of *A. longum* bacteria cells is reconstructed using DLET and compared to results from the conventional SIRT algorithm.

6.1.2 Experimental procedure and results

The cells were prepared¹ in a near-native, frozen-hydrated state without staining, dehydration or fixation artefacts and the cells then imaged as described by Tocheva et al. (2011). Single axis tilt series were collected with an angular step of 1° in the range $\pm 60^\circ$ (a total of 121 images) using a total dose of $200 e/\text{\AA}^2$, a resolution of 1 nm in bright field TEM mode with a defocus of $10 \mu\text{m}$ on a 300-kV TEM equipped with an energy filter. Figure 6.1 shows an example image from the acquired tilt series at 0° tilt. The dataset was then reconstructed using both the SIRT and DLET algorithms (Fig. Figure 6.2). Segmentation of the microcompartment (in Fig. 6.4) was performed using Amira (FEI) using Otsu's automated thresholding module to represent a 3D surface of the whole microcompartment. The surface was additionally smoothed for visual representation.

Figure 6.2(a), shows an orthogonal slice through the SIRT reconstruction while Figure 6.2(b) is of the DLET reconstruction. As can be seen, the DLET results are of a higher contrast and a reduced noise which enables automated segmentation of the microcompartment (as in Fig. 6.4). This advantage helps to produce higher quality segmentation results with less labour and a less subjective bias from the operator.

¹The preparation and imaging of the *A. longum* was performed by Grant J. Jensen, Professor of Biology, Caltech.

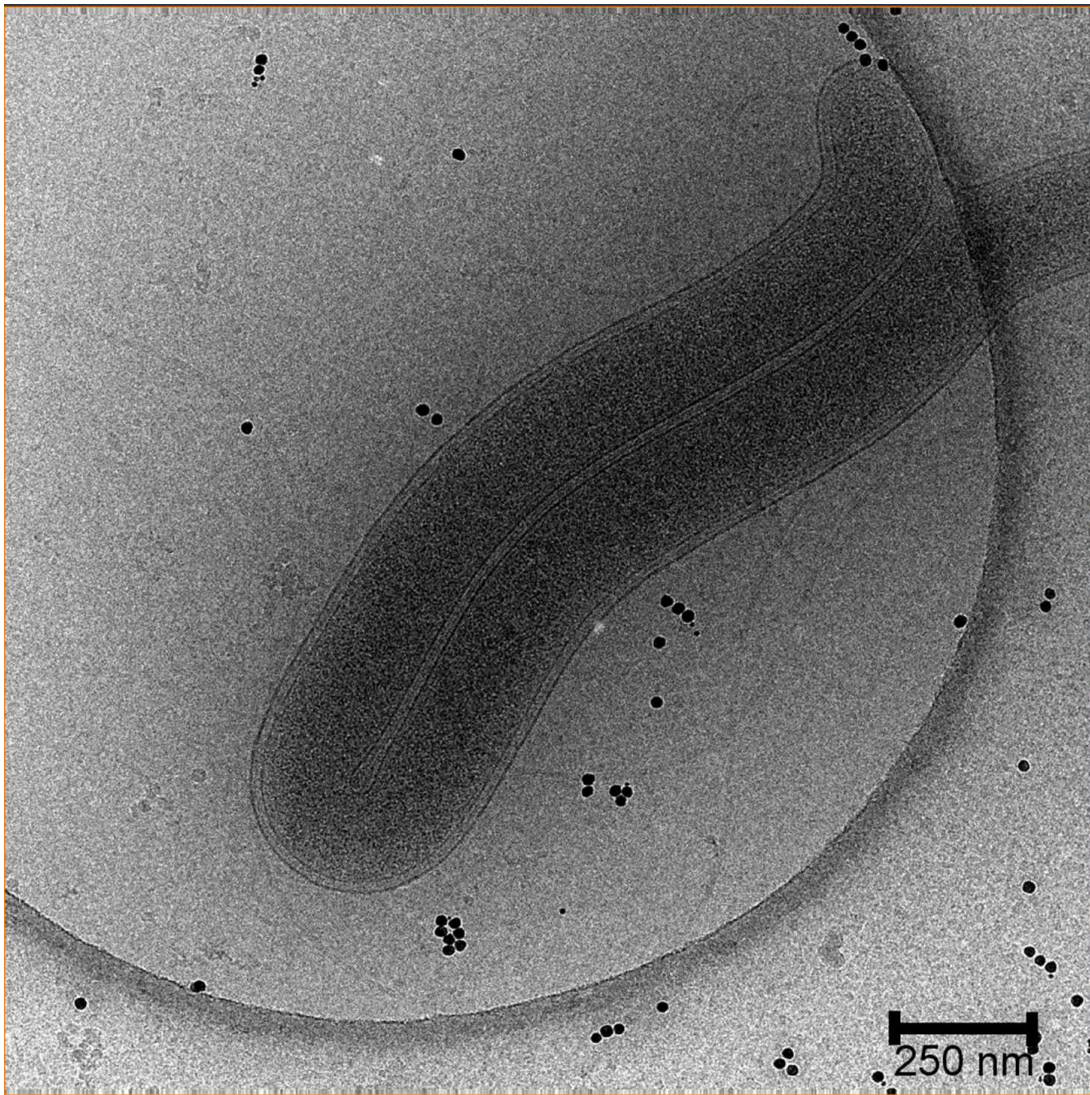


Figure 6.1 | Example of cryoTEM tomography tilt-series projection of *Acetone longum* bacteria cells acquired at 0° degree tilt.

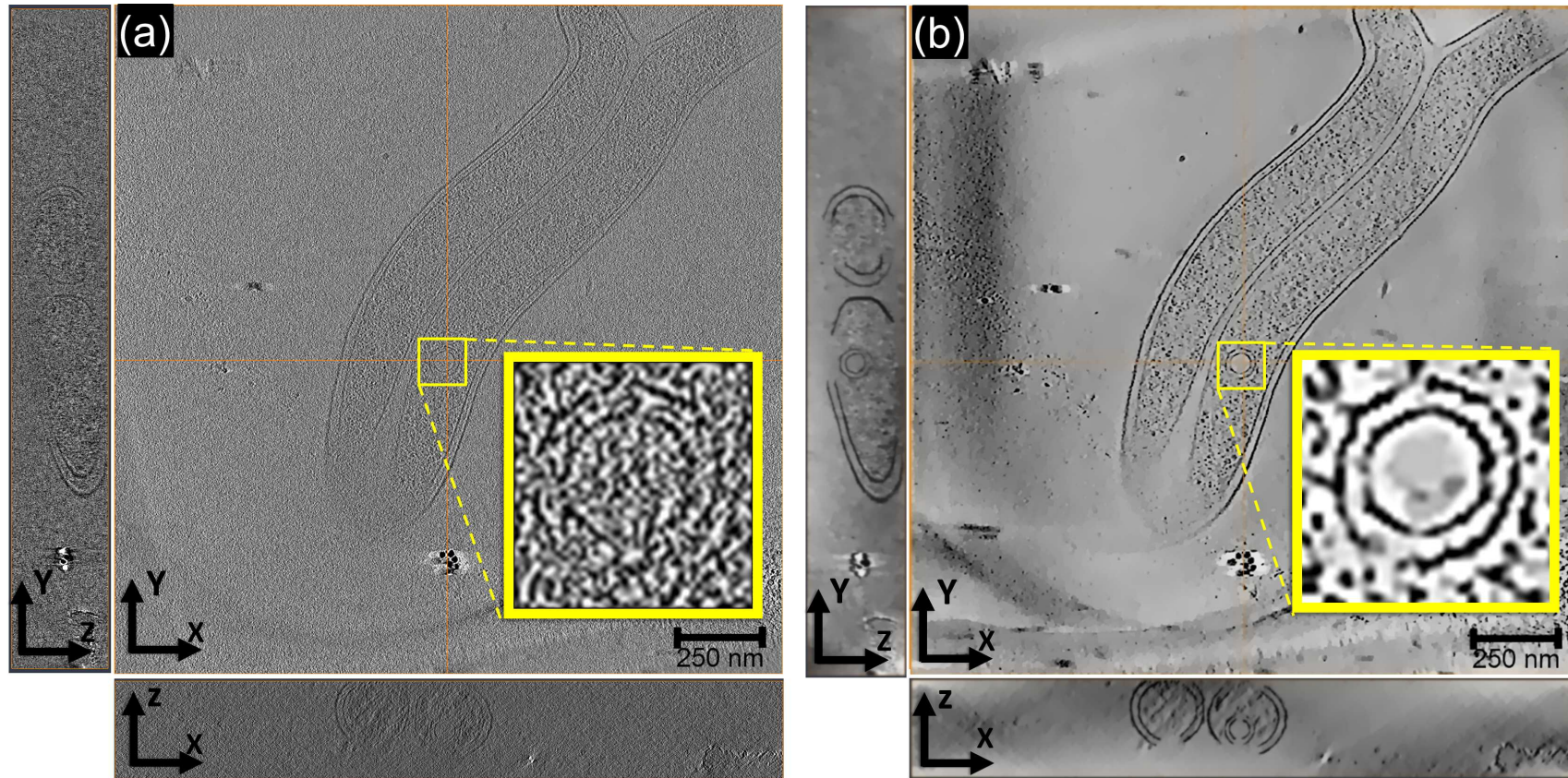


Figure 6.2 | Visual Assessment of the *A. longum* reconstruction from the full tilt series (a total of 121 images, angular step of 1° between $\pm 60^\circ$). The orthoslices were taken from the centre of the (a) SIRT and (b) DLET reconstruction. Both the z-x and y-z slices, were taken in the position indicated by the horizontal, vertical lines respectively, as indicated in the x-y slides. The the x-direction is perpendicular to the tilt axis and the z-direction is the direction of the missing wedge. For consistent comparison, the intensity mapping in each orthoslice is presented with a linear mapping between their maximum and minimum pixel values. Zoomed areas were further enhanced.

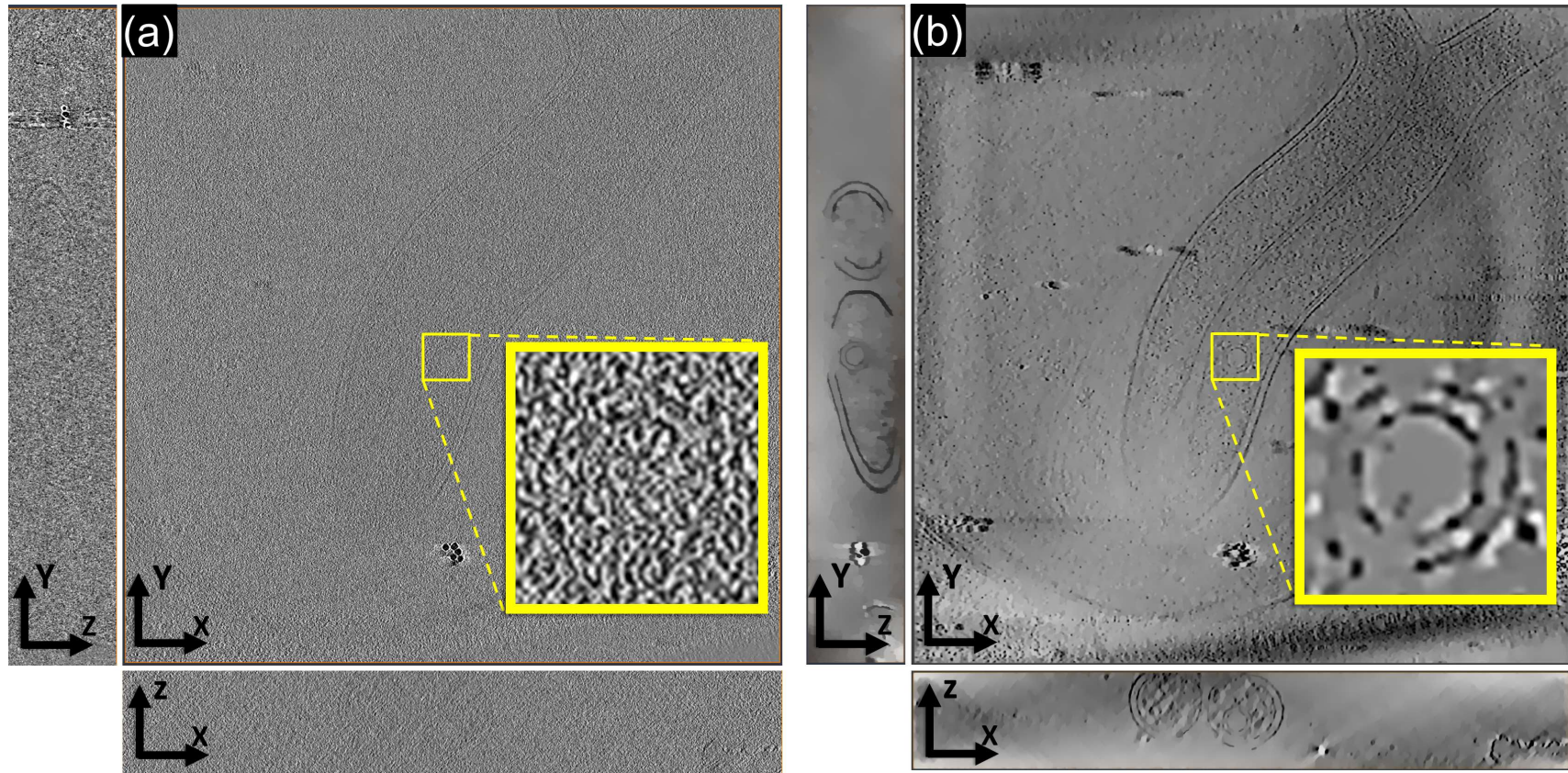


Figure 6.3 | Visual Assessment of the *A. longum* reconstruction from the full tilt series (a total of 25 images, angular step of 5° between $\pm 60^\circ$). The orthoslices were taken from the centre of the (a) SIRT and (b) DLET reconstruction. Both the z-x and y-z slices, were taken in the position indicated by the horizontal, vertical lines respectively, as indicated in the x-y slides. The x-direction is perpendicular to the tilt axis, and the z-direction is the direction of the missing wedge. For consistent comparison, the intensity mapping in each orthoslice is shown is presented with a linear mapping between their maximum and minimum pixel values. Zoomed areas were further enhanced.

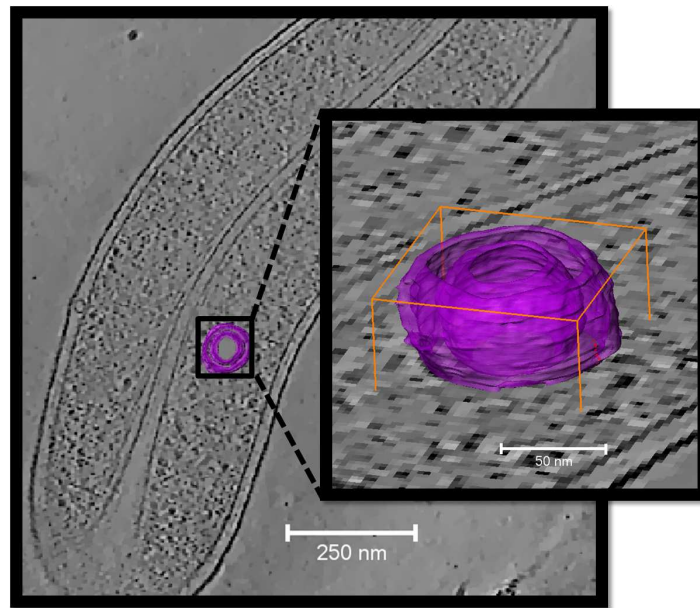


Figure 6.4 | Shows the auto-segmentation results of the intracellular microcompartments in *A. longum*. This result is extracted from the DLET reconstruction in Figure 6.2(a).

Figure 6.3 shows the reconstruction results after reducing the tilt series from 121 to 25 images (i.e. an angular step of 5° between $\pm 60^\circ$) to test the performance of both algorithms. It is clear that the limited total radiation dose and the radial under-sampling results in an increase of noise in the tomogram domain of both reconstructions. Nevertheless, the quality of the DLET reconstruction still exceeds that of the the SIRT reconstruction of the full dataset, and is certainly of acceptable quality for detailed structural analysis.

Movie **Ch6-M01** in Appendix A and Fig. 6.4, shows the segmented intracellular microcompartments in *A. longum* extracted for the DLET reconstruction in Figure 6.2(a).

6.2 Carbon nanofiber for fuel cell catalysts

Low-temperature fuel cells, that are based on hydrogen (e.g. the polymer electrolyte membrane fuel cell, with phosphoric acid fuel), ethanol (direct ethanol fuel cell) or methanol (direct methanol fuel cell) present environmentally-friendly methods for producing electricity by direct electrochemical conversion of hydrogen/methanol/ethanol and oxygen into water (and carbon dioxide). Platinum

crystallites on a conductive support are usually used as oxidation catalysts. In such catalysts, maximising the surface area of the metal particles available for the reactions is critical for maximising the efficiency of these types of fuel cells. This can be done by optimising the structure and dispersion of these metal particles ([Antolini, 2009](#)).

Recently, nanostructured carbon materials with graphitic structure, such as carbon nanofibers (CNFs) were investigated as a possibility for supporting nano-sized electrocatalyst particles in low-temperature fuel cells because of their large surface area and high electrical conductivity ([Zhou et al., 2012](#)).

TEM is an important method for characterising both the catalysts and the carbon nanofibers support in order to determine further processing to increase the electrochemical catalytic activity for oxidation in fuel cells. Electron tomography can be used to examine the dispersion of crystallite nanoparticles in the catalyst supports and can clearly determine the exact location of the particles with respect to tube like nanomaterials.

In this section, a tilt series of carbon nanofibers (CNFs) coated with carbonized polyaniline (PANI) to support Pt catalysts (CNF/HPANI-Pt) is reconstructed using both SIRT and DLET, and a visual assessment is performed comparing both tomograms.

6.2.1 Experimental procedure and results

The tomography tilt-series of (CNFs/HPANI-Pt) were recorded¹ in bright-field TEM mode using a high-tilt sample holder on a JEOL 1400 (120 kV). The tilt series were acquired with dynamic focusing (corrections of focus and horizontal displacement as described in section [2.1.4.1](#)) by using the SerialEM package ([Mastronarde, 2005](#)). A total of 130 images were acquired the tilt range $\pm 65^\circ$ with angular increment of 1° .

Typical 2D TEM images are shown in [Figure 6.5](#). The Pt particles are present on the surface of the carbon fibres as dark-coloured grains. However, it is not clear if there are some Pt nanoparticles inside the fibres. Also, this sample is of a cylindrical shape which is ideal for testing the robustness of the reconstruction algorithms for reducing the missing wedge artefacts.

¹BF-STEM acquisition was performed by Dr Dave Mitchell from University of Wollongong, NSW, Australia.

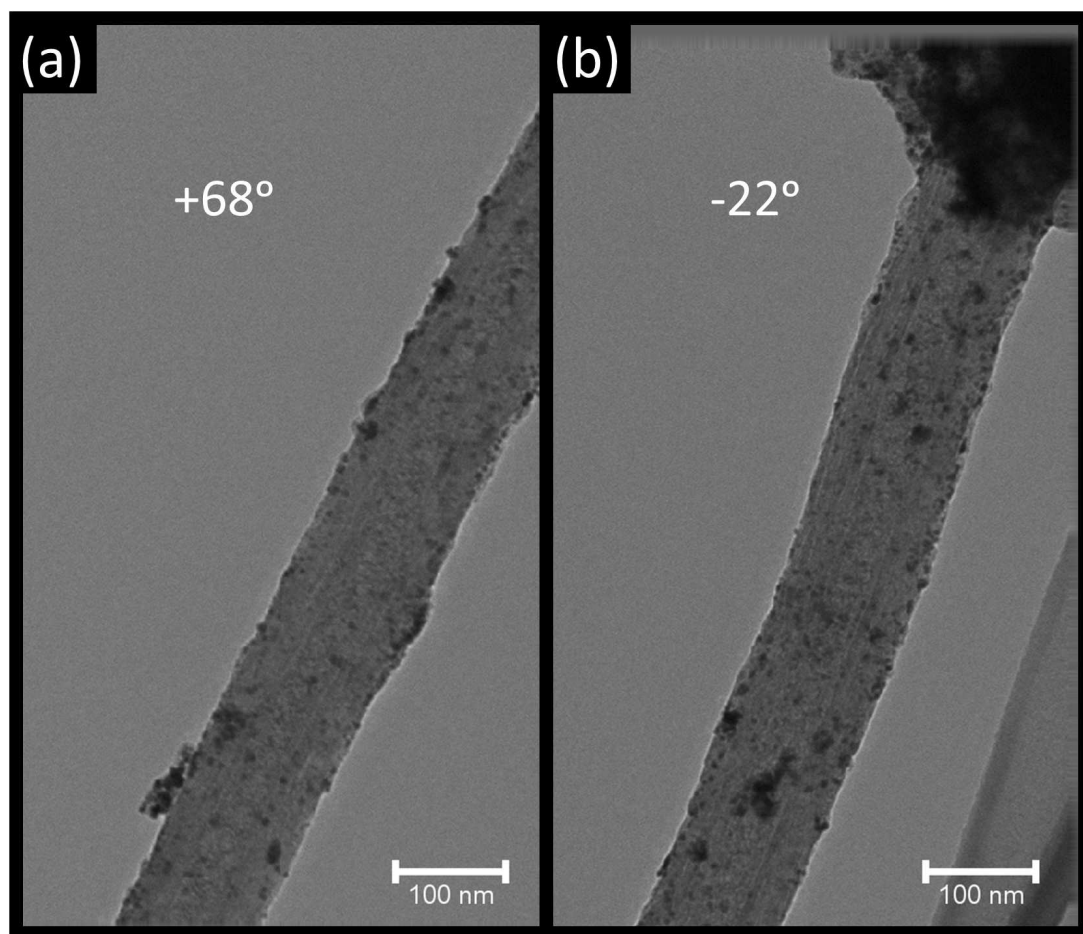


Figure 6.5 | Example of bright-field images of the TEM tomography tilt-series of carbon nanofiber/carbonized polyaniline-supported platinum (CNF/HPANI-Pt) sample. The images shows the carbon nanofiber tilted 90° from (a) $+68^\circ$ and (b) -22° degrees tilt.

The TEM tomograms in Figure 6.6, reveals a coaxial structure in which the CNFs have a hollow core (see also movie Ch6-M03 in Appendix A). The Pt nanoparticles are dispersed both on the inside of the inner tube-wall and on the outer surface of the hollow carbon nanofibers. The inner Pt particles may be unable to contribute to the electrochemical catalytic performance.

The DLET reconstruction shows tomogram with a higher contrast between the Pt nanoparticles and the CNF. The SIRT tomogram failed to reconstruct some of the Pt nanoparticles compared to the DLET results (as indicated by the red arrows in Fig. 6.6(b)). Also, SIRT results showed elongation of the tube in the direction of the missing wedge (z-direction as indicated by the yellow arrows in Fig. 6.6(a)). The elongation was reduced in the DLET reconstruction.

The enhanced contrast of the DLET tomograms enables use of automatic (or semi-automatic) segmentation procedures for extracting surfaces for quantitative studies. Figure 6.7(a) and Movie **Ch6-M02** in Appendix A, shows the segmented tomogram from the SIRT volume. This segmentation was obtained automatically by Otsu thresholding followed by binarisation. The SIRT results show a less faithful surface, and a manual segmentation is still needed to extract the required areas. Figure 6.7(b) and Movie **Ch6-M03** in Appendix A shows the segmentation from the DLET volume.

The location, size, aggregations and distribution of the Pt catalyst nanoparticles in the catalyst support can be extracted for quantitative study and compared with its electrochemical catalytic performance that can be obtained by Chronoamperometry and by measuring the current intensity of the CNF/HPANI-Pt catalyst.

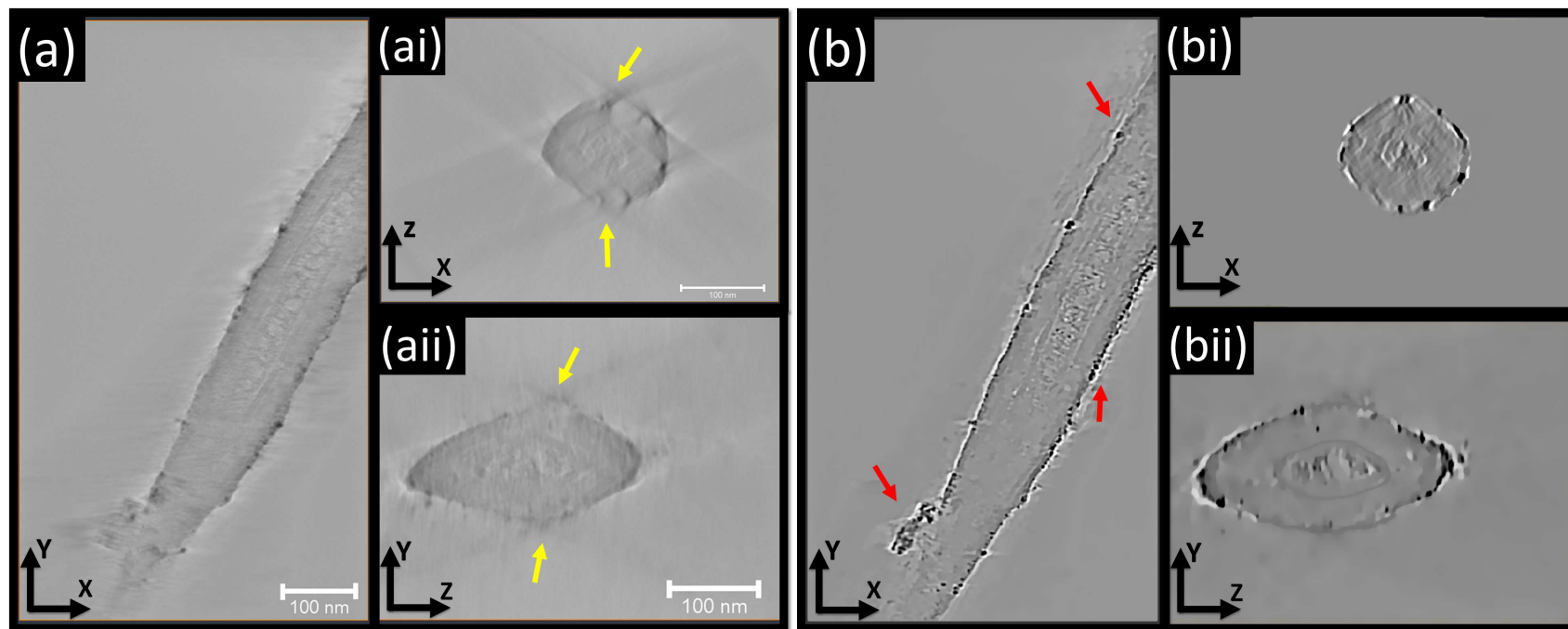


Figure 6.6 | Visual assessment of the CNF/HPANI-Pt reconstruction from a total of 130 images, angular step of 1° between $\pm 65^\circ$. The orthoslices were taken from the center of the (a) SIRT and (b) DLET reconstruction. Both the z-x and y-z slices, were taken through the central horizontal, vertical lines respectively. The the x-direction is perpendicular to the tilt axis and the z-direction is the direction of the missing wedge. The arrows in the SIRT reconstruction (ai, aii) shows the elongation due to the missing wedge which is reduced in the the DLET results (bi, bii).

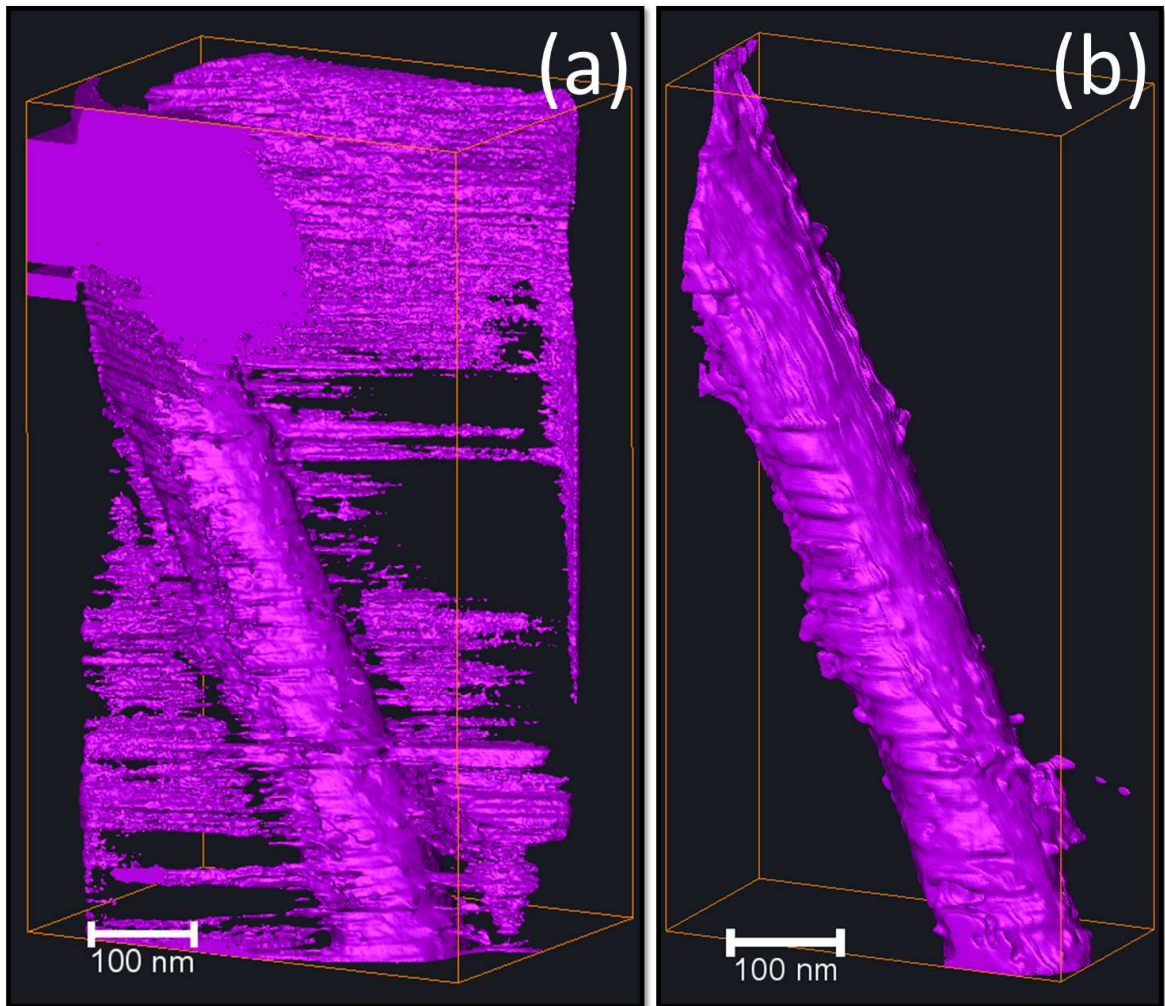


Figure 6.7 | Surfaces extracted using automatic segmentation procedure based on Otsu thresholding method of the (a) SIRT (b) DLET reconstruction.

6.3 Conclusion

This chapter discussed two general applications of DLET algorithm for characterising the 3D morphology of samples in material and biological sciences. It was clear that the effect of noise due to limited total radiation dose and radial under-sampling was further reduced in DLET results compared to SIRT. The main novel results in this chapter are in showing that the elongation along the missing wedge-direction can be reduced using the DLET reconstruction. Also, the DLET reconstruction produced tomograms with a higher contrast than the SIRT results. This enables the use of automatic (or semi-automatic) segmentation procedures for extracting surfaces for quantitative studies. Such automatic segmentation is not possible using tomograms that were reconstructed using traditional methods (e.g. WBP or SIRT).

”
It is very easy to answer many of these fundamental biological questions; you just look at the thing! ... It would be very easy to make an analysis of any complicated chemical substance; all one would have to do would be to look at it and see where the atoms are ... I put this out as a challenge: Is there no way to make the electron microscope more powerful?
”

Richard Feynman, 1959.

7

Conclusions and Outlook

Currently, nanotechnology faces an increasing requirement for 3D characterization of materials. Three-dimensional information can be obtained from a wide range of instruments using electron tomography (ET). ET has evolved greatly and become a standard technique for reconstructing the morphology of nanoscale materials. However, obtaining a qualitative 3D concept of a structure is often insufficient due to the advent of more complex nanostructures and the requirement for quantitative understanding of the nanostructure. Therefore, the focus of ET is moving towards obtaining quantitative information such as volume and lengths and thus the quality and fidelity of reconstruction is of critical importance. The quality of a 3D reconstruction, based on ET, is influenced by a number of experimental factors, such as the maximum tilting range, tilt increment and the alignment of the tilt series. Another important factor that has a significant impact on the quality of a 3D reconstruction is the reconstruction technique. In order to perform a reliable quantitative measurements of segmented tomograms,

development of reconstruction algorithms that minimise under-sampling artefacts in the reconstruction is necessary.

This thesis has addressed advancing the characterisation capabilities of TEM using electron tomography. This was from two perspectives, providing a quality assessment for established ET methods, and developing a high-fidelity and novel method for 3D tomographic reconstruction. Relevant potential applications have also been investigated.

Firstly, this thesis has reviewed the different computational stages involved in ET for materials science, from image acquisition to interpretation of the 3D reconstruction, and provides an introduction to the transmission electron microscopy (TEM) imaging modes that were used in this thesis. This is principally, high annular dark field scanning transmission electron microscopy (HAADF-STEM), electron energy-loss spectroscopy (EELS), energy filtered TEM (EFTEM) and the Bright Field TEM (BF-TEM). Both HAADF-STEM and the EELS mode are commonly used techniques to characterise materials in physical sciences.

The quality assignment investigation of ET tomographic reconstructions has been approached qualitatively and quantitatively using particles of a well-known morphology. The analysis aimed to quantify the influence of different experimental parameters such as tilting increment and missing wedge size on the quality of ET 3D reconstruction. The results of this analysis showed that the type of ET reconstruction algorithm has a significant effect on the fidelity of the reconstructed tomogram. This result has motivated the development of an improved tomographic reconstruction process.

This thesis further extended the ET reconstruction capabilities for high-fidelity 3D structural imaging. This has been via the development of the DLET reconstruction method to achieve reliable electron tomograms for robust quantitative analysis in 3D nano-metrology. The DLET method is based on the powerful theoretical results of the compressed sensing (CS) theory combined with recent advances in machine learning. CS uses image sparsity as a priori knowledge to improve the accuracy of reconstruction, and can require fewer projections than other reconstruction techniques. The performance of CS relies heavily on the degree of sparsity in the selected transform domain, and this depends essentially on the choice of sparsifying transform. The unique feature of DLET technique is that it learns the sparsifying transform adaptively using a dictionary-based approach. By doing so, the learned transform can have enhanced capabilities to compress

the images and therefore improve the reconstruction quality. Also, this adaptive transform can overcome many of the limitation of fixed sparsifying transforms used in recent published works. The DLET algorithm was demonstrated to efficiently reduce missing wedge and star artefacts. Using simulations from complex phantoms. It was shown that this new approach reconstructs the morphology with a higher fidelity than either analytically-based CS reconstruction algorithms or traditional WBP and SIRT. The efficacy of DLET was also demonstrated with several experimental example studies, including using an EFTEM tilt series of polymer solar cells and a cryo-TEM tilt series of an Ebola entry-competent virus-like particle (VLP). It is believed that the technique will become of tremendous importance for 3D nanoscale imaging in physics and biological science.

Furthermore, this thesis has also examined the use of DualEELS in elementally sensitive tilt series tomography in the scanning transmission electron microscope. A procedure is implemented using Fourier-log deconvolution to remove the effects of multiple scattering from the spectra followed by normalisation by the zero loss peak intensity to produce a spectroscopic signal that is linearly dependent on the projected density of the element in each pixel, and this was compared with a procedure that does not include deconvolution (although normalisation by the zero loss peak intensity is still performed). Additionally, a comparison was performed between the 3D reconstruction using the DLET, with the well-established SIRT algorithm. For the sample of VC precipitates extracted from steel in a carbon replica, it is found that the use of this linear signal results in a very even density throughout the precipitate, whereas when deconvolution is omitted, a slight density reduction is observed in the cores of the precipitates (a so-called cupping artefact). Additionally, it is clearly demonstrated that the 3D morphology is much better reproduced using the DLET algorithm, with a reduced elongation in the missing wedge direction. It is therefore concluded that reliable elementally sensitive tilt tomography using EELS is best undertaken with the aid of both appropriate use of DualEELS and a sensible compressed sensing based reconstruction algorithm to make the best use of the limited data and signal to noise, inherent in core-loss EELS.

This thesis has focused the experimental studies on drawn from across a range of physical science and nanotechnology. The broadening use of ET though, inevitably leads to the desire to study more challenging samples which would be easily damaged by overlarge radiation doses. Two final examples were studied: the

acetone longum bacteria using cryo-TEM and a carbon nanofiber supported Pt-based fuel cell catalysts using BF-STEM. However, these results are only qualitative and with resolution in the nanometer range. The obtained results have higher contrast and have a reduced noise which enables reliable automated (or semi-automatic) segmentation. This helps to produce higher quality and robust segmentation for quantitative studies with less labour and a reduction in the subjective bias that is introduced by the operator.

In terms of future work, the analysis of nano-structures using reconstruction methods that incorporate intelligent prior-knowledge about the specimen in the ET reconstruction, similar to the DLET method, should be a particularly fruitful area of investigation. Time-resolved microscopy is a potential application which can benefit from the compressive sensing theory, especially for the 4D electron tomography (e.g., [Kwon and Zewail, 2010](#)). Other cutting edge electron tomography, including statistical parameter estimation for atom counting, STEM-EDX tomography and single particle reconstruction are areas that can benefit of using advanced reconstruction methods such as DLET.

Also, further research could usefully explore other optimal sub-sampling strategies using the signal structure in ET. The recent findings by [Adcock et al. \(2013\)](#) suggest that the optimal sampling strategy depends not just on the overall sparsity of the signal, but also on its structure. By leveraging not just sparsity, but also structure, the CS-based ET reconstruction algorithms, may be further improved enabling more information to be recovered from fewer measurements. Finally, further investigation may examine the possibility to improve the DLET for extremely undersampled data. This could be via the use of Separative Sparse Representation (SSR) which involves training an additional global dictionary to characterise artefact components. Such an approach can be effective as it will add a discriminative nature to the learned dictionary and exclude sparse coefficients that correspond to artefact atoms. This may enhance the dictionary's ability to characterise artefacts that are often hard to suppress without introducing blurring effects such as streak artefacts. Also, the dictionary learning formulation of DLET can be further enhanced via the use of a multi-scale dictionary formulation to enforces sparsity of the reconstructed tomogram at multiple scales (i.e., patch sizes) and combines the outcomes at those scales to achieve superior reconstructions. This approach could further improve the reconstruction fidelity and suppress the under-sampling artefact in extremely reduced datasets. This can be

efficiently implemented using a sequential procedure which begins with the lowest scale and includes the higher scales sequentially over iterations. Also the use of Deep Learning Convolutional Neural Networks and in particular those based on Autoencoders which perform hierarchical feature encoding for reconstruction tasks could be further improve the quality of ET reconstruction since they are capable of synthesising complete feature non-linear hierarchies that capture more of the pattern-space being modelled.

deeper discussion of the recent progress in cutting edge electron tomography (including statistical parameter estimation for atom counting, STEM-EDX tomography, single particle reconstruction).

As a final thought, it should be pointed out that the work in this thesis (especially, chapter 5) is an example of an emerging challenge in microscopy as a result of the large quantity of data being stored and processed. By combining real space and data from other domains such as spectral, gigabytes of data are generated very quickly. Processing these large data volumes is expected to bring significant engineering and science advances. However, with such a big blessing comes big challenges in dealing with large-scale datasets. Running analysis on voluminous datasets by central processing and storage units seems infeasible (if not impossible), and with the advent of time domain, processing must often be performed in real time. This is especially true when medium quality results obtained quickly is more useful than high-quality results obtained slowly. As a consequence, processing and analytic tools need to be re-evaluated in today's high-dimensional electron microscopy data regime. Decentralised and parallelised multi-cores will be preferred. Signal processing tools such as principal component analysis (PCA), dictionary learning and compressed sensing may be effective tools for data reduction. Also the advances in processing methods such as convex optimisation (Cevher et al., 2014) and the sparse Fourier transform Gilbert et al. (2014) will be crucial for rapid analysis. This challenge is cross-disciplinary and known as the "Big Data" problem. Quoting a recent press article "The effect is being felt everywhere, from business to science, from governments to the arts." (Cukier, 2010). There is no doubt that this will be an era of data deluge for microscopy.

Although there is still lots to do in tackling Feynman's 1959 challenge, it is apparent that electron tomography will take a key role in analysing the "complicated chemical substances" in materials and biological sciences.



Supplementary movies

Supporting movies are available on the supplementary DVD.

Ch4-M01: 360° volume rendering views and the segmented surface of the MgO nanocubes that was reconstructed using HAADF-STEM tilt series (with a tilt range of $\pm 75^\circ$ and an increment of 2° between consecutive projections).

Ch4-M02: 360° volume rendering views and the segmented surface of the nanospheres that was reconstructed using BF-TEM tilt series (a tilt range of $\pm 62^\circ$, with an increment of 2° between consecutive projections).

Ch5-M01: 360° volume rendering views and the segmented surface of the Vanadium nanoparticles that was reconstructed using EELS dataset.

Ch5-M02: shows Volume rendered views of the combined volume resulted from reconstructions of Vanadium Maps and Carbon maps.

Ch6-M01: shows the auto-segmentation results of the intracellular microcompartments in *A. longum*. This result is extracted for the DLET reconstruction in Figure 6.2(a).

Ch6-M02: automated segmentation results from SIRT reconstruction using Otsu's method.

Ch6-M03: automated segmentation from DLET reconstruction using Otsu's method.

References

- Adcock, B., Hansen, A., Poon, C., and Roman, B. (2013). Overcoming the coherence barrier in compressed sensing. In *10th international conference on Sampling Theory and Applications (SampTA 2013)*, pages 1–4, Bremen, Germany. [96](#), [97](#), [175](#)
- Aharon, M., Elad, M., and Bruckstein, A. (2006). K -SVD: An algorithm for designing overcomplete dictionaries for sparse representation. *Signal Processing, IEEE Transactions on*, 54(11):4311–4322. [100](#), [101](#), [103](#)
- Al-Afeef, A., Alekseev, A., MacLaren, I., and Cockshott, P. (2015). Electron tomography based on a total generalized variation minimization reconstruction technique. In *Picture Coding Symposium (PCS), 2015*, pages 95–99. [92](#)
- Al-Afeef, A., Cockshott, W. P., MacLaren, I., and McVitie, S. (2016). Electron tomography image reconstruction using data-driven adaptive compressed sensing. *Scanning*, 38(3):251–276. [64](#), [92](#), [146](#), [147](#)
- Alaa, A., Paul, C., Ian, M., , and Sephen, M. (2014). Improved electron tomography image reconstruction using compressed sensing based adaptive dictionaries. In *18th International Microscopy Congress - IMC 2014*, pages IT–10. <http://www.microscopy.cz/proceedings/all.html>. [92](#)
- AlAfeef, A., Bobynko, J., Cockshott, W. P., Craven, A. J., Zuazo, I., Barges, P., and MacLaren, I. (2016). Linear chemically sensitive electron tomography using duals and dictionary-based compressed sensing. *Ultramicroscopy*, 170:96 – 106. [31](#), [145](#), [146](#)

- AlAfeef, A., Cockshott, P., MacLaren, I., and McVitie, S. (2014a). Compressed sensing electron tomography using adaptive dictionaries: a simulation study. *Journal of Physics: Conference Series*, 522(1):012021. [92](#), [134](#)
- AlAfeef, A., Cockshott, P., MacLaren, I., and McVitie, S. (2014b). Compressed Sensing Electron tomography using adaptive dictionaries: a simulation study. *J. Phys.: Conf. Ser.*, 522:012021. [146](#)
- AlAfeef, A., Cockshott, W., and MacLaren, I. (2015a). Dictionary based reconstruction of the 3D morphology of ebola virus. In *Microscopy and Microanalysis MM2015*, volume 21, pages 905–906. Paper: 1172. [146](#)
- AlAfeef, A., Paul Cockshott, W., Barges, P., Zuazo, I., Bobynko, J., Craven, A. J., and Maclaren, I. (2015b). Linear chemically sensitive electron tomography using dualeels and compressed sensing. *Microscopy and Microanalysis*, 21:2341–2342. [31](#)
- Alani, R., Armbruster, B. L., Mitro, R. J., Malaszewski, L., Kozar, R. M., Zolkowski, R., and Suzuki, S. (2002). Double tilt and rotate specimen holder for a transmission electron microscope. US Patent 6,388,262. [51](#)
- Alekseev, A., Hedley, G. J., Al-Afeef, A., Ageev, O. A., and Samuel, I. D. (2015). Morphology and local electrical properties of ptb7: PC 71 bm blends. *Journal of Materials Chemistry A*, 3(16):8706–8714. [92](#), [121](#), [123](#), [126](#), [129](#), [132](#)
- Alpers, A., Gardner, R. J., Knig, S., Pennington, R. S., Boothroyd, C. B., Houben, L., Dunin-Borkowski, R. E., and Batenburg, K. J. (2013). Geometric reconstruction methods for electron tomography. *Ultramicroscopy*, 128(0):42–54. [64](#)
- Antolini, E. (2009). Carbon supports for low-temperature fuel cell catalysts. *Applied Catalysis B: Environmental*, 88(1):1–24. [166](#)
- Aoyama, K., Takagi, T., Hirase, A., and Miyazawa, A. (2008). {STEM} tomography for thick biological specimens. *Ultramicroscopy*, 109(1):70–80. [54](#)
- Arbelaez, P., Maire, M., Fowlkes, C., and Malik, J. (2011). Contour detection and hierarchical image segmentation. *Pattern Analysis and Machine Intelligence, IEEE Transactions on*, 33(5):898–916. [145](#)

- Ardenne, M. (1938). Das elektronen-rastermikroskop, theoretische grundlagen. *Z. Physik*, 109(9. u. 10):553–572. [11](#)
- Arslan, I., Tong, J. R., and Midgley, P. A. (2006). Reducing the missing wedge: high-resolution dual axis tomography of inorganic materials. *Ultramicroscopy*, 106(11):994–1000. [9](#), [46](#), [49](#), [52](#)
- Bajaj, C., Yu, Z., and Auer, M. (2003). Volumetric feature extraction and visualization of tomographic molecular imaging. *Journal of Structural Biology*, 144(1):132–143. [69](#)
- Bals, S., Goris, B., De Backer, A., Van Aert, S., and Van Tendeloo, G. (2016). Atomic resolution electron tomography. *MRS Bulletin*, 41(7):525–530. [38](#)
- Banhart, J. (2008a). *Advanced tomographic methods in materials research and engineering*. Oxford University Press New York. [21](#), [43](#), [62](#), [69](#)
- Banhart, J. (2008b). *Advanced tomographic methods in materials research and engineering*. Oxford University Press New York. [146](#)
- Baraniuk, R. and Steeghs, P. (2007). Compressive radar imaging. In *Radar Conference, 2007 IEEE*, pages 128–133. IEEE. [95](#)
- Bartesaghi, A., Sprechmann, P., Liu, J., Randall, G., Sapiro, G., and Subramaniam, S. (2008). Classification and 3d averaging with missing wedge correction in biological electron tomography. *Journal of structural biology*, 162(3):436–450. [134](#)
- Batenburg, K., Bals, S., Sijbers, J., Kübel, C., Midgley, P. A., Hernandez, J., Kaiser, U., Encina, E., Coronado, E., and Van-Tendeloo, G. (2009). 3D imaging of nanomaterials by discrete tomography. *Ultramicroscopy*, 109(6):730–740. [64](#)
- Batson, P., Dellby, N., and Krivanek, O. (2002). Sub-ångstrom resolution using aberration corrected electron optics. *Nature*, 418(6898):617–620. [11](#)
- Benvenuto, F., Zanella, R., Zanni, L., and Bertero, M. (2010). Nonnegative least-squares image deblurring: improved gradient projection approaches. *Inverse Problems*, 26(2):025004. [62](#)
- Besl, P. and McKay, H. (1992). A method for registration of 3-D shapes. *IEEE Trans. Pattern Anal. Machine Intell.*, 14(2):239–256. [79](#), [147](#)

- Beucher, S. and Meyer, F. (1992). The morphological approach to segmentation: the watershed transformation. *Optical Engineering-New York-Marcel Dekker Incorporated*, 34:433–433. [69](#)
- Bhella, D. and Goodfellow, I. G. (2011). The cryo-electron microscopy structure of feline calicivirus bound to junctional adhesion molecule a at 9-angstrom resolution reveals receptor-induced flexibility and two distinct conformational changes in the capsid protein vp1. *Journal of virology*, 85(21):11381–11390. [35](#), [70](#)
- Binev, P., Dahmen, W., DeVore, R., Lamby, P., Savu, D., and Sharpley, R. (2012). *Compressed sensing and electron microscopy*. Springer. [92](#), [97](#), [118](#)
- Bobin, J., Starck, J.-L., and Ottensamer, R. (2008). Compressed sensing in astronomy. *Selected Topics in Signal Processing, IEEE Journal of*, 2(5):718–726. [95](#)
- Bobyenko, J., MacLaren, I., and Craven, A. J. (2015). Spectrum imaging of complex nanostructures using DualEELS: I. digital extraction replicas. *Ultramicroscopy*, 149:9–20. [143](#)
- Bosman, M., Watanabe, M., Alexander, D., and Keast, V. (2006). Mapping chemical and bonding information using multivariate analysis of electron energy-loss spectrum images. *Ultramicroscopy*, 106(11-12):1024–1032. [143](#)
- Bracewell, R. N. (1956). Strip integration in radio astronomy. *Australian Journal of Physics*, 9(2):198–217. [35](#), [38](#)
- Brydson, R. (2011). *Aberration-Corrected Analytical Transmission Electron Microscopy*, volume 3. John Wiley Sons, Ltd. [46](#)
- Brydson, R. and Hondow, N. (2011). *Electron Energy Loss Spectrometry and Energy Dispersive X-ray Analysis*. John Wiley & Sons, Ltd. [26](#)
- Buades, A., Coll, B., and Morel, J.-M. (2011). Non-local means denoising. *Image Processing On Line*, 1:6. [102](#)
- Candès, E. J., Romberg, J., and Tao, T. (2006). Robust uncertainty principles: Exact signal reconstruction from highly incomplete frequency information. *Information Theory, IEEE Transactions on*, 52(2):489–509. [92](#), [93](#), [95](#), [96](#)

- Candès, E. J. and Wakin, M. B. (2008). An introduction to compressive sampling. *Signal Processing Magazine, IEEE*, 25(2):21–30. [92](#), [93](#), [95](#), [97](#)
- CAO, M., ZHANG, H., LU, Y., NISHI, R., and TAKAOKA, A. (2009). Formation and reduction of streak artefacts in electron tomography. *Journal of Microscopy*, 239(1):66–71. [66](#)
- Carazo, J.-M. (1992). The fidelity of 3d reconstructions from incomplete data and the use of restoration methods. In *Electron tomography*, pages 117–164. Springer. [78](#)
- Cevher, V., Becker, S., and Schmidt, M. (2014). Convex Optimization for Big Data: Scalable randomized, and parallel algorithms for big data analytics. *IEEE Signal Process. Mag.*, 31(5):32–43. [176](#)
- Chan, T., Esedoglu, S., Park, F., and Yip, A. (2005). Recent developments in total variation image restoration. *Mathematical Models of Computer Vision*, 17:17–31. [97](#)
- Chandler, D. M. and Hemami, S. S. (2007). Vsnr: A wavelet-based visual signal-to-noise ratio for natural images. *Image Processing, IEEE Transactions on*, 16(9):2284–2298. [108](#)
- Chandran, K., Sullivan, N. J., Felbor, U., Whelan, S. P., and Cunningham, J. M. (2005). Endosomal proteolysis of the ebola virus glycoprotein is necessary for infection. *Science*, 308(5728):1643–1645. [130](#)
- Chen, C.-C., Zhu, C., White, E. R., Chiu, C.-Y., Scott, M., Regan, B., Marks, L. D., Huang, Y., and Miao, J. (2013). Three-dimensional imaging of dislocations in a nanoparticle at atomic resolution. *Nature*, 496(7443):74–77. [38](#)
- Chen, D., Goris, B., Bleichrodt, F., Mezerji, H. H., Bals, S., Batenburg, K. J., de With, G., and Friedrich, H. (2014). The properties of sirt, TVm, and {DART} for 3D imaging of tubular domains in nanocomposite thin-films and sections. *Ultramicroscopy*, 147:137–148. [68](#)
- Chen, S. S., Donoho, D. L., and Saunders, M. A. (1998). Atomic decomposition by basis pursuit. *SIAM journal on scientific computing*, 20(1):33–61. [96](#), [97](#)

- Clercq, E. D. (2015). Ebola virus (ebov) infection: Therapeutic strategies. *Biochemical Pharmacology*, 93(1):1 – 10. [130](#)
- Cockshott, W. P., Tao, Y., Ao, G., Balch, P., Briones, A. M., and Daly, C. (2003). Confocal microscopic image sequence compression using vector quantization and three-dimensional pyramid. *Scanning*, 25(5):247–256. [100](#)
- Cormack, A. M. (1963). Representation of a function by its line integrals, with some radiological applications. *Journal of Applied Physics*, 34(9):2722–2727. [35](#)
- Cotter, S. F. and Rao, B. D. (2002). Sparse channel estimation via matching pursuit with application to equalization. *Communications, IEEE Transactions on*, 50(3):374–377. [95](#)
- Cramer, H. and Wold, H. (1936). Some theorems on distribution functions. *Journal of the London Mathematical Society*, 1(4):290–294. [40](#)
- Crowther, R. A., DeRosier, D. J., and Klug, A. (1970). The reconstruction of a three-dimensional structure from projections and its application to electron microscopy. *Proceedings of the Royal Society of London. A. Mathematical and Physical Sciences*, 317(1530):319–340. [66](#), [78](#)
- Cukier, K. (2010). *Data, data everywhere: A special report on managing information*. Economist Newspaper. [176](#)
- Daberkow, I., Herrmann, K.-H., Liu, L., Rau, W., and Tietz, H. (1996). Development and performance of a fast fibre-plate coupled CCD camera at medium energy and image processing system for electron holography. *Ultramicroscopy*, 64(14):35–48. [16](#)
- Dai, W., Fu, C., Raytcheva, D., Flanagan, J., Khant, H. A., Liu, X., Rochat, R. H., Haase-Pettingell, C., Piret, J., Ludtke, S. J., et al. (2013). Visualizing virus assembly intermediates inside marine cyanobacteria. *Nature*, 502(7473):707–710. [55](#)
- Davenport, M. A., Duarte, M. F., Eldar, Y. C., and Kutyniok, G. (2012). Introduction to compressed sensing. In Eldar, Y. C. and Kutyniok, G., editors, *Compressed Sensing*, pages 1–64. Cambridge University Press. Cambridge Books Online. [97](#)

- Davis, G., Mallat, S., and Avellaneda, M. (1997). Adaptive greedy approximations. *Constructive approximation*, 13(1):57–98. [100](#)
- Davisson, C. J. (1995). Nobel lectures, physics 1937, clinton j. davisson, the discovery of electron waves, december 13, 1937 and george paget thomson, electronic waves, june 7, 1938. *Nobel Lectures*, 1(2). [11](#)
- De Broglie, L. (1929). The wave nature of the electron. *Nobel lecture*, 12:244–256. [10](#)
- Deans, S. R. (1983). *The Radon Transform and Some of Its Applications*. John Wiley & Sons, NY. [39](#), [40](#), [57](#), [64](#)
- Depover, T., Monbaliu, O., Wallaert, E., and Verbeken, K. (2015). Effect of ti, mo and cr based precipitates on the hydrogen trapping and embrittlement of fe-c-x q&t alloys. *International Journal of Hydrogen Energy*, 40(47):16977–16984. [140](#)
- DeRosier, D. J. and Klug, A. (1968). Reconstruction of three dimensional structures from electron micrographs. *Nature*, 217(5124):130–134. [36](#), [56](#)
- Donoho, D. L. (2006). Compressed sensing. *Information Theory, IEEE Transactions on*, 52(4):1289–1306. [92](#), [93](#), [96](#)
- Donoho, D. L., Elad, M., and Temlyakov, V. N. (2006). Stable recovery of sparse overcomplete representations in the presence of noise. *Information Theory, IEEE Transactions on*, 52(1):6–18. [97](#)
- Donoho, D. L. and Tanner, J. (2005). Neighborliness of randomly projected simplices in high dimensions. *Proceedings of the National Academy of Sciences of the United States of America*, 102(27):9452–9457. [95](#)
- Duarte, M. F., Davenport, M. A., Takhar, D., Laska, J. N., Sun, T., Kelly, K. F., and Baraniuk, R. G. (2008). Single-pixel imaging via compressive sampling. *Signal Processing Magazine, IEEE*, 25(2):83–91. [95](#)
- Duarte, M. F. and Eldar, Y. C. (2011). Structured compressed sensing: From theory to applications. *Signal Processing, IEEE Transactions on*, 59(9):4053–4085. [95](#)

- Egerton, R., Li, P., and Malac, M. (2004). Radiation damage in the tem and sem. *Micron*, 35(6):399–409. [31](#)
- Egerton, R. F. (2008). Electron energy-loss spectroscopy in the TEM. *Rep. Prog. Phys.*, 72(1):016502. [138](#), [139](#)
- Egerton, R. F. (2011). *Electron energy-loss spectroscopy in the electron microscope*. Springer. [26](#), [122](#)
- Elad, M. (2010). *The Quest for a Dictionary*. Springer. [101](#)
- Elad, M. and Aharon, M. (2006). Image denoising via sparse and redundant representations over learned dictionaries. *Image Processing, IEEE Transactions on*, 15(12):3736–3745. [98](#), [101](#), [106](#), [119](#)
- Elfving, T., Hansen, P. C., and Nikazad, T. (2012). Semiconvergence and relaxation parameters for projected sirt algorithms. *SIAM Journal on Scientific Computing*, 34(4):A2000–A2017. [62](#)
- Engan, K., Aase, S. O., and Hakon Husoy, J. (1999). Method of optimal directions for frame design. In *Acoustics, Speech, and Signal Processing, 1999. Proceedings., 1999 IEEE International Conference on*, volume 5, pages 2443–2446. IEEE. [100](#)
- Falke, M., Falke, U., Bleloch, A., Teichert, S., Beddies, G., and Hinneberg, H.-J. (2005). Real structure of the cosi2/si (001) interface studied by dedicated aberration-corrected scanning transmission electron microscopy. *Applied Physics Letters*, 86(20):3103. [29](#)
- Fan, G. Y. and Ellisman, M. H. (2000). Digital imaging in transmission electron microscopy. *Journal of Microscopy*, 200(1):1–13. [15](#)
- Faruqi, A. and Andrews, H. (1997). Cooled CCD camera with tapered fibre optics for electron microscopy. *Nuclear Instruments and Methods in Physics Research Section A: Accelerators, Spectrometers, Detectors and Associated Equipment*, 392(13):233–236. [15](#)
- Feldmann, H. and Geisbert, T. W. (2011). Ebola haemorrhagic fever. *The Lancet*, 377(9768):849–862. [130](#)

- Fernandez, J.-J. (2013). Computational methods for materials characterization by electron tomography. *Current Opinion in Solid State and Materials Science*, 17(3):93–106. [69](#)
- Fessler, J., Sutton, B. P., et al. (2003). Nonuniform fast Fourier transforms using min-max interpolation. *Signal Processing, IEEE Transactions on*, 51(2):560–574. [58](#)
- Fornasier, M. and Rauhut, H. (2011). Compressive sensing. In *Handbook of Mathematical Methods in Imaging*, pages 187–228. Springer. [93](#), [96](#)
- Foucart, S. and Rauhut, H. (2013). *A mathematical introduction to compressive sensing*. Springer. [95](#)
- Frank, J. (2006a). *Electron Tomography: Methods for Three-Dimensional Visualization of Structures in the Cell*. Springer. [52](#), [55](#), [68](#), [69](#), [121](#), [144](#)
- Frank, J. (2006b). *Three-dimensional electron microscopy of macromolecular assemblies: visualization of biological molecules in their native state*. Oxford University Press. [36](#)
- Frank, J. (2010). *Electron Tomography: Methods for Three-Dimensional Visualization of Structures in the Cell*. Springer. [34](#), [49](#), [51](#), [55](#), [56](#), [57](#), [64](#), [102](#), [107](#), [133](#)
- Freundlich, M. M. (1963). ORigin of the electron microscope. *Science*, 142(1):185–188. [11](#)
- Friedrich, H., de Jongh, P. E., Verkleij, A. J., and de Jong, K. P. (2009). Electron tomography for heterogeneous catalysts and related nanostructured materials. *Chemical reviews*, 109(5):1613–1629. [21](#), [66](#)
- Friedrich, H., McCartney, M., and Buseck, P. (2005). Comparison of intensity distributions in tomograms from bf tem, adf stem, haadf stem, and calculated tilt series. *Ultramicroscopy*, 106(1):18–27. [66](#)
- Friedrich, H., Sietsma, J. R., de Jongh, P. E., Verkleij, A. J., and de Jong, K. P. (2007). Measuring location, size, distribution, and loading of nio crystallites in individual sba-15 pores by electron tomography. *Journal of the American Chemical Society*, 129(33):10249–10254. [68](#)

- Gan, L. (2007). Block compressed sensing of natural images. In *Digital Signal Processing, 2007 15th International Conference on*, pages 403–406. IEEE. [93](#)
- Geysermans, P., Finocchi, F., Goniakowski, J., Hacquart, R., and Jupille, J. (2009). Combination of (100), (110) and (111) facets in mgo crystals shapes from dry to wet environment. *Phys. Chem. Chem. Phys.*, 11:2228–2233. [74](#)
- Gilbert, A. C., Indyk, P., Iwen, M., and Schmidt, L. (2014). Recent Developments in the Sparse Fourier Transform: A compressed Fourier transform for big data. *IEEE Signal Process. Mag.*, 31(5):91–100. [176](#)
- Gilbert, P. (1972). Iterative methods for the three-dimensional reconstruction of an object from projections. *Journal of Theoretical Biology*, 36(1):105–117. [56](#), [62](#)
- Goris, B., Backer, A. D., Van-Aert, S., Gmez-Graa, S., Liz-Marzn, L. M., Van-Tendeloo, G., and Bals, S. (2013a). Three-dimensional elemental mapping at the atomic scale in bimetallic nanocrystals. *Nano Letters*, 13(9):4236–4241. [49](#)
- Goris, B., Roelandts, T., Batenburg, K., Mezerji, H. H., and Bals, S. (2013b). Advanced reconstruction algorithms for electron tomography: From comparison to combination. *Ultramicroscopy*, 127:40 – 47. *Frontiers of Electron Microscopy in Materials Science*. [73](#)
- Goris, B., Va-den Broek, W., Batenburg, K., Heidari Mezerji, H., and Bals, S. (2012). Electron tomography based on a total variation minimization reconstruction technique. *Ultramicroscopy*, 113:120–130. [91](#), [92](#), [93](#), [97](#), [118](#)
- Gorodnitsky, I. F. and Rao, B. D. (1997). Sparse signal reconstruction from limited data using focuss: A re-weighted minimum norm algorithm. *Signal Processing, IEEE Transactions on*, 45(3):600–616. [97](#)
- Gregor, J. and Benson, T. (2008). Computational analysis and improvement of sirt. *Medical Imaging, IEEE Transactions on*, 27(7):918–924. [63](#)
- Gross, D., Liu, Y.-K., Flammia, S. T., Becker, S., and Eisert, J. (2010). Quantum state tomography via compressed sensing. *Physical review letters*, 105(15):150401. [95](#)

- Gubbens, A., Barfels, M., Trevor, C., Twesten, R., Mooney, P., Thomas, P., Menon, N., Kraus, B., Mao, C., and McGinn, B. (2010a). The gif quantum, a next generation post-column imaging energy filter. *Ultramicroscopy*, 110(8):962–970. [30](#)
- Gubbens, A., Barfels, M., Trevor, C., Twesten, R., Mooney, P., Thomas, P., Menon, N., Kraus, B., Mao, C., and McGinn, B. (2010b). The GIF Quantum a next generation post-column imaging energy filter. *Ultramicroscopy*, 110(8):962–970. [139](#)
- Guckenberger, R. (1982). Determination of a common origin in the micrographs of tilt series in three-dimensional electron microscopy. *Ultramicroscopy*, 9(1):167–173. [55](#), [144](#)
- Haberfehlner, G., Orthacker, A., Albu, M., Li, J., and Kothleitner, G. (2014a). Nanoscale voxel spectroscopy by simultaneous eels and eds tomography. *Nanoscale*, 6(23):14563–14569. [26](#), [50](#), [51](#)
- Haberfehlner, G., Orthacker, A., Albu, M., Li, J., and Kothleitner, G. (2014b). Nanoscale voxel spectroscopy by simultaneous EELS and EDS tomography. *Nanoscale*, 6(23):14563–14569. [139](#)
- Haugenau, F., Hawkes, P. W., Hutchison, J. L., Satiat-Jeunemaître, B., Simon, G. T., and Williams, D. B. (2003). Key events in the history of electron microscopy. *Microscopy and microanalysis*, 9(2):96–138. [12](#)
- Haider, M., Braunshausen, G., and Schwan, E. (1995). Correction of the spherical aberration of a 200 kv tem by means of a hexapole-corrector. *Optik*, 99(4):167–179. [12](#)
- Han, R., Zhang, F., Wan, X., Fern, J.-J., Sun, F., and Liu, Z. (2014). A marker-free automatic alignment method based on scale-invariant features. *Journal of Structural Biology*, 186(1):167–180. [145](#)
- Hansen, P. (1990). The discrete picard condition for discrete ill-posed problems. *BIT Numerical Mathematics*, 30(4):658–672. [60](#)
- Hansen, P. C. (2010). *Discrete inverse problems: insight and algorithms*, volume 7. Siam. [60](#), [62](#), [76](#)

- Harauz, G. and van Heel, M. (1986). Exact filters for general geometry three dimensional reconstruction. *Optik*, 73(4):146–156. [78](#)
- Hart, R. G. (1968). Electron microscopy of unstained biological material: the polytropic montage. *Science*, 159(3822):1464–1467. [36](#)
- Hawkes, P. W. (2006). The electron microscope as a structure projector. In *Electron tomography*, pages 83–111. Springer. [56](#), [137](#)
- Heidenreich, R. D. (1942). Electron reflections in mgo crystals with the electron microscope. *Physical Review*, 62(5-6):291. [74](#)
- Henderson, R. (2004). Realizing the potential of electron cryo-microscopy. *Quarterly reviews of biophysics*, 37(01):3–13. [36](#)
- Henderson, R. (2013). Avoiding the pitfalls of single particle cryo-electron microscopy: Einstein from noise. *Proceedings of the National Academy of Sciences*, 110(45):18037–18041. [37](#)
- Herman, G. T. (2009). *Fundamentals of computerized tomography: image reconstruction from projections*. Springer. [62](#), [64](#)
- Hernndez-Saz, J., Herrera, M., and Molina, S. (2013). Fabrication of needle-shaped specimens containing subsurface nanostructures for electron tomography. In Wang, Z. M., editor, *FIB Nanostructures*, volume 20 of *Lecture Notes in Nanoscale Science and Technology*, pages 241–266. Springer International Publishing. [44](#)
- Hofer, F., Grogger, W., Kothleitner, G., and Warbichler, P. (1997). Quantitative analysis of efem elemental distribution images. *Ultramicroscopy*, 67(1):83–103. [122](#)
- Hofer, F., Schmidt, F., Grogger, W., and Kothleitner, G. (2016). Fundamentals of electron energy-loss spectroscopy. In *IOP Conference Series: Materials Science and Engineering*, volume 109, page 012007. IOP Publishing. [26](#)
- Hofer, F., Warbichler, P., and Grogger, W. (1995). Imaging of nanometer-sized precipitates in solids by electron spectroscopic imaging. *Ultramicroscopy*, 59(1):15–31. [122](#)
- Hounsfield, G. (1981). Nobel prize acceptance speech. *Med Phys*, 7:283. [36](#)

- Hounsfield, G. N. (1973). Computerized transverse axial scanning (tomography): Part 1. description of system. *The British journal of radiology*, 46(552):1016–1022. [35](#)
- Hudson, B. (1973). The application of stereo-techniques to electron micrographs. *Journal of Microscopy*, 98(3):396–401. [36](#)
- Huynh-Thu, Q. and Ghanbari, M. (2008). Scope of validity of PSNR in image/video quality assessment. *Electron. Lett.*, 44(13):800. [150](#)
- Jarausch, K., Thomas, P., Leonard, D. N., Twesten, R., and Booth, C. R. (2009). Four-dimensional STEM-EELS: Enabling nano-scale chemical tomography. *Ultramicroscopy*, 109(4):326–337. [50](#), [51](#), [137](#), [138](#)
- Jin, L., Milazzo, A.-C., Kleinfelder, S., Li, S., Leblanc, P., Duttweiler, F., Bouwer, J. C., Peltier, S. T., Ellisman, M. H., and Xuong, N.-H. (2008). Applications of direct detection device in transmission electron microscopy. *Journal of Structural Biology*, 161(3):352 – 358. The 4th International Conference on Electron TomographyThe 4th International Conference on Electron Tomography. [15](#)
- Jinschek, J., Batenburg, K., Calderon, H., Kilaas, R., Radmilovic, V., and Kisielowski, C. (2008). 3-D reconstruction of the atomic positions in a simulated gold nanocrystal based on discrete tomography: Prospects of atomic resolution electron tomography. *Ultramicroscopy*, 108(6):589–604. [64](#)
- Kaipio, J. and Somersalo, E. (2006). *Statistical and computational inverse problems*, volume 160. Springer Science & Business Media. [109](#)
- Kak, A. and Slaney, M. (2001). *Principles of Computerized Tomographic Imaging*. Society for Industrial and Applied Mathematics. [40](#), [62](#), [64](#)
- Kane, M. D. and Breznak, J. A. (1991). *Acetonema longum* gen. nov. sp. nov., an h₂/co₂ acetogenic bacterium from the termite, *pterotermes occidentis*. *Archives of microbiology*, 156(2):91–98. [160](#)
- Kato, M., Kawase, N., Kaneko, T., Toh, S., Matsumura, S., and Jinnai, H. (2008). Maximum diameter of the rod-shaped specimen for transmission electron microtomography without the missing wedge. *Ultramicroscopy*, 108(3):221–229. [50](#), [51](#)

- Kawase, N., Kato, M., Nishioka, H., and Jinnai, H. (2007). Transmission electron microtomography without the missing wedge for quantitative structural analysis. *Ultramicroscopy*, 107(1):8–15. [47](#), [66](#), [84](#), [86](#), [92](#)
- Kelly, T. F. and Miller, M. K. (2007). Atom probe tomography. *Review of Scientific Instruments*, 78(3):031101. [38](#)
- Kirkland, A. and Hutchison, J. (2007). *Nanocharacterisation*, volume 3. Royal Society of Chemistry. [54](#), [65](#), [69](#)
- Klabunde, K. (2004). *Nanoscale Materials in Chemistry*. Wiley. [74](#)
- Klug, A. (1983). From macromolecules to biological assemblies (nobel lecture). *Angewandte Chemie International Edition in English*, 22(8):565–582. [36](#)
- Koster, A., Chen, H., Sedat, J., and Agard, D. (1992). Automated microscopy for electron tomography. *Ultramicroscopy*, 46(1):207–227. [52](#), [53](#)
- Koster, A. J. and Bárcena, M. (2007). Cryotomography: low-dose automated tomography of frozen-hydrated specimens. In *Electron Tomography*, pages 113–161. Springer. [78](#)
- Koster, A. J., Grimm, R., Typke, D., Hegerl, R., Stoschek, A., Walz, J., and Baumeister, W. (1997). Perspectives of molecular and cellular electron tomography. *Journal of structural biology*, 120(3):276–308. [52](#), [53](#)
- Kremer, J. R., Mastronarde, D. N., and McIntosh, J. (1996). Computer visualization of three-dimensional image data using imod. *Journal of Structural Biology*, 116(1):71–76. [54](#)
- Krivanek, O., Dellby, N., and Lupini, A. (1999). Towards sub-Å electron beams. *Ultramicroscopy*, 78(1):1–11. [12](#)
- Krivanek, O., Lovejoy, T., and Dellby, N. (2015). Aberration-corrected stem for atomic-resolution imaging and analysis. *Journal of microscopy*, 259:165172. [12](#), [33](#)
- Krivanek, O. L., Gubbens, A. J., and Dellby, N. (1991). Developments in eels instrumentation for spectroscopy and imaging. *Microscopy Microanalysis Microstructures*, 2(2-3):315–332. [30](#)

- Kübel, C., Voigt, A., Schoenmakers, R., Otten, M., Su, D., Lee, T.-C., Carlsson, A., and Bradley, J. (2005). Recent advances in electron tomography: Tem and haadf-stem tomography for materials science and semiconductor applications. *Microscopy and Microanalysis*, 11(05):378–400. [2](#)
- Kwon, O.-H. and Zewail, A. H. (2010). 4d electron tomography. *Science*, 328(5986):1668–1673. [175](#)
- Landweber, L. (1951). An iteration formula for fredholm integral equations of the first kind. *American journal of mathematics*, 73:615–624. [63](#)
- Lange, A., Kupsch, A., Hentschel, M. P., Manke, I., Kardjilov, N., Arlt, T., and Grothausmann, R. (2011). Reconstruction of limited computed tomography data of fuel cell components using direct iterative reconstruction of computed tomography trajectories. *Journal of Power Sources*, 196(12):5293–5298. [64](#)
- Lanzavecchia, S., Cantele, F., Bellon, P., Zampighi, L., Kreman, M., Wright, E., and Zampighi, G. (2005). Conical tomography of freeze-fracture replicas: a method for the study of integral membrane proteins inserted in phospholipid bilayers. *Journal of Structural Biology*, 149(1):87–98. [52](#)
- Larson, P. E., Hu, S., Lustig, M., Kerr, A. B., Nelson, S. J., Kurhanewicz, J., Pauly, J. M., and Vigneron, D. B. (2011). Fast dynamic 3D mr spectroscopic imaging with compressed sensing and multiband excitation pulses for hyperpolarized ^{13}C studies. *Magnetic Resonance in Medicine*, 65(3):610–619. [96](#)
- Lauterbur, P. C. (2004). All science is interdisciplinary—from magnetic moments to molecules to men. *Bioscience reports*, 24(3):165–178. [36](#)
- Leary, R., Saghi, Z., Midgley, P. A., and Holland, D. J. (2013a). Compressed sensing electron tomography. *Ultramicroscopy*, 131:70–91. [73](#)
- Leary, R., Saghi, Z., Midgley, P. A., and Holland, D. J. (2013b). Compressed sensing electron tomography. *Ultramicroscopy*, 131:70–91. [89](#), [91](#), [92](#), [97](#)
- LeBeau, J. M. and Stemmer, S. (2008). Experimental quantification of annular dark-field images in scanning transmission electron microscopy. *Ultramicroscopy*, 108(12):1653–1658. [25](#)

- Lentzen, M., Jahnen, B., Jia, C., Thust, A., Tillmann, K., and Urban, K. (2002). High-resolution imaging with an aberration-corrected transmission electron microscope. *Ultramicroscopy*, 92(3):233–242. [12](#)
- Leschner, J., Biskupek, J., Chuvilin, A., and Kaiser, U. (2010). Accessing the local three-dimensional structure of carbon materials sensitive to an electron beam. *Carbon*, 48(14):4042–4048. [52](#)
- Liu, J., Huang, T.-Z., Selesnick, I. W., Lv, X.-G., and Chen, P.-Y. (2015). Image restoration using total variation with overlapping group sparsity. *Information Sciences*, 295:232–246. [97](#)
- Lloyd, S. (1982). Least squares quantization in PCM. *Information Theory, IEEE Transactions on*, 28(2):129–137. [100](#)
- Lowe, D. (1999). Object recognition from local scale-invariant features. In *Proceedings of the Seventh IEEE International Conference on Computer Vision*. IEEE. [145](#)
- Lucas, G., Burdet, P., Cantoni, M., and Hebert, C. (2013). Multivariate statistical analysis as a tool for the segmentation of 3d spectral data. *Micron*, 52:49–56. [143](#)
- Lucic, V., Forster, F., and Baumeister, W. (2005). Structural studies by electron tomography: from cells to molecules. *Annu. Rev. Biochem.*, 74:833–865. [143](#)
- Lustig, M., Donoho, D., and Pauly, J. M. (2007). Sparse MRI: The application of compressed sensing for rapid mr imaging. *Magnetic Resonance in Medicine*, 58(6):1182–1195. [92](#), [93](#), [95](#), [96](#), [97](#), [101](#), [111](#)
- Lustig, M., Donoho, D. L., Santos, J. M., and Pauly, J. M. (2008). Compressed sensing MRI. *Signal Processing Magazine, IEEE*, 25(2):72–82. [95](#), [96](#)
- MacLaren, I. and Ramasse, Q. M. (2014). Aberration-corrected scanning transmission electron microscopy for atomic-resolution studies of functional oxides. *International Materials Reviews*, 59(3):115–131. [11](#), [12](#), [33](#)
- Maign, A. and Twesten, R. (2009). Review of recent advances in spectrum imaging and its extension to reciprocal space. *J Electron Microsc (Tokyo)*, 58:99–109. [142](#)

- Mairal, J., Bach, F., Ponce, J., and Sapiro, G. (2010). Online learning for matrix factorization and sparse coding. *The Journal of Machine Learning Research*, 11:19–60. [103](#), [107](#)
- Mairal, J., Elad, M., and Sapiro, G. (2008). Sparse representation for color image restoration. *Image Processing, IEEE Transactions on*, 17(1):53–69. [98](#)
- Mansfield, P. (2004). Snapshot magnetic resonance imaging (nobel lecture). *Angewandte Chemie International Edition*, 43(41):5456–5464. [36](#)
- Marton, L. (1934). Electron microscopy of biological objects. *Phys. Rev.*, 46:527–528. [11](#)
- Marziliano, P., Dufaux, F., Winkler, S., and Ebrahimi, T. (2004). Perceptual blur and ringing metrics: application to JPEG2000. *Signal processing: Image communication*, 19(2):163–172. [98](#)
- Mastronarde, D. (2006). Tomographic Reconstruction with the IMOD Software Package. *Microsc. Microanal.*, 12(S02):178–179. [76](#), [145](#), [146](#), [147](#), [149](#)
- Mastronarde, D. N. (1997). Dual-axis tomography: An approach with alignment methods that preserve resolution. *Journal of Structural Biology*, 120(3):343–352. [47](#), [49](#)
- Mastronarde, D. N. (2005). Automated electron microscope tomography using robust prediction of specimen movements. *Journal of structural biology*, 152(1):36–51. [53](#), [166](#)
- McIntosh, R., Nicastro, D., and Mastronarde, D. (2005). New views of cells in 3D: an introduction to electron tomography. *Trends in cell biology*, 15(1):43–51. [34](#)
- McKenna, K. P., Sushko, P. V., and Shluger, A. L. (2007). Inside powders: A theoretical model of interfaces between mgo nanocrystallites. *Journal of the American Chemical Society*, 129(27):8600–8608. [74](#)
- Medalia, O., Weber, I., Frangakis, A. S., Nicastro, D., Gerisch, G., and Baumeister, W. (2002). Macromolecular architecture in eukaryotic cells visualized by cryoelectron tomography. *Science*, 298(5596):1209–1213. [21](#)

- Messaoudi, C., de Loubresse, N. G., Boudier, T., Dupuis-Williams, P., and Marco, S. (2006). Multiple-axis tomography: applications to basal bodies from paramoecium tetraurelia. *Biology of the Cell*, 98(7):415–425. [52](#)
- Mezerji, H. H., den Broek, W. V., and Bals, S. (2011). A practical method to determine the effective resolution in incoherent experimental electron tomography. *Ultramicroscopy*, 111(5):330–336. [68](#), [78](#)
- Midgley, P. A. (2005). Tomography using the transmission electron microscope. In *Handbook of Microscopy for Nanotechnology*, pages 601–627. Springer. [22](#)
- Midgley, P. A. and Dunin-Borkowski, R. E. (2009). Electron tomography and holography in materials science. *Nature materials*, 8(4):271–280. [21](#), [92](#)
- Midgley, P. A. and Weyland, M. (2003). 3D electron microscopy in the physical sciences: the development of z-contrast and efem tomography. *Ultramicroscopy*, 96(3):413–431. [21](#), [22](#), [28](#), [39](#), [43](#), [57](#), [66](#), [68](#), [92](#)
- Midgley, P. A., Weyland, M., Thomas, J. M., and Johnson, B. F. G. (2001). Z-contrast tomography: a technique in three-dimensional nanostructural analysis based on rutherford scattering. *Chem. Commun.*, pages 907–908. [25](#)
- Midgley, P. A., Weyland, M., Yates, T., Arslan, I., DUNIN-BORKOWSKI, R., and Thomas, J. (2006). Nanoscale scanning transmission electron tomography. *Journal of microscopy*, 223(3):185–190. [21](#)
- Miller, M. and Forbes, R. (2009). Atom probe tomography. *Materials Characterization*, 60(6):461–469. [38](#)
- Milne, J. L. and Subramaniam, S. (2009). Cryo-electron tomography of bacteria: progress, challenges and future prospects. *Nature Reviews Microbiology*, 7(9):666–675. [21](#)
- Mobus, G. and Inkson, B. J. (2007). Nanoscale tomography in materials science. *Materials Today*, 10(12):18–25. [34](#), [43](#)
- Monsegue, N., Jin, X., Echigo, T., Wang, G., and Murayama, M. (2012). Three-dimensional characterization of iron oxide (α-Fe₂O₃) nanoparticles: Application of a compressed sensing inspired reconstruction algorithm to electron tomography. *Microscopy and Microanalysis*, 18:1362–1367. [92](#), [93](#), [97](#)

- Mostofi, Y. (2011). Compressive cooperative sensing and mapping in mobile networks. *Mobile Computing, IEEE Transactions on*, 10(12):1769–1784. [95](#)
- Nankivell, J. (1963). The theory of electron stereo microscopy. *Optik*, 20:171–198. [36](#)
- Natarajan, B. K. (1995). Sparse approximate solutions to linear systems. *SIAM journal on computing*, 24(2):227–234. [100](#)
- Natterer, F. (1986). *The mathematics of computerized tomography*, volume 32. Siam. [64](#)
- Nellist, P., Behan, G., Kirkland, A., and Hetherington, C. (2006). Confocal operation of a transmission electron microscope with two aberration correctors. *Applied physics letters*, 89(12):124105. [37](#)
- Nellist, P. D. and Wang, P. (2012). Optical sectioning and confocal imaging and analysis in the transmission electron microscope. *Annual Review of Materials Research*, 42:125–143. [37](#)
- Nicoletti, O., de la Peña, F., Leary, R. K., Holland, D. J., Ducati, C., and Midgley, P. A. (2013). Three-dimensional imaging of localized surface plasmon resonances of metal nanoparticles. *Nature*, 502(7469):80–84. [138](#)
- Nooruddin, F. and Turk, G. (2003). Simplification and repair of polygonal models using volumetric techniques. *Visualization and Computer Graphics, IEEE Transactions on*, 9(2):191–205. [123](#)
- Oikonomou, C. M. and Jensen, G. J. (2016). A new view into prokaryotic cell biology from electron cryotomography. *Nature Reviews Microbiology*. [160](#)
- Olshausen, B. A. and Field, D. J. (1997). Sparse coding with an overcomplete basis set: A strategy employed by v1? *Vision research*, 37(23):3311–3325. [100](#)
- Oregan, B. and Grifitzi, M. (1991). A low-cost, high-efficiency solar cell based on dye-sensitized. *nature*, 353(6346):737–740. [2](#)
- Otsu, N. (1975a). A threshold selection method from gray-level histograms. *Automatica*, 11(285-296):23–27. [118](#), [147](#)

- Otsu, N. (1975b). A threshold selection method from gray-level histograms. *Automatica*, 11(285-296):23–27. [68](#), [79](#), [115](#)
- Patil, S. and Ravi, B. (2005). Voxel-based Representation Display and Thickness Analysis of Intricate Shapes. In *Ninth International Conference on Computer Aided Design and Computer Graphics (CAD-CG05)*. IEEE. [148](#)
- Pawel Penczek, Michael Marko, K. B. and Frank, J. (1995). Double-tilt electron tomography. *Ultramicroscopy*, 60(3):393–410. [47](#), [49](#)
- Penczek, P. A. (2010). Chapter one - fundamentals of three-dimensional reconstruction from projections. In Jensen, G. J., editor, *Cryo-EM, Part B: 3-D Reconstruction*, volume 482 of *Methods in Enzymology*, pages 1–33. Academic Press. [64](#)
- Pennycook, S. (1989). Z-contrast stem for materials science. *Ultramicroscopy*, 30(1):58–69. [21](#), [25](#)
- Pennycook, S., Lupini, A., Varela, M., Borisevich, A., Peng, Y., Oxley, M., Van-Benthem, K., and Chisholm, M. (2007). Scanning transmission electron microscopy for nanostructure characterization. In *Scanning Microscopy for Nanotechnology*, pages 152–191. Springer. [25](#)
- Pennycook, S. and Nellist, P. (1999). Z-contrast scanning transmission electron microscopy. In *Impact of electron and scanning probe microscopy on materials research*, pages 161–207. Springer. [21](#), [25](#), [57](#)
- Pennycook, S. J. and Nellist, P. D. (2011). *Scanning transmission electron microscopy: imaging and analysis*. Springer Science & Business Media. [21](#), [26](#), [43](#)
- Perona, P. and Malik, J. (1990). Scale-space and edge detection using anisotropic diffusion. *IEEE Transactions on pattern analysis and machine intelligence*, 12(7):629–639. [79](#)
- Peyré, G. (2011). A review of adaptive image representations. *Selected Topics in Signal Processing, IEEE Journal of*, 5(5):896–911. [101](#)
- Pilhofer, M., Ladinsky, M. S., McDowall, A. W., and Jensen, G. J. (2010). Bacterial tem: new insights from cryo-microscopy. *Methods in cell biology*, 96:21–45. [160](#)

- Protter, M. and Elad, M. (2009). Image sequence denoising via sparse and redundant representations. *Image Processing, IEEE Transactions on*, 18(1):27–35. [98](#)
- Qiu, X., Audet, J., Wong, G., Pillet, S., Bello, A., Cabral, T., Strong, J. E., Plummer, F., Corbett, C. R., Alimonti, J. B., et al. (2012). Successful treatment of ebola virus-infected cynomolgus macaques with monoclonal antibodies. *Science translational medicine*, 4(138):138ra81–138ra81. [133](#)
- Radermacher, M. (1988). Three-dimensional reconstruction of single particles from random and nonrandom tilt series. *Journal of Electron Microscopy Technique*, 9(4):359–394. [58](#), [66](#), [67](#), [78](#), [84](#), [92](#)
- Radermacher, M. and Hoppe, W. (1980). Properties of 3-D reconstruction from projections by conical tilting compared to single-axis tilting. In *Proceedings of the 7th European Congress on Electron Microscopy*, volume 1, pages 132–133. [66](#), [84](#)
- Rudin, L., Osher, S., and Fatemi, E. (1992). Non-linear total variation noise removal algorithm. *Phys D*, 60:259–268. [97](#)
- Radon, J. (1917). Über die bestimmung von funktionen durch ihre integralwerte 294 längs gewisser mannigfaltigkeiten, ber. *Verh. Säch. Akad. Wiss. Leipzig*, 295:262–277. [35](#), [38](#), [39](#)
- Rebled, J., Yedra, L., Estrade, S., Portillo, J., and Peiro, F. (2011). A new approach for 3d reconstruction from bright field tem imaging: beam precession assisted electron tomography. *Ultramicroscopy*, 111(9):1504–1511. [137](#)
- Rice, U. (2015). Compressive sensing resources @ONLINE. April 2014. Url: <http://dsp.rice.edu/cs>. [97](#)
- Roberts, P., Chapman, J., and MacLeod, A. (1982). A CCD-based image recording system for the CTEM. *Ultramicroscopy*, 8(4):385–396. [15](#)
- Rockmore, D. N. (2000). The FFT: An algorithm the whole family can use. *Computing in Science & Engineering*, 2(1):60–64. [58](#)
- Rose, H. (1971). Properties of spherically corrected achromatic electron lenses(spherically corrected electron lenses with improved resolving capacity and aberration compensation). *Optik,(Stuttgart)*, 33(1):1–24. [12](#)

- Ruska, E. (1987). The development of the electron microscope and of electron microscopy (nobel lecture). *Angewandte Chemie International Edition in English*, 26(7):595–605. [10](#), [11](#)
- Saghi, Z., Holland, D. J., Leary, R., Falqui, A., Bertoni, G., Sederman, A. J., Gladden, L. F., and Midgley, P. A. (2011). Three-dimensional morphology of iron oxide nanoparticles with reactive concave surfaces. a compressed sensing-electron tomography (cs-et) approach. *Nano Letters*, 11(11):4666–4673. [73](#), [89](#), [91](#), [92](#), [93](#), [97](#), [118](#)
- Saghi, Z., Xu, X., and Mbus, G. (2008). Electron tomography of regularly shaped nanostructures under non-linear image acquisition. *J Microsc*, 232:186–95. [154](#)
- Saghi, Z., Xu, X., and Möbus, G. (2009). Model based atomic resolution tomography. *Journal of Applied Physics*, 106(2):024304. [38](#)
- Saghi, Z., Xu, X., Peng, Y., Inkson, B., and Möbus, G. (2007). Three-dimensional chemical analysis of tungsten probes by energy dispersive x-ray nanotomography. *Applied Physics Letters*, 91(25):251906. [26](#)
- Saxton, W., Baumeister, W., and Hahn, M. (1984). Three-dimensional reconstruction of imperfect two-dimensional crystals. *Ultramicroscopy*, 13(1):57–70. [52](#)
- Sayood, K. et al. (2002). Statistical evaluation of image quality measures. *Journal of Electronic imaging*, 11(2):206–223. [109](#)
- Scarano, D., Bertarione, S., Cesano, F., Spoto, G., and Zecchina, A. (2004). Imaging polycrystalline and smoke mgo surfaces with atomic force microscopy: a case study of high resolution image on a polycrystalline oxide. *Surface science*, 570(3):155–166. [74](#)
- Schaffer, B., Grogger, W., and Kothleitner, G. (2004). Automated spatial drift correction for efem image series. *Ultramicroscopy*, 102(1):27–36. [129](#)
- Scherzer, O. (1936). Über einige fehler von elektronenlinsen. *Zeitschrift für Physik*, 101(9):593–603. [12](#), [32](#)
- Scott, J., Thomas, P., MacKenzie, M., McFadzean, S., Wilbrink, J., Craven, A., and Nicholson, W. (2008a). Near-simultaneous dual energy range eels spectrum imaging. *Ultramicroscopy*, 108(12):1586–1594. [30](#)

- Scott, J., Thomas, P., MacKenzie, M., McFadzean, S., Wilbrink, J., Craven, A., and Nicholson, W. (2008b). Near-simultaneous dual energy range EELS spectrum imaging. *Ultramicroscopy*, 108(12):1586–1594. [139](#)
- Scott, M., Chen, C.-C., Mecklenburg, M., Zhu, C., Xu, R., Ercius, P., Dahmen, U., Regan, B., and Miao, J. (2012). Electron tomography at 2.4-angstrom resolution. *Nature*, 483(7390):444–447. [38](#), [103](#)
- Sidky, E. Y. and Pan, X. (2008). Image reconstruction in circular cone-beam computed tomography by constrained, total-variation minimization. *Physics in medicine and biology*, 53(17):4777. [97](#)
- Smith, D. and Welch, E. (2011). Non-sparse phantom for compressed sensing MRI reconstruction. In *International Society for Magnetic Resonance in Medicine 19th Scientific Meeting-ISMIRM*, volume 11, page 2845. [113](#), [118](#), [119](#)
- Spence, J. (1981). *Experimental high-resolution electron microscopy*. Monographs on the physics and chemistry of materials. Clarendon Press. [11](#)
- Spencer, G. and Duquette, D. (1998). The role of vanadium carbide traps in reducing the hydrogen embrittlement susceptibility of high strength alloy steels. Technical report, DTIC Document. [140](#)
- Spoto, G., Gribov, E., Ricchiardi, G., Damin, A., Scarano, D., Bordiga, S., Lamberti, C., and Zecchina, A. (2004). Carbon monoxide mgo from dispersed solids to single crystals: a review and new advances. *Progress in Surface Science*, 76(35):71–146. [74](#)
- Stevens, A., Yang, H., Carin, L., Arslan, I., and Browning, N. D. (2014). The potential for Bayesian compressive sensing to significantly reduce electron dose in high-resolution stem images. *Microscopy*, 63(1):41–51. [92](#)
- Subramaniam, S., Bartesaghi, A., Liu, J., Bennett, A. E., and Sougrat, R. (2007). Electron tomography of viruses. *Current opinion in structural biology*, 17(5):596–602. [2](#)
- Sugimori, H., Nishi, T., and Jinnai, H. (2005). Dual-axis electron tomography for three-dimensional observations of polymeric nanostructures. *Macromolecules*, 38(24):10226–10233. [66](#)

- Szlam, A., Gregor, K., and LeCun, Y. (2012). Fast approximations to structured sparse coding and applications to object classification. In *European Conference on Computer Vision*, pages 200–213. Springer. [107](#)
- Szost, B., Vegter, R., and Rivera-Díaz-del Castillo, P. E. (2013). Hydrogen-trapping mechanisms in nanostructured steels. *Metallurgical and Materials Transactions A*, 44(10):4542–4550. [140](#)
- Tao, Y. and Cockshott, W. (2004). 3d microscopic image coding by finite-state vector quantization in an enhanced image pyramid. In *SPIE on Medical Imaging*, volume 2004, pages 1895–1905. [100](#)
- Thomas, J. M. and Midgley, P. A. (2011). The modern electron microscope: A cornucopia of chemico-physical insights. *Chemical Physics*, 385(1):1–10. [21](#)
- Thomas, P. and Twesten, R. (2012). A Simple Model Based Approach for Robust Quantification of EELS Spectra and Spectrum-Images. *Microsc Microanal*, 18(S2):968–969. [139](#)
- Thomson, G. P. (1966). *JJ Thomson, discoverer of the electron*. Number 48. Anchor Books. [10](#)
- Tibshirani, R. (1996). Regression shrinkage and selection via the lasso. *Journal of the Royal Statistical Society. Series B (Methodological)*, pages 267–288. [97](#)
- Tocheva, E. I., Li, Z., and Jensen, G. J. (2010). Electron cryotomography. *Cold Spring Harbor perspectives in biology*, 2(6):a003442. [160](#)
- Tocheva, E. I., Matson, E. G., Cheng, S. N., Chen, W. G., Leadbetter, J. R., and Jensen, G. J. (2014). Structure and expression of propanediol utilization microcompartments in *acetonebacterium* longum. *Journal of bacteriology*, 196(9):1651–1658. [160](#), [161](#)
- Tocheva, E. I., Matson, E. G., Morris, D. M., Moussavi, F., Leadbetter, J. R., and Jensen, G. J. (2011). Peptidoglycan remodeling and conversion of an inner membrane into an outer membrane during sporulation. *Cell*, 146(5):799–812. [161](#)
- Tong, J., Arslan, I., and Midgley, P. (2006). A novel dual-axis iterative algorithm for electron tomography. *Journal of Structural Biology*, 153(1):55–63. [49](#)

- Tong, J. and Midgley, P. (2006). A novel dual-axis reconstruction algorithm for electron tomography. *Journal of Physics: Conference Series*, 26(1):33. [49](#)
- Tosic, I. and Frossard, P. (2011). Dictionary learning. *Signal Processing Magazine, IEEE*, 28(2):27–38. [100](#)
- Tran, E. E., Borgnia, M. J., Kuybeda, O., Schauder, D. M., Bartesaghi, A., Frank, G. A., Sapiro, G., Milne, J. L., and Subramaniam, S. (2012). Structural mechanism of trimeric hiv-1 envelope glycoprotein activation. *PLoS Pathog*, 8(7):e1002797. [135](#)
- Tran, E. E., Simmons, J. A., Bartesaghi, A., Shoemaker, C. J., Nelson, E., White, J. M., and Subramaniam, S. (2014). Spatial localization of the ebola virus glycoprotein mucin-like domain determined by cryo-electron tomography. *Journal of virology*, 88(18):10958–10962. [49](#), [133](#), [134](#)
- Treacy, M. M. (2011). Z dependence of electron scattering by single atoms into annular dark-field detectors. *Microscopy and Microanalysis*, 17(06):847–858. [25](#)
- Tropp, J. A. (2004). Greed is good: Algorithmic results for sparse approximation. *Information Theory, IEEE Transactions on*, 50(10):2231–2242. [97](#)
- Tropp, J. A. and Gilbert, A. C. (2007). Signal recovery from random measurements via orthogonal matching pursuit. *Information Theory, IEEE Transactions on*, 53(12):4655–4666. [97](#), [101](#)
- Tropp, J. A. and Wright, S. J. (2010). Computational methods for sparse solution of linear inverse problems. *Proceedings of the IEEE*, 98(6):948–958. [97](#), [103](#)
- Tsaig, Y. and Donoho, D. L. (2006). Extensions of compressed sensing. *Signal processing*, 86(3):549–571. [93](#)
- Uchic, M. D., Holzer, L., Inkson, B. J., Principe, E. L., and Munroe, P. (2011). Three-dimensional microstructural characterization using focused ion beam tomography. *32(5):408–416*. [38](#)
- van Bavel, S. S. and Loos, J. (2010). Volume organization of polymer and hybrid solar cells as revealed by electron tomography. *Advanced Functional Materials*, 20(19):3217–3234. [51](#), [66](#), [68](#), [85](#), [86](#), [109](#)

- Van-Den-Berg, E. and Friedlander, M. P. (2008). Probing the pareto frontier for basis pursuit solutions. *SIAM Journal on Scientific Computing*, 31(2):890–912. [103](#)
- Van-den Broek, W., Rosenauer, A., Goris, B., Martinez, G., Bals, S., Van-Aert, S., and Van-Dyck, D. (2012). Correction of non-linear thickness effects in haadf stem electron tomography. *Ultramicroscopy*, 116:8–12. [57](#), [154](#)
- Van-Dyck, D., Jinschek, J. R., and Chen, F.-R. (2012). /big bang/'tomography as a new route to atomic-resolution electron tomography. *Nature*, 486(7402):243–246. [38](#)
- Varah, J. (1979). A practical examination of some numerical methods for linear discrete ill-posed problems. *SIAM Review*, 21(1):100–111. [60](#)
- Verbeeck, J. and Van-Aert, S. (2004). Model based quantification of EELS spectra. *Ultramicroscopy*, 101(2-4):207–224. [139](#)
- Vincent, L. and Soille, P. (1991). Watersheds in digital spaces: an efficient algorithm based on immersion simulations. *IEEE Transactions on Pattern Analysis & Machine Intelligence*, 6:583–598. [69](#)
- Volkman, N. (2010). Chapter two - methods for segmentation and interpretation of electron tomographic reconstructions. In Jensen, G. J., editor, *Cryo-EM, Part C: Analyses, Interpretation, and Case studies*, volume 483 of *Methods in Enzymology*, pages 31–46. Academic Press. [69](#)
- Vollmer, W. (2012). Bacterial outer membrane evolution via sporulation. *Nature chemical biology*, 8(1):14–18. [160](#)
- Vulović, M., Ravelli, R. B., van Vliet, L. J., Koster, A. J., Lazić, I., Lücken, U., Rullgård, H., Öktem, O., and Rieger, B. (2013). Image formation modeling in cryo-electron microscopy. *Journal of structural biology*, 183(1):19–32. [68](#)
- Wang, X., Lockwood, R., Malac, M., Furukawa, H., Li, P., and Meldrum, A. (2012). Reconstruction and visualization of nanoparticle composites by transmission electron tomography. *Ultramicroscopy*, 113:96–105. [66](#)
- Wang, Z., Bovik, A. C., Sheikh, H. R., and Simoncelli, E. P. (2004). Image quality assessment: from error visibility to structural similarity. *Image Processing, IEEE Transactions on*, 13(4):600–612. [76](#), [108](#), [109](#), [125](#), [150](#)

- Weickert, J. (1998). *Anisotropic diffusion in image processing*, volume 1. Teubner Stuttgart. 79
- Weyland, M. and Midgley, P. A. (2003). Extending energy-filtered transmission electron microscopy (efTEM) into three dimensions using electron tomography. *Microscopy and Microanalysis*, 9(6):542–555. 29, 121, 122
- Weyland, M. and Midgley, P. A. (2004). Electron tomography. *Materials Today*, 7(12):32–40. 21, 40
- Weyland, M., Midgley, P. A., and Thomas, J. M. (2001). Electron tomography of nanoparticle catalysts on porous supports: a new technique based on rutherford scattering. *The Journal of Physical Chemistry B*, 105(33):7882–7886. 25, 68
- WHO (2015). *Ebola situation report*. World Health Organization. URL: <http://apps.who.int/ebola/ebola-situation-reports>. 130
- Williams, D. B. and Carter, C. B. (2009). *Transmission Electron Microscopy: A Textbook for Materials Science*. Springer, NY. 2, 8, 12, 13, 15, 16, 24, 26, 27, 28, 34, 36, 43, 44, 46, 74, 103
- Wilson, K. (1993). Nobel lectures in physics 1981–1990. 11
- Winkler, H. and Taylor, K. A. (2006). Accurate marker-free alignment with simultaneous geometry determination and reconstruction of tilt series in electron tomography. *Ultramicroscopy*, 106(3):240–254. 55
- Wipf, D. P. and Rao, B. D. (2004). Sparse Bayesian learning for basis selection. *Signal Processing, IEEE Transactions on*, 52(8):2153–2164. 97
- Wolf, D., Lubk, A., and Lichte, H. (2014). Weighted simultaneous iterative reconstruction technique for single-axis tomography. *Ultramicroscopy*, 136:15–25. 64
- Wright, J., Ma, Y., Mairal, J., Sapiro, G., Huang, T. S., and Yan, S. (2010). Sparse representation for computer vision and pattern recognition. *Proceedings of the IEEE*, 98(6):1031–1044. 101

- Xu, R., Chen, C.-C., Wu, L., Scott, M., Theis, W., Ophus, C., Bartels, M., Yang, Y., Ramezani-Dakhel, H., Sawaya, M. R., et al. (2015). Three-dimensional coordinates of individual atoms in materials revealed by electron tomography. *Nature materials*, 14(11):1099–1103. [38](#)
- Yaguchi, T., Konno, M., Kamino, T., and Watanabe, M. (2008). Observation of three-dimensional elemental distributions of a si device using a 360-tilt {FIB} and the cold field-emission {STEM} system. *Ultramicroscopy*, 108(12):1603–1615. [50](#), [51](#)
- Yang, X. (2012). *Semiconducting Polymer Composites: Principles, Morphologies, Properties and Applications*. John Wiley & Sons. [22](#)
- Yedra, L., Eljarrat, A., Arenal, R., Pellicer, E., Cabo, M., Lopez-Ortega, A., Estrader, M., Sort, J., Baro, M. D., Estradé, S., et al. (2012a). Eel spectroscopic tomography: Towards a new dimension in nanomaterials analysis. *Ultramicroscopy*, 122:12–18. [137](#), [138](#)
- Yedra, L., Eljarrat, A., Arenal, R., Pellicer, E., Cabo, M., Lopez-Ortega, A., Estrader, M., Sort, J., Baro, M. D., Estrade, S., et al. (2012b). Eel spectroscopic tomography: Towards a new dimension in nanomaterials analysis. *Ultramicroscopy*, 122:12–18. [137](#), [138](#)
- Yedra, L., Eljarrat, A., Rebled, J. M., López-Conesa, L., Dix, N., Sánchez, F., Estradé, S., and Peiró, F. (2014). Eels tomography in multiferroic nanocomposites: from spectrum images to the spectrum volume. *Nanoscale*, 6(12):6646–6650. [137](#)
- Yin, F.-F., Giger, M. L., and Doi, K. (1990). Measurement of the presampling modulation transfer function of film digitizers using a curve fitting technique. *Medical physics*, 17(6):962–966. [78](#)
- Zach, J. and Haider, M. (1995). Correction of spherical and chromatic aberration in a low voltage sem. *Optik*, 98(3):112–118. [12](#)
- Zampighi, G., Zampighi, L., Fain, N., Wright, E., Cantele, F., and Lanzavecchia, S. (2005). Conical tomography ii: A method for the study of cellular organelles in thin sections. *Journal of Structural Biology*, 151(3):263–274. [52](#)

- Zhang, J., Liu, S., Xiong, R., Ma, S., and Zhao, D. (2013). Improved total variation based image compressive sensing recovery by nonlocal regularization. In *2013 IEEE International Symposium on Circuits and Systems (ISCAS2013)*, pages 2836–2839. IEEE. [97](#)
- Zheng, Q. S., Braunfeld, M. B., Sedat, J. W., and Agard, D. A. (2004). An improved strategy for automated electron microscopic tomography. *Journal of structural biology*, 147(2):91–101. [53](#)
- Zheng, S. Q., Matsuda, A., Braunfeld, M. B., Sedat, J. W., and Agard, D. A. (2009). Dual-axis target mapping and automated sequential acquisition of dual-axis em tomographic data. *Journal of structural biology*, 168(2):323–331. [53](#)
- Zheng, S. Q., Sedat, J., and Agard, D. (2010). Chapter twelve-automated data collection for electron microscopic tomography. *Methods in enzymology*, 481:283–315. [53](#)
- Zhou, C., Liu, Z., Du, X., Mitchell, D. R. G., Mai, Y.-W., Yan, Y., and Ringer, S. (2012). Hollow nitrogen-containing core/shell fibrous carbon nanomaterials as support to platinum nanocatalysts and their tem tomography study. *Nanoscale research letters*, 7(1):1–11. [166](#)
- Ziese, U., Kbel, C., Verkleij, A. J., and Koster, A. J. (2002). Three-dimensional localization of ultrasmall immuno-gold labels by haadf-stem tomography. *Journal of Structural Biology*, 138(12):58–62. [68](#)

Index

- aberration—corrected, 37
- Acetone, 160
- ADF detector, 14
- ADF—STEM, 25
- algorithms, 97
- aliasing, 96, 112
- amorphous materials, 23
- anisotropic, 66
- anisotropic diffusion, 79
- artifacts, 47, 160
- atom—probe tomography, 36
- Bacteria, 159
- beam—induced changes, 31
- beam-sensitive specimens, 52
- BF—TEM, 24
- Bragg scattering, 23
- carbon nanofibers, 166
- catalysts, 166
- CCD, 14, 15, 28, 30
- central slice through, 41
- chemical fixing, 160
- chemically sensitive, 137
- chromatic aberration, 33
- Chronoamperometry, 168
- coaxial structure, 168
- collection angle, 25
- compressive sensing, 95
- condenser system, 12
- core—loss, 30
- Coulombic force, 18
- cross-correlation, 55
- cryo-EM, 14, 36
- cryo-tomography, 160
- crystalline materials, 23
- CS theory, 97
- CS-phantom, 113
- CSTV, 124, 126
- DART, 64
- dehydration, 160
- detection quantum efficiency, 16
- diffraction contrast, 23
- diffraction pattern, 13
- Direct detectors, 14
- Discrete Cosines Transform, 97
- DLET, 109, 125, 126, 146, 161
- Dual—axis, 49
- dual-tilt, 53
- DualEELS, 31, 138, 141
- EBOV, 130
- EDX, 26
- EDXS, 26
- EELS, 26, 138
- EELS spectrum, 27
- EF-TEM, 28

- EFTEM, 121
- Electron gun, 12
- electron microscopy, 10
- elongation, 66, 84, 112
- Ernst Ruska, 9
- feature-based methods, 55
- Feline Calicivirus, 69
- FIB, 50
- fiducial marker-based alignment, 54
- field emission gun, 12
- finite-differences, 97
- fluorescent screen, 14
- focused ion beam, 36, 129
- Fourier, 41
- fuel cells, 165
- GIF, 14, 30
- GIF Quantum detector, 30
- glycoprotein spikes, 133
- Gram-negative, 160
- HAADF–STEM, 25, 74
- Hamming, 42
- high–loss, 27
- high-energy beam, 17
- ill-posed, 61
- IMOD, 76, 134, 146
- inelastic, 27
- inner–shell, 27
- ionization damage, 31
- JEOL ARM200F, 14, 74, 141
- knock-on damage, 52
- Landweber SIRT, 63
- low–loss region, 27
- low–loss spectrum, 30
- Magnesium Oxide, 74
- magnetic prism, 28
- magnetic resonance imaging, 36
- marker-free alignment, 55
- mass–thickness, 23
- mass-thickness contrast, 56
- Max Knoll, 9
- microcompartments, 161
- mis-alignment, 89
- missing wedge, 46, 50, 66, 84, 116
- Nobel Prize, 10
- NUFFT, 58
- numerical aperture, 37
- NVIDIA, 111
- objective lens, 13
- octahedra, 148
- on–axis holder, 50
- Otsu method, 68
- parameters, 106
- plastic embedding, 160
- prior knowledge, 64, 102
- Projection Requirement, 56
- projection requirement, 137
- PSNR, 111, 150
- Pt catalyst, 168
- Radon space, 39
- Radon transform, 56
- Ram–lack, 42
- resolution, 86
- Rutherford scattering, 18, 25
- SAD, 13

-
- Saxton, 51
- scanning confocal electron microscopy, 37
- scintillator, 15
- sectioning, 160
- segmentation, 168
- semi-convergence, 63
- SerialEM, 166
- SIFT, 145
- single axis, 39
- single particle microscopy, 36
- sinogram, 58, 102, 111
- SIRT, 72, 146, 161
- SNR ratio, 30
- solar cell, 121
- sparse, 95
- spatial resolution, 17
- specimen holder, 54
- Spectrometer, 14
- spherical aberration, 33
- sporulation, 159
- SSIM, 76, 111, 125, 150
- staining, 160
- STEM, 54
- STEM detector, 25
- stereo microscopy, 36
- Stereology, 36
- SVD, 59
- thermionic gun, 12
- Tikhonov, 61
- Total Variation, 97
- Truncated SVD, 61
- vacuum chamber, 13
- vanadium carbide, 140
- virtual markers, 56, 145
- WBP, 57, 72
- Z-contrast, 24
- zero-loss peak, 27